DISS. ETH NO. 25033

Creeping constrained landslides under extreme environmental and seismic conditions

A thesis submitted to attain the degree of

DOCTOR OF SCIENCES of ETH ZURICH

(Dr. sc. ETH Zurich)

presented by

PHILIPP WOLFGANG WALTER OBERENDER

MSc ETH in Civil Engineering, ETH Zurich

born on 27.04.1986

citizen of

Germany

accepted on the recommendation of :

Prof. Dr. Alexander Puzrin

Prof. Dr. Dimitri Val

Prof. Dr. Ioannis Anastasopoulos

2018

Acknowledgement

My first and foremost gratitude goes to Prof. Dr. Alexander Puzrin for giving me the chance to work on this interesting research problem and for his support during this work. Without his geotechnical expertise this work would not have been possible. I am very grateful to him for letting me grow professionally but also personally.

I would also like to express my gratitude to my co-advisor Prof. Dr. Dimitri Val whose pointers to literature, comments and discussion have always been of great value. Also a special thanks for hosting me in Edinburgh.

Also, I am deeply grateful to my co-examiners Prof. Dr. Ioannis Anastasopoulos and Prof. Dr. Dimitri Val for reading and examining this thesis.

I am very grateful to Ernst Bleiker who helped me greatly with my experiments during my time at IGT which made this work possible. The same gratitude also goes to Heinz Buschor and Andreas Kieper who maintain the lab and supported my experimental and field work. I am grateful to Rene Rohr for his work in the laboratory and in the field.

I would like to thank Ingrid Mettler and Esther Schilling for their help in many administrative tasks.

I am deeply grateful to Dr. Markus Schwager, Dr. Dominik Hauswirth, Dr. Pascal Minder, Balz Friedli and Andreas Stöcklin for the many valuable discussions and their inspirations throughout the years but also for their friendship. Also, I am thankful for the ideas, the support and discussions with my colleagues: Dr. Michael Iten, Dr. Pavel Trapper, Dr. Carlo Rabaiotti, Dr. Alessandra Carrera, Ivo Sterba, Dr. Markus Caprez, Dr. Andreas Schmid, Dr. Andreas Trabesinger, Frank Fischli, David Perozzi, Simon Hug, Cristian Buss, Marc Kohler and Roman Hettelingh.

I consider myself very lucky to have been a part of this great group and appreciate the time that I shared with you.

Finally, I would like to express my deepest and sincerest gratitude to my wife, Stella Schieffer, my parents, Gabriele Vitzthum-Oberender and Carl-Heinz Oberender, and my sister, Sofie Oberender. Without their constant support I would not have reached this point. Thank you.

Abstract

Creeping landslides are a common natural hazard in mountainous areas. Due to the growth of settlements and infrastructure in the mountains the amount of people and structures threatened by this hazard grows continuously.

However, to date there are no established methodologies that allow capturing the behavior of creeping landslides and modelling risks from all possible loading scenarios remains challenging. In particular capturing the effect of pore pressure fluctuations dependent on weather events and climate change is important. Also, earthquake loading in seismically active areas (in Switzerland for example in the Cantons Valais or Grisons) makes it necessary to model the influence of seismically induced ground shaking on creeping landslides.

When it comes to models that reproduce the long-term behavior of creeping landslides under the influence of precipitation changes, the difference in scales between reality and laboratory tests makes basing models for creeping landslides purely on laboratory experiments difficult. Therefore this work involves field observations of the landslides behavior as much as possible and complements those with laboratory tests if available. To facilitate this herein called "observation guided constitutive modelling (OGCM)" approach the creeping landslide is simplified as a sliding body moving on a slip surface and treated as a series of macro element "tests" which allow deriving material models directly from observations. At the foot the landslide may be constrained, i.e. deformations come to a still. The constitutive models of the slip surface and the sliding body are derived from combinations of simple visco-elastic-plastic models and allow reproducing a number of phenomena such as elastic deformation, time dependent creep, relaxation of stresses but also failure including hardening or softening. The approach allows finding a model for the case of the Brattas landslide in St. Moritz which due to its complex nature with changing behavior along its length and over time is a challenging case to model.

Assessing seismically induced deformations of a creeping landslide cannot follow this approach since observations of landslides during earthquakes are not available. Therefore the model proposed herein uses knowledge about the landslide from non-seismic loading situations and laboratory tests of the cyclic behavior of the landslide material. The approach chosen is an extension to the well-known Newmark's approach. The landslide is again modelled as sliding mass sitting on layers of weak material in which the actual slip surface is situated. The model allows accounting for the development of excess pore pressure in parts of the sliding body and rate effects on the actual slip surface. For both phenomena constitutive models have been derived and implemented in the model formulation.

Ultimately these models aim to allow for risk analysis of creeping landslides. Therefore simple exposure models are derived and with the models of the landslide, hazard in terms of displacement of the landslide can be produced. The estimation of risk for structures is discussed and for the example case of the leaning tower in St. Moritz derived.

Zusammenfassung

Kriechende Rutschungen sind eine Naturgefahr die in vielen Gebirgsregionen angetroffen werden kann. Da Siedlungen und Infrastruktur auch in den Bergen wachsen, nimmt auch die Zahl an Personen und Bauwerken zu die durch diese Naturgefahr bedroht werden.

Trotz dieser Tatsache konnte bis heute keine Methode etabliert werden, die es erlaubt das Verhalten von kriechenden Rutschenden zu reproduzieren und passende Modelle zu kalibrieren bleibt eine Herausforderung. Die Einwirkungen auf kriechende Rutschungen sind einerseits Variationen des Porenwasserdrucks die durch Niederschlag hervorgerufen werden, auf der anderen Seite befinden sich viele dieser Rutschungen in seismisch aktiven Gebieten (in der Schweiz z.B. der Kanton Wallis), daher ist die Belastung durch Erdbeben eine weiteres Einwirkungsszenario welches untersucht werden muss. In dieser Arbeit wurden Modelle für beide Situationen erarbeitet und untersucht.

Der Grössenunterschied zwischen Materialproben die im Labor untersucht werden können und der tatsächlichen Grösse des Problems macht es sehr schwer Modelle für das Langzeitverhalten von kriechenden Rutschungen ausschliesslich durch Laborversuche zu definieren. Daher wird in dieser Arbeit vorgeschlagen, für Modelle kriechender Rutschungen soweit als möglich Beobachtungen des tatsächlichen Verhaltens der Rutschung zu Rate zu ziehen und diese durch Laborversuche zu ergänzen falls Phänomene nicht durch Beobachtungen erfasst werden können. Um diesen s.g. „observation guided constitutive modelling" Ansatz zu ermöglichen, wird die Rutschung vereinfacht als Rutschmasse auf einer Gleitfläche angenommen als Serie von Grossversuchen behandelt. Am Fusse der Rutschung kann die Rutschung blockiert sein, d.h. sie kommt zum Stillstand. Die Materialmodelle für die Rutschmasse und die Gleitfläche werden durch Kombinationen einfacher visko-elastischer-plastischer Elemente beschreiben und erlauben es eine Reihe von Phänomenen abzubilden, wie z.B. elastische Verformungen, zeitabhängiges Kriechen, Spannungsrelaxation oder auch ein Versagen der Rutschmasse mit ver- oder entfestigendem Verhalten. Durch dieses Vorgehen lässt sich ein Modell finden welches das Verhalten der Brattas Rutschung in St. Moritz abbilden kann. Durch ihre Komplexität mit sich änderndem Verhalten entlang der Rutschung aber auch über die Zeit hinweg stellt sie eine besondere Herausforderung für das Erarbeiten geeigneter Modelle dar.

Dem entgegen, kann die Reaktion von kriechenden Rutschungen auf die Einwirkung durch Erdbeben nicht durch die Analyse von Beobachtungsdaten ermittelt werden, da solche Daten nicht existieren. Aus diesem Grund wird hier vorgeschlagen Wissen über die Rutschung unter normalen Umständen mit Daten aus Laborversuchen über das zyklische Verhalten des

Rutschmaterials zu kombinieren. Der hier gezeigte Ansatz kann als Erweiterung des bekannten „Newmark Rutschblock Modells" verstanden werden. Die Rutschung wird wiederum schlicht als Rutschblock modelliert welcher auf einer Schicht aus geschwächtem Material bewegt in der sich die eigentliche Gleitfläche gebildet hat. Das Modell erlaubt es die Entwicklung von Porenwasserüberdrücken, sowie das Geschwindigkeitsabhängige Verhalten des Scherwiederstandes entlang der Gleitfläche zu berücksichtigen. Für beide Phänomene wurden Materialmodelle entwickelt und in das Model integriert.

Letztendlich zielen die Modelle darauf ab Risikoanalysen für kriechende Rutschungen zu ermöglichen. Um dies zu tun wurden einfache Modelle für Einwirkungen auf die Rutschung entwickelt und zusammen mit den Modellen für die Rutschung selbst kann so die Bedrohung durch die Rutschung in Form von zu erwartenden Verformungen abgeschätzt werden. Möglichkeiten für die Risikonalyse von Bauwerken in kriechenden Rutschungen werden diskutiert und am Beispiel des schiefen Turms von St. Moritz gezeigt.

Table of contents

List of figures

List of tables

1 Introduction

1.1 Rationale of the thesis

Creeping landslides are a common threat in mountainous areas. These landslides are characterized by very slow movements caused by seasonal changes in environmental conditions, continuous viscous flow in the sliding soil mass, rate-dependent shear resistance on the sliding surface, or a combination of these factors. In the Swiss alps, a total of 6% of the country's area is estimated to be affected by slope instabilities (Lateltin, 1997). At the same time, growing urbanization in mountainous areas and more need for infrastructure leads to more and more conflicts between manmade structures and permanent (creeping) landslides. Examples of such conflicts are:

(i)   the deflection of roads or hydropower pipelines whilst crossing such landslides;

(ii)   damages to houses that have been knowingly or unknowingly built into a landslide;

(iii)   the threat posed by creeping landslides along the banks of an artificial reservoir lake.

All these examples illustrate cases in which the creeping slope continuously damages structures built inside it but also poses the threat of a potentially dramatic acceleration. Therefore, an understanding of the mechanisms governing such landslides is crucial in order to

(i)   judge the risk for already existing structures,

(ii)   allow risk estimations for future development projects and

(iii)   provide guidelines for proper construction of new structures or reinforcement of existing ones.

The necessary mechanical understanding is not limited to "normal" circumstances, i.e. the behaviour of the landslide for average loading scenarios, but needs to involve situations in which the landslide experiences exceptional loading, e.g. heavy rain events or earthquakes.

It is not easy to derive tools to perform the above-mentioned tasks, since the mechanics of creeping landslides can be very complex with varying behaviour both along the length and over the depth of the landslide, often unknown geometry, and large uncertainties regarding the properties of the different features governing the landslide. Therefore, defining a priori models that account for all these challenges and uncertainties is almost impossible. Consequently, in order to derive robust models, one should also use observations of the landslide whenever available.

The complexity of the problem, which includes phenomena such as rate dependency that until today have never been quantified reliably, in combination with large uncertainties, can also make it difficult to use standard tools such as finite element method (FEM). Deriving models that try to reproduce 2D or 3D geometry, time-dependent material parameters, hydro-mechanical coupling, large deformations and possibly interaction between soil and built structures becomes an almost impossible task and makes models extremely inflexible. It seems more promising to use an approach which simplifies the landslide, reducing it to a number of important elements in order to study their influence and interaction. Such simplified models can help to build better understanding of the landslide, can be updated if more information becomes available and may even be used to predict the landslide's development.

Beyond that, the task becomes even more challenging, because, for events that occur only rarely (such as the seismic loading of creeping landslides), almost no observational data is available. Overall, the effects of seismic exposure on permanent landslides have had hardly any attention, though many creeping landslides are situated in seismically active areas. Here, fundamental mechanical models, based upon knowledge from observations during "non-exceptional" loading and experimental insight into the material behaviour, are the only way of gaining some insight into the behaviour of the landslide for such loading situations.

In both loading cases, models foster knowledge regarding further necessary experimental investigation and observational methods, and allow decisions on where further research should focus its attention. Furthermore, these models allow some quantification as to what reactions can be expected from a creeping landslide given a particular exposure.

1.2 Main objectives of the thesis

The goal of this thesis is to improve the understanding of the mechanisms of constrained creeping landslides and their reaction to precipitation or seismic events. This understanding is intended to be used to improve the risk assessment for creeping landslides.

To achieve these goals, simple phenomenological models for the landslide in different loading situations are formulated. The aim is to develop tools that allow one to derive models based both on data from laboratory experiments and, if available, on field observations of the landslide. Basing the models not simply on laboratory data aims to make them more reliable for simulations of large-scale field behaviour.

The process of calibrating and applying the models will be demonstrated using the well-documented case of the Brattas landslide in St. Moritz. The complexity of the Brattas, with varying behaviour both over time and along the landslide, makes it a good example to demonstrate the process of model calibration for models of steady and transient state (where transient in this work means the landslide behaviour under the influence of precipitation) and to illustrate the process of hazard analysis for the Brattas landslide.

Since data with respect to the response of a creeping landslide to seismic effects is almost non-existent, this thesis intends to derive a model that combines the knowledge of the landslide under steady and transient state conditions with knowledge from cyclic loading tests of the materials from the landslide.

For all proposed models, the goal is to keep them simple enough to foster understanding of influence and interactions of various parts of the model and to allow them to be used in hazard analysis.

Lastly, this thesis investigates how the information that has been gained about the behaviour of creeping landslides could be used as input for the assessment of risk for structures in such landslides.

1.3 Structure of the thesis

This thesis is structured in four main parts containing in total 11 chapters. The four main parts treat the following topics:

Part I: Literature review and introduction of the example case

Part I is split into an overview of work that has been done with respect to the topics investigated here (chapter 2) and the introduction of the case study that has been used in all further chapters to apply the results of the investigations (chapter 3). Herein all the available data about the example case, the Brattas landslide in St. Moritz, is summarized to avoid unnecessary repetition of the data when used in other parts of the thesis.

Part II: Development of a model to analyse the steady and transient state of creeping landslides

Part II proposes an approach to deriving a phenomenological model for creeping landslides under steady state and transient conditions (weather influence) (chapter 4). The approach proposes to heavily involve observations of the landslide behaviour and to use a flexible modelling approach that allows for updates of the model if or when new phenomena are observed. Application of the approach is demonstrated using data for the Brattas landslide (chapter 5).

Part III: Analysis of seismic impact on creeping slopes

Part III proposes a conceptual model that allows investigation of the effect of seismic loading on permanent landslides (chapter 6). Constitutive models are shown for the materials of the landslide parts that are assumed to dominate the behaviour during seismic loading (the slip surface (chapter 7) and the weak soil material around it (chapter 8)). Lastly, application of the model for seismic loading of the creeping slope is demonstrated (chapter 9).

Part IV: Hazard and risk assessment for creeping slopes and conclusions

The last part completes the investigations by proposing ideas on how to link the mechanical models with environmental exposures to produce hazard scenarios. Further, some potential ways to analyse vulnerability and consequences without relying on empirical relations are given (chapter 10).

The final chapter summarizes the conclusions drawn for this work and proposes some ideas for future research (chapter 11).

Part I: Background information and introduction of the example case

Abstract

Modelling creeping landslides has been a focus of geotechnical research for some time, which is why there are many proposed approaches to how this specific natural hazard could be assessed. Part I aims to summarize several important ideas proposed in literature in order to provide context and methods of comparison for the models and results derived within the scope of this thesis.

Additionally, the second half of Part I introduces the case study that has provided both the motivation and source of information for large parts of this study: the Brattas landslide in St. Moritz. Summarizing all available information that has been available before or has been found during this study should provide a complete picture of the data that forms the basis of the models proposed in later chapters.

2 Background and state of the art

2.1 Early investigations and range of topics

Being an important problem, the investigation of slow permanent (creeping) landslides has been a subject of interest in geotechnical research for some time (Bjerrum, 1967; Skempton, 1964; Skempton and Larochel, 1965; Terzaghi, 1950, e.g. 1936). Even today, deriving suitable models for creeping landslides in particular for extraordinary loading situations is still not an easy task, and no "standard" procedure has been established. This chapter aims to provide a short summary of available information on the topics that have been treated within the scope of this thesis. The chapter is structured to give background and state of the art information for the following topics:

(i)   First, background information on models for landslide under "normal", i.e. steady state and transient (i.e. influence of precipitation) conditions, is provided.

(ii)   Second, the few found studies on the effect of extreme weather phenomena and climate change on creeping landslides are summarized.

(iii)   The third part shows the work that has been done regarding seismic loading of creeping slopes. A short review on some material models that can be used in the assessment of earthquake landslide interaction is also given.

(iv)   The last part outlines some approaches to the assessment of risk due to slow landslides.

2.2 Modelling creeping landslides under steady state and transient conditions

Understanding of failure mechanisms of creeping landslides continues to be of critical importance for assessment and mitigation of their hazard (e.g. Glastonbury and Fell, 2008; Puzrin and Schmid, 2011, 2012; Schulz et al., 2009).

Creeping landslides are a particular kind of slope stability problem because, in contrast to rapidly occurring landslides, they represent a challenge for classical slope stability analysis. On the one hand, because creeping landslides either move continuously or experience episodes of reactivation, they are already in a state of failure. Therefore, the classical limiting equilibrium approaches, which cannot describe evolution of movements, are not directly applicable. Dynamic analysis, which is suitable for modelling rapid landslides, is also not helpful, because the displacement rates in creeping landslides usually do not exceed a few centimetres per year, and inertia forces affecting dynamic motion are negligible. It follows

that successful modelling of the landslide evolution can only be achieved if certain components of the boundary value problem formulation can be treated as time- and rate-dependent, particularly time-dependent loading history and rate-dependent material properties, or a combination of both.

Since precipitation has been shown to be particularly relevant for the movement of creeping landslides (Schindler, 1982; Schlüchter, 1988), the time-dependent loading is often introduced by relating precipitation to pore water pressure changes. For that, simple hydrological models based on linear reservoir theory have been shown to adequately relate precipitation to pore pressure changes in order to investigate slope movements (e.g. Angeli et al., 1996; Van Asch et al., 1996). Other approaches use hydromechanical or hydrogeological coupling in order to calculate pore pressure fields in a landslide (e.g. François et al., 2007; Laloui et al., 2004, 2009; Tacher et al., 2005; Tacher and Bonnard, 2007).

For the slip surface, strain-softening and progressive failure have been broadly recognized as a source of slope instabilities and have been analysed by Skempton (1964), Law and Lumb (1978), etc.. A combination of time-dependent loading and pore pressure changes with progressive failure has been introduced in the works of Bernander and Gustaas (1984), Hansbo et al. (1985), and Wiberg et al. (1990). Besides the loading history, time dependency can be introduced by the use of rate-dependent constitutive models. Several authors have used rate dependency of shear strength on the slip surface or in the shear zone to explain landslide movements and integrated it into a model in order to predict landslide displacements (e.g. Bernander and Olofsson, 1981; Gottardi and Butterfield, 2001; Van Asch, 1984; Van Asch et al., 2007; Wang et al., 2010; Wiberg et al., 1990).

The time-dependent volumetric behaviour of the sliding mass has been modelled, e.g. by Wiberg et al. (1990) and Maugeri et al. (2006). Not only creep but also relaxation has been shown to be of importance once it comes to modelling seasonal reactivation of landslides (e.g. Picarelli et al., 2004). An extensive review on flow rules and their applications to landslide modelling can be found in Vulliet and Hutter (1988a, 1988b, 1988c). Depending on the boundary conditions of the landslide, the pressure may reach high enough levels to cause failure in the landslide body. This failure and the subsequent post-failure evolution have also been treated as time- and rate-dependent processes, e.g. Puzrin and Schmid (2011, 2012).

2.3   Models for creeping landslides under extreme weather conditions and changing climate

The effect of changing climate on the development of creeping landslides in the Alps has been investigated by e.g. Tacher and Bonnard (2007) who conclude that climate change may not necessarily have severe adverse effects on large creeping landslides. Comegna et al. (2013) analyse the influence of climate change on the movement of stiff clay slopes, showing that owing to less precipitation and increasing temperatures, a decrease in movement rates can be expected.

Further investigation of the influence of changing climate on creeping landslides has rarely been done. Potential reasons for that are the lack of long-term data series of landslide movements and hydrological conditions that are necessary to calibrate models, but also the lack of suitable exposure models, i.e. weather models that are capable of reproducing weather variation correctly over a long time.

To the author's knowledge, the effect of extreme precipitation or extreme snowmelts on creeping landslides has not yet had much attention in the literature.

2.4   Models for the seismic analysis of creeping landslides

Despite the progress in modelling of creeping landslide behaviour under transient loading in general, the effects of earthquake loading on the stability of creeping landslides largely remain an open question. The relevance of this problem becomes obvious when we consider that creeping landslides do exist in seismically active regions, and a catastrophic acceleration of such a pre-existing landslide may threaten both human lives and structures. For example, in Switzerland in the seismically more active canton of Vallais, the Ganterbridge at the Simplon Pass, a major traffic link between Switzerland and Italy, is founded partially within a creeping slope (Puzrin et al., 2012). Other examples of infrastructure threatened by creeping slopes are reservoirs at which some of the flanks exhibit creep tendencies and may require extensive stabilization works (e.g. Macfarlan 2009), though the actual risk of collapse is unknown.

The lack of reliable models to capture earthquake influence on creeping landslides is not only due to the absence of consistent observations of landslide behaviour during earthquakes but also due to the complexity of phenomena and interactions that govern the behaviour of creeping landslides during seismic loading, such as:

(i)   the rate dependency of shear strength along the boundary between stable and unstable soil (see also 2.2);

(ii)   the strain-dependent reduction of shear strength along the same boundary (see also 2.2) which can potentially cause a rapid acceleration of the landslide;

(iii) build-up of excess pore pressures during earthquake loading;

(iv)   complex boundary conditions in the landslide's toe region potentially causing failure of the landslide body followed by a mechanically and geometrically non-linear post-failure landslide evolution.

Most of the existing approaches for seismic slope stability analysis, such as pseudo static approaches, dynamic finite element models or Newmark's method (Jibson, 1993; Newmark, 1965), if at all applicable, neglect several of these phenomena. This can lead to a non-conservative overestimation of the landslide's safety during seismic loading.

Observations of the reaction of creeping landslides to earthquakes are mostly not well documented, which makes identifying the important phenomena difficult. Often, higher displacement rates are reported after the seismic event than before (Lacroix et al., 2015) causing a large part of displacement to accumulate after the event. Jibson et al. (1994) report some general landslide cases from the Racha earthquake in Georgia with slopes that either experienced very little co-seismic displacement or moved at some delay after the earthquake. The authors suspect, as the reason for the first phenomenon, visco-plastic damping, i.e. rate effects; and for the second, excess pore pressures or increased permeability after the earthquake. Rate effects and softening along an existing slip surface in slow and fast shearing have been investigated via shear tests in several studies (Bishop et al., 1971; Lemos, 2003; Lupini et al., 1981; Schulz et al., 2009; Tika et al., 1996; e.g. Wang et al., 2010) and have been integrated into e.g. Newmark models (Schulz and Wang, 2014; Togo et al., 2014) for seismic analysis.

The development of excess pore pressures is a well-known behaviour of non-sheared soil material in cyclic loading, and the resulting potential build-up of excess pore pressures has been widely investigated in triaxial (e.g. Sancio, 2003), simple shear (e.g. Donahue, 2007; Sanin, 2010) and ring shear tests (Ostric et al., 2013; e.g. Sassa et al., 2004).There is a large number of approaches aiming to model the development of excess pore pressures due to cyclic or seismic loading. The following list gives a brief overview and a few examples of different modelling approaches:

(i)   The first approach herein is the use of empirical models that aim to establish empirical relations between seismic parameters to the development of excess pore pressures. Matasović & Vucetic (1995) propose an empirical formula based on staged cyclic tests to relate pore pressure to the degradation index (Idriss et al., 1976, 1978) using the equivalent number of cycles of a ground motion and the shear strain amplitude. Green et al. (2000) relate dissipated energy in shearing to residual pore pressure using cyclic triaxial, torsional shear and shaking table tests on silt and sand-silt mixtures.

(ii)   The second category of models is those based on plasticity theory that use coupling of deviatoric and volumetric strains in order to capture the effect of excess pore pressure development in undrained conditions. Examples for multi-surface models are given by Elgamal et al. (2003), Yang & Elgamal (2008) and Yang et al. (2003) based upon purely deviatoric kinematic hardening according to Prevost (1985).
        Houlsby (1992) shows how dilatancy and anisotropy may be introduced as kinematic constraints in order to respect fundamental laws of thermo-mechanics. These constraints can be used in e.g. multi-surface kinematic hardening plasticity models to capture the development of excess pore pressures (e.g. Houlsby and Mortara, 2004).

(iii)   A last approach is bounding surface models. Here, as before, shear-volume coupling is used to link deviatoric and volumetric behaviour. In contrast to plasticity models, these models define hardening modulus and flow rule via the distance between the current stress state on a yield surface inside a bounding surface and its projection point on the bounding surface (Dafalias and Popov, 1975). An overview of the mathematical foundations can be found in Dafalias (1986).

The above-mentioned approaches and models allow the effect of pore pressure generation and cyclic degradation to be captured. However, deriving model parameters and application in boundary value problems, such as landslide analysis, is often not easy.

For the analysis of seismic slope or landslide displacements, excess pore pressure generation is considered often only in form of empirical relations (Biondi et al., 2000). Deng et al. (2010) demonstrate the modification of the Newmark method to account for externally imposed excess pore pressures, but do not clarify how these pore pressures would be derived. Generally, in these approaches, the generation of excess pore pressures is not related to the actual displacement history of the slope.

Very few studies investigate the development of excess pore pressure in soils with a pre-existing slip surface. In experiments, Gratchev and Sassa (2015) and Saito et al. (2006) report

excess pore pressure development in ringshear tests (using undrained ringshear devices developed at Kyoto University (Sassa et al., 2004)) on clay and sand-clay mixtures that had previously been sheared to residual state (i.e. the state at large deformations when clay particles have aligned).

In models for landslides with pre-existing slip surfaces, the effect of excess pore pressure development is often neglected, which the authors justify by assuming that the slip surface has reached residual state, and the development of pore pressure is unclear but considered unlikely (Pradel et al. 2005; Schulz & Wang 2014). Although this assumption may be true for the slip surface itself, it neglects to consider the surrounding soil that might still develop excess pore pressures.

2.5 Risk analysis for creeping landslides

Risk assessment for landslides has been the subject of research for some time, as landslides are a major natural hazard. Switzerland, as an alpine country, is particularly subjected to landslide hazard, and a total of 6% of the country's area is estimated to be affected by slope instabilities (Lateltin et al., 2005). Several frameworks have been proposed for assessing and managing the risk of landslides, e.g. Westen et al. (2005), Dai et al. (2002), Nadim and Kjekstad (2006), Lee and Jones (2004), and Ho et al. (2000), but few frameworks deal specifically with the risk associated with creeping landslides.

As a first part of the risk assessment process, the hazard due to the landslide has to be assessed. For landslides in general, four different methods exist (modified from Guzzetti et al. (1999); Dai et al. (2002)): (i) analysis of landslide inventories, (ii) heuristic methods, (iii) statistical methods and (iv) geotechnical or physical models. Geotechnical and physical models have been discussed in 2.2, 2.3 and 2.4.

In addition to the actual hazard model (e.g. a mechanical model of the landslide), exposures that influence the landslide's behaviour need to be represented. Here, apart from manmade exposures, in particular the influence of weather variations and seismic loading need to be captured. To the author's knowledge, weather prediction models for Switzerland exist only in terms of long-term climate scenarios (CH2011, 2011) or weather prediction models that cannot yet capture the inter-annual variability of weather parameters (Keller, 2015), which can be important for creeping landslides whose behaviour may be influenced by long-term variations rather than short-term events. Also for seismic exposures, apart from a catalogue of earthquakes with characteristics suitable for Switzerland (Laue, 2014), no clear procedure

of how to choose suitable acceleration time histories for different regions in Switzerland is available.

Secondly, vulnerability – the probability for a structure to suffer damage from a creeping landslide – has to be estimated. Vulnerability of persons is usually neglected, owing to the low velocity of the slides. For structures, the assessment of vulnerability is not easy as they are subjected to the continuous deformations inflicted by the landslide which cause continuous damages. Often, empirical relations between velocity and damage are the approach of choice to derive vulnerability functions; e.g. Mansour et al. (2010) use a large number of documented slow landslide cases to relate velocities to qualitative damage estimates. A similar approach is taken by the Swiss National Platform for Natural Hazard (Planat), which provides vulnerability coefficients for classes of structures based upon intensity of permanent landslides, which in turn is primarily based on landslide velocity supplemented by criteria for differential movements, reactivation potential and thickness of the landslide (Bründl et al., 2009; Krummenacher and Franciosi, 2009). However, it seems difficult to relate generalized vulnerability functions to structures without taking into account the specific properties of the structure; also, it has been questioned whether the use of displacement rates rather than the accumulated displacement to assess damages is the correct approach (Picarelli, 2011). Piccarelli and Russo (2004) summarize some interactions of different structures with slow landslides and propose best practices for these structures if built in slow landslides. The authors, however, provide only qualitative proposals for best practices and no means for the design of structures or quantitative risk analysis.

Combinations of empirical and mechanical approaches to assess damage for structures are demonstrated by Fotopoulou (2013) or Palmisano et al. (2016) and Palmisano (2011). These approaches mainly consider damages due to landslide-induced settlements of reinforced concrete frames or masonry walls.

Uzielli (2015a, 2015b) demonstrates the application of a risk assessment framework for slow landslides based upon a statistical hazard model and empirical vulnerability functions that take into account several properties of a building such as structural typology, building age and foundation type.

In general, no framework seems to have been established to assess the hazard from creeping slopes and risk for particular structures in such slopes.

3 Case Study: The Brattas landslide in St. Moritz

3.1 Introduction

Modelling creeping landslides under different loading conditions such as varying precipitation patterns and earthquakes requires gathering as much information as possible about the landslide under investigation. Using the fullest possible data set from a combination of field and laboratory investigations of a landslide site allows one to derive models that are best suited for predictive analysis of such sites. The Brattas landslide in St. Moritz, Switzerland is a good example for the potential sources of information that can be used to calibrate and verify the landslide models derived later in this thesis.

The Brattas landslide is particularly challenging to model, as it exhibits varying behaviour both in space along the landslide and over time. Additionally, the landslide is overbuilt in its lower part with modern and historic structures, the oldest dating back to the 16th century – the leaning church tower of the St. Mauritius church – making it even more important to understand its future behaviour in order to assess potential hazards to structures and to people living on the slope.

At the same time, because of ongoing heavy construction activity, the Brattas landslide is well monitored and studied. The large amount of displacement monitoring data, as well as field and laboratory investigations, allows a number of important phenomena of creeping landslides to be identified, and thus allows appropriate models to be derived and calibrated.

The following chapter summarizes the most important information about the landslide that has been collected recently and in the past.

3.2 General description of the landslide

The ski resort town of St. Moritz (1822m a.s.l.) is to a large extent built on the Brattas landslide, which causes damage to buildings and infrastructure and is constrained at the bottom by a rock outcrop. This rock outcrop divides the stable part of the slope with the town centre of St. Moritz, from the unstable, creeping part which is mainly used as a residential area but also includes shops and historic buildings at its bottom end.

Detailed information about geometry and geology of the landslide can be found in E. R. Müller (1992), Sterba et al. (2000), Puzrin and Sterba (2006) and Puzrin and Schmid (2011). The geometry of the landslide is summarized in Table 3-1, and Figure 3-1 a/b shows the plan and a geological section of the landslide.

Feature	Value	Source
Length [m]	Ca. 700	Geodesic monitoring
Width [m]	400-600	Geodesic monitoring
Slope inclination [°]	20	Schlüchter (1988)
Average depth of slip surface (h) [m]	20	Estimated from inclinometer measurements
Thickness of slip surface (d) [cm]	20	Borehole logging

Table 3-1: Geometry of the landslide

The sliding body (i.e. the moving landslide mass) has a length of 600-750m, a thickness of 17-41m, and is built of a silty soil matrix with boulder inclusions: essentially a moraine material deposited on top of a so-called palaeo-soil interlayer (Schlüchter, 1988) between the sliding mass and the stable ground.
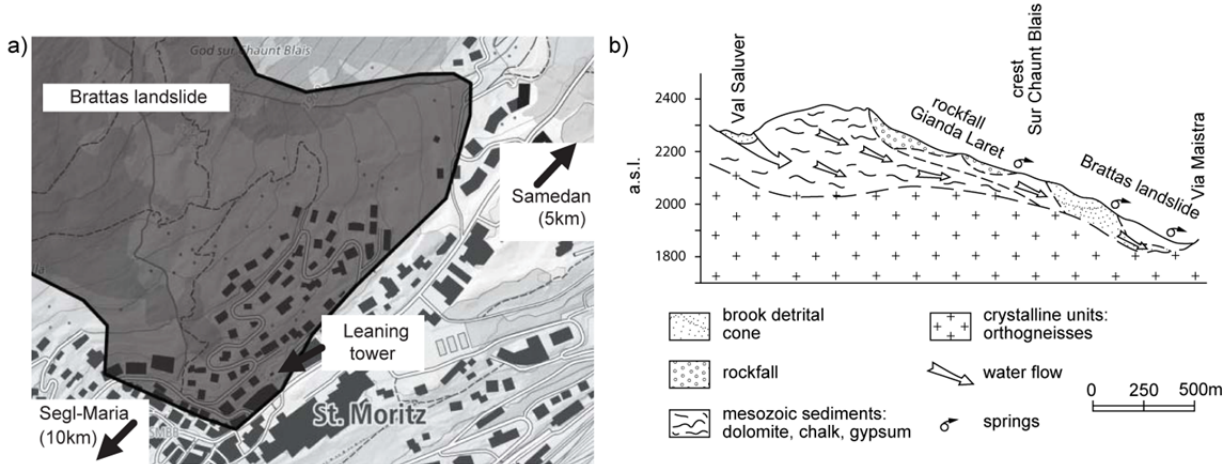
Figure 3-1: Brattas Landslide: the plan (after Swisstopo) and the geological section (after Müller and Messina, 1992)

The palaeo-soil layer is a weaker clayey layer including organic matter that has been identified in borings. In this narrow zone, most of the landslide's displacement is localized thus forming the so-called slip surface which is not an actual surface but a narrow shear zone (both terms are used in this work synonymously). Figure 3-2 shows recent inclinometer readings and a bore log of a boring performed in 2015, in which the weak layer has been identified via later on conducted inclinometer measurements as a ca. 20cm thick layer containing lots of fine material as well as organic matter (wood).

In boring 1501 (Figure 3-2), the basal slip surface is at around 18.5 m depth and an additional secondary slip surface has formed over recent years at approx. 4.5 m depth. This secondary mode of deformation may be due to the local conditions. For most of the other inclinometer readings, the deformation is localized in the primary shear zone.

The landslide's hydrology is complex with multiple levels of water carrying layers. Its precipitation catchment area is larger than the landslide and involves the mountainous areas above the landslide – Schlattain Brook and Val Saluver (Sterba et al., 2000). Hydrological investigations (Richard and Zeller, 1972) indicated that the ground in the area has a significant retention potential that provides a constant water supply to the unstable area, leading to relatively balanced groundwater conditions.
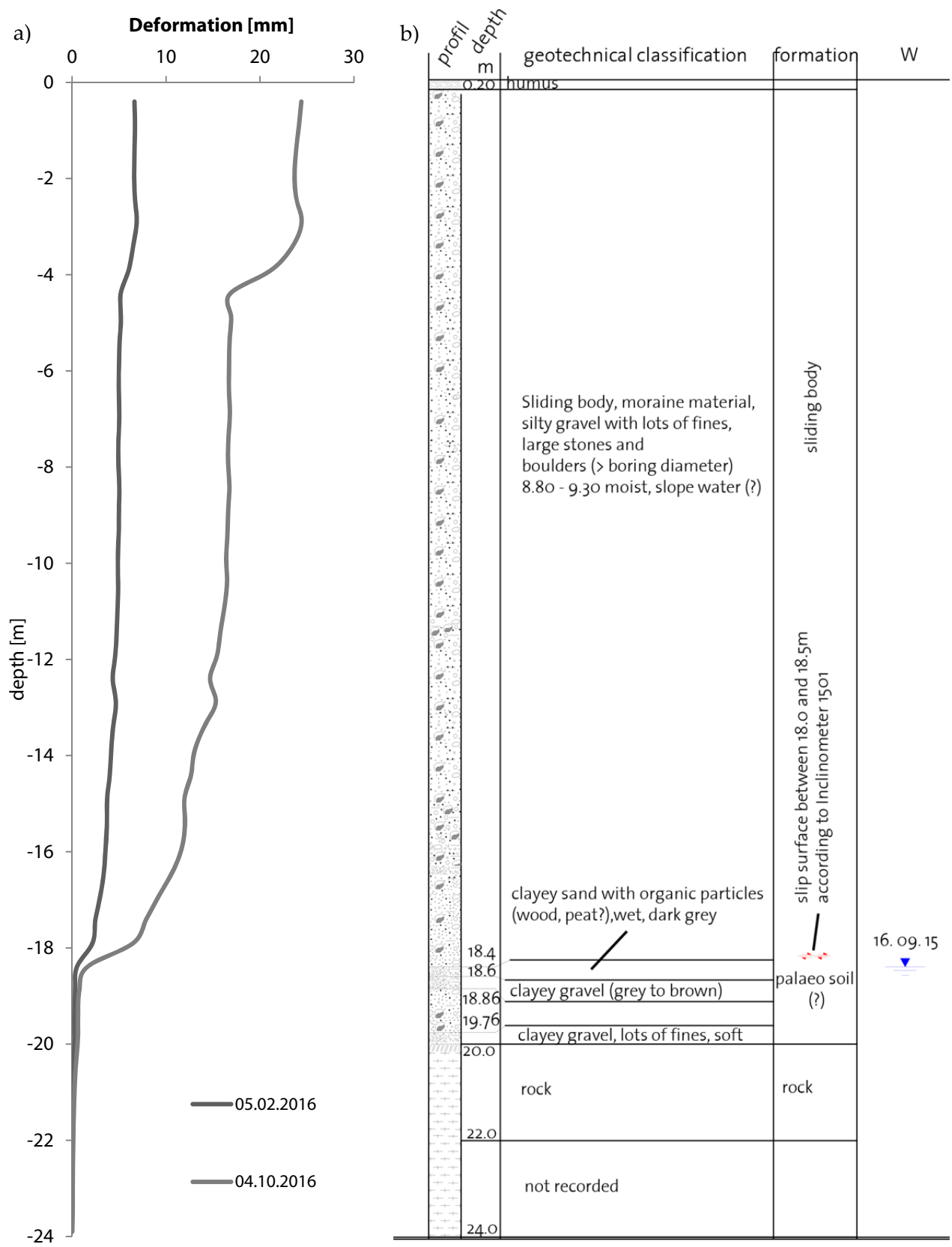
Figure 3-2: a) Inclinometer measurements and b) bore-log for boring 1501 behind the leaning tower

3.3 Displacement monitoring

Landslide movements are the easiest and most reliable field observation data that can be gathered from landslides. In St. Moritz, both surface deformations via geodesic and GPS monitoring and deformations along the basel slip surface via inclinometer readings are collected.

At the landslide's foot, the rock outcrop causes the lower part of the landslide to come to a standstill, leading to significant compression and heave in the foot zone (Puzrin and Schmid, 2011).

The displacement rates (Figure 3-3a) then increase uphill from the rock outcrop and can go up to 0.8 m/yr (Figure 3-3b). Additional measurements in the "Gianda Laret" rockslide situated further uphill (above 700 m) (see Figure 3-1b) show lower displacement rates than in the Brattas area, confirming the hypothesis that the two instabilities move separately.
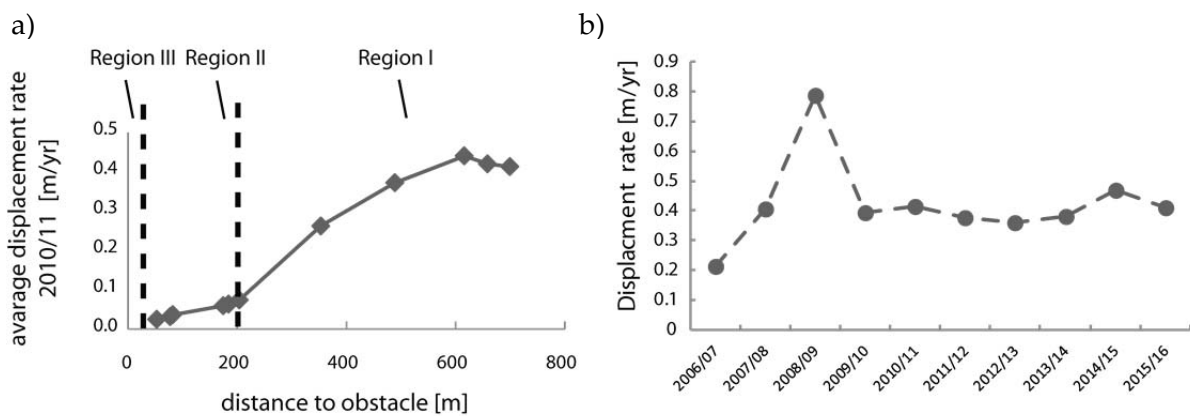
Figure 3-3: Observations of landslide displacement. a) Displacement rates along the length of the landslide measured in 2011/12, b) displacement rates measured at the top end of the landslide over the past decade

Measurements of horizontal displacements within the compression zone at the landslide foot (Figure 3-4) indicate a more than threefold increase in displacement rates in the last 23 years. The onset of landslide acceleration can be observed around September 1991, when the time–displacement curve changes its curvature.

Further landslide acceleration may have potentially devastating consequences, in particular for sensitive structures, such as the 16th century leaning tower of St. Moritz, located within the compression zone of the landslide. The Tower was stabilized in 1986 (before the landslide acceleration), and its inclination was partially corrected by lifting it with hydraulic jacks and placing it on a new foundation on three Teflon bearing pads (Sterba et al., 2000). Additional corrections took place in 2005 and 2013.
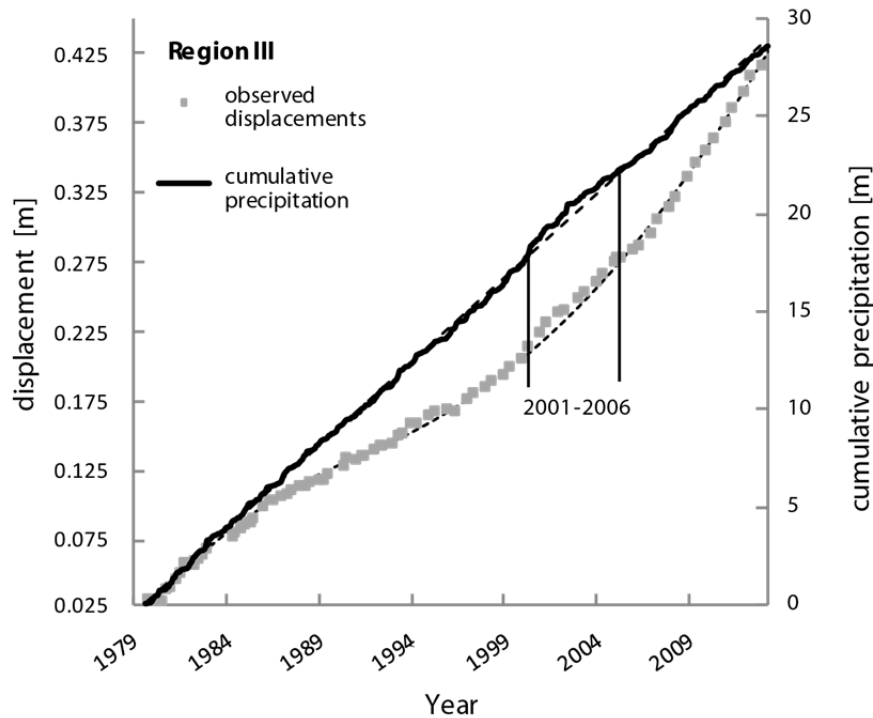
Figure 3-4: Displacements in Region III in the vicinity of the leaning tower and the observed precipitation, averaged between neighbouring weather stations of Samedan and Segl Maria (source: MeteoSchweiz).

In the lower 150–200 m of the landslide, the density of construction is high. Observations of displacements in this area are carried out using inclinometers and geodesic measurements. These movement measurements are complemented with increx, synthetic aperture radar (SAR) (Bovenga et al., 2012) and fibre optic (Iten et al., 2009) monitoring. In the area around the leaning tower, very close to the lower boundary of the landslide, data is available for more than 30 years (Figure 3-4). In the upper part, yearly GPS measurements of displacement rates with ca. 1 cm precision started in 2006.

Periodic displacement data for the area of the village has also been collected by two measurement campaigns which surveyed a set of points inside and outside the moving area (Tschudi and Angst, 1999; Staub, 2006).

Combining these observations allows information to be gathered on the spatial and temporal variations of displacement patterns. Of course, the amount of available data varies between the different sections of the landslide and decreases, broadly speaking, as one moves uphill along the slope.

3.3.1   Displacement regions

For the purpose of easing modelling attempts, the landslide has been split into three regions (see Figure 3-3a), which either already exhibit significant difference in behaviour or are likely to do so due to a known difference in properties. The data from the GPS measurements along the length of the landslide suggests two major displacement regions. As can be seen from Figure 3-3a, the lower 200 m of the landslide exhibit relatively small strain rates (less than 0.05% per year – Region II). Above this area, the strain rates are almost three times larger (Region I), indicating a change either in soil properties or in mechanical behaviour. These two regions also differ in terms of construction development: Region I represents a combination of forest and meadow areas, while Region II is heavily overbuilt.

Region III can be identified in the lower 20–30m of the landslide and, in spite of also being overbuilt, will be treated separately from Region II. This is because in contrast to the other two regions, it is likely to be significantly influenced by the rock outcrop at its lower boundary. The data collected in the vicinity of the leaning tower in Region III (Figure 3-4) shows a deceleration and reacceleration of the landslide. The strain rates in the lower 20–30 m reach high values. Since no changes in pore pressure or in precipitation have been observed during the onset of acceleration (see precipitation data in Figure 3-4), this again indicates a change in the nature of mechanical behaviour (e.g., onset of yielding).

3.3.2   Influence of precipitation on displacement development

Despite the fact that the onset of acceleration in 1991 was not caused by precipitation changes, for other periods the reaction of the slope to changes in precipitation can be clearly observed. In Figure 3-4, the precipitation data recorded at a location in the vicinity of St. Moritz shows, between the years 2001 and 2006, a significant deviation from the long term mean, resulting in a deviation of the measured displacements from the general trend.

The large yearly fluctuations of displacement rates observed in Region I (Figure 3-3b) also seem to be influenced by the precipitation variations. However, the correlation is less direct than is observed in Region III (see Figure 3-5) possibly because of the water retention of the ground and strong influence of the alpine winter and snowmelt.
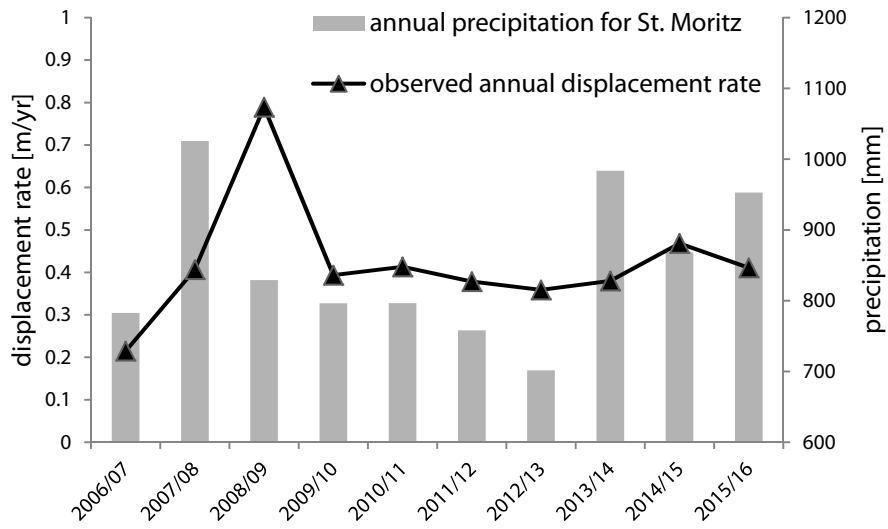
Figure 3-5: Comparison between displacement rates in region I and precipitation (measurement periods of approx. 1 year)

3.4 Laboratory and field tests

3.4.1 Laboratory tests

Triaxial Testing:

A first series of monotonic and cyclic triaxial tests was performed on fine material from the landslide body taken during previous bore campaigns. The material investigated is from 10m (sample 47139) and 15.9m (sample 47146, close to the shear zone) depth.

In preparation for the tests, all material was dried and grains larger 4 mm were removed, i.e. only the material forming the matrix of the sliding body can be tested. After this, the material was mixed with water until it reached a state close to the liquid limit. To prepare the samples, the slurry was filled in layers into a "pre-consolidation" container where it was allowed to deposit under vacuum. It was then pre-consolidated under oedometer conditions to a stress lower than the intended consolidation stress in the triaxial test. Since the material is relatively well graded with particles from the sand, silt and clay fraction, this procedure is intended to provide sufficient saturation and at the same time avoid segregation of the coarser and finer parts. After consolidation in the triaxial apparatus, undrained monotonic or cyclic tests have been performed on the samples.

The main goal of the investigation was to determine whether there is a potential of pore pressure development in the sliding body and possibly to quantify it.

The stress paths from monotonic undrained strain controlled tests on samples 47139 and 47147 (see Figure 3-6a and c) first show the development of excess pore pressures, causing the stress path to curve to the left, until it reaches the so-called phase transformation line when material behaviour changes from contractive to dilative, causing the pore pressures to drop again (i.e. effective stress increases).

The deviatoric behaviour shows the degradation of stiffness as the samples are sheared. For sample 47139, the constant volume failure state is not reached (Figure 3-6b); for sample 47146, this state is almost reached as strains increase with no further increase of the deviatoric stress (Figure 3-6d). Sample 47146 was also fully unloaded until the phase transformation surface was reached in axial extension.
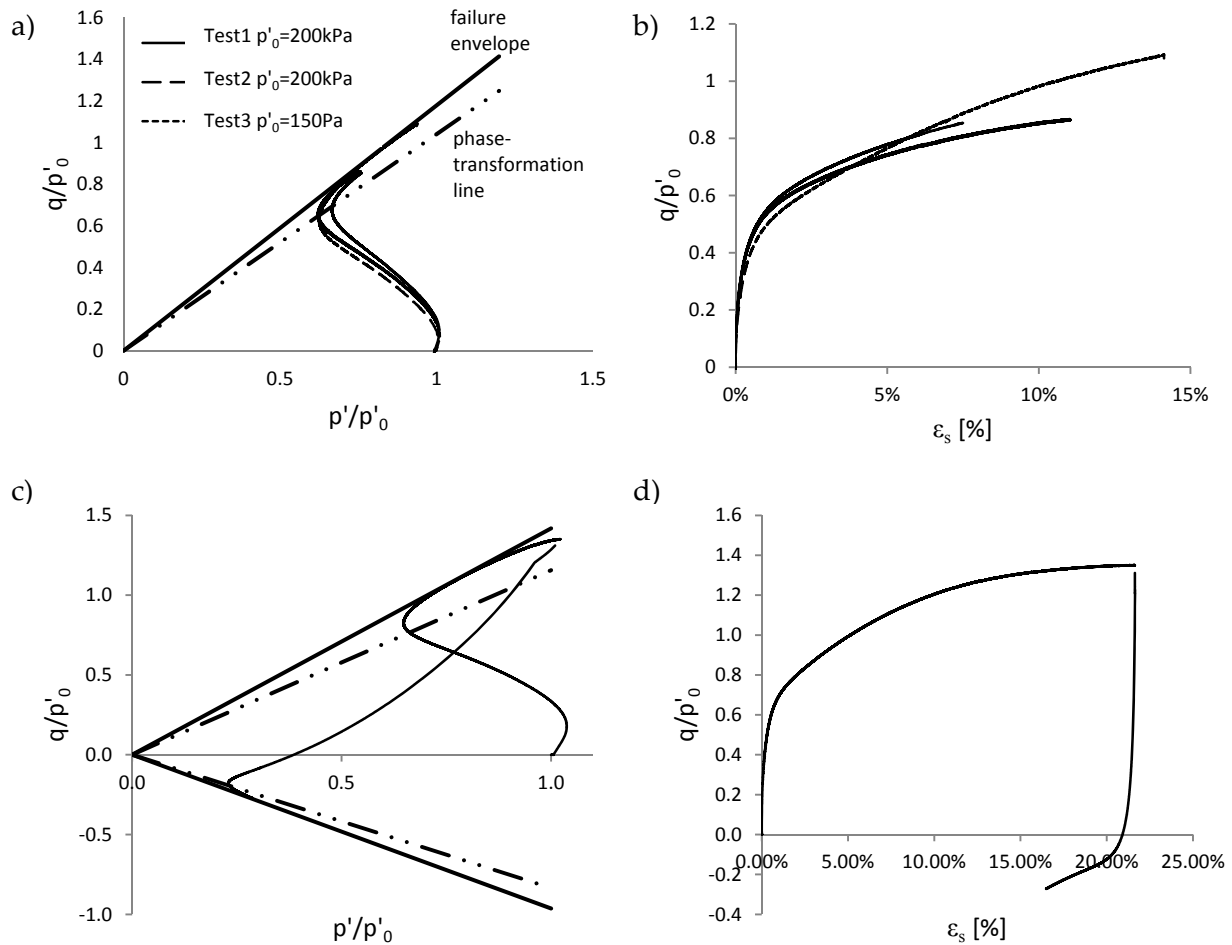
Figure 3-6: Undrained monotonic strain controlled triaxial tests on samples from St. Moritz (borehole 601), where q is the deviatoric stress, p' is the mean effective stress and ε_s is the shear strain: a) normalized stress path, sample 47139; b) deviatoric behaviour, sample 47139; c) normalized stress path, sample 47146; d) deviatoric behaviour, sample 47146

Undrained cyclic triaxial tests were performed to gain more data on cyclic response of the material of the sliding body. In order to be able to separate rate effects in later studies, stress controlled cyclic tests with approximately constant strain rate throughout each test were performed. For all tests, the strain rate was in the same range between 2.2×10^{-6} and 2.6×10^{-6} $[s^{-1}]$.
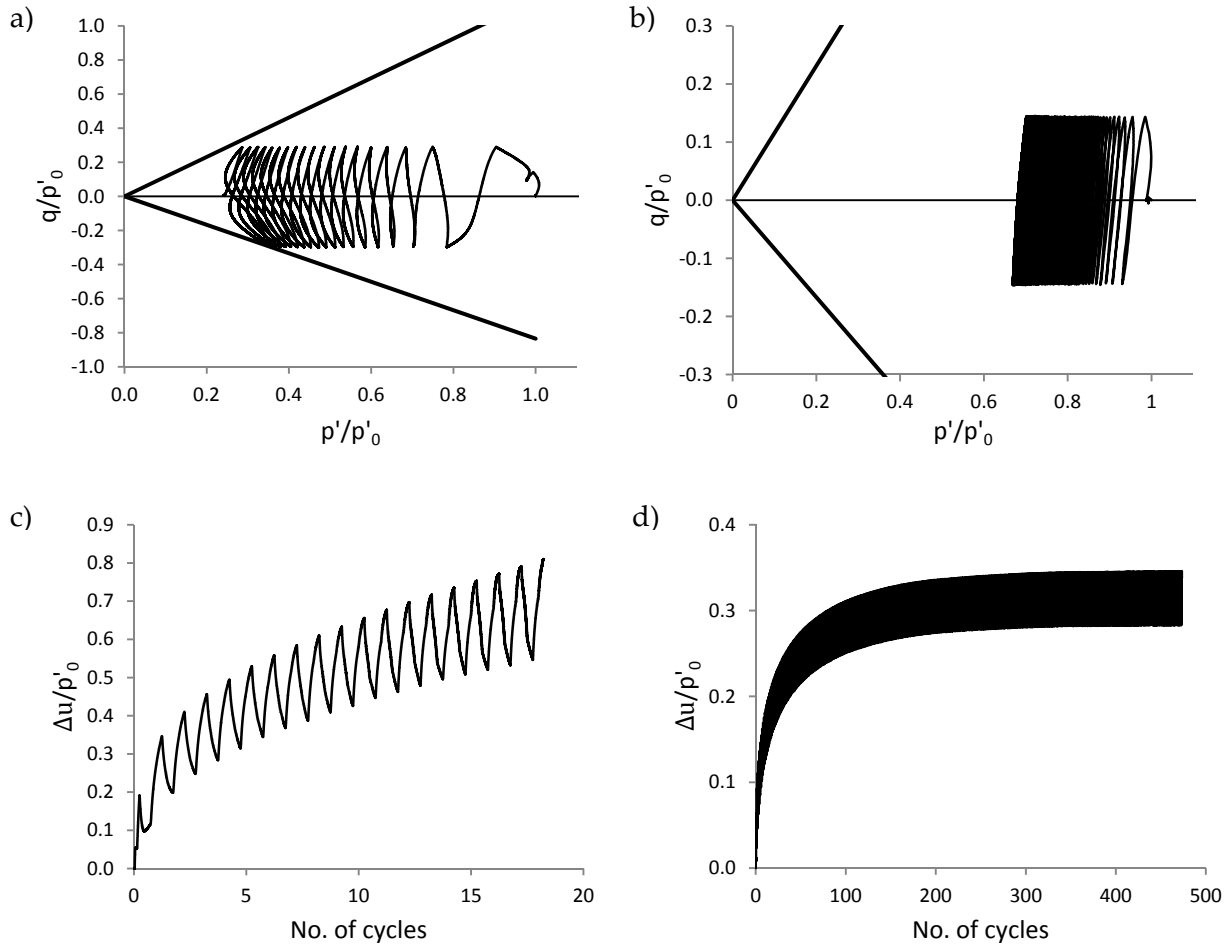
Figure 3-7: Undrained cyclic triaxial tests on sample 47139. a) Stress path for CSR=0.15, b) stress path for CSR=0.075, c) development of excess pore pressure (Δu) for CSR=0.15, d) development of excess pore pressure (Δu) for CSR=0.075

Figure 3-7 shows symmetric undrained cyclic tests (i.e. no deviatoric initial stress, $q_0 = 0$) on sample 47139. In Figure 3-7 also the influence of different cyclic stress ratios (CSR) on the development of excess pore pressures can be seen. Where CSR is defined as half of the deviatoric stress amplitude Δq divided by the horizontal effective stress σ'_h (Kramer, 1996):

$$\text{CSR} = \frac{\Delta q}{2\sigma'_h}. \tag{3-1}$$

As to be expected, excess pore pressures develop significantly more rapidly during the test with larger CSR (Figure 3-7a, c), whereas in the test with smaller CSR (Figure 3-7b, d), after a stage of excess pore pressure build-up a steady state is reached and no more excess pore pressures develop (this behaviour is called shake down).

Sample 47146 was tested similarly and additionally asymmetrically, i.e. the sample was consolidated anisotropically ($\sigma'_{h0} \neq \sigma'_{v0}$) and then undrained cyclic loading ($q_0 \pm \Delta q$) was

applied. The stress ratio chosen for the anisotropic consolidation corresponds to the approximate stress ratio in the field in the depth of the shear zone:

$$\frac{\tau_g}{\sigma'} = \frac{q_0}{2\sigma'_{h0}} \rightarrow \sigma'_{h0} = \frac{\sigma'}{\sigma' + 2\tau_g}\sigma'_{v0} = K \cdot \sigma'_{v0} \tag{3-2}$$

where τ is the shear stress and σ' the effective normal stress at depth of the sample in the field; q_0 is the static deviatoric stress, σ'_{h0} the horizontal effective stress and σ'_{v0} the vertical effective stress in the triaxial test.

Figure 3-8 shows a comparison between pore pressure development for isotropic and anisotropic consolidated samples for similar cyclic stress ratios. In contrast to simple shear tests, which are presumed to resemble field conditions better, pore pressure development in triaxial condition reduces in anisotropic consolidated samples.
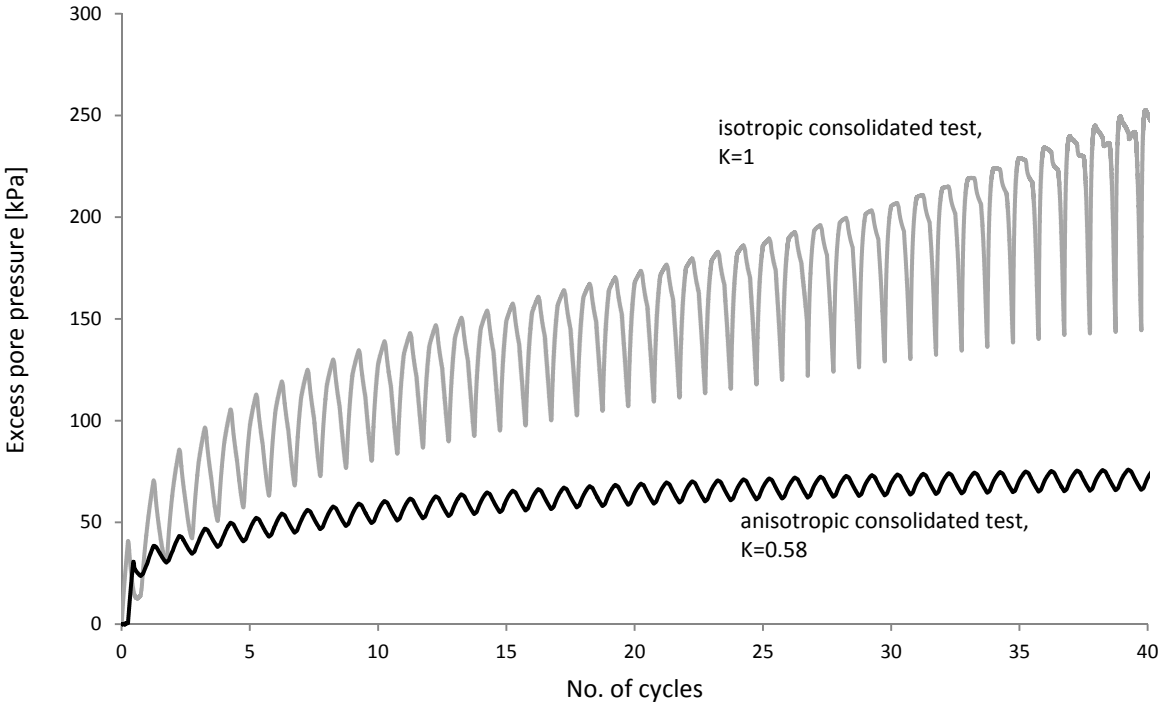
Figure 3-8: Development of excess pore pressure for tests of similar cyclic stress ratio, isotropic consolidated (grey line, Test 8, CSR=0.17) and anisotropic consolidated (black line, Test 7.1, CSR=0.15)

All tests can be found in appendix I-1.

Both cyclic and monotonic tests show a behaviour as expected for silty material. Clearly, a potential exists for development of excess pore pressures in the landslide body, which can potentially reduce the shear resistance in the shear zone during earthquake loading.

Oedometer Tests:

Puzrin et al. (2008) performed an extensive series of oedometer tests on matrix material of the sliding body from different depths. Via these tests, the compression (C_c) and reconsolidation index (C_s) and thus the tangent bulk modulus can be estimated. Permeability has also been derived for samples from varying depth. It has to be mentioned that oedometer tests also only allow testing of the matrix material of the landslides, and grains larger 4mm had to be removed (Puzrin et al., 2005).

Additionally, a new test was performed on the remaining material close to the slip surface in order to have more insight into the properties close to that surface. Results of this test are shown in Figure 3-9. The results of the material close to the slip surface show slightly lower values of C_s and C_c than the material above, which is to be expected, and they are close to values reported for silty soils in the literature (e.g. Donahue (2007)). The values of void ratio are not uncommon for glacial till deposits (Terzaghi et al., 1996).
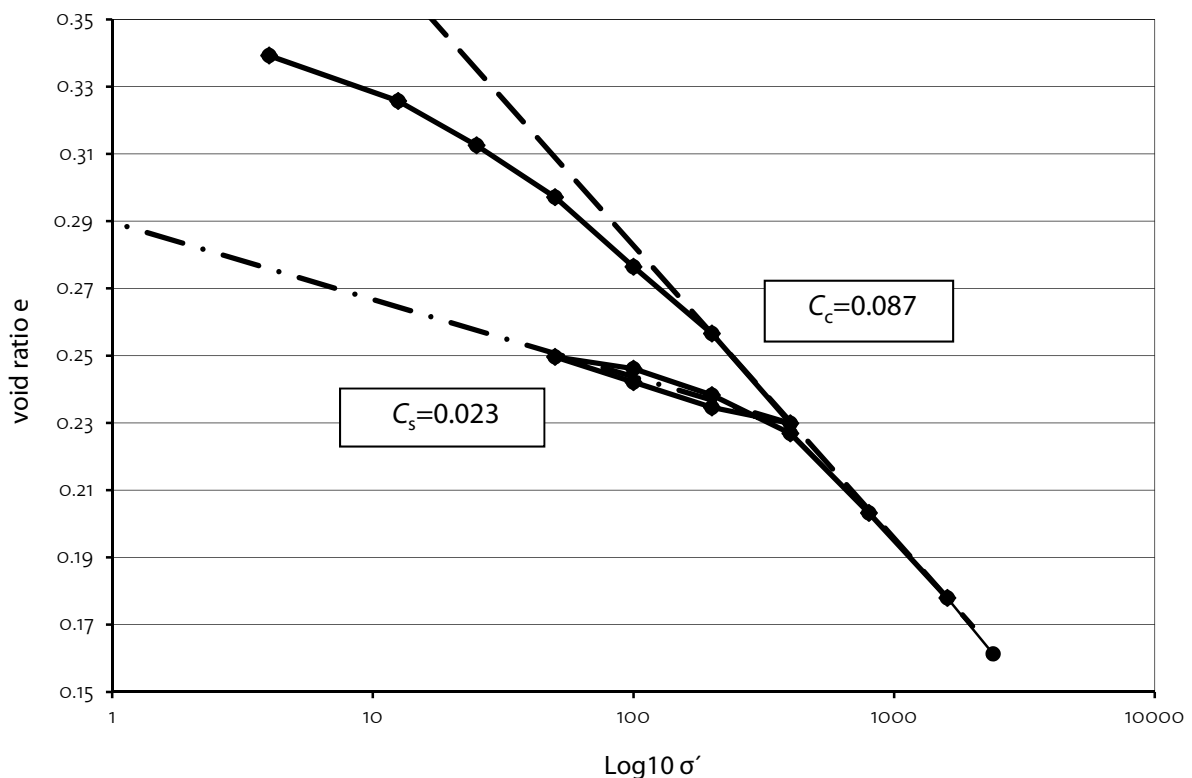
Figure 3-9: Results of oedometer test on sample 47146

Puzrin and Schmid (2011) performed ringshear tests on material that was suspected to be from the shear zone. The sample with the lowest shear strength was assumed to be from the slip surface. Additionally, variations of the shearing rate allowed them to estimate the rate dependency to be approximately 2.5% per log cycle on the slip surface (Figure 3-10).
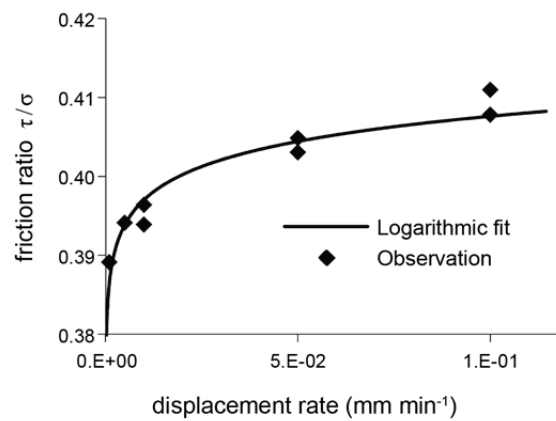
Figure 3-10: Rate dependency of the shear strength observed in ringshear tests, reproduced from data from Puzrin and Schmid (2011)

3.4.2 Field measurements

In order to gain further insight into the landslide's mechanics, a number of established and novel field investigation methods have been used, to complement observations of the landslide displacement.

Inclinodeformeter measurements:

Measurements of earth pressure changes performed with the recently developed inclinodeformeter (IDM) device allowed insight into the development of stresses within the body of the landslide (for details see Schwager (2013)). Schwager and Puzrin (2014) showed that the pressure in the landslide body in the compression zone is changing only little. The observed pressure changes are too small for the observed displacements to be purely elastic, indicating that the landslide has started yielding in the compression zone. Continued IDM measurements showed deformations of inclinometer pipes (change in ovalization $\Delta\Omega$ as defined by Schwager (2013)) of the same order of magnitude as reported by Schwager and Puzrin (2014), confirming their results (Figure 3-11).
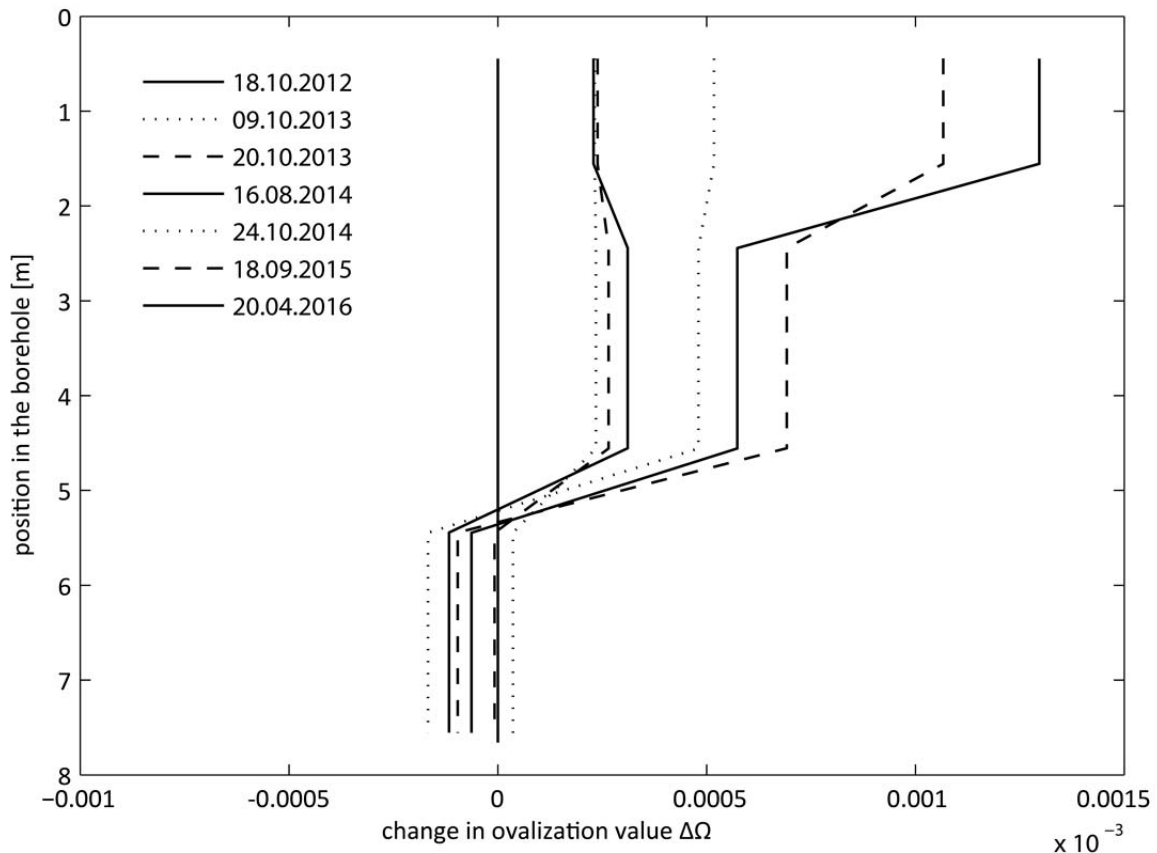
Figure 3-11: Pipe deformation (ovalization change $\Delta\Omega$) of inclinometer 1104 in St. Moritz (close to the bottom boundary of the landslide) measured by IDM

Dilatometer measurements:

Puzrin et al. (2008) used Cambridge dilatometer and Marchetti flat dilatometer probes to investigate the stiffness of the sliding body of the Brattas landslide. These measurements can be used as estimates of the stiffness of the sliding body in modelling attempts. Values in this study ranged from approximately 6MPa to 50MPa.

Additionally, the Marchetti flat dilatometer can be used to get estimates for the in-situ friction angle (Marchetti, 1997). The results showed friction angles ranging from 30° to 35°. Considering that the dilatometer tests produce parameters mainly for the matrix material of the sliding body, these values agree with triaxial tests that show similar results for tests on the matrix material.

Piezometer measurements:

Since pore pressure fluctuations along the slip surface are one major influence on the displacement rate of a creeping landslide, gathering information about these fluctuations is important. As mentioned, the Brattas landslide has very complex hydrological conditions with sometimes several groundwater storeys. Therefore, it is important to place a piezometer into the layer that is of interest, which is the one containing the slip surface. Thanks to prior knowledge of the depth of the shear zone in the vicinity of the leaning tower, in 2012 an automatic piezometer was installed that is believed to measure the pore pressure in the shear zone. This piezometer allows the reaction of pore pressures in the shear zone to be measured with high temporal resolution. This data can be used as additional information to calibrate a landslide and hydrological model for the transient state, i.e. to capture the influence of precipitation events on landslide movements.

Figure 3-12 shows the hourly piezometer readings and the monthly average. In July 2016, construction works next to the leaning tower commenced, and these significantly influenced the pore pressure fluctuations, making the readings past July 2016 unfortunately useless. As can be seen from Figure 3-12, up to 2014 the annual behaviour is dominated by two distinctive peaks caused by the snowmelt in spring and the rainy months in autumn. After the snowmelt in 2014, these peaks become less dominant. In 2015, no clear autumn peak can be observed.

For the Brattas landslide, it seems that the longer-lasting wet periods in spring and autumn influence the pore pressure fluctuations more than single heavy rain events. The two most

distinctive short-term peaks are due to a failure of the monitoring system and to drilling of a new inclinometer.
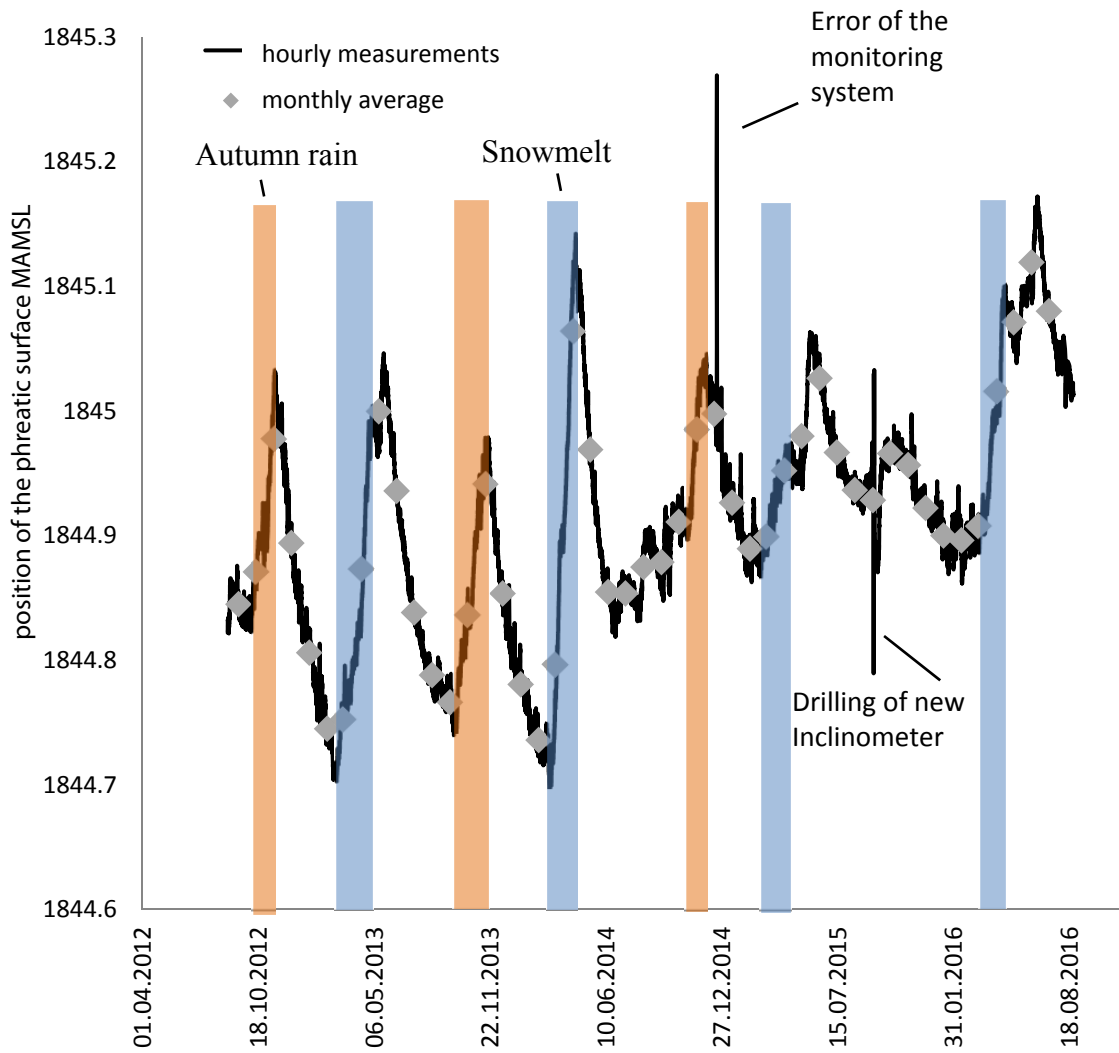
Figure 3-12: Piezometer readings of pore pressures on the slip surface in the vicinity of the leaning tower

3.5 Previous modelling attempts of the Brattas landslide

Several attempts have been made to understand and model the behaviour of the Brattas landslide. These attempts were able to explain some of the observations of the landslide's behaviour, but, owing to incomplete data, it has not been possible to capture the full behaviour of the entire landslide both in time and space.

Puzrin and Sterba (2006) attempted to model the behaviour of the Brattas slide using data of displacement monitoring in the lower 200 m of the landslide and measurements of the displacement rates in the period 1979–1998. The model (Figure 3-13) assumed visco-elastic behaviour of the sliding mass (described by a Kelvin-Voight model, parameters E and η) and rate-dependent residual shear strength on the slip surface (parameters τ_r and η_τ). That combination allowed them to capture displacement deceleration observed in Region III and the velocity profile increasing with the distance from the landslide bottom in Regions I and II. An analytical solution allowed for inverse analysis to be carried out using the observed data to estimate the model parameters. Owing to incomplete records, the acceleration of the landslide in the foot zone could not be discovered at that time, which prevented the authors from analysing the behaviour in case of failure of the landslide body.
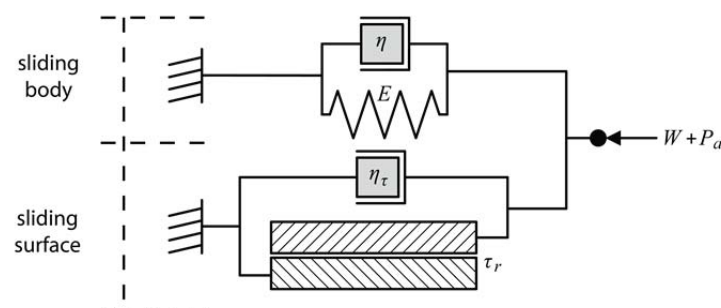
Figure 3-13: Puzrin and Sterba (2006) model (*W* and *P$_a$* are weight of the landslide body and active pressure acting on the upper boundary)

Once the subsequent data set for the period between 1998 and 2010 became available, reacceleration of the slope, starting approximately at the end of 1991, became evident, while no significant changes in pore pressures and precipitation were observed. The inability to explain that reacceleration using the Puzrin and Sterba (2006) mechanism led to a modification of the model (Puzrin and Schmid, 2011), which assumed visco-elastic-plastic behaviour for the sliding mass (see Figure 3-14). On the slip surface, rate-independent softening behaviour of the shear strength (τ^*) has been considered by Puzrin and Schmid

(2011), leading to a progressively propagating failure along the slip surface and continuously increasing pressure at the bottom of the landslide.
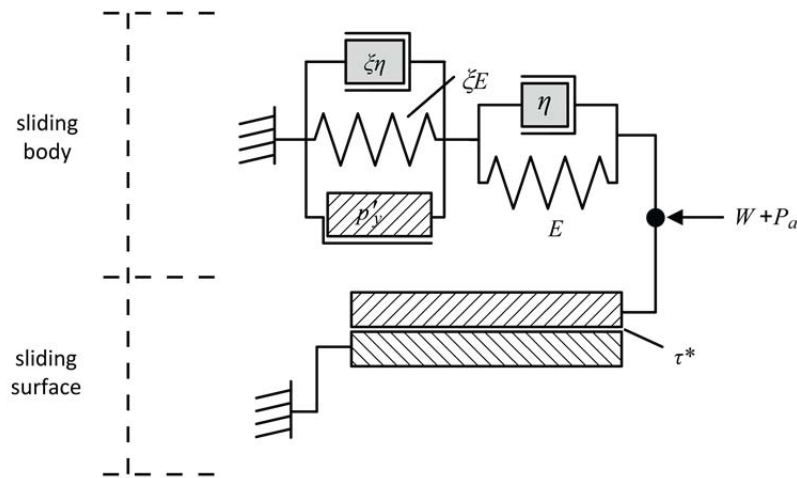
Figure 3-14: Puzrin and Schmid (2011) model (W and P$_a$ are weight of the landslide body and active pressure acting on the upper boundary)

The model allowed the reacceleration stage to be captured, by introducing a second, much softer Kelvin–Voigt group, activated once a certain yield stress (p'_y, close to the passive earth pressure) is reached. The drop in viscosity and stiffness can be controlled via a yield factor ξ. The model focused on Region III of the landslide, where displacement sensitive structures such as the leaning tower of St. Moritz are concentrated. An analytical solution of the problem has been derived allowing for deceleration and reacceleration phases in Region III. However, subsequent numerical simulations of the entire landslide showed that the constitutive model derived using the data from Region III could not describe landslide behaviour in Regions I and II with sufficient accuracy. Also, Puzrin and Schmid neglected the rate dependency along the slip surface, as it is only 2.5% per log cycle. This simplification is reasonably as long as only steady state behaviour (no pore pressure fluctuations) is investigated. If the aim is to model pore-pressure-induced fluctuations of the displacement rate, even small rate dependency can have significant influence and should be investigated.

3.6   Damage to structures in the landslide

The continuous movements of the landslide cause damage to structures and infrastructure. Since the Brattas landslide has a positive velocity gradient (i.e. velocity increases from bottom to top), buildings experience compression.

Looking at buildings, the houses with the most significant damage seem to be the ones closest to the boundary, i.e. the one or two rows of houses at the foot of the landslide. This

observation agrees with a qualitative damage survey from 1983 (Bendel, 1983). From the displacement profile in Regions II and III (Figure 3-3 and Figure 3-4) it becomes obvious that, in this area, compressive strains induced by the landslide are high, whereas above the deformation gradient reduces, i.e. compressive strains are lower. Additionally, the density of construction is very high at the landslide foot, with large houses and underground storeys leading to the houses being deeply embedded (up to four storeys) at their upslope side.

Above the first houses, the degree of damage reduces and seems more related to differential movements of different parts of houses than to compression of the structures. Figure 3-15a shows a house at the upper end of the overbuilt part where the major damage is a vertical crack which also progresses inside that indicates the separation of the two halves of the house. Looking at the displacement field of the region (Figure 3-15b), one can see that the displacement field slightly rotates over the width of the landslide, potentially causing lateral stretching of houses in this region.
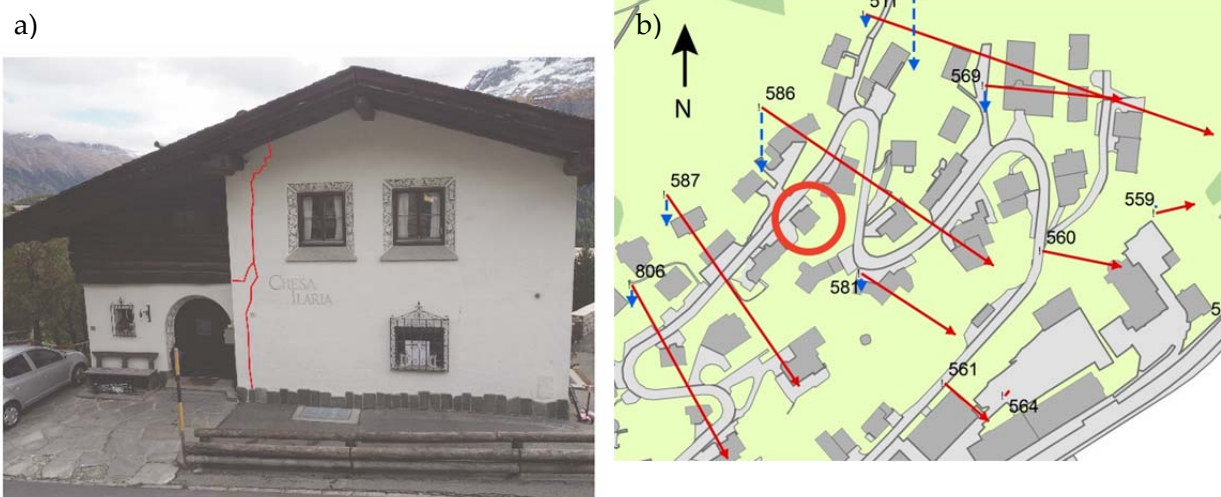
Figure 3-15: a) Example of damage at a house in Region II (main crack highlighted in red); b) situation of the house and measured velocity field (Staub, 2006) of the landslide (red circle indicates the example house)

Another particular structure situated in the creeping slope is, as mentioned, the leaning tower of St. Moritz. The tower is the church tower of the St. Mauritius church built in the 16th century. The nave of the church has been dismantled a long time ago; the tower kept its structural integrity but started inclining downslope. There have been several stabilization attempts in the past which were only able to reduce the rate of rotation of the tower. The most recent attempt was undertaken in the 1980s when two concrete slabs were constructed underneath the tower within the sliding body. Between the actual tower foundation and the concrete slabs, adjustable bearings were installed that allow the tower to be periodically lifted in order to compensate for some amount of accumulated rotation. Figure 3-16 shows measurements of the deflection of the leaning tower at the height of its bell chamber. The

tower has been stabilized twice, as shown in the figure, whenever it has reached 2m deflection. This criterion was set by the community of St. Moritz, since the structural limit for the deflection is unclear and 2m is the largest ever observed deflection.

Within the tower, several monitoring systems allow its deflection to be measured hourly. Similar to the displacement measurements nearby, the rotation or deflection of the tower accelerates after 1991.
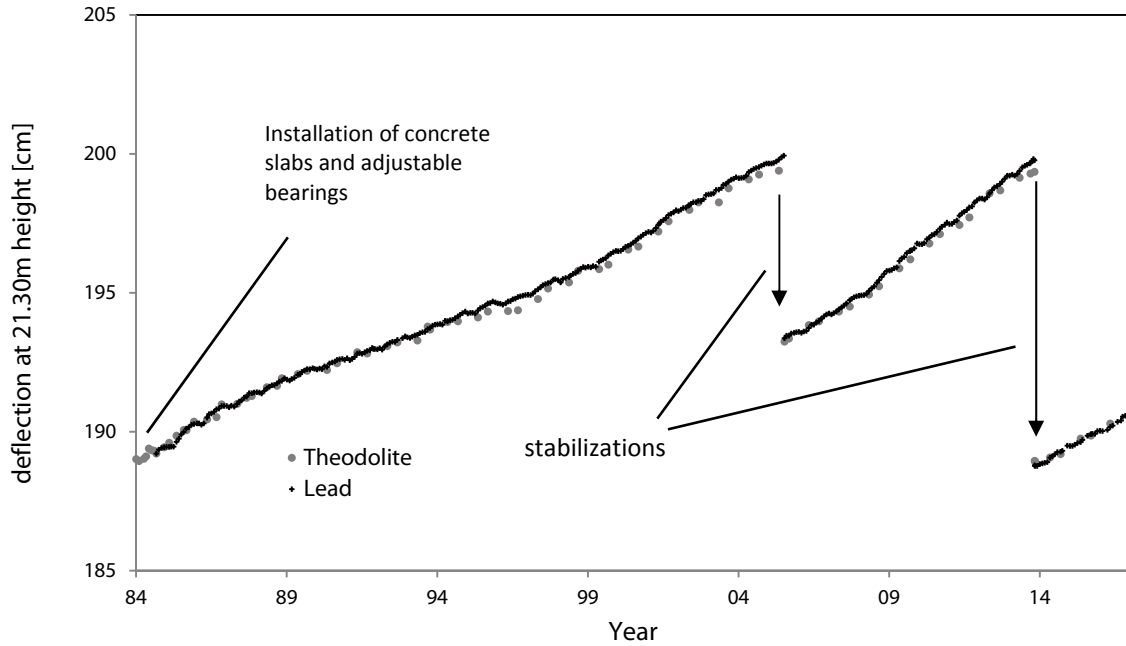
Figure 3-16: Measurements of the leaning tower's deflection at level of the bell chamber (21.30m)

3.7 Summary and discussion of the available data

The creeping Brattas landslide has been chosen as an exemplary case to demonstrate the later presented methods for derivation of creeping landslide analysis models in non-seismic and seismic loading conditions, as well as for some applications of risk assessment.

For benchmarking non-seismic creeping landslide models, displacement observations are the most reliable source of data. In the Brattas case, displacement records are available for more than 30 years in the foot zone of the landslide. This data is completed by additional measurements along the entire length of the landslide since 2006 and less frequent periodic measurements in the lower 200m of the landslide. The observations allow a picture to be obtained of the landslide's behaviour along its entire length and not at only one point. As can be seen from the data, this behaviour can change significantly along the length and also in time, which has been qualitatively reflected by dividing the landslide into three major displacement regions. Having divided the landslide systematically into regions of similar phenomenological behaviour, other sources of information can then be used to identify potential external or internal influences causing the changes in behaviour. In the Brattas case, construction activity in the lower part of the landslide, with large structures sometimes including significant underground parts (e.g. parking lots), and better drainage, as well as the fact that the landslide has undergone significant compression in this part, could potentially be the reason for the different displacement rates and rate fluctuations observed in regions I and II.

In region III long-term displacement records show a stage of deceleration and reacceleration. In order to identify reasons for such behaviour, further investigations and monitoring data have been consulted. First of all, construction activity has been ruled out as a potential source, since no major construction has been undertaken during the time of onset of acceleration, and it could hardly explain the deceleration and long-lasting reacceleration of the landslide. A change in pore pressures, which one would usually suspect as a potential reason for an acceleration, has not been observed in piezometer readings; neither has a change in the precipitation trend. Therefore, a change in the mechanical behaviour, i.e. an internal influence, has been left as the only explanation, leading to the assumption that the landslide started yielding because of the high pressures in the foot zone. Further evidence for this hypothesis has been gathered by continued measurements of earth pressure change with the novel IDM. These measurements, which show very small changes in pressure in the foot zone, indicate such a small material stiffness that it can only be explained by plastic deformations of the soil.

Hydrological investigations indicate a large water retention potential of the ground in the area, which indicates that fast pore pressure fluctuations could be damped. This hypothesis is supported by the long-time displacement data from the foot zone where the major influence of precipitation is observed during a long-term precipitation fluctuation between 2001 and 2006. Fluctuations of the annual displacement rate are observed in the measurements of the upper part, but these fluctuations do not coincide directly with fluctuations of annual amount of precipitation. Frequent automatic piezometer readings are only available since 2012 and allow further insight into what influences pore pressures the most, even though observations are limited to one point in the slope. These readings indicate, for most years, two pore pressure peaks due to snowmelt in spring and precipitation during the autumn month. These two peaks are more pronounced than peaks due to short-term heavy rain events. These observations combined allow a potential picture of the precipitation influence to be pieced together. In particular, the indirect reaction to precipitation makes modelling the hydrology more difficult but necessary since precipitation is one major driver of the landslide velocity.

In contrast to non-seismic behaviour, for the influence of earthquakes no observations can be used. Though St. Moritz is situated in a relatively seismic active zone in Switzerland and some earthquakes have been recorded by accelerometers in the leaning tower, none of them have been strong enough to cause measurable displacement of the landslide. Therefore, the only way to derive models for seismic assessment of creeping slopes seems to be a bottom-up approach. Based upon experimental investigations of the material from the sliding body and the landslide's shear zone, constitutive models for the involved soils during cyclic and eventually seismic loading can be derived. These models can be integrated into formulations of the boundary value problem. For the Brattas landslide, ring-shear tests and triaxial tests revealed two major phenomena that need to be addressed in potential models of the landslide: (i) rate dependency of shear strength in the shear zone and (ii) development of excess pore pressures in the sliding body.

Lastly, the Brattas landslide is especially interesting because of the structures built in its lower part. Proposals of structural damage assessment due to creeping landslides deal often with structures with relatively low stiffness built on the crest of the landslide. In such cases, assessing damages based on deformations could potentially work. Also, the interesting case of the leaning tower of St. Moritz can be considered as deformation-controlled structure-landside interaction. In contrast to that, other structures in St. Moritz are built into the landslide sometimes with several storeys underground at the slope site. These structures are strong and stiff enough that they do not behave as purely deformation-controlled but are not

sufficiently strong to withstand the significant pressures imposed by the landslide. This can lead to severe structural and non-structural damage, particularly in houses at the landslide foot. Assessment of vulnerability for these structures is more difficult and the interaction between soil and structure needs to be taken into consideration.

Overall, owing to the variety of observed characteristics, the Brattas landslide is an interesting but also challenging case to be captured in a model. The constructions on the slope make understanding the displacement development more complex but also very relevant. Previous and ongoing investigation works on the landslide not only provide observational data but also allow accessing a collection of soil samples and taking periodically new soil samples.

Appendix I.1: Results of triaxial tests

Test 1
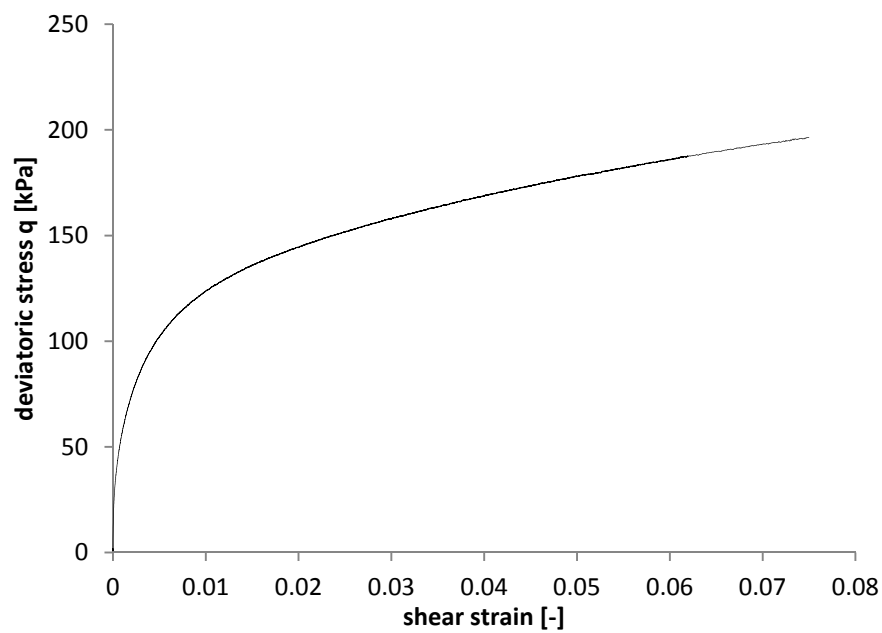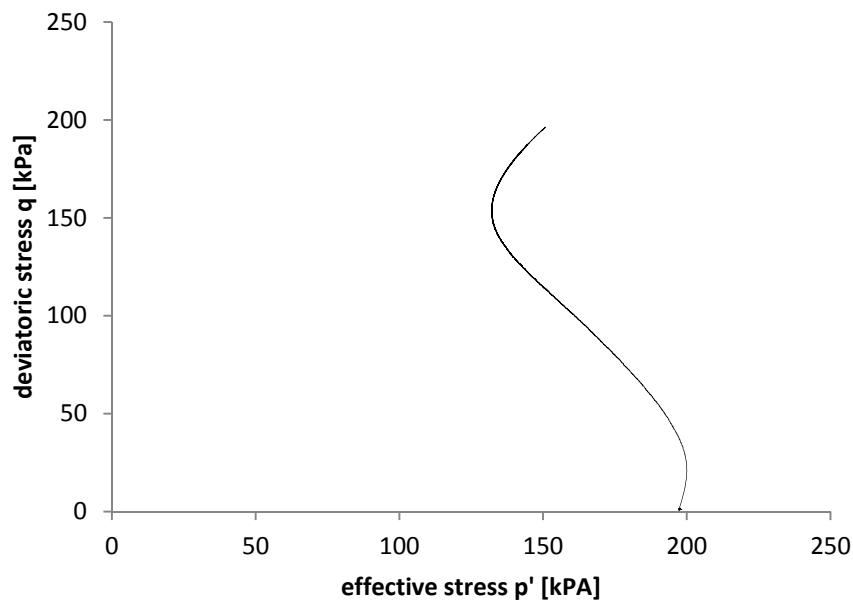
Test Nr.:	0601-1	Height [mm]	88.67	p'_0 [kPa]	198
Sample:	47139	Diameter [mm]	36.99	OCR	1
Sample Depth [m]	10.35	Volume [cm^3]	95.3	Loading velocity [mm/sec]	0.0002
PI	7.44	λ$_{wet}$ [kN/m^3]	21.5	B-Value	0.97
LL	0.295	Void ratio	0.44		

Note: $\mathrm{CSR_{TX}} = \frac{\Delta q}{2 \cdot \sigma'_3} = \frac{\Delta q}{2 \cdot \sigma'_h}$

Test 2
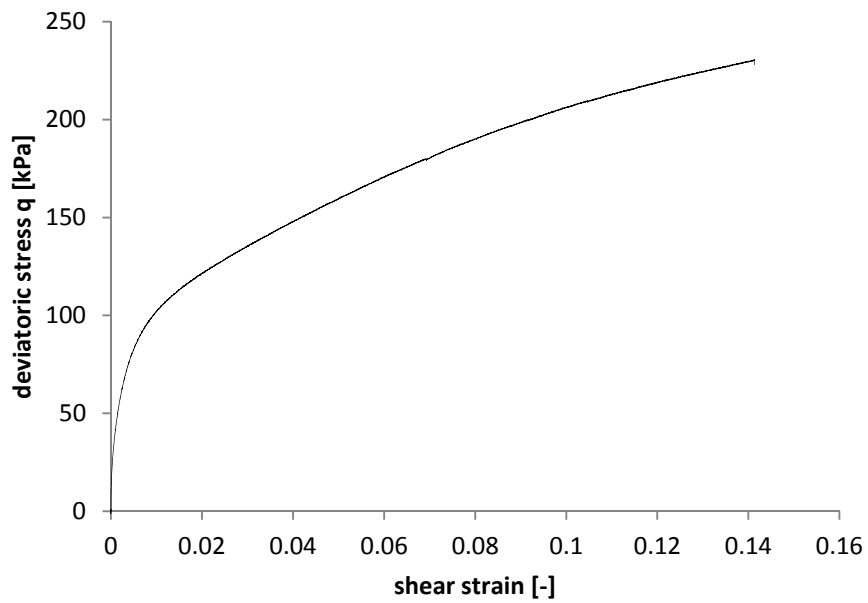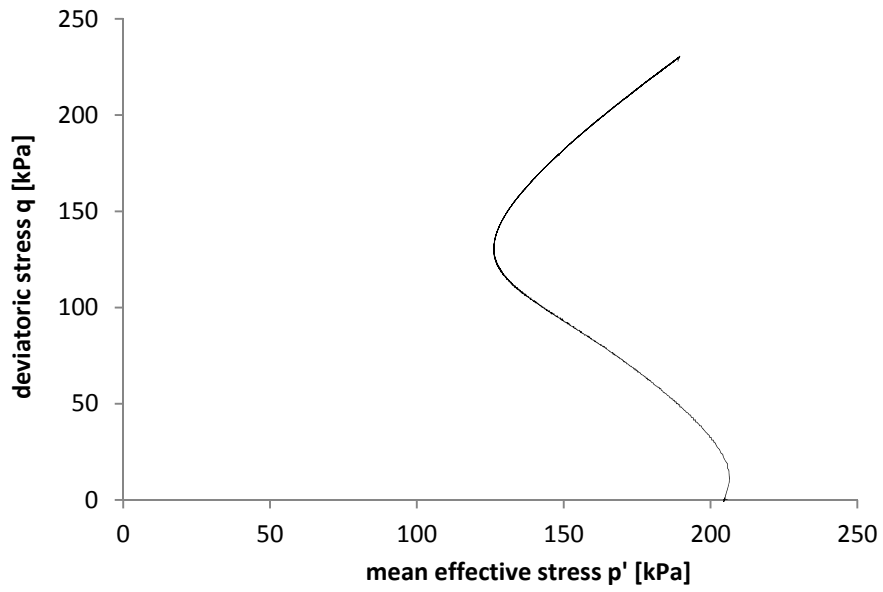
Test Nr.:	0601-2	Height [mm]	78.33	p'_0 [kPa]	206
Sample:	47139	Diameter [mm]	37.12	OCR	1
Sample Depth [m]	10.35	Volume [cm^3]	84.78	Loading velocity [mm/sec]	0.0002
PI	7.44	λ_{wet} [kN/m^3]	21.5	B-Value	0.96
LL	0.295	Void ratio	0.41		

Note: $\mathrm{CSR_{TX}} = \frac{\Delta q}{2 \cdot \sigma'_3} = \frac{\Delta q}{2 \cdot \sigma'_h}$

Test 3
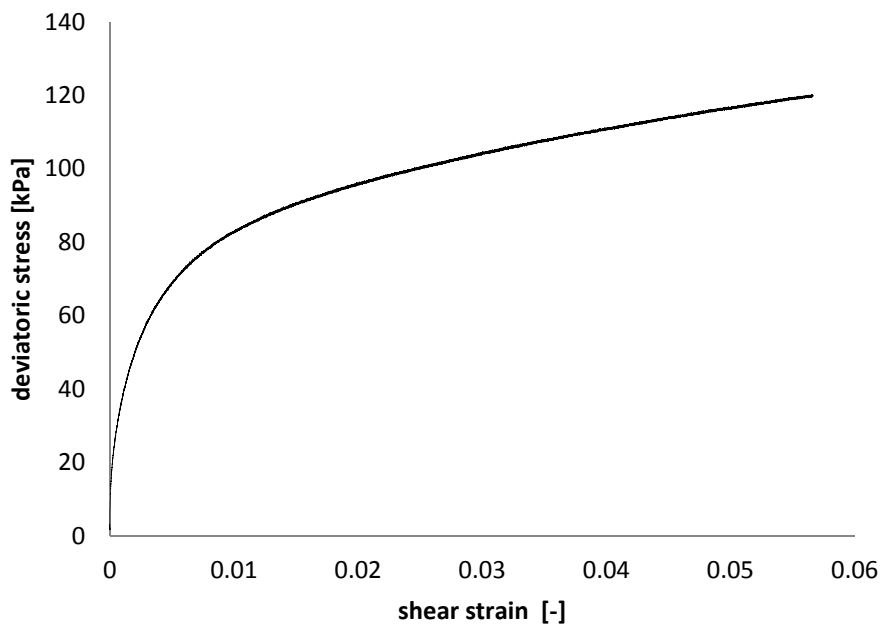
Test Nr.:	0601-3	Height [mm]	76.26	p'_0 [kPa]	154
Sample:	47139	Diameter [mm]	37.53	OCR	1
Sample Depth [m]	10.35	Volume [cm³]	84.36	Loading velocity [mm/sec]	0.0002
PI	7.44	λ_{wet} [kN/m³]	21.9	B-Value	0.95
LL	0.295	Void ratio	0.43		

Note: $\mathrm{CSR_{TX}} = \frac{\Delta q}{2 \cdot \sigma'_3} = \frac{\Delta q}{2 \cdot \sigma'_h}$

Test 4
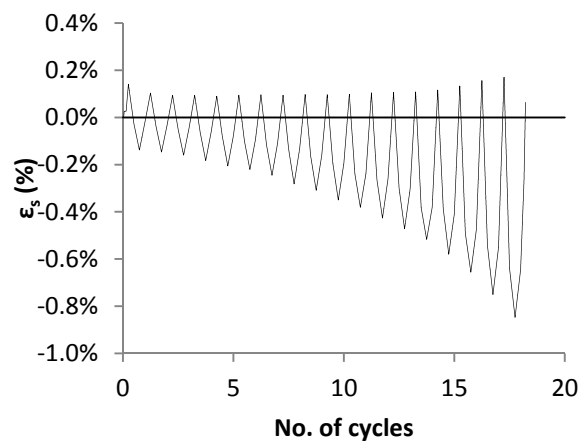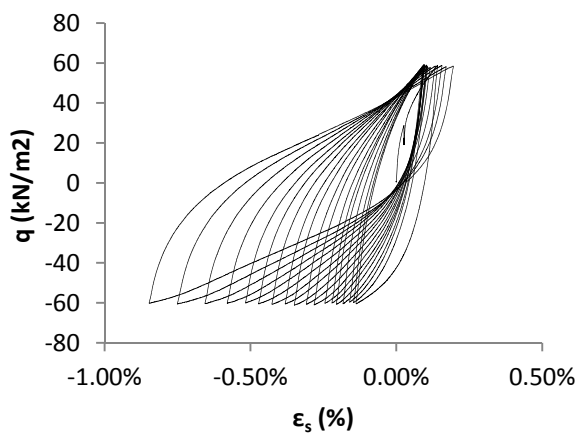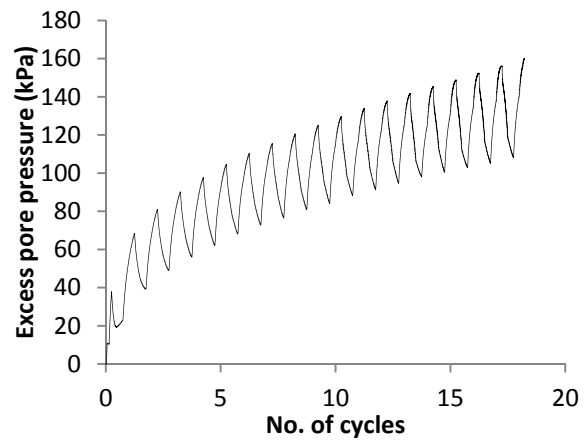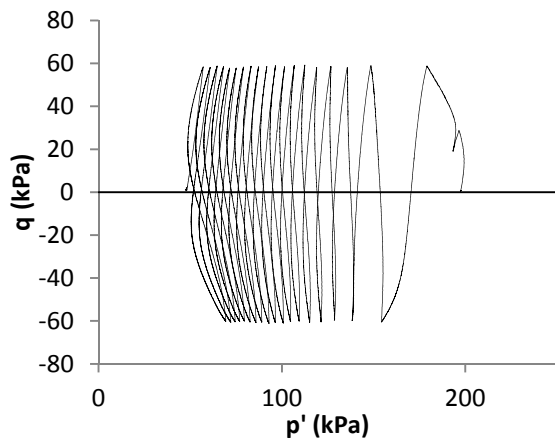
Test Nr.:	0601-4	Height [mm]	91.16	p'_0 [kPa]	203
Sample:	47139	Diameter [mm]	37.93	$CSR_{TX}=CSRT_{X1}$	0.15
Sample Depth [m]	10.35	Volume [cm^3]	103.01	OCR	1
PI	7.44	λ_{wet} [kN/m^3]	21.54	Loading velocity [mm/sec]	0.0002
LL	0.295	Void ratio	0.45	B-Value	0.97

Note: $CSR_{TX} = \dfrac{\Delta q}{2 \cdot \sigma'_3} = \dfrac{\Delta q}{2 \cdot \sigma'_h}$

Test 5
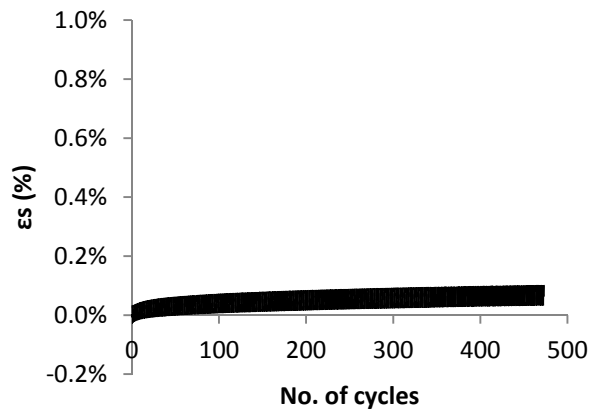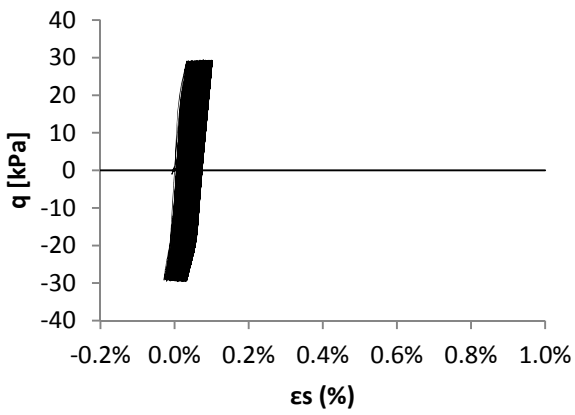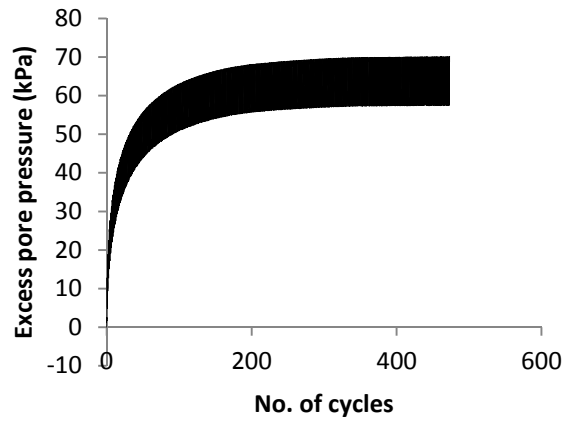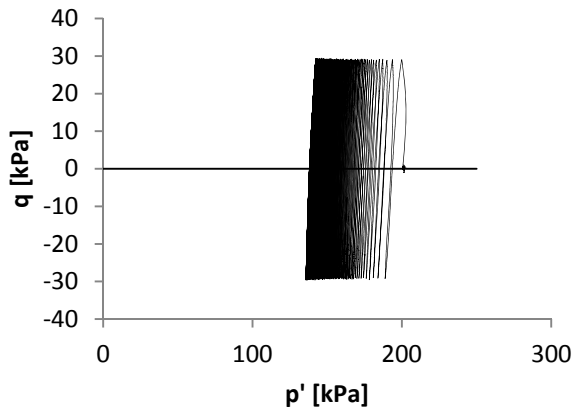
Test Nr.:	0601-5	Height [mm]	84.93	p'_0 [kPa]	203
Sample:	47139	Diameter [mm]	37.48	$CSR_{TX}=CSRT_{X1}$	0.075
Sample Depth [m]	10.35	Volume [cm^3]	93.69	OCR	1
PI	7.44	λ_{wet} [kN/m^3]	21.23	Loading velocity [mm/sec]	0.0002
LL	0.295	Void ratio	0.45	B-Value	0.96

Note: $\text{CSR}_{\text{TX}} = \frac{\Delta q}{2 \cdot \sigma'_3} = \frac{\Delta q}{2 \cdot \sigma'_h}$

Test 6
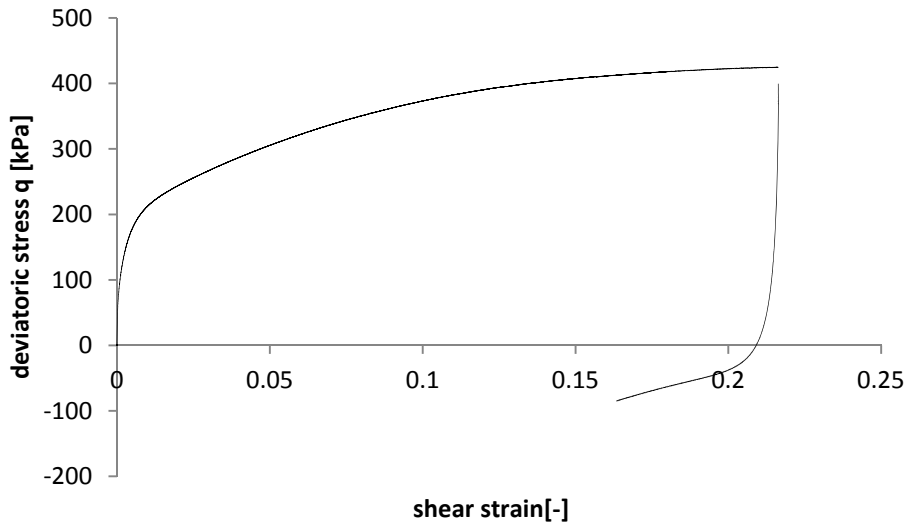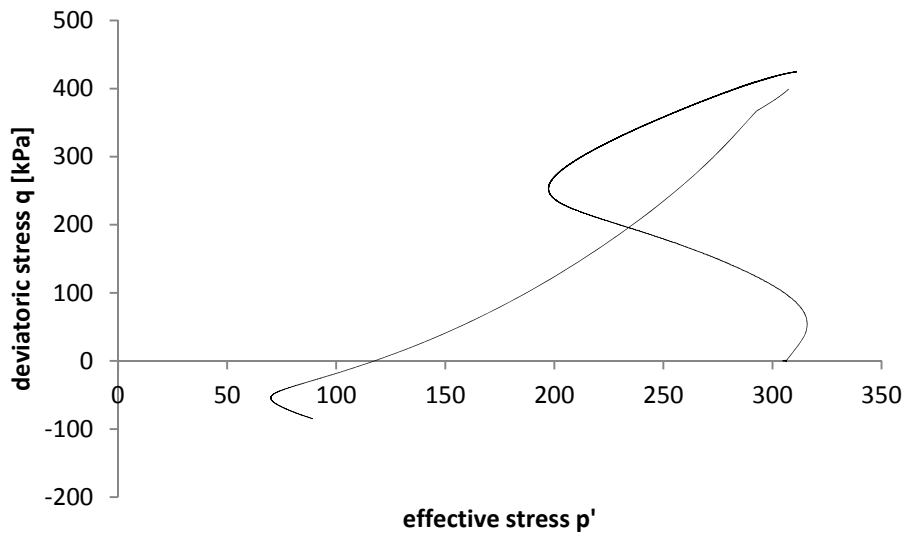
Test Nr.:	0601-11	Height [mm]	79.34	p'_0 [kPa]	206
Sample:	47147	Diameter [mm]	37.14	OCR	1
Sample Depth [m]	15.90	Volume [cm^3]	85.96	Loading velocity [mm/sec]	0.0002
Void ratio	0.49	λ$_{wet}$ [kN/m^3]	21.35	B-Value	0.93

Note: $CSR_{TX} = \frac{\Delta q}{2 \cdot \sigma'_3} = \frac{\Delta q}{2 \cdot \sigma'_h}$

Test 7

Test 7 has been performed in several stages, i.e. the deviatoric stress amplitude has been increased when no additional excess pore pressure develops.

Stage 7.1
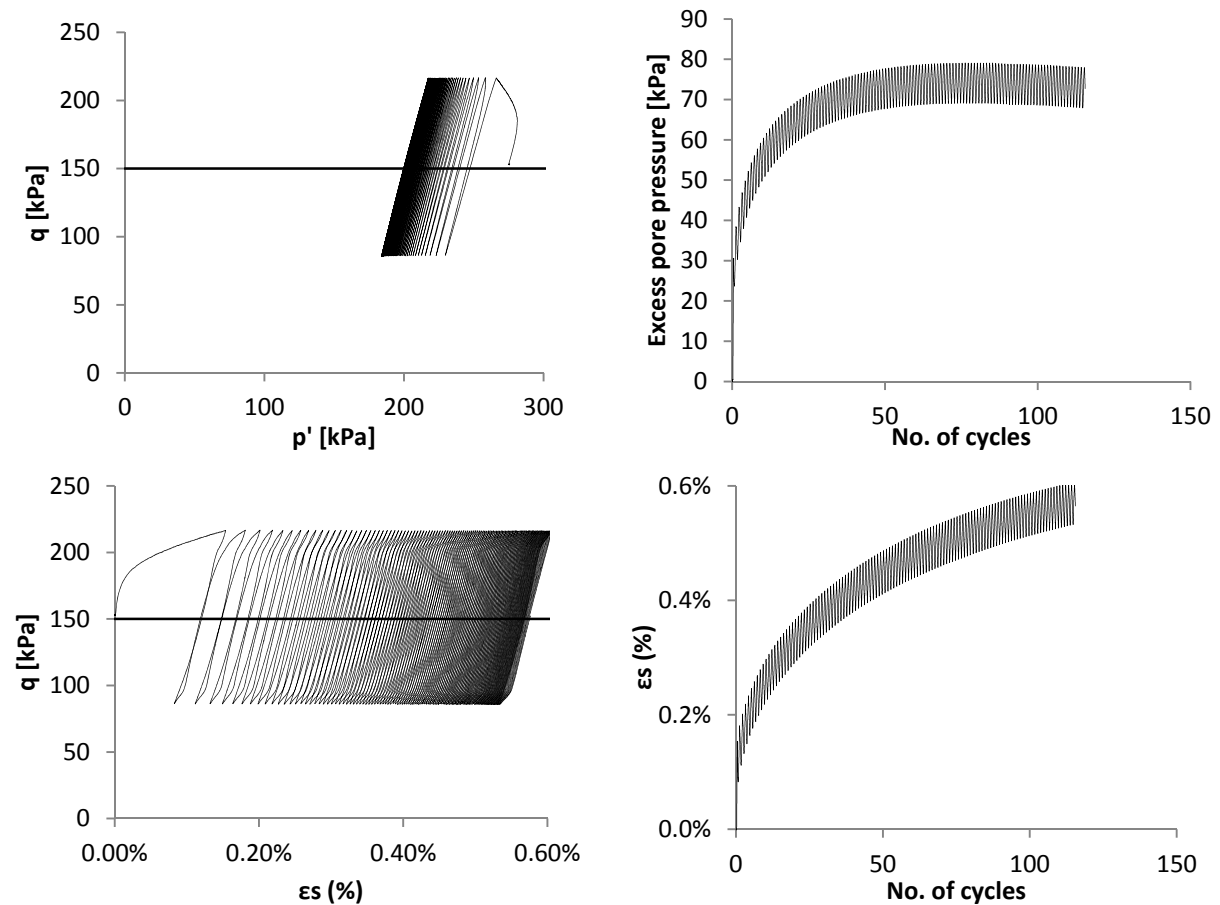
Test Nr.:	0601-11	Height [mm]	100.29	p'_0 [kPa]	276
Sample:	47147	Diameter [mm]	37.96	CSR_{TX}	0.15
Sample Depth [m]	15.90	Volume [cm^3]	113.52	CSR_{TX1}	0.09
Void ratio	0.53	λ_{wet} [kN/m^3]	21.08	OCR	1
		B-Value	0.93	Loading velocity [mm/sec]	0.0002

Note: $CSR_{TX} = \dfrac{\Delta q}{2 \cdot \sigma'_3} = \dfrac{\Delta q}{2 \cdot \sigma'_h}$; $CSR_{TX1} = \dfrac{\Delta q}{2 \cdot \sigma'_1}$

Test 7 (multi stage)

Stage 7.2
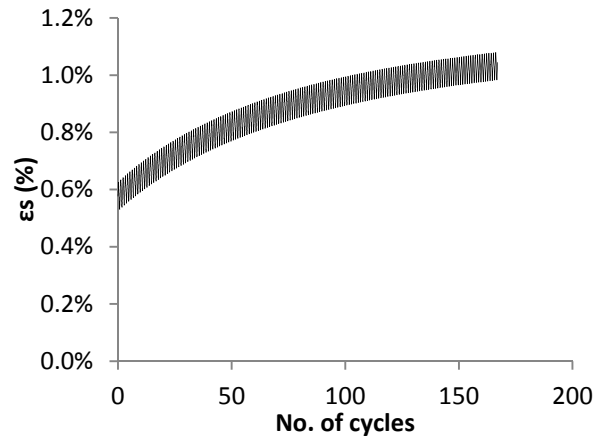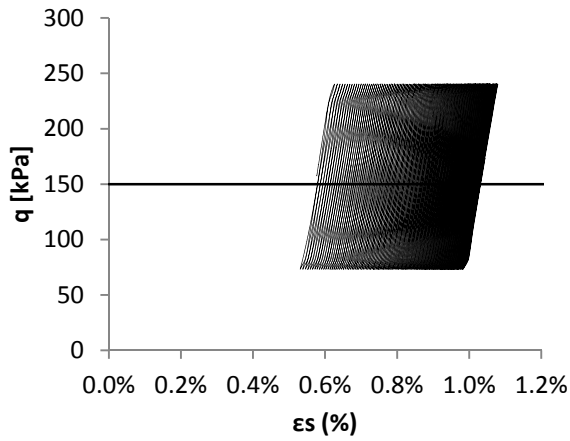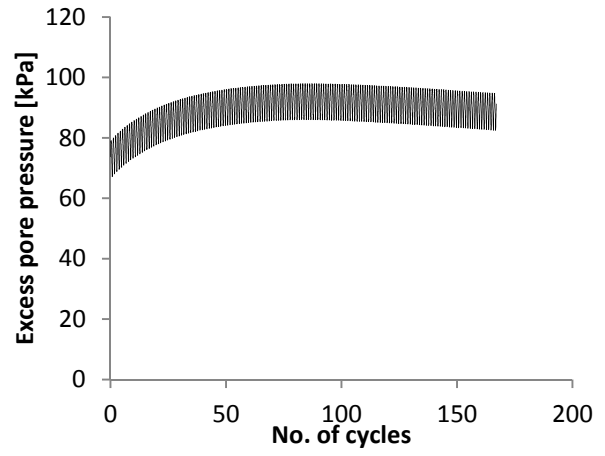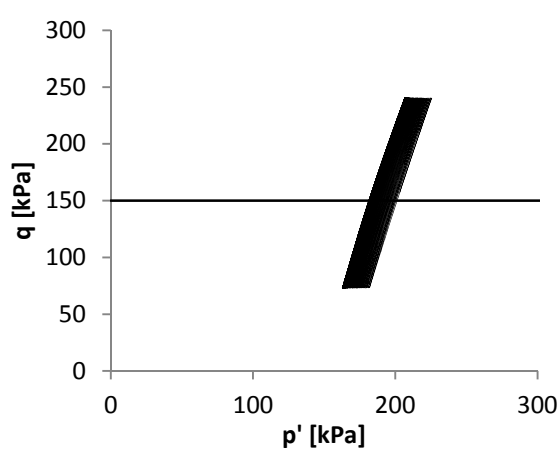
Test Nr.:	0601-11	Height [mm]	100.29	p'_0 [kPa]	276
Sample:	47147	Diameter [mm]	37.96	CSR_{TX}	0.19
Sample Depth [m]	15.90	Volume [cm^3]	113.52	CSR_{TX1}	0.12
Void ratio	0.53	λ_{wet} [kN/m^3]	21.08	OCR	1
		B-Value	0.93	Loading velocity [mm/sec]	0.0002

Note: $CSR_{TX} = \frac{\Delta q}{2 \cdot \sigma'_3} = \frac{\Delta q}{2 \cdot \sigma'_h}$; $CSR_{TX1} = \frac{\Delta q}{2 \cdot \sigma'_1}$

Test 7 (multi stage)

Stage 7.3
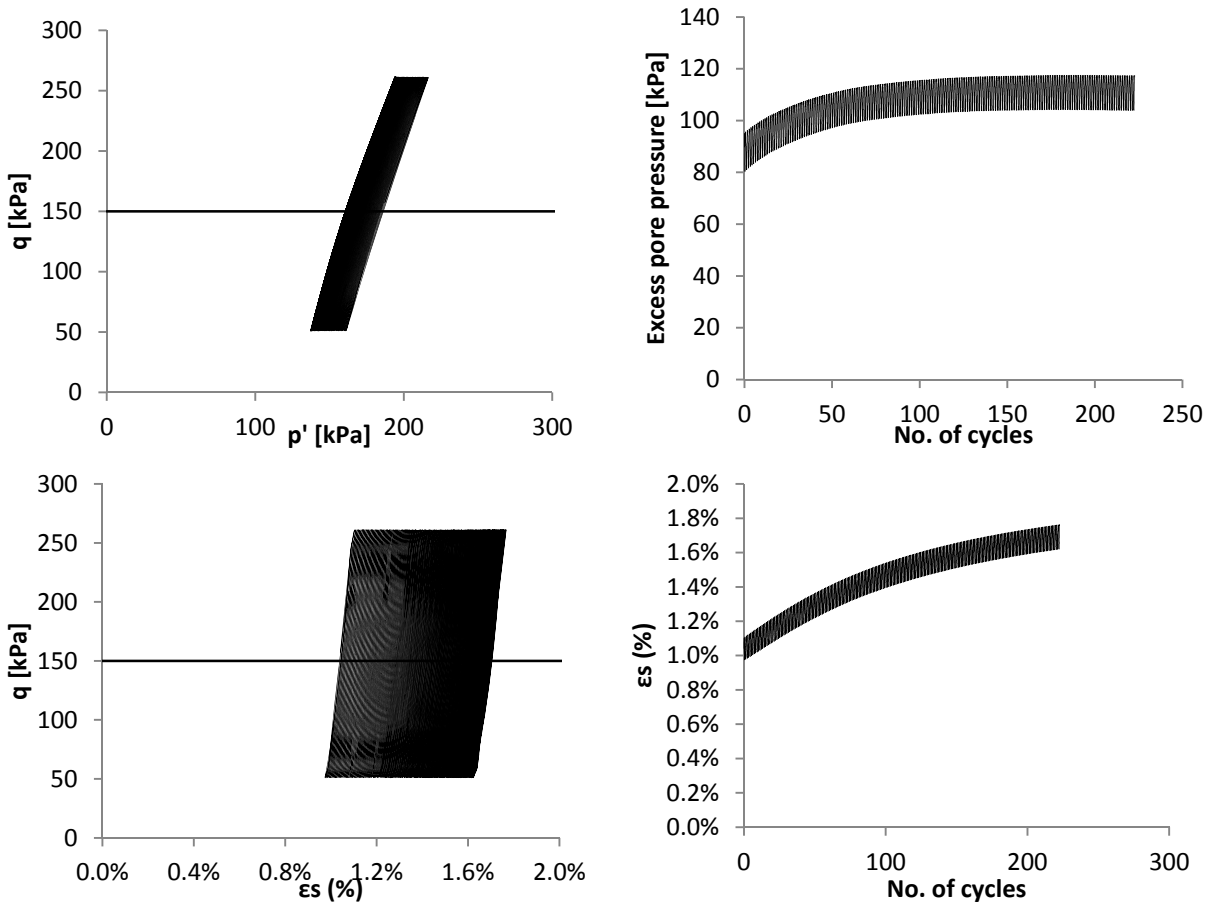
Test Nr.:	0601-11	Height [mm]	100.29	p'_0 [kPa]	276
Sample:	47147	Diameter [mm]	37.96	CSR_{TX}	0.24
Sample Depth [m]	15.90	Volume [cm^3]	113.52	CSR_{TX1}	0.14
Void ratio	0.53	λ_{wet} [kN/m^3]	21.08	OCR	1
		B-Value	0.93	Loading velocity [mm/sec]	0.0002

Note: $\mathrm{CSR_{TX}} = \frac{\Delta q}{2 \cdot \sigma'_3} = \frac{\Delta q}{2 \cdot \sigma'_h}$; $\mathrm{CSR_{TX1}} = \frac{\Delta q}{2 \cdot \sigma'_1}$

Test 7 (multi stage)

Stage 7.4
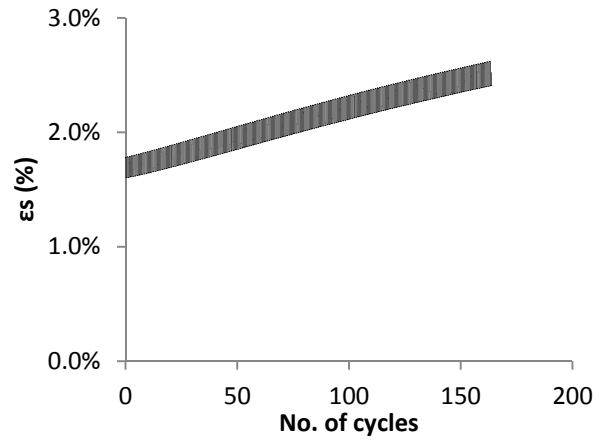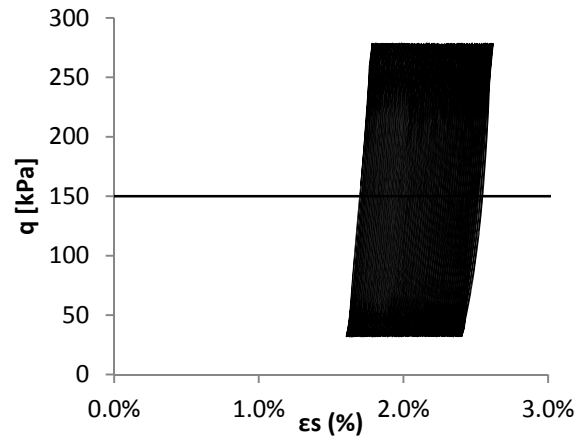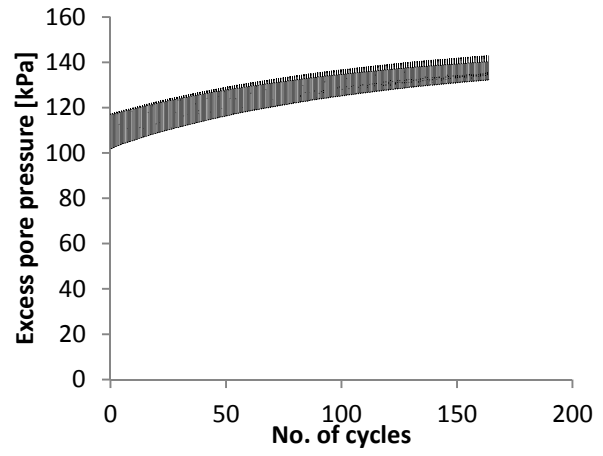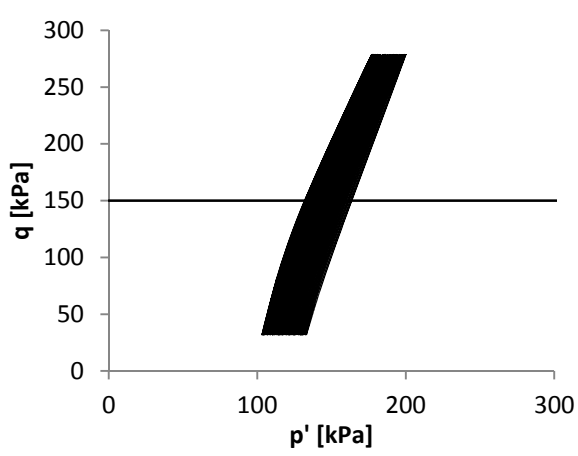
Test Nr.:	0601-11	Height [mm]	100.29	p'_0 [kPa]	276
Sample:	47147	Diameter [mm]	37.96	CSR_{TX}	0.28
Sample Depth [m]	15.90	Volume [cm^3]	113.52	CSR_{TX1}	0.17
Void ratio	0.53	λ_{wet} [kN/m^3]	21.08	OCR	1
		B-Value	0.93	Loading velocity [mm/sec]	0.0002

Note: $\mathrm{CSR_{TX}} = \frac{\Delta q}{2 \cdot \sigma'_3} = \frac{\Delta q}{2 \cdot \sigma'_h}$; $\mathrm{CSR_{TX1}} = \frac{\Delta q}{2 \cdot \sigma'_1}$

Test 7 (multi stage)

Stage 7.5
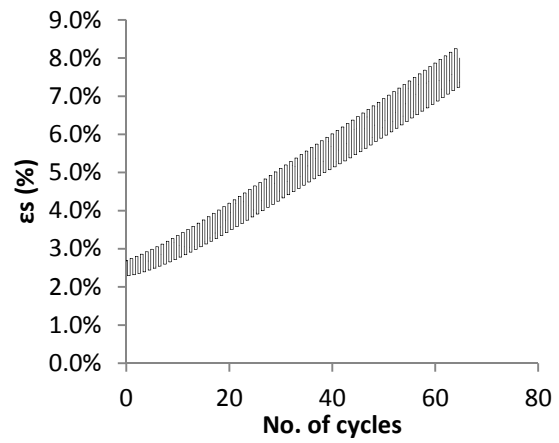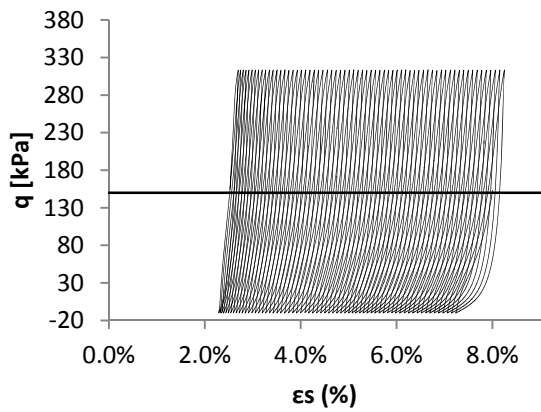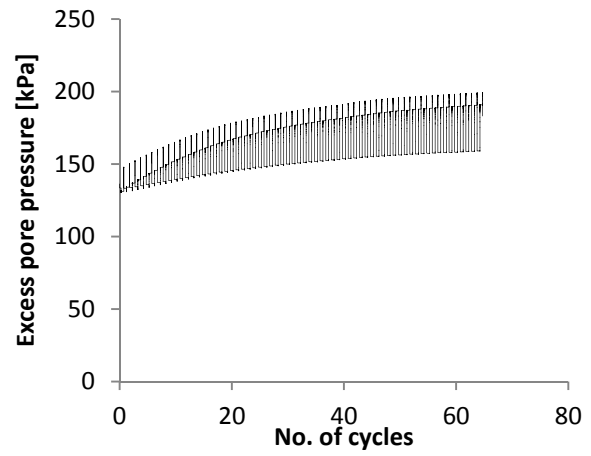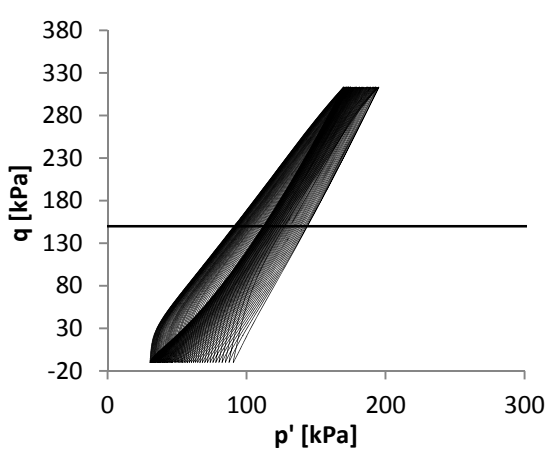
Test Nr.:	0601-11	Height [mm]	100.29	p'_0 [kPa]	276
Sample:	47147	Diameter [mm]	37.96	CSR_{TX}	0.35
Sample Depth [m]	15.90	Volume [cm^3]	113.52	CSR_{TX1}	0.21
Void ratio	0.53	λ_{wet} [kN/m^3]	21.08	OCR	1
		B-Value	0.93	Loading velocity [mm/sec]	0.0002

Note: $\text{CSR}_{TX} = \frac{\Delta q}{2 \cdot \sigma'_3} = \frac{\Delta q}{2 \cdot \sigma'_h} \, ; \text{CSR}_{TX1} = \frac{\Delta q}{2 \cdot \sigma'_1}$

Test 8
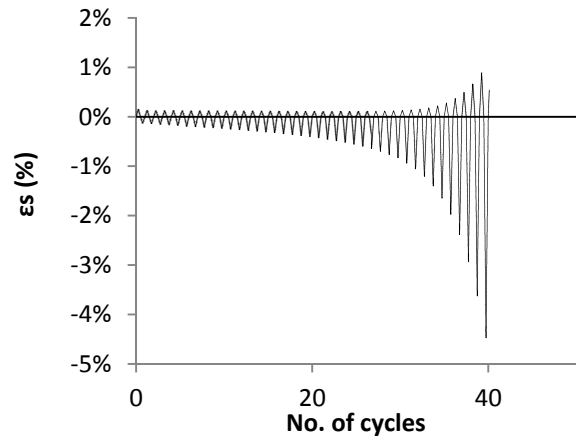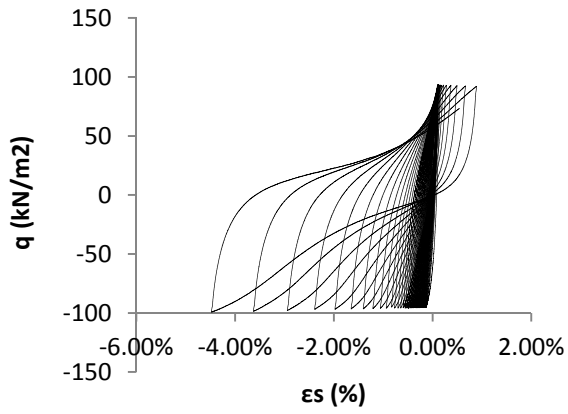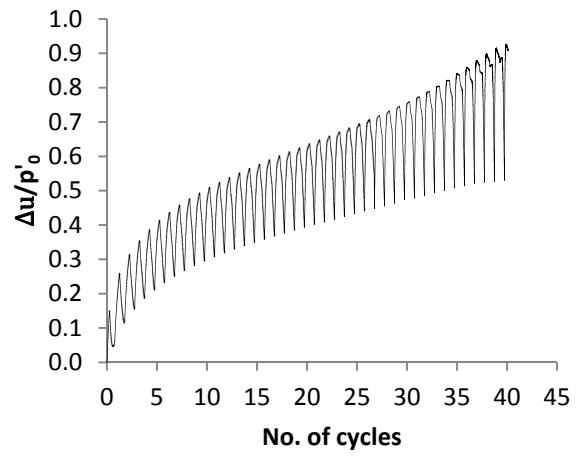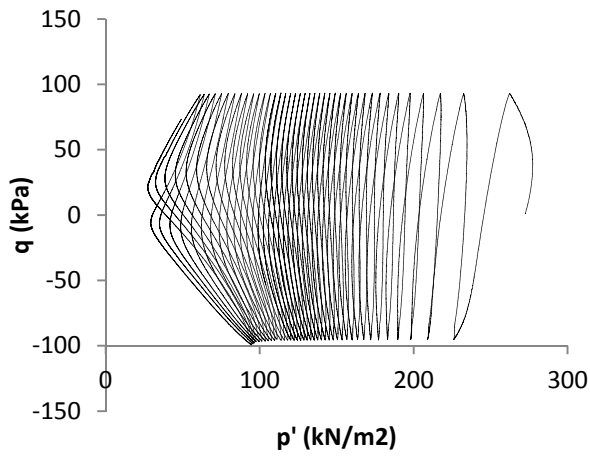
Test Nr.:	0601-11	Height [mm]	76.2	p'_0 [kPa]	273
Sample:	47147	Diameter [mm]	37.23	$CSR_{TX}=CSR_{TX1}$	0.17
Sample Depth [m]	15.90	Volume [cm³]	82.92	OCR	1
Void ratio	0.61	λ_{wet} [kN/m³]	21.08	Loading velocity [mm/sec]	0.0002
		B-Value	0.96		

Note: $\text{CSR}_{TX} = \frac{\Delta q}{2 \cdot \sigma'_3} = \frac{\Delta q}{2 \cdot \sigma'_h}$

Test 9
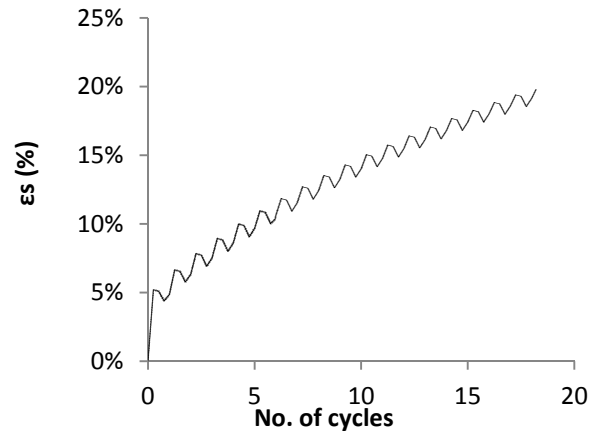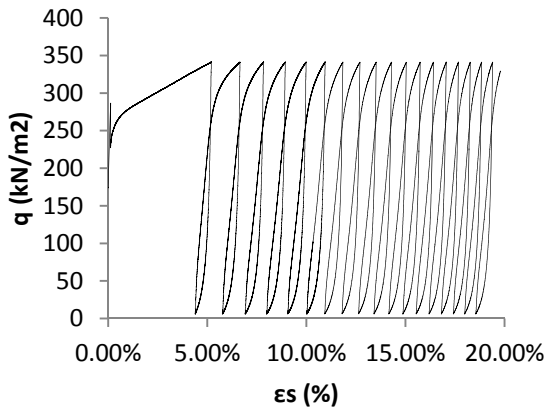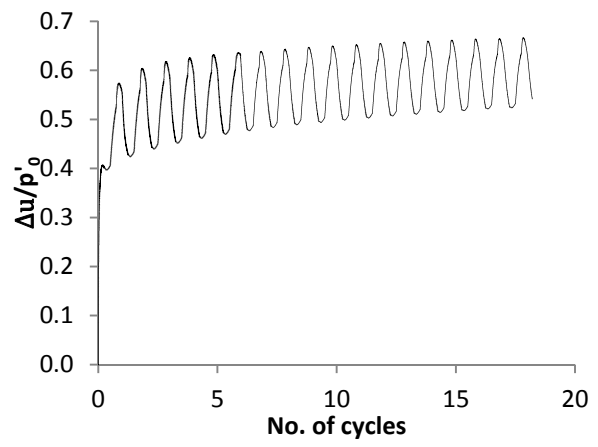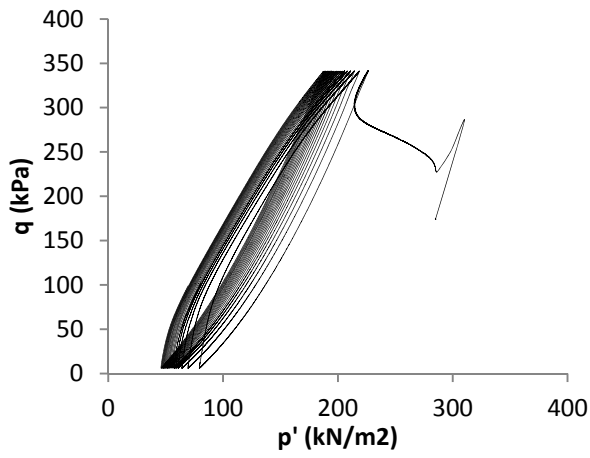
Test Nr.:	0601-11	Height [mm]	78.41	p'_0 [kPa]	285
Sample:	47147	Diameter [mm]	37.27	CSR_{TX}	0.29
Sample Depth [m]	15.90	Volume [cm^3]	85.86	CSR_{TX1}	0.21
Void ratio	0.55	λ_{wet} [kN/m^3]	20.93	OCR	1
		B-Value		Loading velocity [mm/sec]	0.0002

Note: $CSR_{TX} = \frac{\Delta q}{2 \cdot \sigma'_3} = \frac{\Delta q}{2 \cdot \sigma'_h}$; $CSR_{TX1} = \frac{\Delta q}{2 \cdot \sigma'_1}$

Test 10
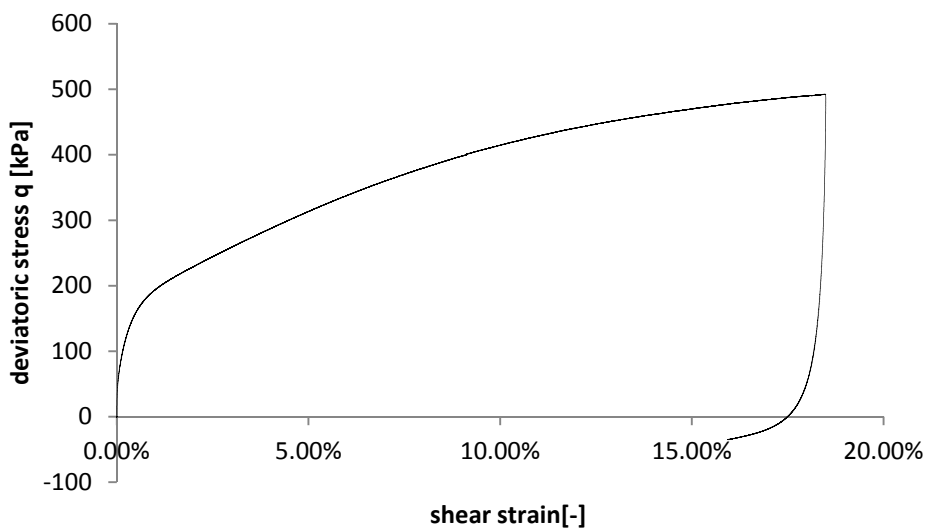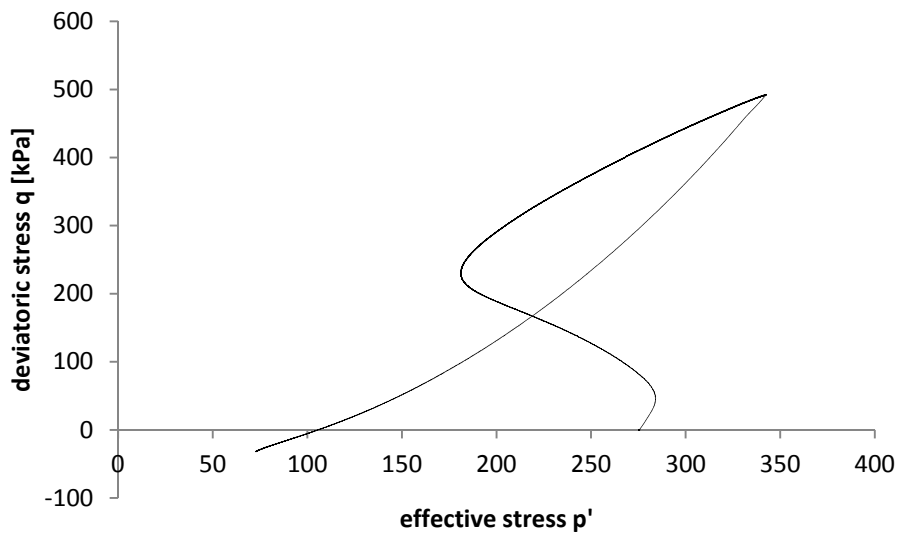
Test Nr.:	0601-11	Height [mm]	85.78	p'_0 [kPa]	276
Sample:	47147	Diameter [mm]	37.35	OCR	1
Sample Depth [m]	15.90	Volume [cm^3]	92.58	Loading velocity [mm/sec]	0.0002
Void ratio	0.51	λ_{wet} [kN/m^3]	21.23	B-Value	

Note: $CSR_{TX} = \frac{\Delta q}{2 \cdot \sigma'_3} = \frac{\Delta q}{2 \cdot \sigma'_h}$

REFERENCES

Angeli, M.G., Gasparetto, P., Menotti, R.M., Pasuto, A., Silvano, S., 1996. A visco-plastic model for slope analysis applied to a mudslide in Cortina d'Ampezzo, Italy. Q. J. Eng. Geol. 29, 233–240.

Bendel, H., 1983. Brattas Hang, St. Moritz; Geotechnische Zonierung - Gebaeudeaufnehmen.

Bernander, S., Gustaas, H., 1984. Consideration of in situ stresses in clay slopes with special reference to progressive failure analysis, in: NGM-84, Nordisk Geoteknikermöte. Statens geotekniska institut (SGI), Linköping, pp. 417–430.

Bernander, S., Olofsson, I., 1981. On formation of progressive failures in slopes. 10th ICSMFE Conference

Biondi, G., Cascone, E., Maugeri, M., Motta, E., 2000. Seismic response of saturated cohesionless slopes. Soil Dyn. Earthq. Eng. 20, 209–215. https://doi.org/10.1016/S0267-7261(00)00051-8

Bishop, A.W., Green, G.E., Garga, V.K., Andresen, A., Brown, J.D., 1971. A New Ring Shear Apparatus and Its Application to the Measurement of Residual Strength. Géotechnique 21, 273–328. https://doi.org/10.1680/geot.1971.21.4.273

Bjerrum, L., 1967. Progressive failure in slopes of overconsolidated plastic clay and clay shales. J. Soil Mech. Found. Div. 93, 1–49.

Booker, J.R., Rahman, M.S., Seed, H.B., 1976. GADFLEA: a computer program for the analysis of pore pressure generation and dissipation during cyclic or earthquake loading.

Bovenga, F., Wasowski, J., Nitti, D.O., Nutricato, R., Chiaradia, M.T., 2012. Using COSMO/SkyMed X-band and ENVISAT C-band SAR interferometry for landslides analysis. Remote Sens. Environ. 119, 272–285. https://doi.org/DOI 10.1016/j.rse.2011.12.013

Bründl, M., Romang, H., Holthausen, N., Merz, H., Bischof, N., 2009. Allgemeine Darstellung des Risikokonzepts.

CH2011, 2011. Swiss Climate Change Scenarios CH2011 (Report). Zurich.

Comegna, L., Picarelli, L., Bucchignani, E., Mercogliano, P., 2013. Potential effects of incoming climate changes on the behaviour of slow active landslides in clay. Landslides 10, 373–391. https://doi.org/10.1007/s10346-012-0339-3

Dafalias, Y.F., 1986. Bounding surface plasticity. I: Mathematical foundation and hypoplasticity. J. Eng. Mech. 112, 966–987.

Dafalias, Y.F., Popov, E.P., 1975. A Model of Nonlinearly Hardening Materials for Complex Loading. Acta Mech. 21, 173–192.

Dai, F.C., Lee, C.F., Ngai, Y.Y., 2002. Landslide risk assessment and management: an overview. Eng. Geol. 64, 65–87.

Deng, J., Tsutsumi, Y., KAmeya, H., Kokesi, J., 2010. A modified procedure to evaluate earthquake-induced displacements of slopes containing a weak layer. Soils Found. 50, 413–420. https://doi.org/10.3208/sandf.50.413

Donahue, J.L., 2007. The liquefaction susceptibility, resistance, and response of silty and clayey soils. PhD thesis, University of California Berkeley.

Elgamal, A., Yang, Z., Parra, E., Ragheb, A., 2003. Modeling of cyclic mobility in saturated cohesionless soils. Int. J. Plast. 19, 883–905. https://doi.org/10.1016/S0749-6419(02)00010-4

Fotopoulou, S.D., Pitilakis, K.D., 2013. Vulnerability assessment of reinforced concrete buildings subjected to seismically triggered slow-moving earth slides. Landslides 10, 563–582. https://doi.org/10.1007/s10346-012-0345-5

François, B., Tacher, L., Bonnard, C., Laloui, L., Triguero, V., 2007. Numerical modelling of the hydrogeological and geomechanical behaviour of a large slope movement: the Triesenberg landslide (Liechtenstein). Can. Geotech. J. 44, 840–857. https://doi.org/10.1139/t07-028

Glastonbury, J., Fell, R., 2008. Geotechnical characteristics of large slow, very slow, and extremely slow landslides. Can. Geotech. J. 45, 984–1005. https://doi.org/Doi 10.1139/T08-021

Gottardi, G., Butterfield, R., 2001. Modelling ten years of downhill creep data, in: 15th International Conference on Soil Mechanics and Geotechnical Engineering Location. Istanbul, pp. 99–102.

Gratchev, I.B., Sassa, K., 2015. Shear Strength of Clay at Different Shear Rates. J. Geotech. Geoenvironmental Eng. 141, 6015002. https://doi.org/10.1061/(ASCE)GT.1943-5606.0001297

Green, R.A., Mitchell, J.K., Polito, C.P., 2000. An Energy-Based Excess Pore Pressure Generation Model for Cohesionless Soils. Proc. John Booker Meml. Symp.

Guzzetti, F., Carrara, A., Cardinali, M., Reichenbach, P., 1999. Landslide hazard evaluation: a review of current techniques and their application in a multi-scale study, Central Italy. Geomorphology 31, 181–216.

Hansbo, P., Larsson, R., Runesson, K., Wiberg, N.-E., 1985. On the bahviour of natural slopes with emphasis on progrssive failure. Proceedings of the eleventh international conference on soil mechanics and foundation engineering, San Francisco, 12-16 August 1985.

Ho, K., Leroi, E., Roberds, B., 2000. Quantitative Risk Assessment: Application, Myths and Fututre Direction, in: International Conference on Geotechnical and Geological Engineering. pp. 236–312.

Houlsby, G.T., 1992. Interpretation of dilation as a kinematic constraint, in: Proceedings of the Workshop on Modern Approaches to Plasticity. Horton, Greece, pp. 19–38.

Houlsby, G., Mortara, G., 2004. A continuous hyperplasticity model for sands under cyclic loading, in: Cyclic Behaviour of Soils and Liquefaction Phenomena. Taylor & Francis, pp. 21–26. https://doi.org/10.1201/9781439833452.ch3

Idriss, E.I.M., Dobry, R., Doyle, E.H., Singh, R.D., 1976. Behavior of Soft Clays Under Loading Conditions.

Idriss, I.M., Dobry, R., Singh, R.D., 1978. Non-Linear Behavior of Soft Clays during Cyclic Loading. J. Geotech. Eng. Div. 104, 1427–1447.

Iten, M., Schmid, A., Hauswirth, D., Puzrin, A.M., 2009. Defining and monitoring of landslide boundaries using fiber optic systems. Int. Symp. Predict. Simul. Methods Mitig. Geohazard .

Jibson, R.W., 1993. Predicting earthquake-induced landslide displacements using Newmark's slidingblock analysis. Transp. Res. Rec. 1411, 9–17.

Jibson, R.W., Prentice, C.S., Borissoff, B. a, Rogozhin, E. a, Langer, C.J., 1994. Some observations of landslides triggered by the 29 April 1991 Racha earthquake, Republic of Georgia. Bull. Seismol. Soc. Am. 84, 963–973.

Keller, D.E., 2015. A Weather generator for current and future climate conditions. PhD thesis, ETH Zurich. https://doi.org/10.3929/ETHZ-A-010469558

Kramer, S.L., 1996. Geotechnical Earthquake Engineering, Prentice-Hall, Inc. https://doi.org/10.1007/ 978-3-540-35783-4

Krummenacher, B., Franciosi, G., 2009. Risikokonzept für Naturgefahren - Leitfaden; Teil B: Anwendungen des Risikokonzepts: Prozess permanente Rutuschungen.

Lacroix, P., Berthier, E., Maquerhua, E.T., 2015. Earthquake-driven acceleration of slow-moving landslides in the Colca valley, Peru, detected from Pléiades images. Remote Sens. Environ. 165, 148–158. https://doi.org/10.1016/j.rse.2015.05.010

Laloui, L., Ferrari, A., Bonnard, C., 2009. Geomechanical modeling of the Steinernase landslide (Switzerland). 1st Ital. Work. Landslides.

Laloui, L., Tacher, L., Moreni, M., Bonnard, C., 2004. Hydro-mechanical modeling of crises of large landslides : application to the La Frasse Landslide.

Lateltin, O., 1997. Berücksichtigung der Massenbewegungsgefahren bei raumwirksamen Tätigkeiten.

Lateltin, O., Haemmig, C., Raetzo, H., Bonnard, C., 2005. Landslide risk management in Switzerland. Landslides 2, 313–320. https://doi.org/10.1007/s10346-005-0018-8

Laue, J., 2014. Allgemeine Konzepte des seismischen Entwurfs und der Bemessung in der Geotechnik mit Anwendung auf Hänge. Mitteilungen der Geotech. Schweiz 168, 37–52.

Law, K.T., Lumb, P., 1978. Limit Equilibrium-Analysis of Progressive Failure in Stability of Slopes. Can. Geotech. J. 15, 113–122. https://doi.org/Doi 10.1139/T78-009

Lee, E. M., Jones, D.K.C., 2004. Landslide Risk Assessment.

Lemos, L.J.L., 2003. Shear behaviour of pre-existing shear zones under fast loading–insights on the landslide motion. International Conference Fast Slip Movements Predict. Prev. Risk Mitigation, Sorrento, Naples.

Lupini, J.F., Skinner, A.E., Vaughan, P.R., 1981. The drained residual strength of cohesive soils. Géotechnique 31, 181–213. https://doi.org/10.1680/geot.1981.31.2.181

Macfarlane, D.F., 2009. Observations and predictions of the behaviour of large, slow-moving landslides in schist, Clyde Dam reservoir, New Zealand. Eng. Geol. 109, 5–15. https://doi.org/http://dx.doi.org/10.1016/j.enggeo.2009.02.005

Mansour, M.F., Morgenstern, N.R., Martin, C.D., 2010. Expected damage from displacement of slow-moving slides. Landslides 8, 117–131. https://doi.org/10.1007/s10346-010-0227-7

Marchetti, S., 1997. The flat dilatometer: Design applications, in: Proceedings. Citeseer, pp. 1–25.

Matasović, N., Vucetic, M., 1995. Generalized Cyclic-Degradation-Pore-Pressure Generation Model for Clays. J. Geotech. Eng. 121, 33–42. https://doi.org/10.1061/(ASCE)0733-9410(1995)121:1(33)

Maugeri, M., Motta, E., Raciti, E., 2006. Mathematical modelling of the landslide occurred at Gagliano Castelferrato (Italy). Nat. Hazards Earth Syst. Sci. 6, 133–143.

Müller, E.R., Messina, G., 1992. Geotechnisches Gutachten: Rutschhang Sass Runzöl-Brattas (Report). Büchi und Müller AG.

Nadim, F., Kjekstad, O., Peduzzi, P., Herold, C., Jaedicke, C., 2006. Global landslide and avalanche hotspots. Landslides 3, 159–173. https://doi.org/DOI 10.1007/s10346-006-0036-1

Newmark, N.M., 1965. Effects of Earthquakes on Dams and Embankments. Geotechnique 15, 109–129.

Ostric, M., Sassa, K., He, B., Takara, K., Yamashiki, Y., 2013. Portable Ring Shear Apparatus and Its Application, in: Landslide Science and Practice. Springer Berlin Heidelberg, Berlin, Heidelberg, pp. 365–369. https://doi.org/10.1007/978-3-642-31445-2_47

Palmisano, F., 2011. Landslide structural vulnerbility of masonry buildings. PhD thesis, Politecnico di Bari.

Palmisano, F., Vitone, C., Cotecchia, F., 2016. Methodology for Landslide Damage Assessment. Procedia Eng. 161, 511–515. https://doi.org/10.1016/j.proeng.2016.08.679

Picarelli, L., Russo, C., 2004. Remarks on the mechanics of slow active landslides and the interaction with man-made works.

Picarelli, L., Urciuoli, G., Russo, C., 2004. Effect of groundwater regime on the behaviour of clayey slopes. Can. Geotech. J. 41, 467–484. https://doi.org/Doi 10.1139/T04-009

Picarelli, L., 2011. Discussion to the paper "Expected damage from displacement of slow-moving slides" by M.F. Mansour, N.R. Morgenstern and C.D. Martin. Landslides 8, 553–555. https://doi.org/10.1007/s10346-011-0292-6

Pradel, D., Smith, P.M., Stewart, J.P., Raad, G., 2005. Case history of landslide movement during the Northridge earthquake. J. Geotech. Geoenvironmental Eng. 131, 1360–1369. https://doi.org/Doi 10.1061/(Asce)1090-0241(2005)131:11(1360)

Prevost, J.H., 1985. A simple plasticity theory for frictional cohesionless soils. Int. J. Soil Dyn. Earthq. Eng. 4, 9–17. https://doi.org/10.1016/0261-7277(85)90030-0

Puzrin, A.M., Messerklinger, S., Schmid, A., 2008. The in-situ stiffness of the sliding layer in a creeping landslide, in: 4th International Symposium on Deformation Characteristics of Geomaterials. 22.11.2008-24.11.2008, Atlanta, pp. 407–412.

Puzrin, A.M., Schmid, A., 2011. Progressive failure of a constrained creeping landslide. Proc. R. Soc. A - Math. Phys. Eng. Sci. 467, 2444–2461. https://doi.org/DOI 10.1098/rspa.2011.0063

Puzrin, A., Schmid, A., 2012. Evolution of stabilised creeping landslides. Geotechnique 62, 491–501.

Puzrin, A.M., Schmid, A., Iten, M., Schwager, M., Hauswirth, D., 2005. Interaktion Strasse-Hangstabilität: Monitoring und Rückwärtsrechnung.

Puzrin, A.M., Schmid, A., Schwager, M. V, Eberhardt, E., Froese, C., Keith Turner, A., Leroueil, S., 2012. Case studies of constrained creeping landslides in Switzerland, in: 11th International Symposium on Landslides and Engineered Slopes ISL. Taylor & Francis Group, Banff, Canada, pp. 1795–1800.

Puzrin, A.M., Sterba, I., 2006. Inverse long-term stability analysis of a constrained landslide. Geotechnique 56, 483–489.

Richard, F., Zeller, J., 1972. Untersuchungen über den Einfluss der Skipistenschneise auf die Rutschung Sass Runzöl -St. Moritz. Birmensdorf.

Saito, R., Fukuoka, H., Sassa, K., 2006. Experimental Study on the Rate Effect on the Shear Strength. Disaster Mitig. Debris Flows, Slope Fail. Landslides Exp. 421–427.

Sancio, R.B., 2003. Ground Failure and Building Performance in Adapazari, Turkey, Ground Failure and Building Performance in Adapazari, Turkey. PhD thesis, University of California Berkeley.

Sanin, M.V., 2010. Cyclic shear loading response of Fraser River delta silt. https://doi.org/10.14288/1.0062865

Sassa, K., Fukuoka, H., Wang, G., Ishikawa, N., 2004. Undrained dynamic-loading ring-shear apparatus and its application to landslide dynamics. Landslides 1, 7–19. https://doi.org/10.1007/s10346-003-0004-y

Schindler, C., 1982. Problemreiche Hinterlassenschaft: Geologie und Wasserverhältnisse in Braunwald. Neujahrsbote 1982 für das Glarner Hinterland 16, 131–140.

Schlüchter, C., 1988. Instabilities in the area of St. Moritz, Switzerland - Geology, chronology, geotechnology, in: Bonnard, C. (Ed.), 5th International Symposiun on Landslides. Balkema, Lausanne, pp. 1375–1380.

Schulz, W.H., Kean, J.W., Wang, G.H., 2009. Landslide movement in southwest Colorado triggered by atmospheric tides. Nat. Geosci. 2, 863–866. https://doi.org/Doi 10.1038/Ngeo659

Schulz, W.H., Wang, G., 2014. Residual shear strength variability as a primary control on movement of landslides reactivated by earthquake-induced ground motion: Implications for coastal Oregon, U.S. J. Geophys. Res. Earth Surf. 119, 1617–1635. https://doi.org/10.1002/2014JF003088

Schwager, M. V, 2013. Development, analysis and applications of an "inclinodeformeter" device for earth pressure measurements ETH Library. https://doi.org/10.3929/ethz-a-010183078

Schwager, M. V, Puzrin, A., 2014. Inclinodeformeter pressure measurements in creeping landslides: analytical solutions and field applications. Geotechnique 64, 447–462.

Skempton, A.W., 1964. Long-term stability of clay slopes. Geotechnique 14, 77–102. https://doi.org/10.1680/geot.1964.14.2.77

Skempton, A.W., Larochel, P., 1965. Bradwell Slip - a Short-Term Failure in London Clay. Geotechnique 15, 221–242.

Staub, P., 2006. Bericht 301: Geodätische Geländeüberwachung: Hangrutschungsmessung im Gebiet Gianda Laret-Brattas, Gemeinde St. Moritz. Zürich.

Sterba, I., Lang, H.-J., Amann, P., 2000. The Brattas landslide in St. Moritz, in: GeoEng. Technomic, Lancaster, PA, Melbourne/Australia, pp. 144–146.

Tacher, L., Bonnard, C., 2007. Hydromechanical modelling of a large landslide considering climate change conditions. Int. Conf. Landslides Clim. Chang. .

Tacher, L., Bonnard, C., Laloui, L., Parriaux, A., 2005. Modelling the behaviour of a large landslide with respect to hydrogeological and geomechanical parameter heterogeneity. Landslides 2, 3–14. https://doi.org/DOI 10.1007/s10346-004-0038-9

Terzaghi, K., 1936. Stability of slopes of natural clay, in: Casagrande, A., Rutledge, P.C., Watson, J.D. (Eds.), First International Conference on Soil Mechanics and Foundation Engineering. Reprinted by HarvardPrinting Office, Cambridge, Mass., Cambridge, MA 1, pp. 161–165.

Terzaghi, K., 1950. Mechanism of Landslides, in: Engng. Geol. Geol. Soc. Am. , Berkley, pp. 83–123.

Terzaghi, K., Peck, R.B., Ralph B., Mesri, G., 1996. Soil mechanics in engineering practice. Wiley.

Tika, T., Vaughan, P., Lemos, L., 1996. Fast shearing of pre-existing shear zones in soil. Geotech. 46 197–233. https://doi.org/10.1680/geot.1996.46.2.197

Togo, T., Shimamoto, T., Dong, J.-J., Lee, C.-T., Yang, C.-M., 2014. Triggering and runaway processes of catastrophic Tsaoling landslide induced by the 1999 Taiwan Chi-Chi earthquake, as revealed by high-velocity friction experiments. Geophys. Res. Lett. 41, 1907–1915. https://doi.org/10.1002/2013GL059169

Tschudi, D., Angst, R., 1999. Diplomvermessungskurs Semedan 1998, Rutschhang Brattas (Report). Institut für Geodäsie und Photogrammetrie, ETH Zürich, St. Moritz.

Uzielli, M., Catani, F., Tofani, V., Casagli, N., 2015a. Risk analysis for the Ancona landslide—I: characterization of landslide kinematics. Landslides 12, 69–82. https://doi.org/10.1007/s10346-014-0474-0

Uzielli, M., Catani, F., Tofani, V., Casagli, N., 2015b. Risk analysis for the Ancona landslide—II: estimation of risk to buildings. Landslides 12, 83–100. https://doi.org/10.1007/s10346-014-0477-x

Van Asch, T.W.J., 1984. Creep processes in landslides. Earth Surf. Process. Landforms 9, 573–583. https://doi.org/10.1002/esp.3290090611

Van Asch, T.W.J., Hendriks, M.R., Hessel, R., Rappange, F.E., 1996. Hydrological triggering conditions of landslides in varved clays in the French Alps. Eng. Geol. 42, 239–251. https://doi.org/Doi 10.1016/0013-7952(95)00082-8

Van Asch, T.W.J., Van Beek, L.P.H., Bogaard, T.A., 2007. Problems in predicting the mobility of slow-moving landslides. Eng. Geol. 91, 46–55. https://doi.org/DOI 10.1016/j.enggeo.2006.12.012

Vulliet, L., Hutter, K., 1988a. Continuum Model for Natural Slopes in Slow Movement. Geotechnique 38, 199–217.

Vulliet, L., Hutter, K., 1988b. Viscous-Type Sliding Laws for Landslides. Can. Geotech. J. 25, 467–477.

Vulliet, L., Hutter, K., 1988c. Set of Constitutive Models for Soils under Slow Movement. J. Geotech. Eng. 114, 1022–1041.

Wang, G., Suemine, A., Schulz, W.H., 2010. Shear-rate-dependent strength control on the dynamics of rainfall-triggered landslides, Tokushima Prefecture, Japan. Earth Surf. Process. Landforms 35, n/a-n/a. https://doi.org/10.1002/esp.1937

Westen, C.J., Asch, T.W.J., Soeters, R., 2005. Landslide hazard and risk zonation—why is it still so difficult? Bull. Eng. Geol. Environ. 65, 167–184. https://doi.org/10.1007/s10064-005-0023-0

Wiberg, N.E., Koponen, M., Runesson, K., 1990. Finite-element Analysis of Progressive Failure in Long Slopes. Int. J. Numer. Anal. Methods Geomech. 14, 599–612.

Yang, Z., Elgamal, A., 2008. Multi-surface cyclic plasticity sand model with lode angle effect. Geotech. Geol. Eng. 26, 335–348. https://doi.org/10.1007/s10706-007-9170-3

Yang, Z., Elgamal, A., Parra, E., 2003. Computational Model for Cyclic Mobility and Associated Shear Deformation. J. Geotech. Geoenvironmental Eng. 129, 1119–1127. https://doi.org/10.1061/(ASCE)1090-0241(2003)129:12(1119)

NOTATION – PART I

C_c	consolidation index
C_s	swelling index
d	thickness of shear zone (slip surface)
Δu	excess pore pressure
$\Delta\Omega$	change in ovalization of a inclinometer pipe
e	void ratio
E	elastic stiffness in visco-elastic models
ε_s	shear strain (triaxial test)
γ_{wet}	unit weight in triaxial tests
h	depth of the slip surface
LL	liquid limit
η	viscosity in visco-elastic models
η_τ	viscosity symbolizing rate effects along the slip surface
PI	plasticity index
P_a	active earth pressure
p'	mean effective stress in triaxial test
p'_0	initial mean effective stress in triaxial test
p'_y	yield stress
q	deviatoric stress in triaxial test
σ'	normal effective stress at slip surface
σ'_h	horizontal effective stress in triaxial test
σ'_v	vertical effective stress in triaxial test
σ'_{v0}	initial principal effective stress in triaxial test

τ_g gravitational shear stress at depth of the slip surface

τ^* shear resistance on the slip surface

τ_r residual shear strength on the slip surface

W weight of the landslide body

ξ yield factor

Part II: Development of a method to analyse the steady and transient state of creeping landslides

Abstract

Creeping landslides are common in mountainous areas, causing significant damage to buildings and infrastructure. The major difficulty in modelling of these landslides is inability of laboratory tests to reproduce adequately the macro behaviour in the creeping soil masses. The proposed approach of observation-guided constitutive modelling (OGCM) addresses this issue by considering a creeping landslide as a series of macro elements, in which monitoring of displacements and pore water pressures allows the derivation of suitable constitutive models and their parameters. This part proposes three generalized models describing the behaviour of pore water pressures, the sliding layer and the slip surface, which can be adapted to fit the observational data. The three models are integrated into the boundary value problem, whose solution helps to explain the evolution of the landslide and to predict its future behaviour using probabilistic approaches. When applied to the St. Moritz Brattas landslide in Switzerland, the calibrated landslide models proved to be successful in describing the complex behaviour of all three distinctive regions of the landslide.

Most of this part has been published as an article in *Géotechnique* (Oberender and Puzrin, 2016).

4 Observation-guided constitutive modelling for creeping landslides – Concept

4.1 Introduction

The understanding of the mechanics of creeping landslides can be greatly facilitated by successful numerical modelling of the transient creeping landslide behaviour (which in this context means the influence of weather variations) within a framework of the mechanics of continuum media. The modelling is complicated by: (i) complex, environmentally influenced hydrological behaviour affecting the landslide displacements; (ii) the presence of discontinuities (sliding surfaces with localized shear strains); and (iii) the high level of heterogeneity of the sliding masses. Therefore, the success of the numerical modelling heavily depends on the appropriate choice of: (i) a "hydrological model" relating precipitation to pore water pressures; (ii) a constitutive model of the soil behaviour at the interface between the sliding mass and the stable ground; and (iii) a constitutive model for the landslide body.

Derivation of reliable hydrological and constitutive models is a challenging task. In particular, the large scale of the landslides and significant uncertainties in their hydrological conditions undermine reliability of the sophisticated hydrological modelling. Furthermore, soil heterogeneity leads to significant deviations between the soil behaviour in the element lab tests and the macro behaviour on the slip surface and in the sliding mass. This is particularly relevant to the time- and rate-dependent components of the soil behaviour. As a result, when constitutive models derived using only lab test data are incorporated into a boundary value problem, they often fail to simulate the observed landslide behaviour reliably.

The work presented here proposes a different, "macro" approach to constitutive modelling of creeping landslides, based on their observed behaviour: observation-guided constitutive modelling (OGCM). In this approach, the sliding body can be viewed as series of macro elements subjected during the evolution of the landslide to compression by the neighbouring elements and shearing at the slip surface. This series of interconnected full-scale compression tests (with characteristic length being of the order of the landslide thickness) can be then interpreted in terms of macro soil behaviour, provided that the loads, displacements and pore water pressures are known for each element over a period of time. This data can be derived as a combination of field monitoring (of displacements, precipitation and, where available, earth and water pressures) and solutions of simple transient 1D boundary value problems.

In order to enable interpretation of such macro element behaviour, this work proposes generalized hydrological and constitutive models which are capable of reproducing a wide variety of the observed phenomena. Calibration of the models against the observed macro behaviour of a particular landslide is carried out as a two-step procedure. In the first step, we identify those features of the generalized models that are critical in reproducing the observed landslide behaviour. The non-critical features can then be neglected, significantly simplifying the model. In the second step, parameters of the simplified models can be derived from the inverse analysis of the corresponding boundary value problem.

The generalized models utilized in observation-guided constitutive modelling of creeping landslides should:
- be able to simulate all critical time-dependent features observed in creeping slopes;
- be sufficiently simple to allow for inverse analysis and the future stochastic risk analysis, which may involve hundreds of thousands of computer runs;
- enable easy simplifications by removing features non-critical for specific landslides;
- be able to ensure thermomechanical consistency, avoiding unrealistic generation or dissipation of energy during landslide evolution.

All these requirements, including the thermomechanical consistency (e.g. Einav and Randolph, 2006; Houlsby and Puzrin, 2000), can be satisfied by constructing such models from simple visco-elastic-plastic rheological elements, resulting in a hierarchical structure that allows for potential further simplifications.

The proposed OGCM approach has two advantages. Firstly, it is flexible enough to be adapted to various cases of creeping slopes (and even to different portions of the same slope) and enables easy updating as additional information becomes available. It can account for soil properties varying along the landslide and different boundary conditions at the foot of the landslide, such as those encountered in Brattas, Ganter and Combe Chopin creeping landslides in the Swiss Alps (Puzrin and Schmid, 2011, 2012). Secondly, the proposed generalized models are built of elementary rheological components, which simplify both the understanding of their role in the combined model behaviour and their removal from the model when their function appears unnecessary.

4.2   Formulation of the simplified boundary value problem

The generalized hydrological and constitutive models will be formulated in the following sections within the framework of a boundary value problem described by a conceptual 1D model for landslide (Figure 4-1), as proposed by Puzrin and Schmid (2012).
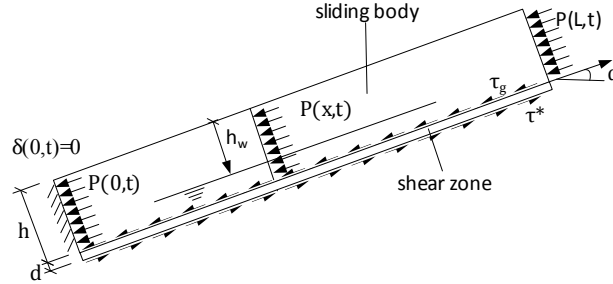
Figure 4-1: Conceptual model for the landslide geometry

The landslide model consists of a deformable soil layer of height h and inclination α, which is sliding above the slip surface, formed by a zone of intense shearing of thickness d. The phreatic surface is located at depth h_w. At the bottom, the sliding layer (also called sliding body) can be either free standing or constrained by an obstacle, conditions described either by the active earth pressure or by zero displacement, respectively. Equilibrium of the average earth pressures P in the sliding body is given by:

$$h\frac{\partial P}{\partial x} = \tau^* - \tau_g \tag{4-1}$$

where $\tau_g = \gamma_s \cdot h \cdot \sin(\alpha)$ is the gravitational shear stress with γ_s being the unit weight of soil; τ^* is the shear strength, which is a function of the effective stresses acting on the slip surface:

$$\sigma'_n = \big(\gamma_s h - \gamma_w(h - h_w)\big)\cdot\cos\alpha \tag{4-2}$$

which are subject to changes in the phreatic surface level, defined from the hydrological model. Assuming that the pressure at the top boundary of the landslide is known (typically between the at-rest and active pressure), one can derive the earth pressure at each point along the length (L) of the landslide by integrating equilibrium equation (4-1) top down and using the constitutive model for the interface behaviour on the slip surface:

$$P(x,t) = P(L,t) - \frac{1}{h}\int_x^L \big(\tau^*(\delta,\dot{\delta}) - \tau_g\big)dx \tag{4-3}$$

In order to calculate landslide displacements, a constitutive model for the sliding body is required, relating strains caused by these displacements to the earth pressures (4-3). Supplementing equations (4-2) and (4-3) with the initial and boundary conditions and with the required hydrological and constitutive models completes the problem formulation, which can be solved using a finite difference framework.

4.3   Generalized constitutive and hydrological model

4.3.1 Hydrological model

The effect of precipitation is taken into account by using a simple hydrological model. A portion of the monthly effectively precipitated volume of water p will run off on the slope surface and into those aquifers that are fully contained above the slip surface, therefore not affecting pore water pressures on the sliding surface. Of the remaining portion c_p, which will infiltrate into the slope and can potentially affect pore water pressures on the sliding surface, one part will be discharged, while the remaining part will be stored. From the mass conservation it follows that

$$c_p p = \Delta S + Q \tag{4-4}$$

where ΔS is the incremental change of the stored volume of water in the slope per chosen time increment; Q is the volume of the monthly discharge of the water from the slope, which is proportional to the total stored volume of water via a modified linear reservoir model (Van Asch et al., 1996, Buma, 2000):

$$Q = \frac{S}{k} \tag{4-5}$$

where k is the discharge coefficient. Similar to Buma (2000), the model can account for seasonality by assuming that all precipitation occurring in months with an average temperature below freezing is stored and released during the first month with average temperature above freezing. While this simplifying assumption has been validated for the Brattas landslide using piezometer readings (section 5.1), more complex snowmelt models can be readily incorporated into the proposed framework.

The monthly storage increment can then be derived from equations (4-4) and (4-5):

$$\Delta S = c_p p - \frac{S}{k} \tag{4-6}$$

Equation (4-6) can be solved numerically provided the initial condition (S_0) is known. It can, however, be shown that the effects of this initial condition vanish after a few years. Therefore, in order to decrease the influence of the error in the estimate of initial storage on the subsequent model predictions, simulation of the storage should begin sufficiently in advance of the actual time of interest.

Finally, the change in depth of the phreatic surface, affecting the shear strength on the sliding surface, can be linked to the calculated monthly change in storage via the porosity n:

$$\Delta h_w = -\frac{\Delta S}{n} \qquad (4\text{-}7)$$

It will be shown that in spite of its simplicity, the proposed hydrological model is capable of capturing both the seasonal variation in the phreatic surface position and the potential long-term trends.

4.3.2 Model of the slip surface

Taking into account that the sliding surface represents a localized zone of intense shearing with constant thickness (d), the shear strain (γ) and shear strain rate ($\dot{\gamma}$) can be related to the landslide displacement (δ) and velocity ($\dot{\delta}$) by:

$$\gamma = \frac{\delta}{d} \text{ and } \dot{\gamma} = \frac{\dot{\delta}}{d} \qquad (4\text{-}8)$$

allowing for the constitutive relationships to be formulated in the shear stress–displacement space. The constitutive relation for the slip surface has to account for strain softening, rate dependency and, if necessary, elastic pre-failure deformations. This can be achieved by using a combination of elastic, yielding and viscous elements (Figure 4-2a), adopted to fit the complexity of the specific case study, with the simplest formulation presented below.
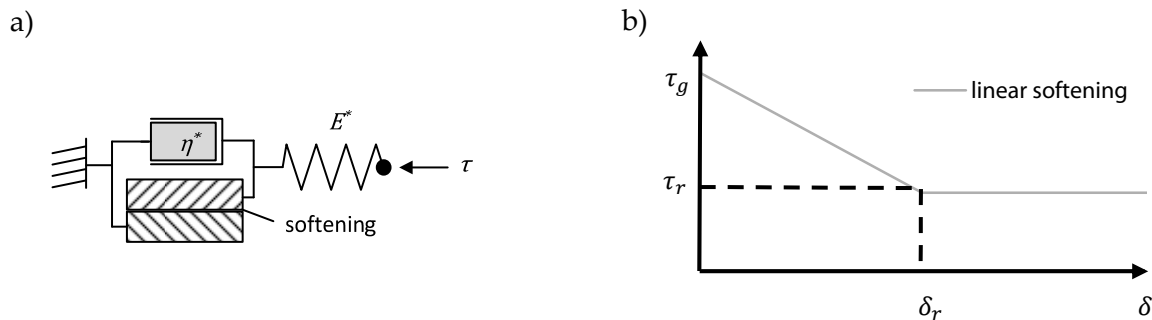
Figure 4-2: Constitutive model of the slip surface: a) rheological elements; b) idealized softening behaviour.

For cases in which the peak strength on the sliding surface has been exceeded, the pre-failure elastic deformations can be neglected (achieved by turning the elastic element into a rigid one: $E^*=\infty$). For the yielding element, perfect plasticity with a linear softening behaviour (Figure 4-2b) is used allowing the shear resistance to drop from its initial value at rest, i.e. in equilibrium with the gravitational shear stress (τ_g), to the residual shear strength (τ_r).

For the initial at-rest state of the landslide it is assumed that the soil has already overcome the peak strength during previous sliding and softened down to the mobilised friction angle of

$$\tan\varphi_g = \frac{\tau_g}{\sigma'_n(t=0)} \tag{4-9}$$

providing the initial condition for the partially softened friction angle corresponding to the shear strength in equilibrium with the gravitational shear stress. The term "residual strength" is used here in a somewhat broader sense than that introduced by Skempton (1985) for clays, indicating in the context of mixed soil conditions the minimum strength attained by soil after significant shearing deformation.

Finally, assuming also linearity of the viscous element in Figure 4-2a, and combining it with the linear strain softening of the yielding element and initial condition (4-9), the shear strength τ^* can be expressed as a linear function of strain and strain rate, or displacement and velocity (Figure 4-2a):

$$\tau^* = \left(\tan\varphi_g\left(1 - \frac{\delta}{\delta_r}\right) + \tan\varphi_r\frac{\delta}{\delta_r}\right)\sigma'_n + \eta^*\dot\delta \quad \text{for } \delta \leq \delta_r \tag{4-10}$$

$$\tau^* = \sigma'_n\tan\varphi_r + \eta^*\dot\delta \quad \text{for } \delta > \delta_r \tag{4-11}$$

where η^* is the viscosity coefficient of the shear strength and δ_r is the displacement at which the material has fully softened; φ_r is the residual effective friction angle. Equations (4-10) and (4-11) can easily be reformulated to account for pressure dependency of the viscous part if deemed necessary:

$$\tau^* = \left(\tan\varphi_g\left(1 - \frac{\delta}{\delta_r}\right) + \tan\varphi_r\frac{\delta}{\delta_r} + \eta^*\dot\delta \right)\sigma'_n \quad \text{for } \delta \leq \delta_r \tag{4-12}$$

$$\tau^* = \sigma'_n\left(\tan\varphi_r + \eta^*\dot\delta \right) \quad \text{for } \delta > \delta_r \tag{4-13}$$

More complex functions could be introduced as well, for example, Einav and Randolph (2006) suggest a Herschel–Bulkley type rate dependency with exponential softening:

$$\tau^* = \sigma'_{test}\left(\tan\varphi_r + \left(\tan\varphi_g - \tan\varphi_r\right)e^{-3\frac{\gamma}{\gamma_r}}\right)\left(\frac{1 + \eta^*_{HB}\left(\frac{\dot\gamma}{\dot\gamma_0}\right)^\beta}{1 + \eta^*_{HB}}\right) \tag{4-14}$$

with $\dot\gamma = \dfrac{\dot\delta}{d}$ and $\gamma = \dfrac{\delta}{d}$

The choice of an appropriate function depends on the laboratory observations but also on the situation to be modelled. Appendix II.3 discusses the effect of using a Herschel–Bulkley type rate dependency with exponential softening.

4.3.3   Model of the sliding body

Similar to the sliding surface model in Figure 4-2a, the generalized constitutive model for the sliding mass behaviour is built out of the basic rheological elements (Figure 4-3). It includes a visco-elastic part, represented by the Burgers model (Burgers, 1935), allowing for immediate elastic deformations, delayed creep and relaxation, in series with a visco-plastic part, allowing for failure or yielding, using a spring and a dashpot in parallel with a yielding element.
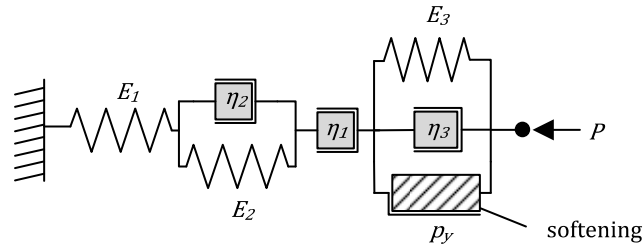
Figure 4-3: Generalized constitutive model of the sliding layer

Here, as previously, the yielding element allows for softening behaviour through linear dependency of the yield stress p_y on plastic strain:

$$p_y = P_p - \Delta p \left(\frac{\varepsilon_3}{\varepsilon_{ref}} \right) \text{ for } \varepsilon_3 \leq \varepsilon_{ref} \tag{4-15}$$

$$p_y = P_p - \Delta p \text{ for } \varepsilon_3 > \varepsilon_{ref} \tag{4-16}$$

where P_p is the passive earth pressure derived after Chu (1991); Δp and ε_{ref} are parameters controlling the drop in strength. The spring and dashpot in the plastic part allow for strain hardening and strain rate dependency. Strains in different parts of the model can be calculated using the following relationships (Figure 4-3):

$$P = E_1 \varepsilon_1 = \eta_1 \dot{\varepsilon}_4 = E_2 \varepsilon_2 + \eta_2 \dot{\varepsilon}_2 = \begin{cases} 0 & P \leq p_y \\ E_3 \varepsilon_3 + \eta_3 \dot{\varepsilon}_3 + p_y & P > p_y \end{cases} \tag{4-17}$$

$$\varepsilon = \varepsilon_1 + \varepsilon_2 + \varepsilon_3 + \varepsilon_4 \tag{4-18}$$

Combining above equations produces the partial differential equation relating earth pressure to the total strain in the element. The generalized model can be simplified by removing elements when the observed landslide behaviour does not exhibit corresponding features.

4.4   Numerical implementation

The boundary value problem formulated above is solved numerically by discretizing the landslide body into elements of height h and equal length dx, chosen to be sufficiently small to avoid significant mesh dependency.

For each time step dt, a displacement increment is assumed along the sliding body, producing shear stresses at the interface, calculated using the interface constitutive model (4-10)–(4-11). Earth pressure distribution along the landslide body can then be calculated by substituting these shear stresses into the equilibrium equation (4-3). Substituting the resulting pressures into the constitutive model of the sliding mass (4-15)–(4-18) produces strains in the landslide body. Numerical integration of the strains gives a new displacement increment. The solution is iterated until the difference between the assumed and the calculated displacement increment becomes sufficiently small. The numerical scheme uses backward finite differences in time. Convergence is achieved using Broyden's method (Broyden, 1965).

In the transient case, the fluctuations of the phreatic surface are numerically derived using the following explicit numerical scheme:

$$\Delta S_{i+1} = \frac{c_p p_i - \dfrac{S_i}{k}}{\dfrac{1}{\Delta t} + \dfrac{1}{2k}} \tag{4-19}$$

From the change in storage, the monthly average phreatic depth can be calculated as:

$$h_{w,i+1}^{average} = \frac{h_{w,i} + h_{w,i+1}}{2} \tag{4-20}$$

with $h_{w,i+1} = h_{w,i} - \frac{\Delta S_{i+1}}{n}$

In the case of transient landslide behaviour (i.e. for changing precipitation), a drop in pore pressures leads to an increase of shear strength along the slip surface. The algorithm in its original form can misinterpret this as an increase in the mobilised shear resistance, potentially leading to the prediction of unrealistic uphill displacements. Therefore, a distinction is required between the shear strength and the mobilised shear resistance, which is achieved by locking the zones of uphill displacements, allowing those zones to undergo relaxation. In order to ensure compatibility of stresses and strains, the boundaries of these zones are defined using an iterative procedure.

4.5   Scope of the model

Figure 4-4 shows examples of the model performance under steady and transient precipitation conditions (the parameters for the model are given in Appendix II.1). For the hypothetical case of a constant precipitation rate (steady state – phreatic surface remains at the same height) the following four stages can be observed in the landslide behaviour (Figure 4-4a): (i) an initial acceleration stage in which continuous softening on the slip surface leads to progressive failure; (ii) a stage of stabilization, after the shear strength has dropped to its residual level at the top end of the slide; (iii) a reacceleration stage, observed if pressure at the toe is large enough to cause passive failure and activation of the plastic part; (iv) depending on the chosen parameters, the visco-plastic model either produces a constant velocity or allows again for a re-stabilization.

In the transient precipitation case (Figure 4-4b), we assume that phreatic surface height fluctuates sinusoidally around the steady state rate during the year, leading to fluctuations in the displacement rate. Although the model undergoes the same stages as for the constant precipitation rate (steady state), displacements in the transient state are accumulated faster, making the stages shorter in time.
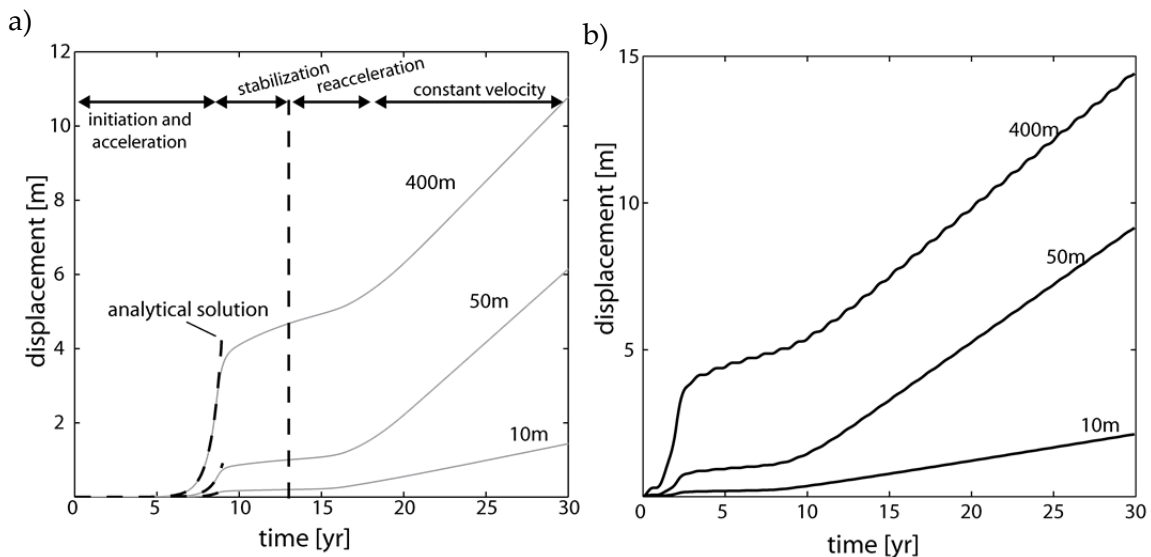
Figure 4-4: Model behaviour in steady and transient states; a) displacement over time in steady state (at different distances to the boundary); b) displacement over time in transient state (at different distances to the boundary)

For partial validation of the numerical procedure, an analytical solution has been developed for a particular case of continuous linear softening and linear rate dependency along the entire sliding surface (Appendix II.2). This condition corresponds to the initial acceleration stage of the landslide evolution, when displacements in the deformable sliding layer are too

small for the residual strength to be reached even in the upper, faster moving part of the landslide. As observed in Figure 4-4a, the analytical solution (shown by dashed lines) compares well with the results of the numerical model in this initial acceleration stage. This is hardly surprising, since at the beginning of the landslide evolution the numerical model of the sliding surface also undergoes linear softening, until at $\delta > \delta_r$ it reaches the residual strength, leading to the stabilization stage, which deviates from the analytical solution in Figure 4-4a.

5 Observation-guided constitutive modelling for creeping landslides – Application: The Brattas landslide in St. Moritz

As described in chapter 3, observations of the Brattas landslide allow three principal displacement regions to be distinguished:

- Region I: Upper 500 m with high strain and displacement rates and strong fluctuations of annual velocity.

- Region II: Overbuilt part of the landslide in the lower 200 m with smaller strain rates and fluctuations.

- Region III: Foot zone of the landslide with high strain rates and a presumable change in mechanical behaviour.

On the one hand, Brattas landslide is a challenging case for OGCM application because of its complex structure, consisting of three different displacement regions interacting with each other. On the other hand, this complexity allows a demonstration of the versatility of the OGCM approach and of an optimized strategy for its application. This strategy aims to reduce the number of parameters obtained through the back-calculation and requires the following five important decisions to be made:

1. Which of the generalized models (hydrological, slip surface, sliding layer) should reflect variation in mechanical behaviour between the three displacement regions?

2. Should the models vary between the three displacement regions only in terms of their parameters or also be allowed to change conceptually?

3. Which of the parameters of the models should be based on the laboratory test data and which can be back-calculated by fitting the observations?

4. In which order should the three regions be treated in order to minimize the effect of their interaction on the back-calculation of the model parameters?

5. What is the appropriate time step to be adopted for the model simulations?

With respect to the first two questions, no significant changes have been observed along the Brattas landslide in either the hydrological conditions or the properties of the palaeo-soil layer containing the sliding surface. Therefore, only the sliding body model will be allowed to vary for the three displacement regions, both in terms of its parameters and in terms of its possible simplifications. With respect to the model parameters, for the slip surface model most of them could be estimated from the laboratory ringshear tests. In contrast, for the hydrological and sliding layer models, laboratory and field test data is less reliable, and parameters must be back-calculated using observations: piezometer readings and landslide displacement measurements. With respect to the order in which the regions are treated, the top-down approach will be adopted for calibration of the models, starting with Region I,

because of its simpler static conditions and limited effect of other regions on its behaviour. Finally, a time step of one month was adopted for the numerical simulations in the Brattas case study, because on the one hand the frequency of displacement observations (between 2 and 8 months) does not allow model predictions to be validated for displacements at shorter time steps, and on the other hand monthly time steps are still sufficiently small to account for seasonality of landslide behaviour. Furthermore, monthly time steps enable the numerical algorithm to converge more easily and allow for a much more efficient modelling procedure.

5.1   Calibration of the hydrological model

Parameters of the hydrological model (4-4)–(4-7) can be back-calculated using available data from piezometer readings or directly from observations of displacement. In the study presented here, a combined approach has been adopted: because reliable automatic readings of pore pressures allowing seasonal variations to be captured have only been available since 2012, the long-term variations in trend as also indicated by hydrological investigations have been calibrated using observed displacement fluctuations.

While the available meteorological readings often provide only total precipitation P_{tot}, the hydrological model requires as an input effective precipitation equal to the total precipitation minus the actual evapotranspiration (AE). Potential evapotranspiration (PE) has been calculated following Thornthwaite's method (Thornthwaite, 1948), using measured mean monthly temperature. This makes it particularly suitable for predictions, because only two exposure parameters (precipitation and temperature) have to be simulated. Actual evapotranspiration is normally taken to be equal to the potential evapotranspiration, except for cases in which effective precipitation becomes negative. In such cases, actual evapotranspiration is assumed to be equal to the total precipitation:

$$AE = PE \ \text{ for } P_{tot} \geq PE \tag{5-1}$$

$$AE = P_{tot} \text{ for } P_{tot} < PE \tag{5-2}$$

Since no St. Moritz specific meteorological data is available for the period of interest (1991 to present), the data from two neighbouring stations, Samedan and Segl Maria (Source: MeteoSwiss), has been used to recreate St. Moritz data. For available St. Moritz mean monthly temperatures between 1959 and 1982, a linear correlation has been established between temperatures in Samedan and St. Moritz, which appeared to be much stronger than the correlation between St. Moritz and Segl Maria. In contrast, for monthly precipitation, the average of the data from Samedan and Segl Maria has been used, which showed a closer correlation with the existing 1959–1982 St. Moritz data than each station separately.

Figure 5-1 shows the observed deviation of the phreatic surface from the initially measured position against the deviation simulated using the hydrological model (4-4)–(4-7) with parameters summarized in Table 5-1. The model reproduces the measured seasonal fluctuations reasonably well up to the year 2014, when it over-predicted the rise of the phreatic surface due to intensive snowmelt and some of the fluctuations due to strong rains during the year. This may be due to either higher than predicted surface runoff for snowmelt after snowy winters or strong rain events, or better drainage conditions at the landslide toe where piezometer readings are taken. In order to test the landslide model sensitivity to such local over-predictions, both the modelled fluctuations and the recorded pore pressure fluctuations were used as an input.

In general, the very simple hydrological model can over-predict the effect of strong rains and snowmelts. However, as can be seen in Figure 5-1, in the long run the model stabilizes, which is the reason that despite its simplicity it can be used to predict the long-term deformations of the landslide reasonably well.

Parameter	Value
h_{w0} [m]	15.841
c_p [-]	0.35
k [month]	8.82
n [-]	0.205

Table 5-1: Parameters of the hydrological model
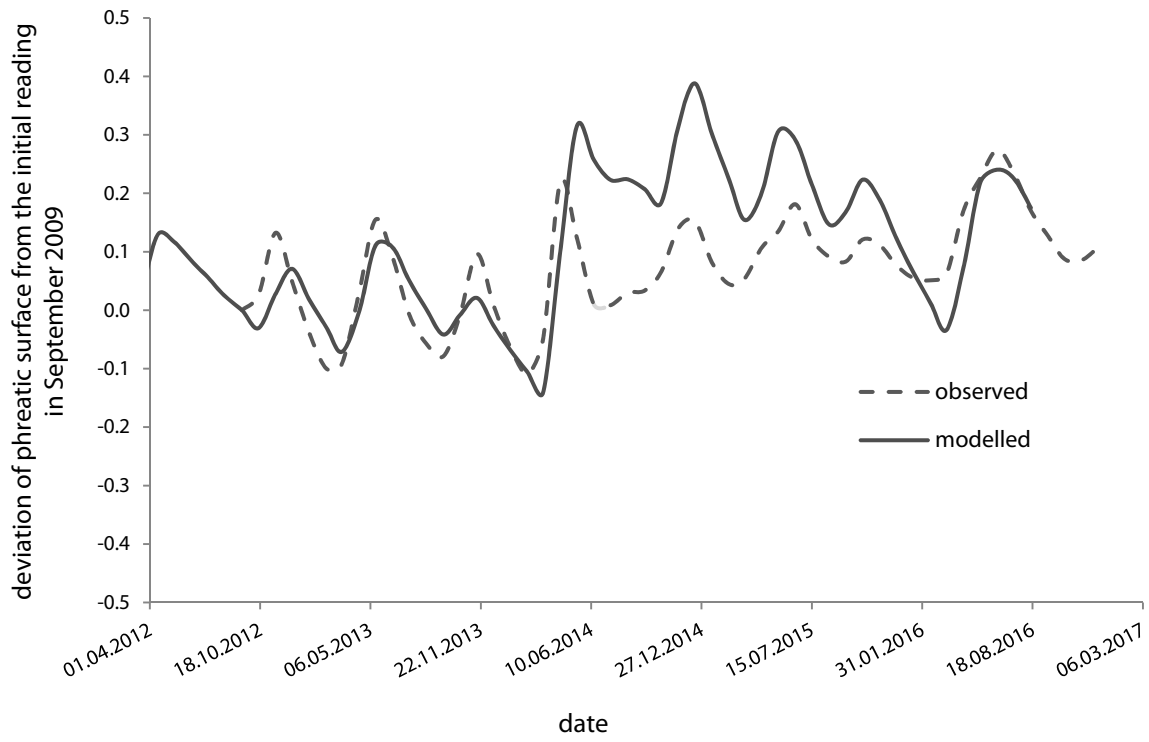
Figure 5-1: Comparison between the observed and predicted phreatic surface fluctuations.

5.2 Calibration of the slip surface model

Figure 5-2 shows the rate dependency of the residual friction ratio ($\tan(\varphi) = \frac{\tau_r}{\sigma\prime}$) observed in ringshear tests by Puzrin and Schmid (2011) on the material from the shear zone. As can be seen, a logarithmic fit with parameters K and c to the data describes the behaviour in this test reasonably well

$$\tan(\varphi) = K \cdot \ln(\dot{\delta}_{test}) + c \tag{5-3}$$

where $\dot{\delta}_{test}$ is the displacement rate in the test.
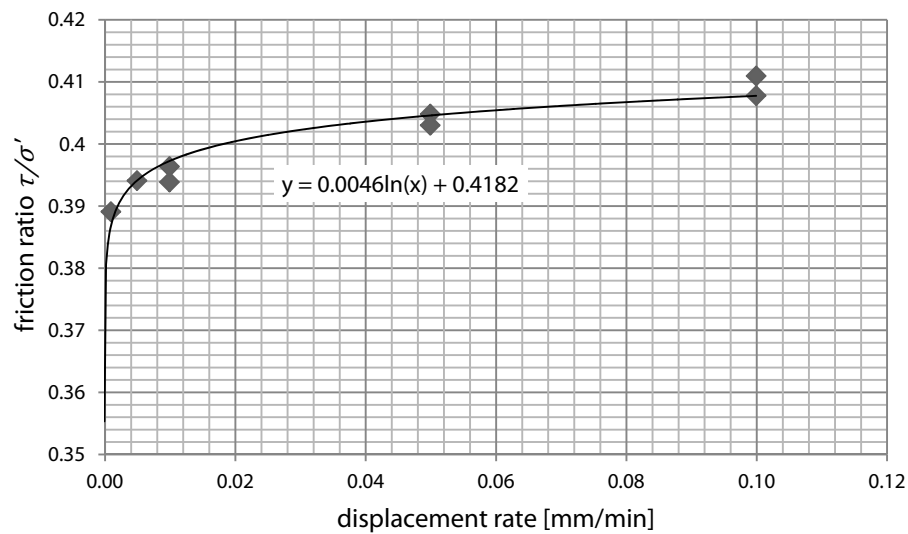
Figure 5-2: Dependency of shear strength on displacement rate according to ringshear test data by Puzrin and Schmid (2011)

Since the thickness of the shear band in the test and the thickness of the shear zone in the field (i.e. the zone where the landslide displacement is primarily concentrated; compare Figure 3.2 in 3.3) may be different, both the functionals describing softening and rate dependency need to be scaled appropriately. Since the thickness of the shear zone is uncertain, in the test and even more in the field, a range of possible thicknesses for both have been used, resulting in range of scaling factors.

The thickness of the shear band in the laboratory from the tests by Puzrin and Schmid (2011) is not recorded; therefore, a small value of 1 mm as suggested in literature (Alonso et al., 2016) as a low estimate for shear band thickness has been used.

For the estimate of the field thickness, information from bore samples has been used that indicates the weak zone to be approximately 20 cm. Since, from visual inspection of bore samples, it is not clear how much of the weak zone is actually sheared, as a lower bound a

thickness of the shear zone in the field equal to the shear band thickness in the laboratory is used (Table 5-2).

Thickness of the shear zone in the laboratory ($d_{sz,lab}$)	Thickness of the shear zone in the field ($d_{sz,field}$)	Scaling factor (S_c)
1mm	1 mm (assumption: same shear zone thickness as in the laboratory)	1
1mm	20 cm (size of the weak layer estimated from bore samples)	200

Table 5-2: Minimum and maximum assumptions for shear zone thickness in the laboratory and in the field and corresponding scaling factors

The velocity of the landslide at the top end is around 0.001 mm/min (≈0.5 m/yr), and considering the thicknesses of the shear zone in the laboratory and the field, results can be scaled via the shear strain rates to the corresponding field velocities. The scaling leads to a horizontal shift of the test results in the semi-log space depending on the scaling factor. In Figure 5-3a, two examples are shown: one for no scaling, i.e. same shear zone thickness in the test and in the field (S_c=1), and the other for a 200 times thicker shear zone in the field (S_c=200).

For the linear approximation (linear rate dependency), the logarithmic best fit to the scaled test data is extrapolated into the velocity range of the landslide and linearized at the average annual velocity of the landslide, which can lead to moderate underestimation of the rate dependency at lower velocities and overestimation of rate effects for higher velocities (Figure 5-3b). It can be shown that the full landslide model can be calibrated for the full range of scale factors within reasonable parameter ranges. The linearization of the logarithmic relation found for the laboratory results at a target velocity from the field is given as:

$$\tan(\varphi) = K \cdot \left(\frac{\dot{\delta}}{\dot{\delta}_f}\right) + K \cdot \ln\left(\frac{\dot{\delta}_f}{S_c}\right) + c - K = n^*\dot{\delta} + \tan(\varphi_r) \tag{5-4}$$

where $\dot{\delta}_f$ is the velocity in the field at which the logarithmic curve is linearized and S_c is the scaling factor defined as the ratio between field and laboratory shearband thickness; K and c are the parameters of the logarithmic curve described in (5-3). As can be seen, using the linearization based on a logarithmic rate dependency function leads to a rate dependency coefficient (η^*) that is independent of the shear zone thickness with only the shear strength at rest, $\tan(\varphi_r)$, depending on that thickness.
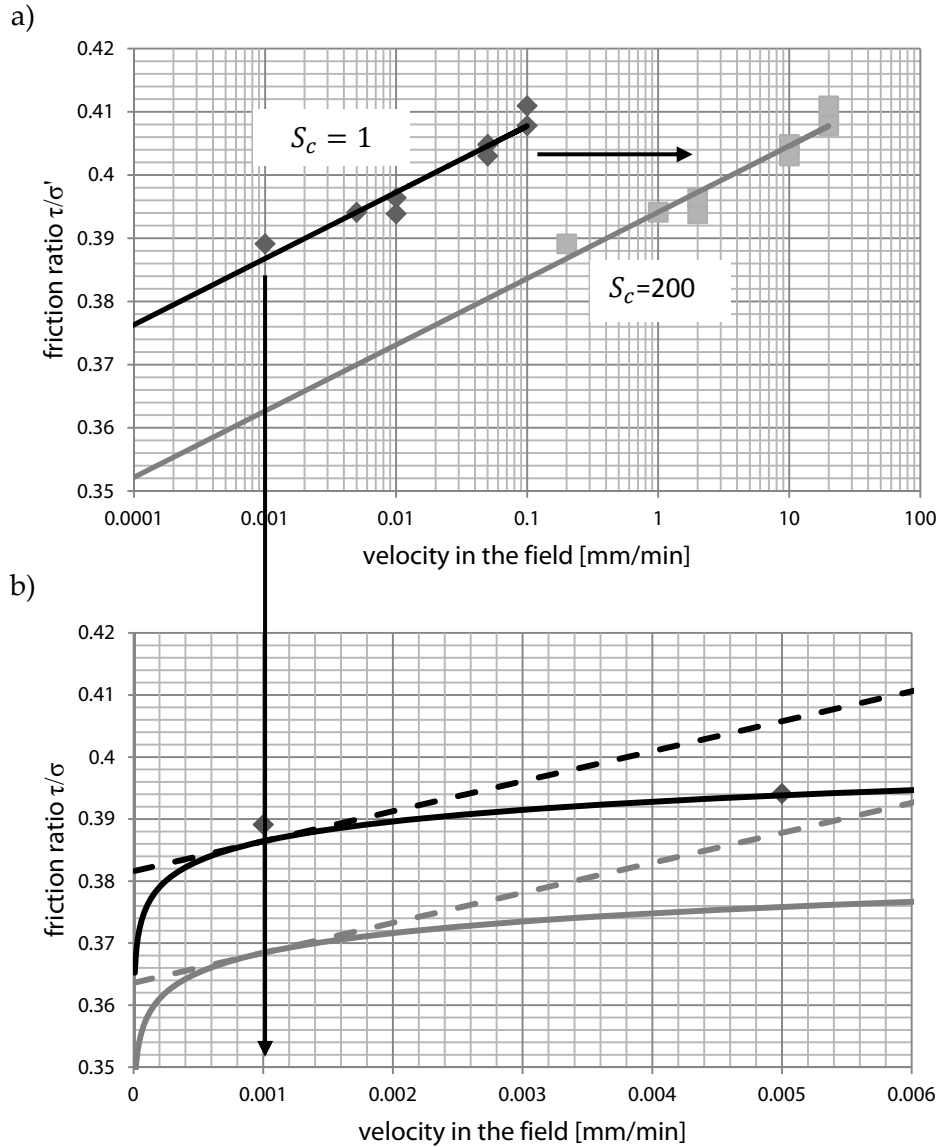
Figure 5-3: a) Ringshear data scaled to corresponding landslide velocities in semi-log representation; b) zoom of the relevant velocity range for the field and linearization of the logarithmic best fits

Since fluctuations of effective stress are small and pressure dependency of the rate-dependent shear strength is unknown, the rate dependency herein is treated as independent from the effective stress fluctuations; using (5-4), the mobilized shear resistance (τ^*) is given in (5-5):

$$\tau^* = K \cdot \left(\frac{\dot{\delta}}{\dot{\delta}_f}\right)\sigma'_{ss} + \sigma'\left(K \cdot ln\left(\frac{\dot{\delta}_f}{S_c}\right) + c\right) = n^*\dot{\delta} + \sigma' \cdot \tan(\varphi_r) \tag{5-5}$$

where σ'_{ss} is the average effective stress as found from simulations of the steady state.

The linear softening behaviour is schematically shown in Figure 5-4. The shear strain at which the material reaches residual strength is difficult to determine from the ringshear tests,

because of the uncertainty in the thickness of the shear band. It therefore must be back-calculated from the observations of the landslide behaviour. It appears that this parameter has the largest effect on the length of the failed compression zone. It is therefore calibrated for the observed length of the failed zone of about 30–40 m.
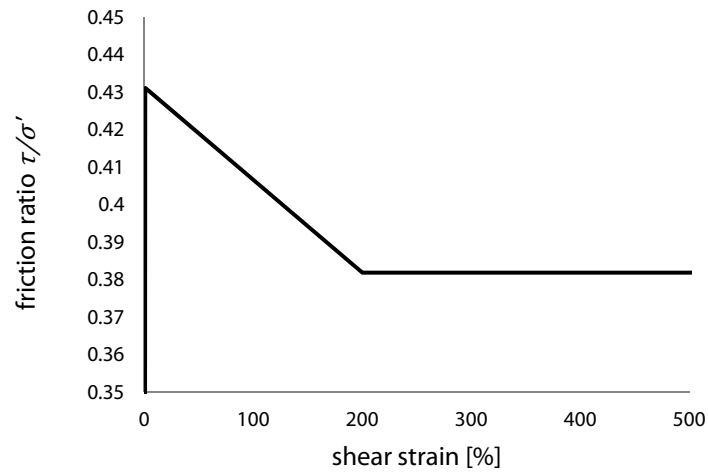
Figure 5-4: Idealized linear softening behaviour of the slip surface using linear softening

Table 5-3 presents the set of parameters for the slip surface model used later for the simulation results of the behaviour of the landslide with shear zone thickness d=5cm. The shear strain for full softening is estimated at 200%, which is within the range assumed by Puzrin and Schmid (2011). Despite the fact that in many cases there is a large discrepancy between the magnitude of rate dependency in laboratory tests and in field observations (see Van Asch et al., 2007), in this study parameters derived from laboratory tests and scaled into the relevant range of velocities in the field seem to represent the field behaviour reasonably well.

Parameter	Value
d [m]	0.05
φ_g [°]	23.2
φ_r [°]	19.98
δ_r [m]	0.1 ($\triangleq$ 200% shear strain)
η^* [kPa s/m]	97.9e6

Table 5-3: Parameters of the constitutive model of the slip surface with linear softening and rate dependency

5.3 Calibration of the sliding layer model

5.3.4 Region I

For the upper Region I (see section 3.3.1 and Figure 3-3 in section 3.3), the landslide has travelled sufficiently far for no further softening to be expected. It also seems reasonable to assume that earth pressures in the sliding layer are not large enough to cause yielding. The observed displacement rates in this region are high and subject to considerable annual changes. These effects can be captured by using a spring and a dashpot in series, i.e., a Maxwell model. The physical meaning of such a model would be that the average high displacement rates are associated with secondary compression, whereas the seasonal fluctuations are due to elastic deformations induced by pore pressure changes. The model can be derived by simplifying the generalized sliding layer model in Figure 4-3 (i.e., $E_2 = E_3 = \infty$). Adopting the remaining Young's Modulus as $E_1 = 6$ MPa and viscosity as $\eta_1 = 350$ MPa $\cdot$ yr allows both the velocity gradient along the slope (Region I, Figure 5-5a) and the yearly fluctuations of displacement rates at particular locations (Figure 5-5b) to be reproduced reasonably well. In these numerical calculations, the average constant velocity of 7cm/yr observed at the lower boundary of Region I was used as a boundary condition.

As can be seen (Figure 5-5b), the uncorrected hydrological model over-predicts the displacement rates in the year 2014–2015, but the error diminishes again in the year 2015–2016. This demonstrates that, despite the simplicity of the hydrological model, displacements are predicted with acceptable accuracy, and the model stabilizes even after deviations in one year. With the corrections to the hydrological input, the model also improves in the observation period 2014–2016.

a)

b)
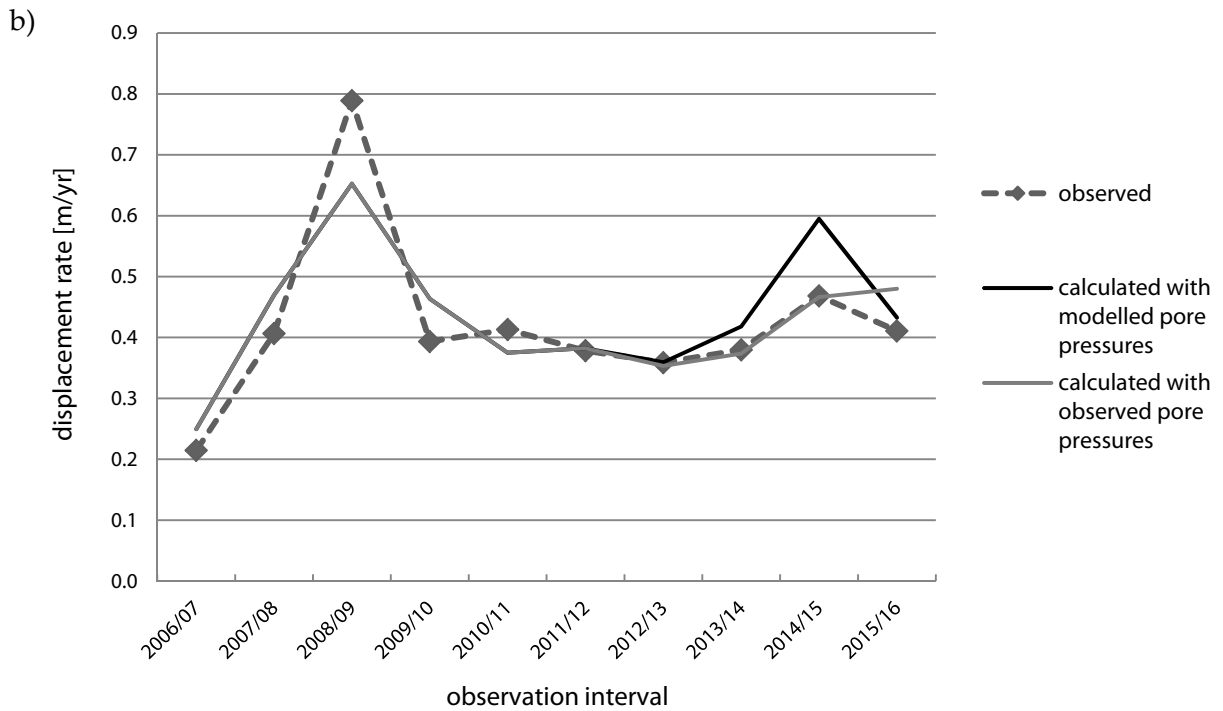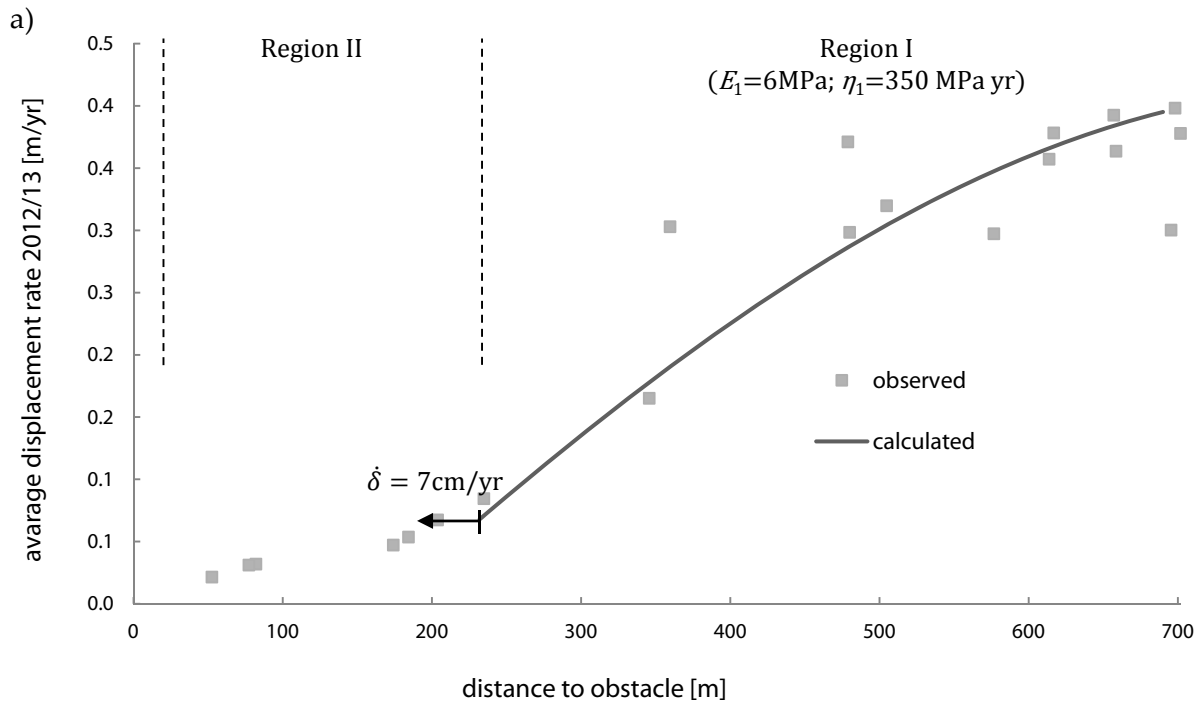
Figure 5-5: a) Model predictions and observations in Regions I and II for the period 2012–2013. b) Model predictions and observations of average displacement rates at the top of the landslide (Region I).

5.3.5 Region II

The same type of reduced constitutive model, but with a different set of parameters, can be used to describe the landslide behaviour in Region II (see section 3.3.1 and Figure 3-3 in section 3.3). Since average displacement rate and fluctuations are significantly lower in this region, the model behaviour can be captured best by having the parameters of the stiffness and viscosity of the Maxwell group increase from the values of the previous section to $E_1 = 40\,\text{MPa}$; $\eta_1 = 5000\,\text{MPa} \cdot \text{yr}$. This increase in stiffness seems plausible, since on the one hand the soil in the lower zones of the landslide has undergone significantly higher compression; on the other hand, the lower 150–250 m of the landslide serves as foundation for numerous structures and infrastructure, implying additional compaction, drainage and underground inclusions.

Using the above sliding layer models for Regions I and II together with the hydrological and slip surface models calibrated in the previous sections, the displacements rates in these two regions were calculated numerically (Figure 5-6). The observed average constant velocity of 2.5 cm/yr at the bottom of Region II was used as a boundary condition.

Figure 5-6 shows the comparison between observations and the model for both regions over the period of 2012–2013. The model allows the principal trend to be captured quite well; deviations are likely to be due to local and three-dimensional (3D) effects. Using the full Burgers model instead of the reduced Maxwell model (i.e., $E_2 < \infty$; $E_3 = \infty$ in Figure 4-3) does not improve accuracy of the simulations of the slope behaviour in these two regions significantly.
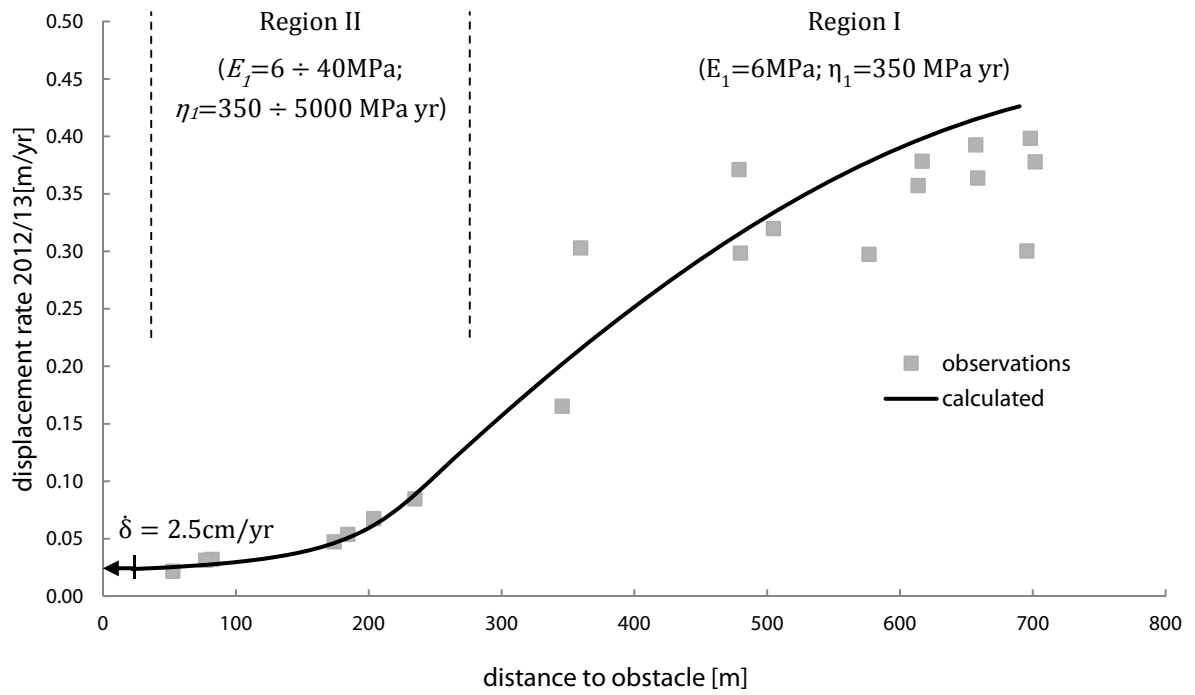
Figure 5-6: Comparison between calculated and observed displacement profiles along Regions I and II

5.3.6 Region III

Once the sliding layer model is calibrated for the top two regions, it can now be calibrated for the lower part of the landslide close to the rock outcrop (Region III in section 3.3.1 and Figure 3-4 in section 3.3). As shown by Puzrin and Schmid (2011), the lowest part of the landslide forms a compression zone, which is the part of the landslide where the shear strength on the sliding surface has not yet reached its residual value. Consequently, the pressure in this section keeps increasing until it reaches the yield pressure, leading to the acceleration of the sliding layer. Schwager et al. (2009) and Schwager and Puzrin (2014) provided further evidence that Region III is indeed yielding by using the novel inclinodeformeter and detecting yearly pressure changes as small as 0.2kPa/yr, incompatible with purely visco-elastic soil behaviour, which has also been confirmed by new measurements (Figure 3-11 in section 3.4.2).

In order to calibrate the sliding layer model for Region III, it is useful to start with the deceleration stage until the onset of yielding in 1991. For simplicity, during this stage the position of the phreatic surface is assumed to be constant (steady state). This stage can be modelled using the Burgers group of the generalized model in Figure 4-3 (i. e., $E_2 < \infty$; $E_3 = \infty$). Parameters E_1 and η_1 are the same as in Region II ($E_1 = 40$ MPa; $\eta_1 = 5000$ MPa $\cdot$ yr). The depth of the phreatic surface in the steady state and the parameters $E_2 = 35$ MPa; $\eta_2 = 385$ MPa $\cdot$ yr of the Burgers model were back-calculated using the observed displacement data from the deceleration stage (Figure 5-7). As noted by Puzrin and Schmid (2011), the behaviour is governed mainly by the ratio E_2/η_2.

In the reacceleration phase (after 1991), the soil starts yielding, activating, in addition to the Burgers group, the yield element in the visco-plastic part in the generalized model in Figure 4-3 (i. e., $E_3 = 0$). Phreatic surface fluctuations (transient state), causing seasonal fluctuations in displacement rates, are modelled by the hydrological model. In order to separate short-term fluctuations from the long-term acceleration trend, the visco-plastic part uses strain softening in combination with strain rate dependency. As a result, the continuous long-term acceleration is caused by a combination of strain softening in the compression zone and earth pressure increase due to softening on the slip surface. The short-term earth pressure fluctuations induced by pore water pressure changes are compensated by the viscosity and cause only small plastic deformations, so that the main portion of fluctuating deformations induced in Region III by precipitation is modelled similarly to Regions I and II as elastic.
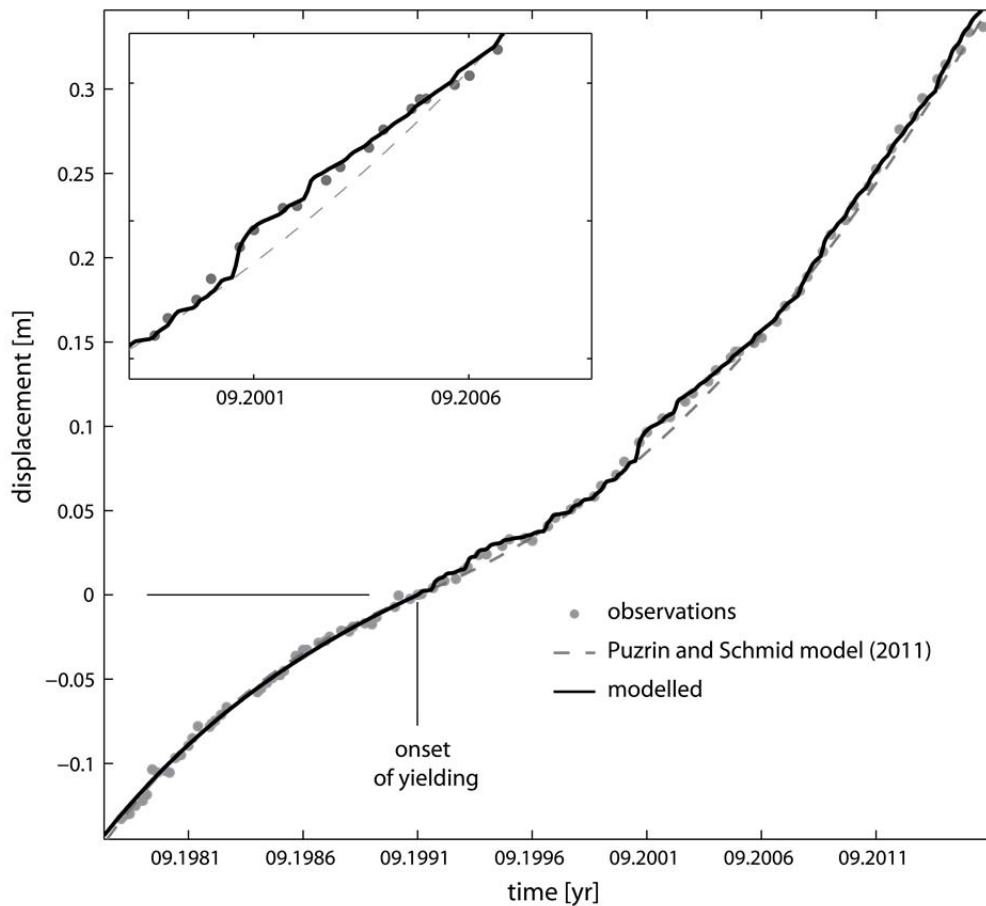
Figure 5-7: Comparison between measured and predicted displacements in Region III.

Figure 5-7 shows the measured (grey dots) vs. calculated transient state displacements (solid line). The model allows good agreement with observations, showing considerable improvement compared to the steady state prediction (dashed line), which was calculated using the Puzrin and Schmid (2011) model updated for more recent observations. By using the transient model, the mean absolute error between 1991 and 2016 drops from 3.6 mm to 2.2 (both with observed piezometer data and with modelled pore pressure). Even more pronounced is the improvement of the accuracy between 2001 and 2006, where the mean absolute error decreases from 6.7 mm to 2.1 mm. Figure 5-8 shows plots of residual errors of the steady state and transient models for the acceleration stage in Region III. The pattern formed by the residuals of the steady state model (Figure 5-8a) and its bias towards positive values indicates that the model cannot adequately capture the phenomena. With the transient model (Figure 5-8b and c) it is possible to reduce both this shift and the standard deviation. Only during the last years (2015–2016) is there a deviation observed between measurements and model. The reason for this is unclear, but there is a possibility that

reconstruction works in late 2014 on the walls surrounding the area around the leaning tower (where the measurements are taken) have altered the movement.
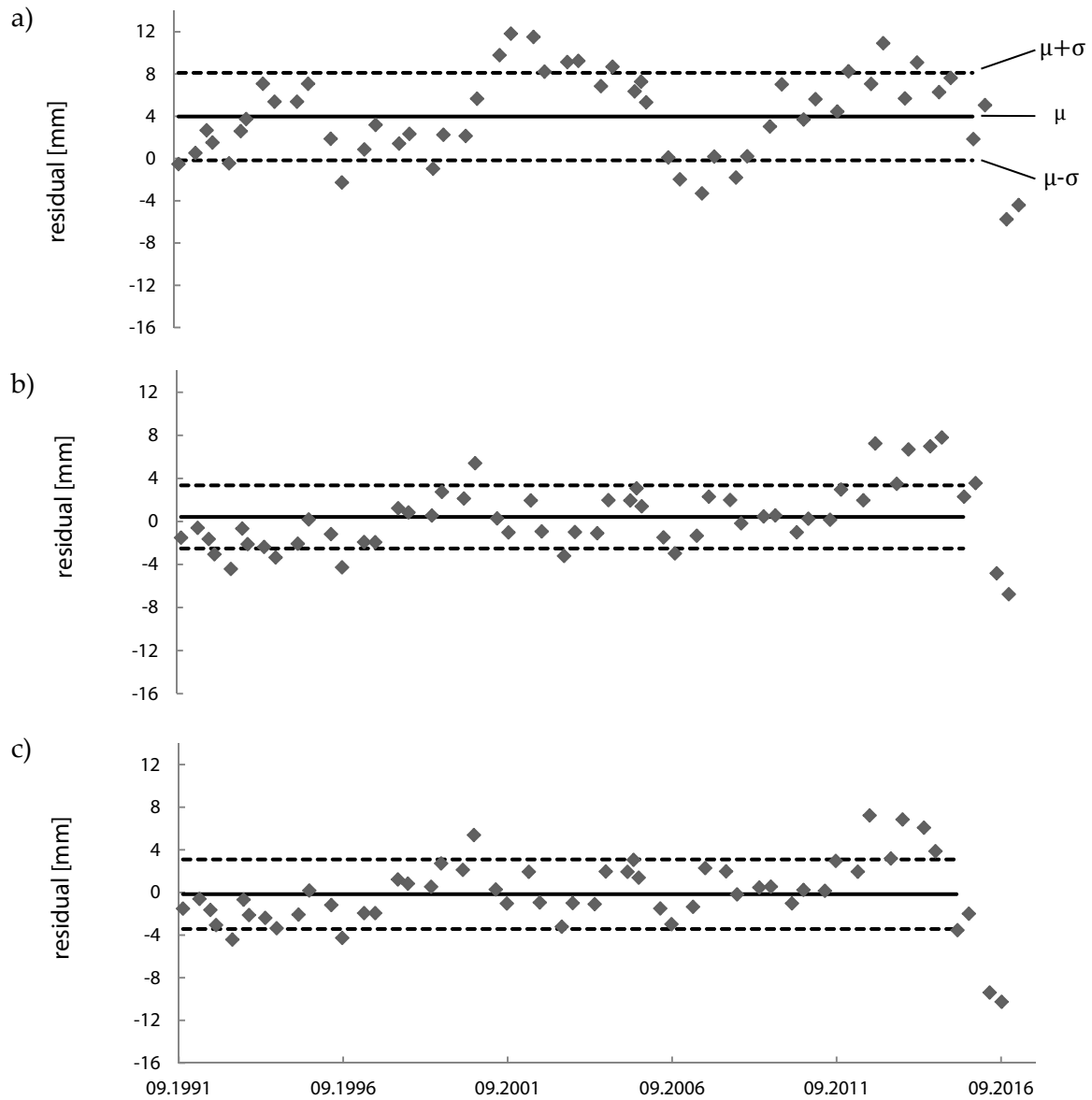
Figure 5-8: Plot of residual errors for the Region III between 1991 and 2016 for: a) steady state model (Puzrin and Schmid, 2011), b) transient state model with measured pore pressures, c) transient state model with modelled pore pressures.

5.4 Combined model

The nine parameters of the combined sliding layer model (Figure 4-3), including all the three regions, are summarized in Table 5-4. These parameters fall in the vicinity of the measured ranges (from Dilatometer tests section 3.4.2). In the combined model, the additional parameters describing the yielding behaviour derived in Region III are also activated for Regions I and II (shaded area in Table 5-4). While this activation only marginally affects the model performance in these regions (with the Maxwell model still dominating the behaviour), it enables the failure to propagate further upslope in the case of a pressure increase, which the Maxwell model alone would not be able to simulate.

Parameter	Region 1	Region 2	Region 3 deceleration	Region 3 reacceleration
E_1 [MPa]	6	$6 \div 40$	40	40
η_1 [MPa yr]	350	$350 \div 5000$	5000	5000
E_2 [MPa]	-	-	35	35
η_2 [MPa yr]	-	-	385	385
η_3 [MPa yr]	155.05	155.05	155.05	155.05
Δp [kPa]	145	145	145	145
ε_{ref} [%]	0.5	0.5	0.5	0.5

Table 5-4: Parameters of the constitutive model of the sliding layer

Figure 5-9 shows a comparison between the model predictions and measurements of displacement rate along the landslide. The model can also capture most of the fluctuations of displacement rate along the length of the landslide (see Figure 5-10). In Region II, not all fluctuations are yet captured, probably owing to the complexity of interactions in this overbuilt part of the landslide. However, further comparison to periodical long-term measurements in Region II (Figure 5-11) show good agreement with the measurements within the central overbuilt zone of the landslide. During only the measurement period 1988–1998 (Figure 5-11a), the model slightly over-predicts the rates at the upper end of the overbuilt part. However, since the influence of precipitation can only be considered from 1991 onwards and accuracy of the measurements in this period is unclear, emphasis in the calibration of the model has been given to the more recent measurements.
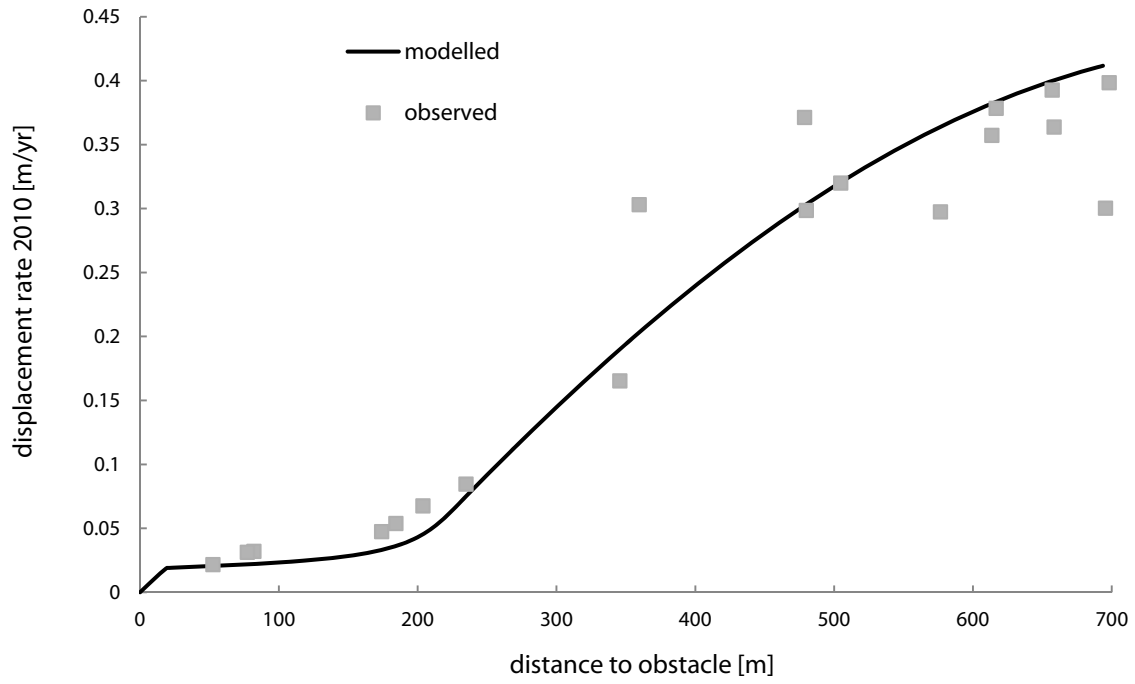
Figure 5-9: Comparison between modelled and observed displacement rate along the landslide
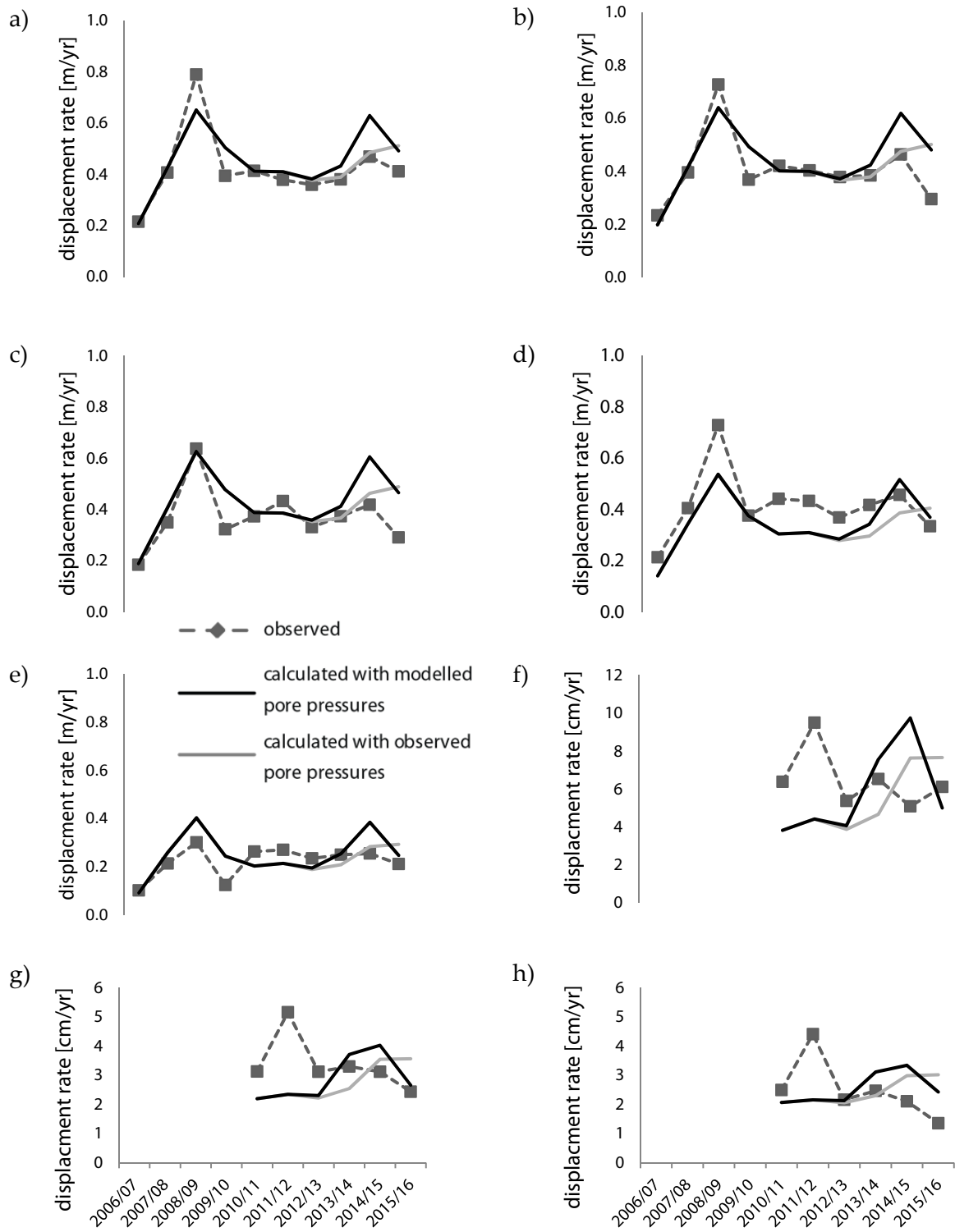
Figure 5-10: Average displacement rate fluctuations in the upper part of the landslide at approximately: a) 690m, b) 660m, c) 624m, d) 480m, e) 358m, f) 190m, g) 78m and h) 52m distance from the bottom of the landslide.
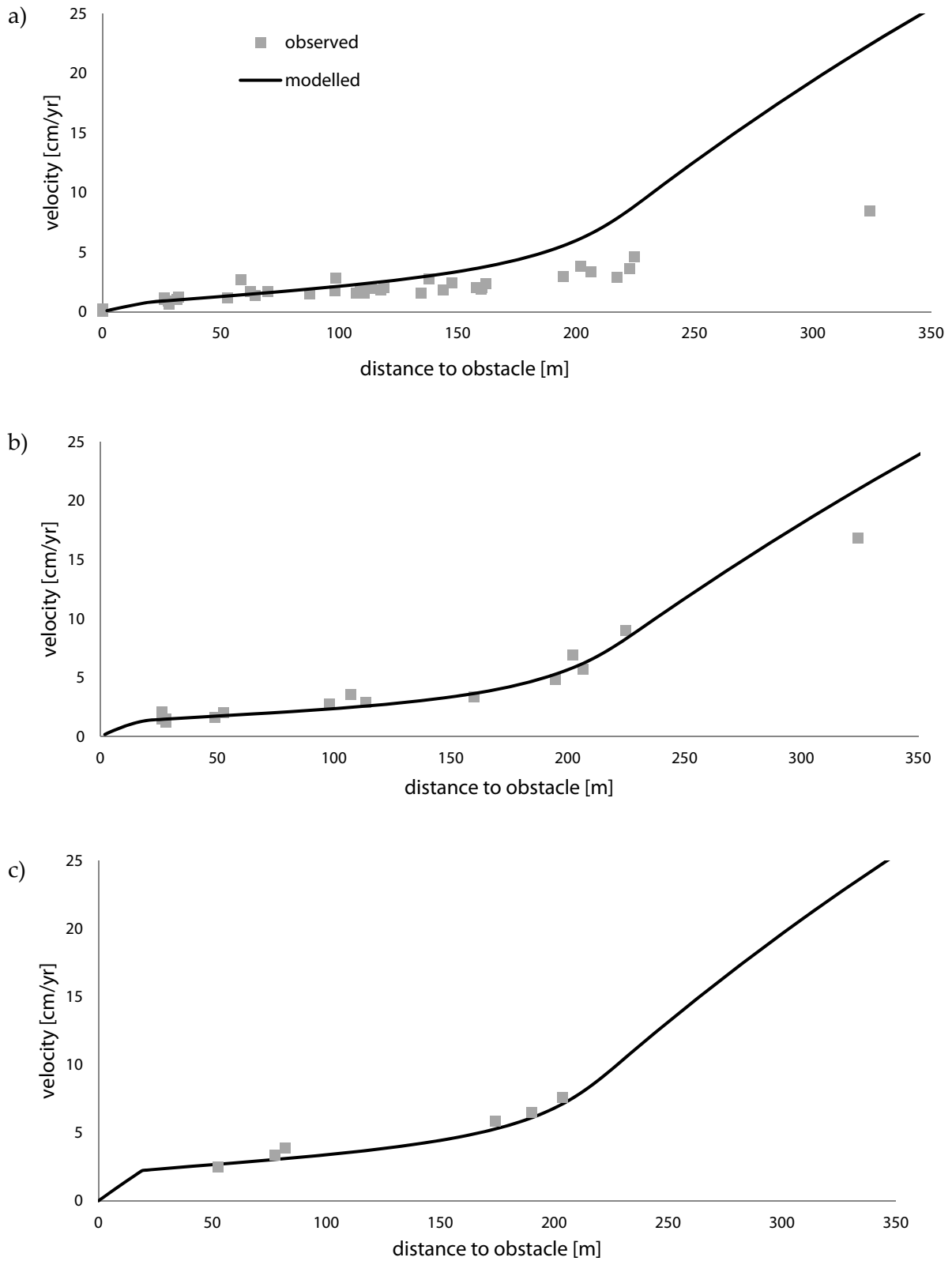
Figure 5-11: Comparison between predicted and observed average displacement rates in the overbuilt area of the landslide (Region II) for the periods a) 1988–1998, b) 1998–2006 and c) 2010–2016

The sliding layer model was combined with the slip surface model (four parameters in Table 5-3) and the hydrological model (four parameters in Table 5-1), and introduced into the boundary value problem (4-3) to simulate Brattas landslide evolution.

Summarizing, these 17 model parameters, which are partially derived from the laboratory tests or back-calculated to fit the observations, allowed for:
- reasonably accurate simulation of the history of the phreatic surface fluctuations as a function of temperature and precipitation (Figure 5-1);
- reasonably accurate simulation of the velocity field along all three different regions of the landslide (Figure 5-9);
- accurate simulation of the history of displacements in the compression zone (Region III), both in terms of the long-term trend and short-term fluctuations (Figure 5-7);
- reasonably accurate simulation of average displacement rate fluctuations at characteristic locations in the upper Regions I and II (Figure 5-10);
- reasonably accurate simulation of long-term behaviour in Region II (Figure 5-11)

Generally, the entire process of calibration might require one or two iterations between the different regions, until a set of parameters is found that allows good agreement with observations in all the regions. However, the stepwise procedure proposed above is considerably more efficient than attempting to calibrate all the parameters at once.

5.5   Discussion

Using the approach of observation-guided constitutive modelling allowed a simple phenomenological model of the Brattas landslide to be derived. The model tries to integrate information about all parts of the landslide and the stages of landslide evolution which are known rather than focusing on only parts of the landslide or finite periods of the landslide's history. This approach allowed some interdependencies to be found between the different landslide regions such as the importance of accounting for rate dependency in all regions even if it is believed to be small. Also, the importance of stress history and long-term pore pressure fluctuations was only discovered by taking into account information on all regions.

The approach allows capturing the phenomenological behaviour with a focus on points for which there is a lot of information available and that are deemed of large importance (e.g. the vicinity of the leaning tower).

As the model is derived from a generalized form, it allows a stage-wise approach in deriving the models necessary for several parts of the landslide, rationalizing the model derivation. The model can be further developed if new phenomena are encountered. Implemented as a method of slices, the calculation tool can also relatively easily be further developed, e.g. to introduce additional regions.

The model works for the entire range of assumed potential shear band thicknesses, making the approach relatively robust. Furthermore, simulations of the past four years of landslide behaviour using a time step of one day and daily averages of pore pressure (from piezometer measurements) instead of monthly averages did not cause significantly different results. This shows that the model for the Brattas also allows the calculation time step to be changed without creating major errors. Therefore the calculation tool is rather efficient as it allows long-term simulations to be run in relatively large time steps that can be reduced at a specific point in time to have a higher temporal resolution. For the Brattas, the complexity of the hydrology unfortunately did not yet allow a hydrological model to be derived that uses daily weather data as input. This task is additionally hindered by the lack of more frequent displacement monitoring along the slope (or at least along parts of the slope) or of more pore pressure monitoring in other parts of the slope to verify the model.

5.6   Conclusion

The complexity and variety of time-dependent phenomena in creeping landslides require a methodology which can be both general and adaptable, relying as much as possible on the monitored data. The proposed concept of observation-guided constitutive modelling (OGCM) seems to satisfy these requirements, presenting a powerful tool not only for back-calculating model parameters but also for deriving constitutive relations from the observations made from monitoring a creeping slope. The landslide body is discretized into linear elements with boundary conditions defined at the top and the bottom of the landslide as well as at its interface with the underlying soil. The loading is defined by gravity and precipitation. The resulting 1D boundary value problem is simple enough to allow the behaviour of each linear element to be derived and to treat it as a compression test with displacements and their rates obtained from the monitoring data. This behaviour can then be described using an appropriately modified form of the proposed generalized constitutive model, combining potential mechanisms that can act in the sliding layer with corresponding constitutive relations describing the behaviour on the slip surface and a hydrological model accounting for the influence of precipitation. This makes it possible to derive constitutive relations directly from observational data and at the same time have models that remain flexible enough to incorporate future phenomena that might not have yet been observed.

The proposed constitutive models can evolve both in time, e.g. by changing from visco-elastic to visco-plastic behaviour, and in space, e.g., where different governing mechanisms can be identified for different parts of the landslide as a result of man-made and natural influences. Such models not only facilitate understanding of the past landslide behaviour, but also allow predictions of the future landslide evolution under both regular conditions and rare events such as extreme precipitation.

Application of the proposed observation-guided constitutive modelling approach was demonstrated using the Brattas landslide as an example, where it was possible to derive potential mechanisms for each of the three different displacement regions based on the high-quality displacement and precipitation data.

Appendix II.1: Parameters used for the example in 4.5

Geometry	Value
Length [m]	400
Height [m]	20
Inclination [°]	20
h_{w0} [m]	13.0
d [m]	0.25
Interface (linear rate dependency and softening)	**Value**
φ_g [°]	23.7
φ_r [°]	19
δ_r [m]	2.5 (=1000%)
η^* [kPa s/m]	60e6
Landslide-body	**Value**
φ_p [°]	30.7
η_1 [MPa yr]	20000
η_2 [MPa yr]	420
E_1 [MPa]	30
E_2 [MPa]	70
η_3 [MPa yr] (post failure)	21
Δp [kPa]	120
$\varepsilon_{p,ref}$ [%]	0.5
Fluctuations (sinusoidal change of the phreatic surface)	**Value**
Δh_w [m]	0.4
Initial conditions	**Value**
Δ [m]	0.00001
$\dot{\Delta}$ [m/yr]	0.00001
$\ddot{\Delta}$ [m/yr^2]	0.00001

Appendix II.2: Analytical solution for the initiation and acceleration stage

For the case of a constant precipitation rate, an analytical solution can be derived for the landslide initiation and acceleration stages, using the Burgers model to describe the behaviour of the sliding body, and linear softening and linear rate dependency to describe behaviour on the slip surface. From the equilibrium equation, earth pressure in the landslide body is given by:

$$h\frac{dp}{dx} = \tau^* - \tau_g \tag{AII.2-1}$$

where for linear softening and rate dependency the shear resistance τ^* is given by:

$$\tau^* = \tau_g - (\tau_g - \tau_r)\frac{\delta}{\delta_r} + \eta^*\dot{\delta} \tag{AII.2-2}$$

where δ_r is the displacement at which the shear strength reaches its residual value. It follows that

$$p' = \frac{1}{h}\left((\tau_r - \tau_g)\frac{\delta}{\delta_r} + \eta^*\dot{\delta}\right) \tag{AII.2-3}$$

where $p' = \frac{dp}{dx}$

The earth pressure is related to the strain in the sliding body via the differential equation of the Burgers model:

$$p + K_1\dot{p} + K_2\ddot{p} = K_3\dot{\varepsilon} + K_4\ddot{\varepsilon} \tag{AII.2-4}$$

$$K_1 = \left(\frac{\eta_1}{E_1} + \frac{\eta_1}{E_2} + \frac{\eta_2}{E_2}\right); K_2 = \frac{\eta_1\eta_2}{E_1 E_2}; K_3 = \eta_1; K_4 = \frac{\eta_1\eta_2}{E_2} \tag{AII.2-5}$$

Differentiating equation (AII.2-4) with respect to x and substituting $\varepsilon = \delta'$ gives

$$p' + K_1\dot{p}' + K_2\ddot{p}' = K_3\dot{\delta}'' + K_4\ddot{\delta}'' \tag{AII.2-6}$$

which after substitution of equation (AII.2-3) into it results in a homogeneous separable differential equation with respect to $\delta(x, t)$.

The boundary conditions are the zero displacement at the toe of the landslide and zero pressure and, consequently, strain at the top:

$$\delta(0, t) = 0; \ \delta'(L, t) = 0 \tag{AII.2-7}$$

where L is the length of the landslide.

The solution for the above boundary value problem is given by:

$$\delta(x,t) = \sum_{k=1}^{n} \sin\left(\frac{2k-1}{2}\pi\frac{x}{L}\right)\left(C_1 e^{H_1 t} + C_2 e^{H_2 t} + C_3 e^{H_3 t}\right) \tag{AII.2-8}$$

where H_1, H_2 and H_3 are the roots of the following cubic equation:

$$
\begin{aligned}
0 = &\left(\frac{1}{h}(\tau_r - \tau_g)\frac{1}{\delta_{cr}}\right) + \left(\frac{\eta^*}{h} + K_1\left(\frac{1}{h}(\tau_r - \tau_g)\frac{1}{\delta_r}\right) + K_3\lambda\right)x \\
&+ \left(K_1\frac{\eta^*}{h} + K_2\left(\frac{1}{h}(\tau_r - \tau_g)\frac{1}{\delta_{cr}}\right) + K_4\lambda\right)x^2 + K_2\frac{\eta^*}{h}x^3
\end{aligned}
\tag{AII.2-9}
$$

with

$$\lambda = \frac{(2k-1)^2}{4}\frac{\pi^2}{L^2} \tag{AII.2-10}$$

The coefficients C1, C2 and C3 can be found from the initial conditions. If one assumes linear distributions for initial displacement, velocity and acceleration,

$$\delta(x,o) = \Delta\frac{x}{L}; \; \dot\delta(x,o) = \dot\Delta\frac{x}{L}; \; \ddot\delta(x,o) = \ddot\Delta\frac{x}{L} \tag{AII.2-11}$$

$\Delta, \dot\Delta$ and $\ddot\Delta$ being the displacement, velocity and acceleration at the top end of the landslide, then the coefficients can be determined from the corresponding sine series for initial displacement:

$$
\begin{aligned}
&\sum_{k=1}^{n} \sin\left(\frac{2k-1}{2}\pi\frac{x}{L}\right)(C_1 + C_2 + C_3) = \Delta\frac{x}{L} \; \rightarrow \\
&(C_1 + C_2 + C_3) = \mu_1 = 2\Delta\frac{4}{(2k-1)^2\pi^2}\sin\left(\frac{2k-1}{2}\pi\right)
\end{aligned}
\tag{AII.2-12}
$$

initial velocity

$$(C_1 H_1 + C_2 H_2 + C_3 H_3) = \mu_2 = 2\dot\Delta\frac{4}{(2k-1)^2\pi^2}\sin\left(\frac{2k-1}{2}\pi\right) \tag{AII.2-13}$$

and initial acceleration

$$(C_1 H_1^2 + C_2 H_2^2 + C_3 H_3^2) = \mu_3 = 2\ddot\Delta\frac{4}{(2k-1)^2\pi^2}\sin\left(\frac{2k-1}{2}\pi\right) \tag{AII.2-14}$$

respectively. The coefficients C_1, C_2 and C_3 are then given by

$$C_1 = -\frac{-H_2 H_3 \mu_1 + H_2 \mu_2 + H_3 \mu_2 - \mu_3}{(H_1 - H_2)(H_1 - H_3)} \tag{AII.2-15}$$

$$C_2 = -\frac{-H_1 H_3 \mu_1 + H_1 \mu_2 + H_3 \mu_2 - \mu_3}{(H_2 - H_1)(H_2 - H_3)} \tag{AII.2-16}$$

$$C_3 = -\frac{H_1 H_2 \mu_1 - H_1 \mu_2 - H_2 \mu_2 + \mu_3}{(H_2 - H_3)(H_3 - H_1)} \tag{AII.2-17}$$

Appendix II.3: Influence of a different rate dependency formulation

The dependency of shear strength on the strain rate and the drop of shear strength due to deformations of the shear zone are very difficult to determine experimentally for the low velocity range of creeping landslides. Whether a rate dependency and softening formulation is sufficient for the situation under investigation can only be assessed by comparing its performance in term of reproducing observations to the performance of more sophisticated formulations.

Rate dependency is often assumed to be of logarithmic nature. In a constrained landslide, using a purely logarithmic formulation is numerically problematic since the velocity drops to zero at the boundary, leading theoretically to an infinite drop of shear strength. In order to avoid this problem, the logarithmic function needs to be cut off at a certain strain rate; or a function similar to the logarithm but with finite shear strength at zero strain rate has to be used.

For the Brattas case, a Herschel–Bulkley (HB) formulation for the rate dependency in combination with an exponential softening formulation has been used to investigate whether the use of an interface formulation with more degrees of freedom improves the capability of the model to capture the observed behaviour.

Similar to the linear rate dependency function, the HB-rate dependency has been estimated using the results of the ringshear tests. The shear band thickness in the test is again assumed to be 1 mm, then the HB-formulation can be fitted to the test data and extrapolated into the very low strain rate range of the landslide (depending on the assumption of the shear zone thickness in the field).

For the laboratory test, the rate dependency is given according to (4-14) as:

$$\tau^* = \sigma'_{test}(\tan\varphi_r)\left(\frac{1 + \eta^*_{HB}\left(\frac{\dot{\gamma}_{test}}{\dot{\gamma}_0}\right)^\beta}{1 + \eta^*_{HB}}\right) \text{ with } \dot{\gamma}_{test} = \frac{\dot{\delta}_{test}}{d_{test}} \tag{AII.3-1}$$

which becomes, for the boundary value problem:

$$\tau^* = \sigma'_n(\tan\varphi_r)\left(\frac{1 + \eta^*_{HB}\left(\frac{\dot{\gamma}_{landslide}}{\dot{\gamma}_0}\right)^\beta}{1 + \eta^*_{HB}}\right) \text{ with } \dot{\gamma}_{landslide} = \frac{\dot{\delta}_{landslide}}{d_{landslide}} \tag{AII.3-2}$$

The exponential softening has been defined such that the material has softened 95% when reaching the residual strain limit γ_r:

$$\tau^* = \sigma_n'\left(\tan\varphi_r + \left(\tan\varphi_g - \tan\varphi_r\right)e^{-3\frac{\gamma_{landslide}}{\gamma_r}}\right) \text{ with } \gamma_{landslide} = \frac{\delta_{landslide}}{d} \qquad \text{(AII.3-3)}$$

The combined interface formulation is given as:

$$\tau^* = \sigma_n'\left(\tan\varphi_r + \left(\tan\varphi_g - \tan\varphi_r\right)e^{-3\frac{\gamma_{landslide}}{\gamma_r}}\right)\left(\frac{1 + \eta_{HB}^*\left(\frac{\dot{\gamma}_{landslide}}{\dot{\gamma}_0}\right)^{\beta}}{1 + \eta_{HB}^*}\right) \qquad \text{(AII.3-4)}$$

In contrast to the linear rate dependency function, the formulation used in (AII.3-4) may, depending on its parameters, change significantly in the range of strain rates lower than the tests without significantly affecting the fit to the test results at higher strain rates. Therefore the parameters of the rate dependency function cannot fully be derived from the experimental results, which makes the calibration of the landslide model via observations of the landslide's behaviour more complicated. A set of example parameters for the Exp.-HB type interface formulation is given in Table AII.3-1:

Parameter description	Symbol	Value
Friction angle at equilibrium	$\varphi_g\,[°]$	24.64
Residual friction angle	$\varphi_r\,[°]$	22.01
Shear strain at 95% softening	$\gamma_r\,[m]$	1000%
Herschel–Bulkley parameter	$\eta_{HB}\,[-]$	0.0857
Herschel–Bulkley parameter	$\dot{\gamma}_0\,[-/min]$	0.0489
Herschel–Bulkley parameter	$\beta\,[-]$	0.1480
Thickness of shear zone	$d\,[cm]$	2

Table AII.3-1: Parameters for slip surface formulation with exponential softening and Herschel–Bulkley type rate dependency

Using the more complicated interface formulation does not significantly influence the model's ability to reproduce the landslide observations. In Region III, no better agreement with the observations (Figure AII.3-1a) has been achieved. The major difference can be observed in the upper part (Region I), where the new interface formulation allows for larger fluctuation of the annual average displacement rate (Figure AII.3-1). These larger fluctuations can be explained since, in contrast to a linear rate dependency formulation, the logarithmic nature of the HB rate dependency causes a smaller increase in mobilized shear strength for the same increase in velocity than does the linear formulation. Thus, if calibrated to achieve a good agreement with the observations in Region III, the linear model does slightly overestimate the rate dependency in the upper regions, leading to a damping of the rate fluctuations which can be avoided with formulation (AII.3-4).
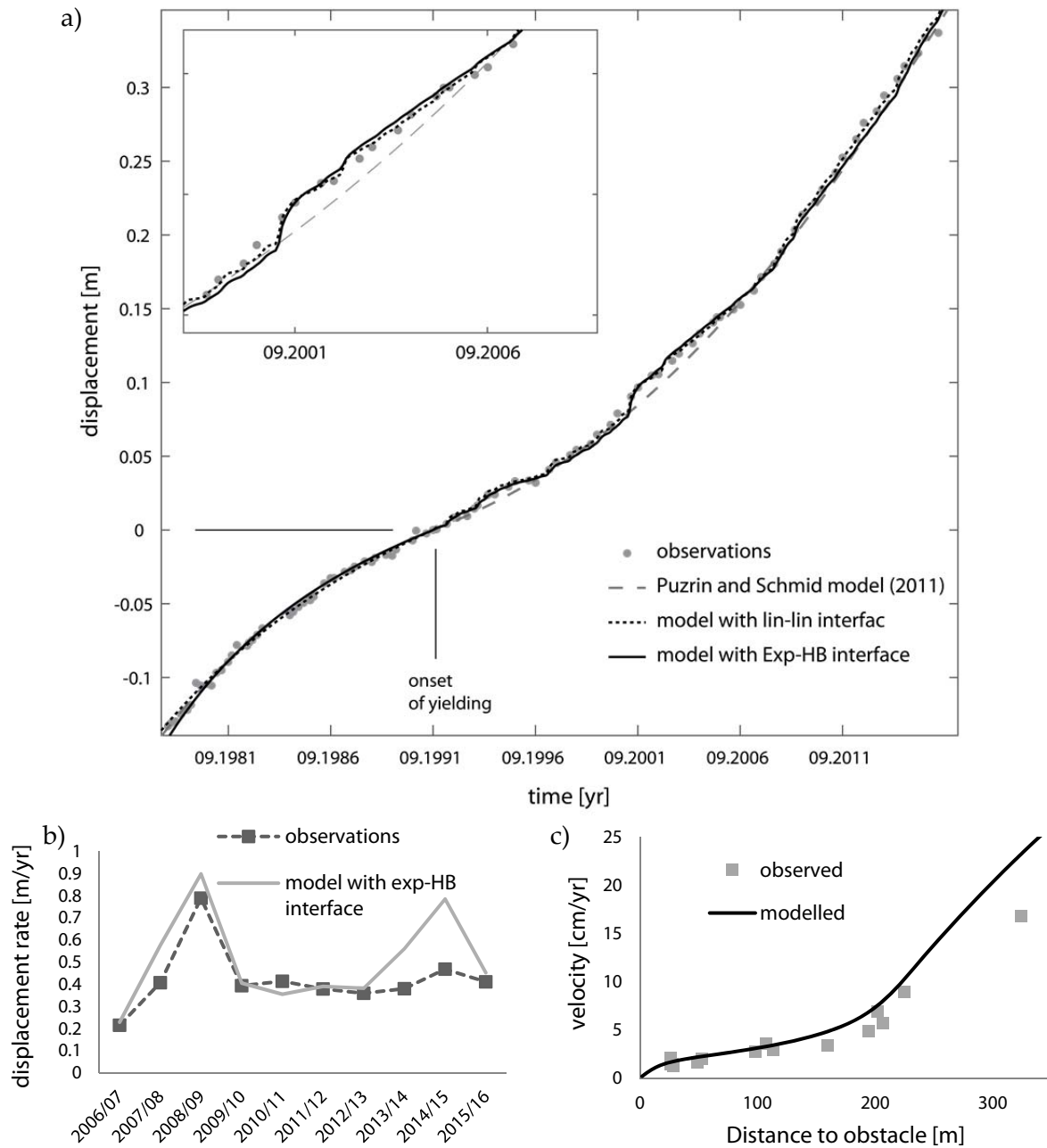
Figure AII.3-1: a) Comparison between measured and predicted displacements in Region III; b) comparison between measured and predicted fluctuations of the displacement rate at the top end (Region I); c) comparison between measured and observed average displacement rates in Region II (1998–2006)

In general, the model does not improve significantly or even degrades slightly (Region II, Figure AII.3-1c), which does not justify using the more complex interface formulation for the long-term simulations of the landslide.

However, in situations where the interface experiences shearing rates significantly larger than during the calibrated state, e.g. during an earthquake, a linear formulation cannot be used. In these cases, the HB formulation that follows the test results at higher strain rates is much more suitable.

REFERENCES

Alonso, E.E., Zervos, A., Pinyol, N.M., 2016. Thermo-poro-mechanical analysis of landslides: from creeping behaviour to catastrophic failure. Géotechnique 66, 202–219. https://doi.org/10.1680/jgeot.15.LM.006

Broyden, C.G., 1965. A Class of Methods for Solving Nonlinear Simultaneous Equations. Math. Comput. 19, 557–593.

Buma, J., 2000. Finding the most suitable slope stability model for the assessment of the impact of climate change on a landslide in southeast France. Earth Surf. Process. Landforms 25, 565–582.

Burgers, J.M., 1935. Mechanical considerations, model systems, phenomenological theories of relaxation and of viscosity, in: First Report on Viscosity and Plasticity. Nordemann Publishing Company, New York.

Chu, S., 1991. Rankine's analysis of active and passive pressures in dry sands. Soils Found. 31, 115–120.

Einav, I., Randolph, M., 2006. Effect of strain rate on mobilised strength and thickness of curved shear bands. Geotechnique 56, 501–504.

Houlsby, G.T., Puzrin, A.M., 2000. A thermomechanical framework for constitutive models for rate-independent dissipative materials. Int. J. Plast. 16, 1017–1047. https://doi.org/10.1016/S0749-6419(99)00073-X

Oberender, P.W., Puzrin, A.M., 2016. Observation-guided constitutive modelling for creeping landslides. Geotechnique 66, 232–247. https://doi.org/doi:10.1680/jgeot.15.LM.003

Puzrin, A., Schmid, A., 2012. Evolution of stabilised creeping landslides. Geotechnique 62, 491–501.

Puzrin, A.M., Schmid, A., 2011. Progressive failure of a constrained creeping landslide. Proc. R. Soc. A - Math. Phys. Eng. Sci. 467, 2444–2461. https://doi.org/DOI 10.1098/rspa.2011.0063

Schwager, M. V, Schmid, A.M., Puzrin, A.M., 2009. Inclinodeformometer: A novel device for measuring earth pressure in creeping landslides, in: International Symposium on Prediction and Simulation Methods for Geohazard Mitigation. Kyoto, Japan, pp. 479–484.

Schwager, M. V, Puzrin, A., 2014. Inclinodeformeter pressure measurements in creeping landslides: analytical solutions and field applications. Geotechnique 64, 447–462.

Skempton, A.W., 1985. Residual strength of clays in landslides, folded strata and the laboratory. Géotechnique 35, 3–18. https://doi.org/10.1680/geot.1985.35.1.3

Thornthwaite, C.W., 1948. An Approach toward a Rational Classification of Climate. Geogr. Rev. 38, 55–94. https://doi.org/Doi 10.2307/210739

Van Asch, T.W.J., Hendriks, M.R., Hessel, R., Rappange, F.E., 1996. Hydrological triggering conditions of landslides in varved clays in the French Alps. Eng. Geol. 42, 239–251. https://doi.org/Doi 10.1016/0013-7952(95)00082-8

Van Asch, T.W.J., Van Beek, L.P.H., Bogaard, T.A., 2007. Problems in predicting the mobility of slow-moving landslides. Eng. Geol. 91, 46–55. https://doi.org/DOI 10.1016/j.enggeo.2006.12.012

NOTATION – PART II

α average slope inclination

β parameter of the Herschel-Bulkeley rate dependency formulation

c_p portion of infiltrated precipitation

γ_s total unit weight

γ shear strain

$\dot{\gamma}$ shear strain rate

$\dot{\gamma}_0$ parameter of the Herschel-Bulkeley rate dependency formulation

γ_w unit weight of water

γ_r reference strain for exponential softening on the slip surface

$\delta(\mathrm{x}, \mathrm{t})$ landslide displacement

$\dot{\delta}(\mathrm{x}, \mathrm{t})$ landslide velocity

δ_r displacement at which the material has softened

E_n elastic parameters of the sliding bodies constitutive model

e_0 average initial void ratio after swelling

ε strain in the sliding body

ε_{ref} parameter to control drop in strength in the sliding body

h depth of sliding surface

h_w average depth of phreatic surface

k Discharge coefficient

L length of the landslide

n porosity

η_n viscous parameters of the sliding bodies constitutive model

η^* viscosity coefficient of the shear strength

η^*_{HB} parameter of the Herschel-Bulkeley rate dependency formulation

P pressure parallel to the slip surface

P_p passive earth pressure

P_a active earth pressure

p_y yield stress

p amount of monthly precipitation

Δp parameter to control drop in strength in the sliding body

Q Monthly discharge

φ_g Angle of friction at equilibrium with gravitational shear stress

φ_p Peak angle of friction in the sliding body

φ_r the residual effective friction angle

$S, \Delta S$ Storage and storage increment

σ'_n effective normal stress on the sliding surface

σ'_{test} effective normal stress in ringshear test

σ'_{ss} effective normal stress on the sliding surface in steady state

τ^* shear strength

τ_g gravitational shear stress

Part III: Analysis of seismic impact on creeping slopes

Abstract

Despite the fact that numerous creeping landslides that potentially threaten human lives or structures are situated in seismically active areas, no tools have been established that allow an assessment of creeping landslides during seismic loading. The complexity of phenomena that are potentially interacting during seismic loading of a creeping landslide makes the development of a suitable model difficult. This study aims to propose a simple model as an extension to Newmark's sliding block method (Newmark, 1965) for the assessment of such landslides during earthquakes. During this study, the focus has been on the following phenomena:

(v)   rate dependency of shear strength along the boundary between stable and unstable soil (see also chapters 4 and 5);

(vi)   build-up of excess pore pressures during earthquake loading in the zone of the pre-existing slip surface.

The following chapters demonstrate both the development of suitable constitutive models for the materials involved to reproduce the two phenomena and the integration of those constitutive models into a conceptual model of the boundary value problem.

Chapter 6 outlines the conceptual model of the boundary value problem, a landslide with predefined slip surface, which will be used to simulate seismic loading on the landslide. Chapters 7 and 8 focus on the derivation of suitable constitutive models to describe the behaviour along the slip surface and the adjacent material. Chapter 10 then demonstrates the application of the complete model for the case of the Brattas landslide in St. Moritz.

The methodology allows the estimation of co-seismic displacements, i.e. displacements that are caused by the loads induced during the earthquake. Additionally, the effect of excess pore pressure development on co-seismic but also on post-seismic displacements, i.e. displacements of the landslide due to an increased rate of creep because of excess pore pressures after the earthquake, will be analysed.

6 Conceptual model for the analysis of creeping slopes during earthquakes

6.1 Introduction

The formulation of a suitable model to describe the boundary value problem of a permanent landslide during earthquake loading is not an easy task, and few approaches have been proposed so far.

The methodology proposed herein aims to formulate a conceptual model to capture all phenomena that have been deemed relevant and to remain simple enough to understand and study their interaction and influence. For this study, particularly the rate dependency of shear strength along an existing slip surface and the development of excess pore pressures around it will be investigated.

Other conceptual approaches such as Newmark's sliding block method (Newmark, 1965) or equivalent force methods are only applicable if the landslide is in static equilibrium. However, the definition of a static safety factor for a creeping landslide is not possible. This chapter shows an extension of a Newmark sliding block model that is based on what, in this work, is called a kinematic rather than a static equilibrium of forces. This kinematic equilibrium of forces for the landslide is only satisfied through rate-dependent mobilization of shear forces along the slip surface (boundary between stable and unstable ground). Additionally, the model will be formulated to be able to account for the development of excess pore pressures.

6.2 Conceptual model formulation

In order to derive a suitable formulation for the boundary value problem, the idea has been to structure the model into parts, where each part has a clearly defined function in the entire analysis structure.

Figure 6-1 shows the graphical representation of the problem formulation.

As in Newmark's proposed formulation (Newmark, 1965), the landslide is treated simply as a block, with the input motion being applied as acceleration time history in the stable ground (see Figure 6-1a). In the case of constrained landslides, the conditions at the boundaries might have to be taken into account (e.g. elastic behaviour or failure). In contrast to the original formulation, the block is moving not on a rigid - perfect plastic interface but on a zone of weaker material (see Figure 6-1b) that contains the actual slip surface.

From the model derived in chapters 4 and 5, it is clear that the shear strength of the intensely sheared zone separating stable from unstable ground (slip surface) depends on the rate of shearing (rate dependency).

As mentioned in chapter 2, development of excess pore pressure in this zone is usually neglected since the material has reached a residual state (Pradel et al., 2005). However, it must be taken into account that the actual slip surface may have developed in a thicker, "weak" layer of fine-grained material. For example, in the Brattas landslide, borings revealed that the actual slip surface is situated in 20–30 cm of fine material which in geological reports has sometimes been referred to as palaeo soils (Schlüchter, 1988). This material may not have been sheared to residual state yet and can therefore still cause the development of excess pore pressures. To account for the development of excess pore pressures in the layer surrounding the slip surface (the so called weak layer in Figure 6-1b), it will be modelled as deformable and contracting or dilating. In theory, it would be possible to divide the entire landslide body into layers that allow for pore pressure development. However, since the body above the fine-grained zone is significantly more heterogeneous with alternating drained and undrained layers, it is unclear whether significant pore pressures can develop. For this first analysis, a simpler formulation with a clearly defined weak zone has been chosen. The rest of the body can be treated as rigid, as in classical Newmark analysis, which also seems reasonable given the relatively stiff nature of the sliding body in fast loading.

Interaction between rate dependency in the slip surface and development of excess pore pressures in the weak zone below or above can be studied by allowing the pore pressures to

propagate from the weak layer into the slip surface, effectively reducing the shear resistance. At the same time, the rate-dependent slip surface controls earthquake-induced shear stress in the weak layer. That means that, as the shear resistance drops, the landslide mass above the slip surface becomes better isolated from the seismic ground excitation.

a) schematic landslide model
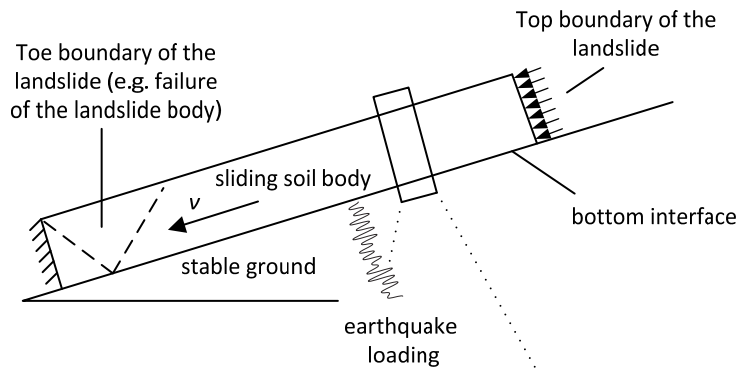
b) schematic landslide profile
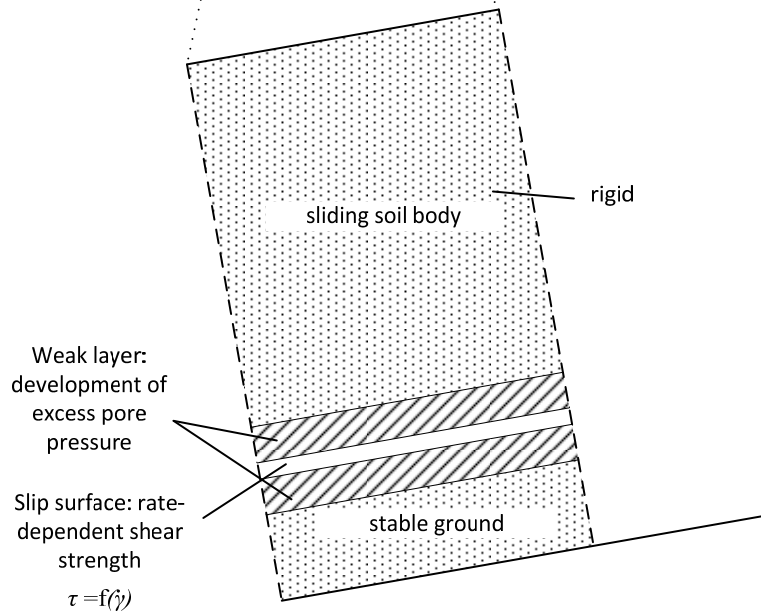
Figure 6-1: Conceptual model of the landslide during seismic loading: a) schematic landslide model; b) schematic landslide profile

7 Modelling rate-dependent shear strength along the slip surface during seismic loading

The properties of the slip surface are taken from the model of the steady and transient state (see chapter 4 and 5). The interface is assumed to be rate-dependent with the rate dependency defined from the ring-shear test shown in chapter 3. Softening of the shear strength can be introduced but is not necessary for landslides that have displaced significantly (e.g. the Brattas above the compression zone at the foot of the landslide), and further softening will be neglected in the analysis.

A significant difference from the simulation of creep, however, is the different range of strain rates that must be modelled for fast loading during earthquakes. The variation of shear strain rate during an earthquake will be obviously much larger than during the creep stage. Therefore, a linear approximation of the rate dependency, which has been sufficient for the small rate variations during creep (see chapter 5), will probably significantly overestimate the mobilized increase in shear strength at high rates. Consequently, a function such as the Herschel–Bulkley (HB) function demonstrated in Appendix II.3 that can better capture the observed shape of rate dependency at higher strain rates should be used. This subject is further discussed in chapter 9.

For the Brattas landslide, the parameters of the HB-rate dependency formulation derived in Appendix II.3 can be used:

Parameter	Symbol	Value
Herschel–Bulkley parameter	η_{HB} [-]	0.0857
Herschel–Bulkley parameter	$\dot{\gamma}_0$ [-/min]	0.0489
Herschel–Bulkley parameter	β_{HB} [-]	0.1480
Thickness of slip surface	d_{ss}[cm]	2

Table 7-1: Properties of the slip surface used in earthquake simulations

Figure 7-1 shows the comparison between the Herschel–Bulkley rate dependency formulation used here and the laboratory tests.
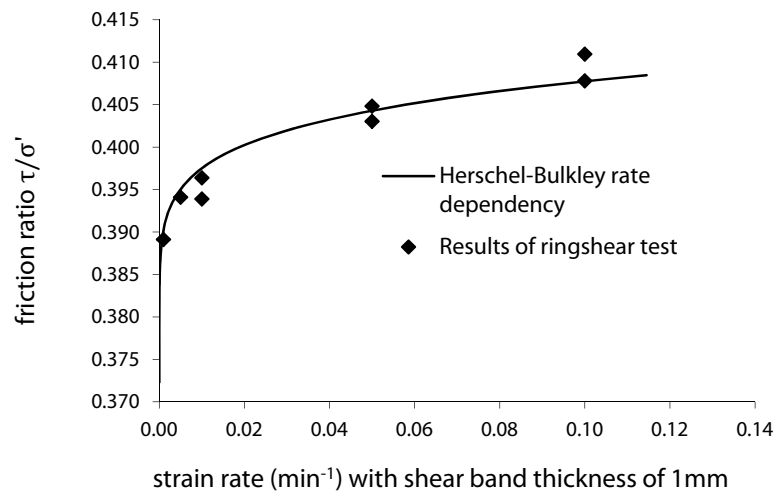
Figure 7-1: Observed rate-dependent shear strength from Puzrin and Schmid (2011) and Herschel–Bulkley model fit

Generally, the measurement of rate dependency over the entire velocity range from creep to velocities during seismic influence is very difficult. At small rates, errors of the test device (e.g. ringshear) may be problematic. At high rates and rate changes, the development of excess pore pressures influences the results and needs to be measured.

8 Modelling excess pore pressure development in the weak layer

8.1 Introduction

As described in chapter 6, the slip surface has formed in a layer of weak material inside the landslide. Depending on the composition of this fine material, cyclic deformation during earthquake loading may lead to a compaction of material which, owing to undrained behaviour during fast loading, causes excess pore pressures to develop. If these excess pore pressures are generated sufficiently close to the slip surface (where no development of excess pore pressures is expected) they can propagate into the actual slip surface, leading to reduction of mobilized shear resistance.

In the case of the Brattas landslide, monotonic and cyclic triaxial tests on fine material from the matrix of the landslide as well as from material of the layers next to the slip surface exhibit the potential for development of excess pore pressure (see chapter 3).

To assess the influence of excess pore pressures developing around the slip surface, it is necessary to use material models that allow this phenomenon to be reproduced. The use of existing models from literature within this work has been shown to be difficult, as either these models are difficult to calibrate and to apply in boundary value problems, or there have been doubts over the range of applicability of these models or their thermomechanical consistency.

Consequently, it has been decided to formulate a material model that specifically describes the development of excess pore pressures for silty soils that can be found in the Brattas landslide but also at other sites. In order to develop a suitable model, data from direct simple shear tests (DSS) from literature (Donahue, 2007; Donahue et al., 2008) has been used to qualitatively and quantitatively calibrate a suitable model. This approach has been chosen since DSS tests are believed to better reproduce the conditions in the field but are not yet available for the material from the Brattas. Using data from similar material allows an approximate model to be found and allows the laboratory tests to be defined that are required to calibrate the mode beforehand, to make best use of the limited sample material from the landslide.

Owing to the nature of the problem (development of excess pore pressures in fast loading for normally consolidated soil), the focus for the calibration of the model has been set on the undrained behaviour rather than on drained slow loading. Phenomena for which almost no

data is available, such as the rate dependency of the material in the weak zone, have been neglected for now.

The procedure for finding this model follows similar principles to those used for the process of "observation-guided constitutive modelling" (see chapter 4). The principles stated in chapter 4 can be reformulated for the derivation of the seismic soil response model as follows.

The model should once again:

- be able to simulate the critical phenomena observed in cyclic tests for conditions resembling the field conditions;
- be sufficiently simple to enable understanding of various interactions and to ease use in stochastic simulations;
- enable simplifications but also extensions if more complex phenomena need to be captured;
- be able to ensure thermomechanical consistency, avoiding unrealistic generation or dissipation of energy during landslide evolution.

Additionally, since the nature of the phenomena makes a certain level of complexity unavoidable, attempts have been made to attribute specific phenomena to certain parameters. This aims to ease the derivation of parameters and allows decisions upon the importance of different model parameters depending on the loading situation.

To achieve these goals, the constitutive models are derived following the framework of hyperplasticity. Focus has been given to a hierarchical structure of the model. Therefore, first, a very fundamental formulation with only one kinematic hardening yield surface of the model will be shown, and its capabilities and limitations will be assessed. Subsequently, a more complex formulation will be derived and assessed in order to demonstrate the improvements over the simple formulation.

This approach aims to demonstrate the steps of the model derivation process first for a simple example and to ease the understanding of the influence of the model's components. It also allows assessment of the trade-off between qualitative and quantitative improvement of the modelled behaviour and the added complexity.

8.2 Formulation of a "one-surface" kinematic hardening hyperplastic model

8.2.1 Potential functions

Following the framework of hyperplasticity (Houlsby and Puzrin, 2000, 2002; Puzrin, 2001; Puzrin and Houlsby, 2001), the material behaviour is derived by differentiation of two scalar potential functions.

From the four commonly used energy functions, the Gibbs free energy (g) is chosen here:

$$g = -\frac{\kappa}{1+e_0} \cdot \sigma' \cdot \left(\ln\left(\frac{\sigma'}{\sigma'_0}\right) - 1 \right) - \frac{\tau^2}{2G} - \sigma' \cdot \alpha_\varepsilon - \tau \cdot \alpha_\gamma + \frac{h\alpha_\gamma^2}{2} - \sigma' \cdot \alpha_E - \tau \cdot \alpha_\Gamma \quad (8\text{-}1)$$

where κ denotes the logarithmic bulk modulus, G is the shear modulus, h denotes the hardening modulus and α_ε, α_γ are internal variables which correspond to volumetric plastic strain and plastic shear strain when the material is yielding. α_E, α_Γ are used as additional internal variables and correspond to volumetric plastic strain and plastic shear strain at failure. Note that the plastic strains are divided into a yielding plastic strain, denoted with small subscripts (α_ε), and a failure plastic strain, denoted with capital subscript (α_E). The incorporation of the hardening modulus h in the Gibbs free energy function corresponds to purely kinematic hardening (Puzrin and Houlsby, 2001).

The second potential function used defines the irreversible behaviour of the material. Consistent with the framework of hyperplasticity, it is defined here as the dissipation function:

$$d = \left((\mu + \beta) \cdot \sigma' + c \right) \cdot \left| \dot{\alpha}_\gamma \right| + (M + B) \cdot \sigma' \cdot |\dot{\alpha}_\Gamma| \geq 0 \quad (8\text{-}2)$$

where μ is the frictional yield parameter, c is the cohesional yield parameter and M is the frictional failure strength.

The dilation parameters β and B are added here such that they vanish in the formulation of the yield surface and failure surface, respectively. These surfaces will be derived from the potential surfaces subsequently. In addition to the two potential functions, the evolution of plastic volumetric strains is controlled via a kinematic constraint on plastic strain increments during yielding:

$$c_1 = \dot{\alpha}_\varepsilon - \beta \left| \dot{\alpha}_\gamma \right| = 0 \quad (8\text{-}3)$$

This constraint can be interpreted as a non-associated flow rule (Houlsby, 1992), connecting plastic volumetric strain increments to plastic shear strain increments with the compaction (dilation) coefficient $\beta = \frac{\dot{\alpha}_\varepsilon}{|\dot{\alpha}_\gamma|}$. To model the generation of pore water pressure in undrained loading, β is chosen with a positive value (note that in the following explanations we maintain the soil mechanical convention of compression positive). Therefore, the soil phase contracts while yielding, and owing to the constant volume constraint during undrained loading ($\dot{\varepsilon} = 0$), this is counterbalanced by an increase of pressure in the pore water. The model is complemented by the introduction of a second constraint on the plastic strain rates at failure that can have a negative value to capture dilative behaviour:

$$c_2 = \dot{\alpha}_V - B|\dot{\alpha}_S| = 0 \qquad (8\text{-}4)$$

8.2.2 Strains

Following the hyperplastic formalism, the strains are derived from the Gibbs free energy function (8-1) by differentiation with respect to the corresponding stresses.

$$\varepsilon = -\frac{dg}{d\sigma'} = \frac{\kappa}{1 + e_0} \cdot \ln \frac{\sigma'}{\sigma'_0} + \alpha_\varepsilon + \alpha_E$$
$$\gamma = -\frac{dg}{d\tau} = \frac{\tau}{G} + \alpha_\gamma + \alpha_\Gamma \qquad (8\text{-}5)$$

By interpreting the internal variables α_i as plastic strains, this formulation shows the decomposition of total strain into elastic and plastic strains.

8.2.3 Yield surface

By differentiating the Gibbs free energy with respect to plastic strains, the "generalized stress" is derived. This is done here for the yielding part only. For failure, the derivation is done analogously.

$$\bar{\chi}_\varepsilon = -\frac{\partial g}{\partial \alpha_\varepsilon} = \sigma'$$
$$\bar{\chi}_\gamma = -\frac{\partial g}{\partial \alpha_\gamma} = \tau - h\alpha_\gamma \qquad (8\text{-}6)$$

Similarly, the dissipative generalized stress is derived by differentiating the dissipation function (8-2) with respect to the plastic strain increment. Since an additional constraint on plastic strain rates was introduced, see equation (8-3), the hyperplastic formalism requires the dissipative generalized stress to be derived from a modified dissipation function

$d' = d + \Lambda c_1$. This modified function is equal to the initially defined dissipation function (8-2) because $c_1 = 0$. Λ denotes a Lagrange multiplier which a priori is not defined.

$$\chi_\varepsilon = \frac{\partial d}{\partial \dot{\alpha}_\varepsilon} + \Lambda \frac{\partial c_1}{\partial \dot{\alpha}_\varepsilon} = \Lambda$$

$$\chi_\gamma = \frac{\partial d}{\partial \dot{\alpha}_\gamma} + \Lambda \frac{\partial c_1}{\partial \dot{\alpha}_\gamma} = \text{sign}(\dot{\alpha}_\gamma) \cdot \left((\mu + \beta) \cdot \sigma' + c\right) - \Lambda \cdot \text{sign}(\dot{\alpha}_\gamma) \cdot \beta$$

(8-7)

with sign(..) as the signum function.

Using Ziegler's Orthogonality Condition $\left(\bar{\chi}_{ij} - \chi_{ij}\right) = 0$ (Ziegler, 1983), the multiplier Λ and the yield surface are defined as

$$\Lambda = \sigma'$$

(8-8)

$$y = \tau - \text{sign}(\dot{\alpha}_\gamma) \cdot (\mu \cdot \sigma' + c) - h\alpha_\gamma = 0$$

(8-9)

The yield surface is therefore interpreted as a linear function in the stress space which is inclined by μ and initially intersects the τ-axis at c. With non-zero plastic shear strain $\dot{\alpha}_\gamma$ the intersection of the yield surface with the τ-axis is shifted kinematically.

8.2.4 Failure surface

Similar to the yield surface, the failure surface is derived via generalized stresses.

$$\bar{\chi}_E = -\frac{\partial g}{\partial \alpha_E} = \sigma'$$

$$\bar{\chi}_\Gamma = -\frac{\partial g}{\partial \alpha_\Gamma} = \tau$$

(8-10)

Using the second constraint (equation (8-4)) on plastic strain rates, the dissipative generalized stress is derived directly by differentiation of the modified dissipation function $d' = d + \Lambda c_2$ with respect to plastic strain increments. Note that the Lagrange multiplier Λ is not the same as the one used for the derivation of the yield surface.

$$\chi_E = \frac{\partial d}{\partial \dot{\alpha}_E} + \Lambda \frac{\partial c_2}{\partial \dot{\alpha}_E} = \Lambda$$

$$\chi_\Gamma = \frac{\partial d}{\partial \dot{\alpha}_\Gamma} + \Lambda \frac{\partial c_2}{\partial \dot{\alpha}_\Gamma} = \text{sign}(\dot{\alpha}_\Gamma) \cdot (M + B) \cdot \sigma' - \Lambda \cdot \text{sign}(\dot{\alpha}_\Gamma) \cdot B$$

(8-11)

Again using Ziegler's "Orthogonality Condition" $\left(\bar{\chi}_{ij} - \chi_{ij}\right) = 0$, the multiplier Λ is eliminated and the failure surface is defined as

$$f = \tau - \text{sign}(\dot{\alpha}_\Gamma)(M) \cdot \sigma'$$

(8-12)

This failure surface corresponds to a purely frictional Mohr–Coulomb failure criterion.

8.2.5 Graphical representation of model

The basic formulation of the one surface model has eight model parameters. In the following section, the physical meaning and derivation of the model parameters are discussed. The response can be divided into three parts: (i) elastic, (ii) yielding and (iii) failure. The deviatoric behaviour of the three regions is schematically illustrated with the spring–slider model in Figure 8-1. It corresponds to a modified linear hardening model with elastic stiffness of G, yield strength of $k\sigma'$ and hardening modulus h. An additional slider corresponding to the failure strength $M\sigma'$ is added in series.
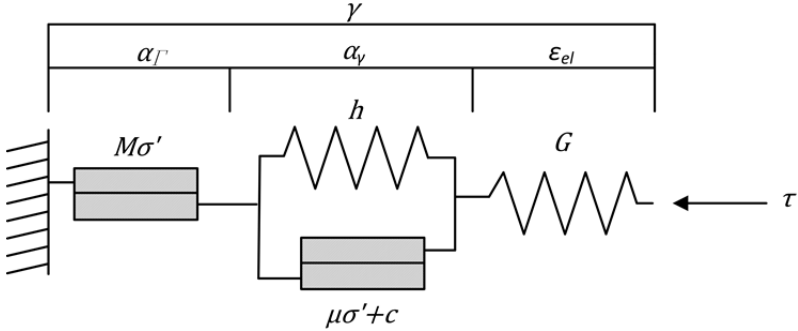
Figure 8-1: Graphical representation of the deviatoric behaviour of the one surface kinematic hardening model

The volumetric behaviour is not illustrated here. However, the plastic volumetric behaviour is coupled via the kinematic constraints (8-3) and (8-4) to the plastic shear strains, and the elastic volumetric behaviour is controlled by the pressure-dependent bulk modulus $K = \sigma'/\kappa$.
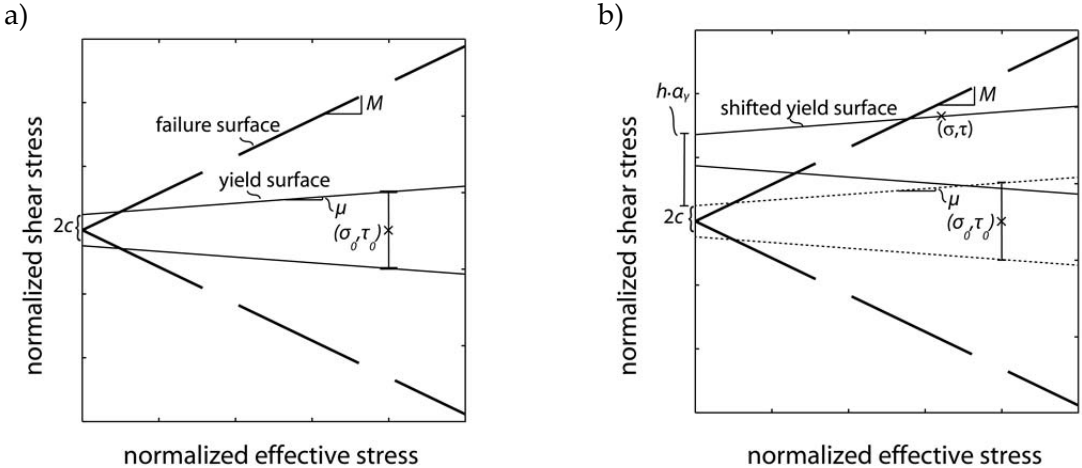
Figure 8-2: Graphical representation of the model features in stress space: a) initial state; b) state during yielding (undrained)

Figure 8-2 shows the representation of the model in stress space with the yield and failure surface. Initially the stress state is inside the yield surface, and the material behaves elastically (Figure 8-2a); once the yield surface is reached, the material deforms plastically,

causing the yield surface to shift owing to kinematic strain hardening (Figure 8-2b). During undrained loading, contraction as described before causes the effective stress to reduce, and thus the stress state also moves towards the left in Figure 8-2b.

8.2.6   Model performance

After deriving the fundamental formulation of the model in the previous section, the next paragraph will demonstrate the derivation and application of the model to various loading conditions.

Incremental response in monotonic shear loading

The response in shear loading is subdivided into the elastic, the yielding and the failure parts:

(i) Elastic part

Assuming no plastic shear strains at the beginning of the loading, the condition for elastic behaviour follows from the yield surface, eq. (8-9).

$$|\tau| < (\mu \cdot \sigma' + c) \tag{8-13}$$

Since the plastic strains are zero, the elastic response follows directly from eq. (8-5) to:

$$\begin{Bmatrix} \dot{\varepsilon}_e \\ \dot{\gamma}_e \end{Bmatrix} = \begin{bmatrix} \dfrac{\kappa}{(1 + e_0)\sigma'} & 0 \\ 0 & \dfrac{1}{G} \end{bmatrix} \begin{Bmatrix} \dot{\sigma}' \\ \dot{\tau} \end{Bmatrix} \tag{8-14}$$

The elastic response is linear for shear loading and stress dependent for normal (volumetric) loading, following the commonly used logarithmic relation.

(ii) Yielding

If the stress state is higher than the initial position of the yield surface but lower than failure,

$$(\mu \cdot \sigma' + c) = |\tau - h\alpha_\gamma| < M \cdot \sigma' \tag{8-15}$$

the plastic strains are no longer zero and are derived by solving eq. (8-9) for the plastic shear strain α_γ.

$$\alpha_\gamma = \frac{\tau - \mathrm{sign}(\dot{\alpha}_\gamma)(\mu \cdot \sigma' + c)}{h} \tag{8-16}$$

Inserting the plastic shear strain into the derived relation for the total shear strains, Eq. (8-5), gives

$$\varepsilon = \frac{\kappa}{(1 + e_0)} \ln \frac{\sigma'}{\sigma'_0} + \beta \left| \frac{\tau - \text{sign}(\dot{\alpha}_\gamma)(\mu \cdot \sigma' + c)}{h} \right|$$

$$\gamma = \frac{\tau}{G} + \frac{\tau - \text{sign}(\dot{\alpha}_\gamma)(\mu \cdot \sigma' + c)}{h} \tag{8-17}$$

The compliance matrix during yielding is derived by differentiation of the total strains with respect to stresses.

$$\begin{Bmatrix} \dot{\varepsilon} \\ \dot{\gamma} \end{Bmatrix} = \begin{bmatrix} \dfrac{\partial \varepsilon}{\partial \sigma'} & \dfrac{\partial \varepsilon}{\partial \tau} \\ \dfrac{\partial \gamma}{\partial \sigma'} & \dfrac{\partial \gamma}{\partial \tau} \end{bmatrix} \begin{Bmatrix} \dot{\sigma}' \\ \dot{\tau} \end{Bmatrix} = \begin{bmatrix} \dfrac{\kappa}{(1 + e_0)\sigma'} - \beta \dfrac{\text{sign}(\dot{\alpha}_{\gamma,1})\text{sign}(\alpha_{\gamma,1})\mu}{h} & \beta \dfrac{\text{sign}(\alpha_\gamma)}{h} \\ -\dfrac{\text{sign}(\dot{\alpha}_\gamma)\mu}{h} & \dfrac{1}{G} + \dfrac{1}{h} \end{bmatrix} \begin{Bmatrix} \dot{\sigma}' \\ \dot{\tau} \end{Bmatrix} \tag{8-18}$$

The behaviour of the model during yielding corresponds to a linear hardening with non-associated flow rule.

(iii) Failure

As the stress state reaches the failure condition:

$$\tau = \text{sign}(\dot{\alpha}_\Gamma)(M) \cdot \sigma' \tag{8-19}$$

the plastic strains at failure α_E, α_Γ are added to the total strain formulation. Using the constraint (8-4), the flow rule becomes:

$$\dot{\alpha}_E = B|\lambda|$$
$$\dot{\alpha}_\Gamma = \lambda \tag{8-20}$$

where λ is a Lagrange multiplier which will be defined subsequently. Using eq. (8-5) the stress increments are expressed as

$$\dot{\sigma}' = \frac{(1 + e_0) \cdot \sigma'}{\kappa}(\dot{\varepsilon} - \dot{\alpha}_\varepsilon - \dot{\alpha}_E) = \frac{(1 + e_0) \cdot \sigma'}{\kappa}(\dot{\varepsilon} - \dot{\alpha}_\varepsilon - B|\lambda|)$$

$$\dot{\tau} = G(\dot{\gamma} - \dot{\alpha}_\gamma - \dot{\alpha}_\Gamma) = G(\dot{\gamma} - \dot{\alpha}_\gamma - \lambda) \tag{8-21}$$

Inserting the stress increments into the consistency (plastic loading) condition

$$\frac{\partial f}{\partial \sigma'}\dot{\sigma}' + \frac{\partial f}{\partial \tau}\dot{\tau} = 0 \tag{8-22}$$

allows solving for the multiplier λ.

$$\lambda = \frac{G(\dot{\gamma} - \dot{\alpha}_\gamma) - \dfrac{(1 + e_0)\sigma'}{\kappa} \cdot \text{sign}(\dot{\alpha}_\Gamma)(M) \cdot (\dot{\varepsilon} - \dot{\alpha}_\varepsilon)}{G - (M) \cdot B \cdot \dfrac{(1 + e_0)\sigma'}{\kappa}} \tag{8-23}$$

Therefore, the plastic strains at failure depend on the total strain increments and the plastic strain increments during yielding and are:

$$\dot{\alpha}_{\mathrm{E}} = \mathrm{B} \left| \frac{G(\dot{\gamma} - \dot{\alpha}_\gamma) - \frac{(1 + e_0)\sigma'}{\kappa} \cdot \mathrm{sign}(\dot{\alpha}_\Gamma)(\mathrm{M}) \cdot (\dot{\varepsilon} - \dot{\alpha}_\varepsilon)}{G - (\mathrm{M}) \cdot \mathrm{B} \cdot \frac{(1 + e_0)\sigma'}{\kappa}} \right|$$

$$\dot{\alpha}_\Gamma = \frac{G(\dot{\gamma} - \dot{\alpha}_\gamma) - \frac{(1 + e_0)\sigma'}{\kappa} \cdot \mathrm{sign}(\dot{\alpha}_\Gamma)(\mathrm{M}) \cdot (\dot{\varepsilon} - \dot{\alpha}_\varepsilon)}{G - (\mathrm{M}) \cdot \mathrm{B} \cdot \frac{(1 + e_0)\sigma'}{\kappa}}$$

(8-24)

The incremental response at failure is given by substitution of (8-24) into (8-21).

$$\begin{Bmatrix} \dot{\sigma}' \\ \dot{\tau} \end{Bmatrix} = \frac{G \frac{(1 + e_0)\sigma'}{\kappa}}{G - MB \frac{(1 + e_0)\sigma'}{\kappa} - MG \frac{(1 + e_0)\sigma'}{\kappa} \cdot \left(B \cdot \mathrm{sign}(\dot{\alpha}_\Gamma) \cdot \mathrm{sign}(\alpha_\gamma) - \beta\right) \cdot \left(\frac{1}{h} - \frac{\mathrm{sign}(\dot{\alpha}_\gamma)}{\mathrm{sign}(\dot{\alpha}_\Gamma)} \frac{\mu}{Mh}\right)} \cdot$$
$$\begin{bmatrix} 1 & -\dfrac{B}{\mathrm{sign}(\dot{\alpha}_\Gamma)} \\ \mathrm{sign}(\dot{\alpha}_\Gamma) \cdot M & -M \cdot B \end{bmatrix} \begin{Bmatrix} \dot{\varepsilon} \\ \dot{\gamma} \end{Bmatrix}$$

(8-25)

Undrained loading

In undrained loading, an additional constraint on the volumetric strain is introduced. Assuming that the bulk of water is infinity and the material is fully saturated, the incompressibility condition

$$\dot{\varepsilon} = 0 \tag{8-26}$$

has to be met. From condition (8-26) and the derived expression for the volumetric strains (8-5), the following expression for the development of mean effective pressure σ' is derived.

$$\sigma' = \sigma'_0 \cdot e^{-\frac{\alpha_v + \alpha_V}{\kappa}} \tag{8-27}$$

An implication of eq. (8-27) is that the mean effective stress decreases with increasing volumetric plastic strains according to an exponential function, slowing down with higher plastic strains. Decreasing mean effective pressure σ' in undrained loading corresponds to an increase of excess pore water pressure $\Delta u = \sigma - \sigma'$. Furthermore, the exponential nature of the development of mean effective pressure limits it to positive values, and therefore the excess pore water pressure cannot exceed the initial value of the mean effective stress $\Delta u \leq \sigma'_0$.

Inserting the incompressibility condition (8-26) into the incremental response during yielding (8-18), and substituting the mean effective stress increment $\dot{\sigma}' = \dot{\sigma} - \Delta\dot{u}$, the incremental response for undrained behaviour is derived, from which the governing expressions for stress- or strain-controlled boundary conditions are developed.

$$\begin{Bmatrix} 0 \\ \dot{\gamma} \end{Bmatrix} = \begin{bmatrix} \dfrac{\kappa}{(1+e_0)\sigma'} - \beta\,\dfrac{\text{sign}(\dot{\alpha}_\gamma)\text{sign}(\alpha_\gamma)\mu}{h} & \beta\,\dfrac{\text{sign}(\alpha_\gamma)}{h} \\[2ex] -\dfrac{\text{sign}(\dot{\alpha}_\gamma)\mu}{h} & \dfrac{1}{G}+\dfrac{1}{h} \end{bmatrix} \begin{Bmatrix} \dot{\sigma} - \Delta\dot{u} \\ \dot{\tau} \end{Bmatrix} \qquad (8\text{-}28)$$

The incremental response at failure in undrained loading is given by (8-25) which can be solved for both stress- and strain-controlled loading conditions. If the material behaviour at failure is dilative, i.e. $B > 0$, the undrained behaviour at failure is stable even in stress-controlled loading: that is "hardening behaviour". For contractive behaviour, on the other hand, a "softening" behaviour would occur at failure in undrained conditions.

Figure 8-3 demonstrates the model performance during undrained monotonic loading. Figure 8-3a shows the stress path composed of a stage of purely elastic behaviour followed by subsequent yielding. During yielding, the effective stress drops, owing to the locked contractive strains leading the development of excess pore pressures. As the slope of the stress path during yielding is dependent on the effective stress state, the response in yielding becomes non-linear. Once the stress path reaches the failure surface, the model can reproduce contractive ($B > 0$), dilative ($B < 0$) or perfectly plastic ($B = 0$) behaviour. In Figure 8-3, dilative behaviour is simulated, causing the stress path to move upwards on the failure surface. The deviatoric stress–strain behaviour (Figure 8-3b) shows the same three stages.
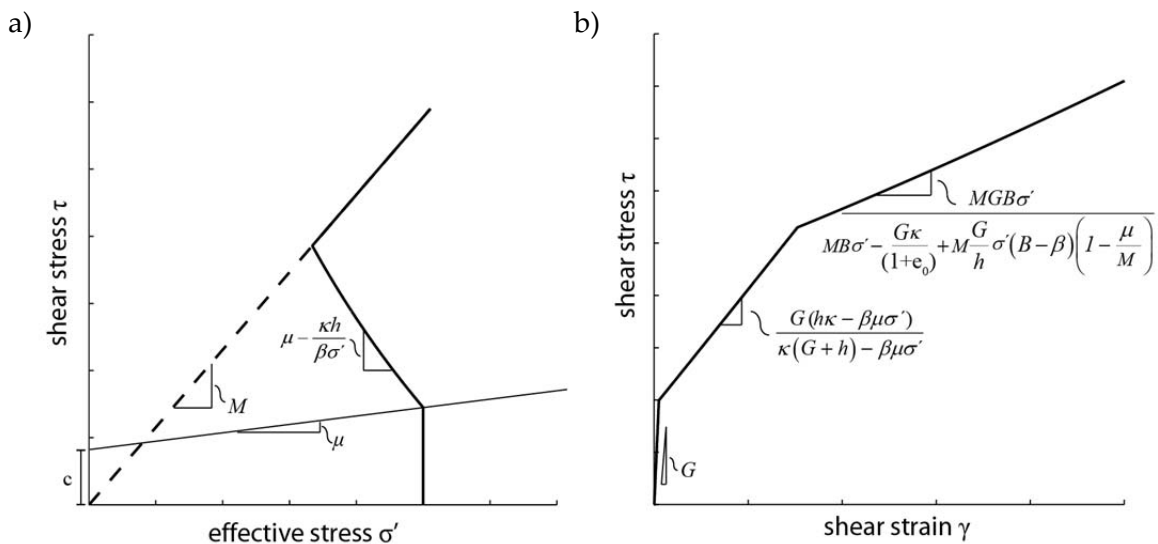
Figure 8-3: Response of the one surface model in undrained monotonic shearing: a) stress paths, b) deviatoric stress-strain behaviour

Behaviour in cyclic unloading/reloading

Analogously to the previous section, the response during cyclic loading is divided into three parts. Generally, the compliance matrices correspond exactly to those derived in the previous section. The only difference is due to the kinematic nature of the yield surface. Therefore, in unloading/reloading the material behaviour remains elastic, eq. (8-14), as long as the stress state is inside the yield surface

$$\left| \tau - h \cdot \alpha_{\gamma,r} \right| < (\mu \cdot \sigma' + c) \tag{8-29}$$

With $\alpha_{\gamma,r}$ being the plastic shear strain at the stress reversal (σ'_r, τ_r)

$$\alpha_{\gamma,r} = \frac{\tau_r - sign(\dot{\alpha}_\gamma)(\mu \cdot \sigma'_r + c)}{h} \tag{8-30}$$

Since during elastic unloading/reloading the mean effective pressure σ' is constant $\sigma' = \sigma'_r$, the yielding condition is:

$$\tau < sgn(\dot{\alpha}_\gamma) \cdot 2 \cdot (\mu \cdot \sigma' + c) - \tau_r \tag{8-31}$$

After reaching this condition, the incremental response behaves according to eq. (8-18) up to the point where conditions for failure, eq. (8-19), are met.

Figure 8-4 illustrates the model behaviour during undrained cyclic loading. As can be seen from the stress path, with every cycle the mean effective stress decreases because of the contractive behaviour. Therefore, the excess pore water pressure increases correspondingly. At the same time, the overall deviatoric stress-strain behaviour is becoming softer with every cycle, i.e. the yield onset starts at a lower stress. This effect is caused by the inclined yield surface with smaller yield strength at lower mean effective stress σ'. In the last cycle, the failure surface is reached, which again causes a significant loss of overall stiffness.

a)

b)
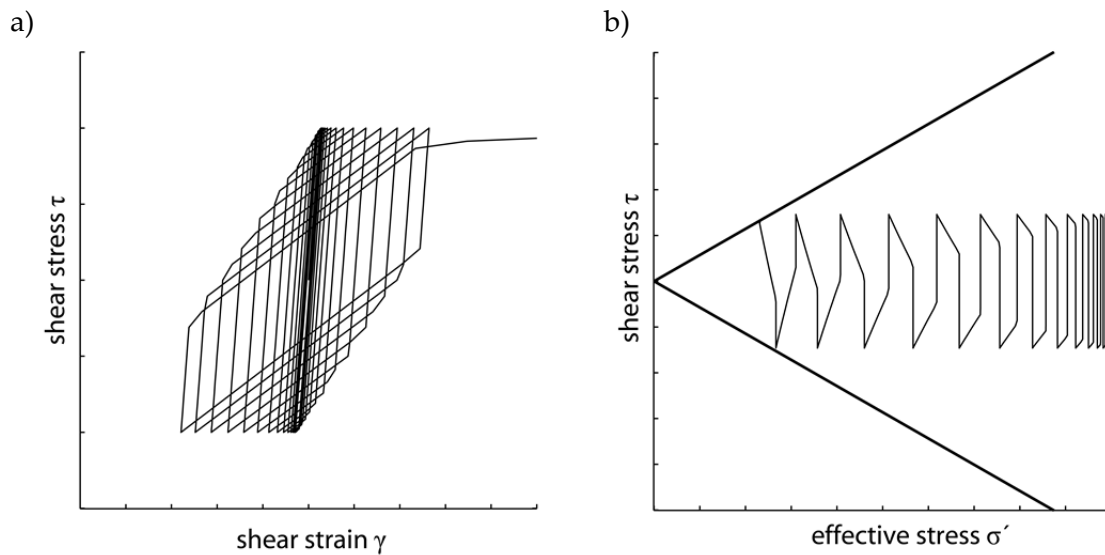
Figure 8-4: Response of the one surface model during stress-controlled undrained cyclic DSS loading: a) deviatoric stress-strain behaviour, b) stress path

Figure 8-5 shows stress paths for cyclic undrained strain-controlled loading with (a) dilative $B < 0$ and (b) contractive $B > 0$ behaviour at failure, respectively. Dilative behaviour at failure leads to a stabilization of the excess pore water pressure generation with increasing number of cycles. This yields a "butterfly" shaped stress path which is frequently described in the literature, e.g. Zergoun and Vaid (1994), Houlsby and Mortara (2004). In contrast, contractive behaviour at failure leads to a constant increase in excess pore water pressures and "softening" stress–strain response with increasing number of cycles.

a)

b)
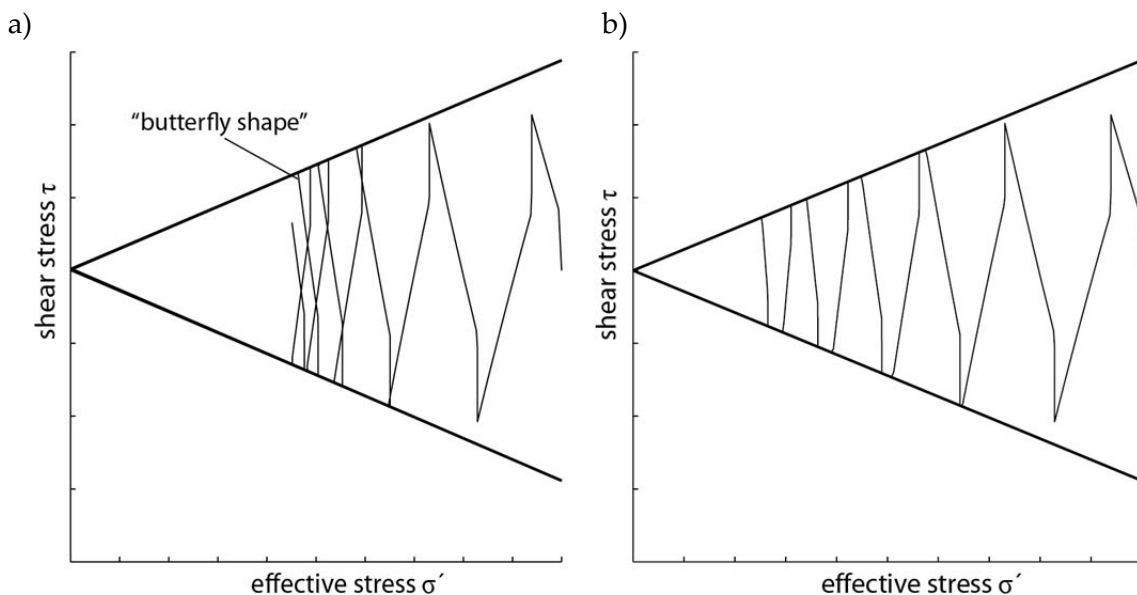
Figure 8-5: Model response during undrained strain-controlled cyclic DSS loading with (a) dilative behaviour at failure and (b) contractive behaviour at failure

8.2.7 Comparison between one surface kinematic hardening model and experimental data

In order to assess the performance of the model and to explore its limitations, a series of direct simple shear (DSS) tests have been simulated that correspond to a number of tests from an extensive investigation program of silty and clayey soils performed at the UC Berkeley by Jennifer Lynn Donahue (2007). To ease the comparison, the data has been read out of the figures provided by Donahue (2007) and is shown as grey lines in the background of plots generated using the model.

The set of tests used here corresponds to low plasticity silts (soils "A" from Donahue (2007)) and has been chosen since it is the most complete one and is, as will be shown later, similar to the soil found in St. Moritz.

The model parameters used for the simulations and their sources are given in Table 8-1:

Parameter		Value	Unit
Elastic stage			
C_s	Swelling index	0.025	[-]
e_0	Void ratio	0.66–0.74	[-]
G	Shear modulus	8	[MPa]
Yielding stage			
k	Frictional yield parameter	0.036	[-]
c	Cohesive yield parameter	$0.108\sigma_0$	[kPa]
β	Dilation (compaction) parameter	0.0375	[-]
h	Hardening modulus	500	[kPa]
Failure			
M	Frictional failure strength	0.58	[-]
B	Dilation coefficient	0.03	[-]

Table 8-1: Parameters of the one surface kinematic hardening model

Figure 8-6 shows the comparison between model and test A6 from the test series that has been used for calibration: that is, the model is calibrated for a target amplitude of $0.173\ \sigma_0'$ and an initial effective stress of $\sigma_0' \approx 140\text{kPa}$. One can see that, overall, the model can reproduce the development of pore pressures (Figure 8-6a and c). The development of excess pore pressures during one cycle is strongly simplified (Figure 8-6a). The model allows for the degradation of the shear modulus before failure (Figure 8-6b). In failure, an immediate increase in strain amplitude per cycle is modelled but no further degradation of stiffness is captured (Figure 8-6d). The butterfly shape of the stress path at low effective stress is underestimated because the opening of the yield surface is fixed, therefore it oscillates on a fixed path and cannot move further towards the apex (Figure 8-6a).

a)

b)

c)

Test A6
$\sigma'_0 = 140$kPa
CSR=0.173

d)
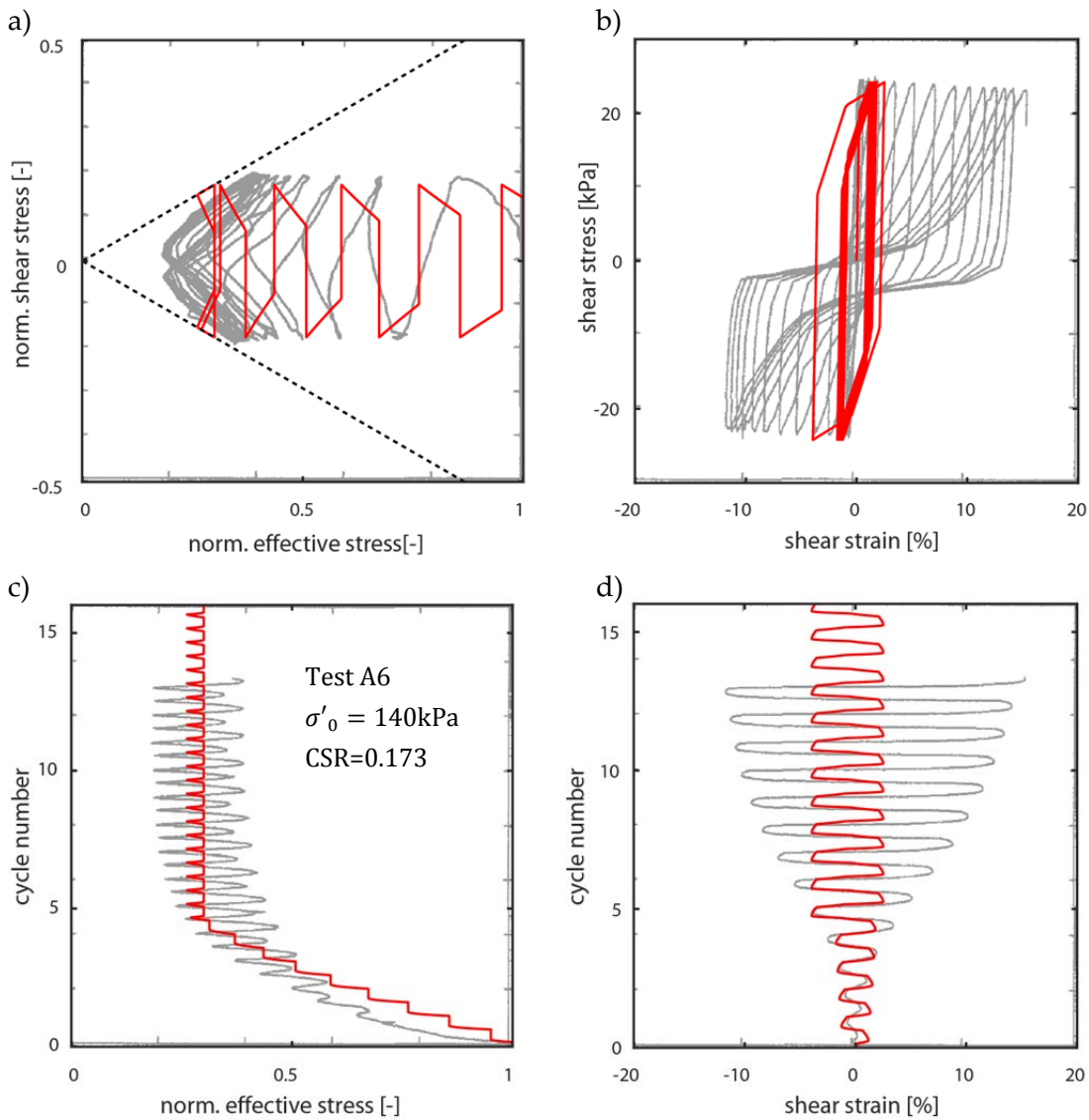
Figure 8-6: Comparison of experimental data from Donahue (2007) (grey line reproduced from original publication for undrained cyclic DSS test A6 with cyclic stress ration (CSR) of 0.173) and simulations (red line): a) stress path; b) stress–strain behaviour; c) normalized vertical effective stress to number of cycles; d) shear strain to number of cycles

Figure 8-7 shows the model's ability to reproduce strain-controlled monotonic tests with the parameters shown above. Despite the fact that the model is calibrated for an amplitude of $0.173\,\sigma'_0$ it can still reproduce the overall behaviour well, both in terms of stress path and stress–strain behaviour. However, if the model were calibrated for smaller amplitudes, the deviation from the observed stress path would increase. Both stress and stress–strain behaviour are almost tri-linear (Figure 8-7a and b). In the stress–strain behaviour, however, the changes in inclination of the simulated path do not correspond to the observed path. In particular, loss of stiffness at the modelled change from contraction to dilation at almost 10% shear strain is not consistent with the observations. The reason is that in the model the change in behaviour is only initiated once the failure surface is reached. Therefore, the shear stress at the point of change is overestimated.
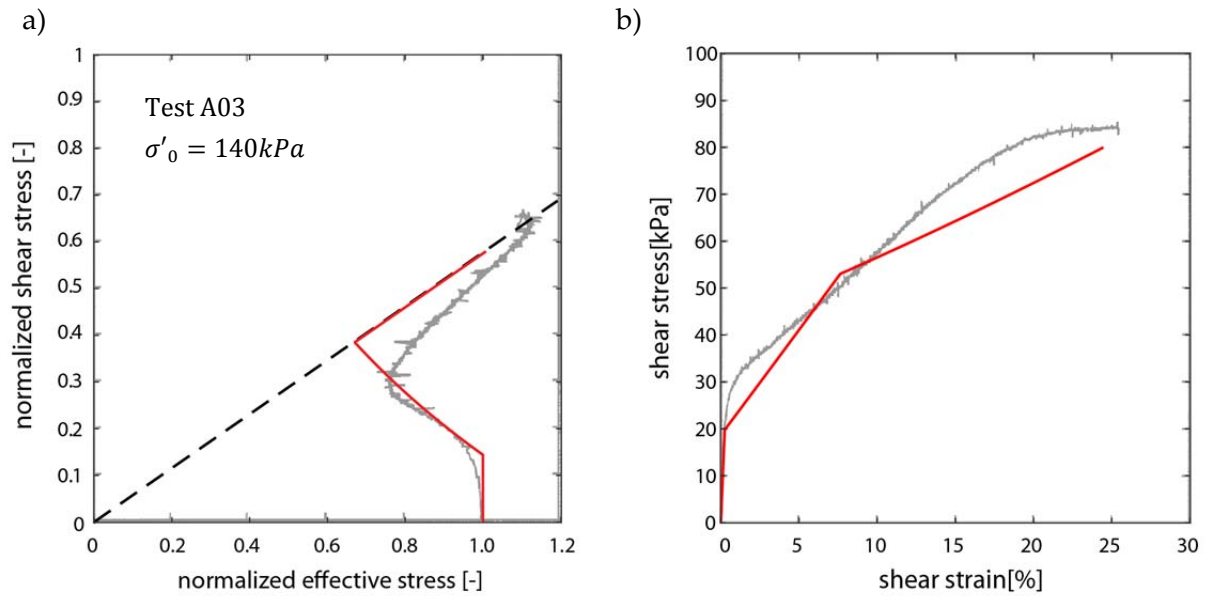
Figure 8-7: Comparison of experimental data from Donahue (2007) (grey line reproduced from original publication for undrained monotonic DSS test A2) and simulations (red line): a) stress path; b) stress–strain behaviour

Figure 8-8a) and b) shows the influence of varying amplitudes. The trend towards greater excess pore pressure per cycle in the case of cycles with larger stress amplitude and less in the case of smaller cycles can be captured approximately.

The influence of changes of the effective overburden stress can be captured, namely less development of excess pore pressures with smaller normal effective stress for similar amplitudes (compare Figure 8-6c and 8-8c) and greater excess pore pressures per cycle for higher confining stresses (compare Figure 8-8b and d).

In all cases, the error between observations and simulations increases with deviation from the reference amplitude and effective stress (amplitude and stress level that has been used for the calibration). Pore pressure built up below the cyclic threshold ($\mu \cdot \sigma'_0 + c$) cannot be reproduced.

a)

Test A11
$\sigma'_0 = 140 kPa$
CSR=0.21

b)

Test A7
$\sigma'_0 = 137 kPa$
CSR=0.164

c)

Test A12
$\sigma'_0 = 70 Pa$
CSR=0.174

d)

Test A13
$\sigma'_0 = 273 kPa$
CSR=0.162
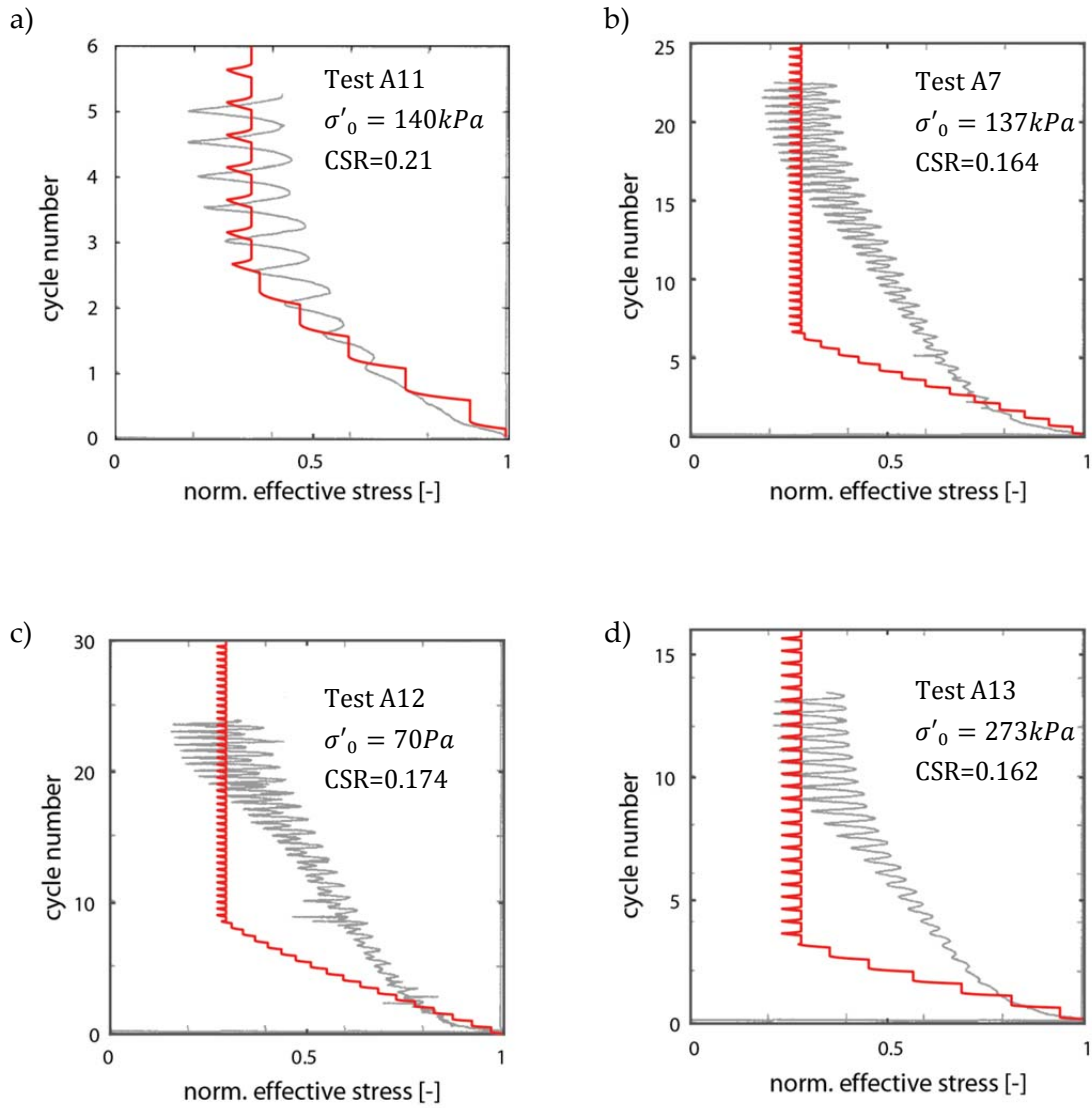
Figure 8-8: Comparison between simulations and experimental results from Donahue (2007) for conditions different from the target amplitude and effective stress: a) larger amplitude, b) smaller amplitude, c) smaller effective stress, d) larger effective stress and smaller amplitude

8.3   Enhanced, two-surface model

As can be seen from section 8.2.7, the previously derived model suffers from some shortcomings that can potentially lead to wrong results. Therefore, it has been decided to derive a second "enhanced" model, aiming to demonstrate the possibilities of enhancing the simple formulation shown before. This model is termed enhanced as, in contrast to the model described in section 8.2, it is formulated using functions for the hardening and compaction/dilation parameters rather than constants, but in contrast to continuous hyperplasticity models it still uses only two distinct yield surfaces (y_0 and y_1) rather than an infinite number of surfaces.

8.3.1   Auxiliary functions

To ease numerical implementation of the model, the functions that are used to describe the development of several parameters are taken from a family of logistic functions described via the hyperbolic tangent and secant.

The three functions used in the following derivations are:

$$L_1(C_n, x) = \tanh(C_n \cdot x) \tag{8-32}$$

$$L_2(C_n, x) = \frac{(1 + \tanh(C_n \cdot x))}{2} \tag{8-33}$$

$$L_3(C_n, x) = \text{sech}(C_n \cdot x) \tag{8-34}$$

where x in (8-32),(8-33) and (8-34) is a placeholder for variables used in the subsequent sections. C_n is a free parameter; if this parameter is not specified it means that $C_n = 1$. The functions describe different shapes of steps between -1 and 1, or between 0 and 1 (see Figure 8-9), where the parameter C_n controls the steepness of the curve. In the positive quadrant, the functions describe steps between 0 and 1, or between 0.5 and 1.
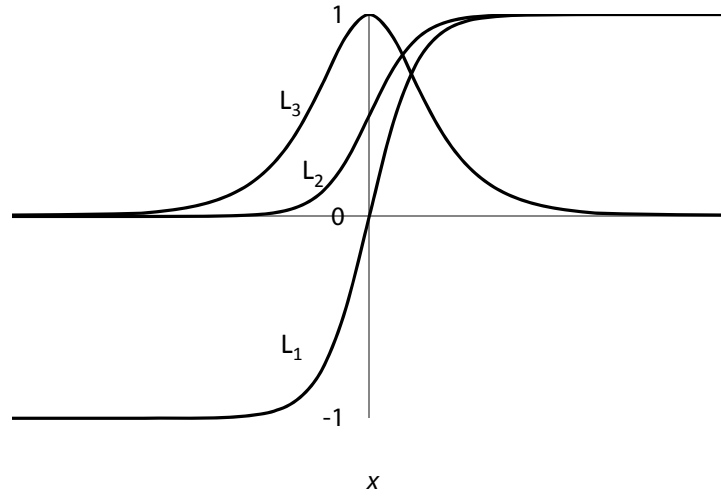
Figure 8-9: Auxiliary functions along a generalized coordinate x

8.3.2 Potential functions

Following the hyperplastic formalism again, the two potential functions are again given in terms of the Gibbs free energy and the dissipation function:

$$g = -\frac{\kappa}{1 + e_0} \cdot \sigma' \cdot \left(\ln\left(\frac{\sigma'}{\sigma'_0}\right) - 1 \right) - \sum_{i=0}^{1} \sigma' \cdot \alpha_\varepsilon^i - \sum_{i=0}^{1} \tau \cdot \alpha_\gamma^i + \frac{h_0 \cdot \left(\alpha_\gamma^0\right)^2}{2} \tag{8-35}$$

$$d = \beta_1^0 \cdot \sigma' \cdot \left|\dot{\alpha}_\gamma^0\right| + \beta_{2,2}^0 \cdot \sigma' \cdot \dot{\alpha}_\gamma^0 +$$

$$\left[\left(\frac{M}{2}\right) \cdot L_1(C_1, a_1^1) + \frac{\beta_1^1}{F_2^1}\right] \cdot \sigma' \cdot \left|\dot{\alpha}_\gamma^1\right| + \left[\left(\frac{M}{2}\right) \cdot L_1(C_1, a_2^1) \cdot \text{sign}(\dot{\alpha}_\gamma^1) + \frac{\beta_2^1}{F_2^1}\right] \cdot \sigma' \cdot \left|\dot{\alpha}_\gamma^1\right| \geq 0 \tag{8-36}$$

α_ε^i, $\dot{\alpha}_\varepsilon^i$, α_γ^i, $\dot{\alpha}_\gamma^i$ are internal variables that correspond to the plastic volumetric and shear strains or strain rates for the two surfaces ($i = 0,1$). In (8-36) and also in the later derivations, a second set of internal variables a_1^i and a_2^i is used. These are hardening parameters that are related to the plastic strains via kinematic constraints. The other variables are the same as in section 8.2.1. If variables appear in both yield surface formulations, the superscript index always denotes the surface they correspond to, and the subscript indices are used as identifier or numbering index that will be introduced in subsequent sections.

As can be seen from (8-35), the Gibbs free energy again contains a term causing kinematic hardening of surface y_0, whereas the behaviour of the surface y_1 will be completely derived from the dissipation. The terms containing β in (8-36) are again added so that these terms vanish in the yield surface formulation.

8.3.3 Strains

Differentiation of the energy function with respect to the stresses allows the strains to be found:

$$\varepsilon = -\frac{dg}{d\sigma'} = \frac{\kappa}{1+e_0}\ln\frac{\sigma'}{\sigma'_0} + \sum_{i=0}^{1}\alpha_\varepsilon^i \tag{8-37}$$

$$\gamma = -\frac{dg}{d\tau} = \sum_{i=0}^{1}\alpha_\gamma^i \tag{8-38}$$

From (8-38), it can be seen that no purely elastic part in shear exists anymore. This is not a problem since, as will be shown, the stress state always remains on the surface y_0.

8.3.4 Constraints and volumetric coupling

The potential functions are complemented by the following constraints. The parameters are given in general form with their dependencies on internal variables. The functions for each parameter are detailed in section 8.3.6.

Surface y_0

$$C_1^0 = \dot\alpha_\varepsilon^0 - \beta_1^0 \cdot \left|\dot\alpha_\gamma^0\right| - \beta_2^0 \cdot \dot\alpha_\gamma^0 = 0 \tag{8-39}$$

$$C_2^0 = \dot{a}_1^0 - F_1^0 = 0 \tag{8-40}$$

where β_1^0 and β_2^0 are dilation/contraction factors:

$$\beta_1^0 = f(a_2^1) \tag{8-41}$$

$$\beta_2^0 = \beta_{2,1}^0 + \beta_{2,2}^0 = f(a_2^1) + f\left(a_2^1, \text{sign}(\dot\alpha_\gamma^0), \text{sign}(\alpha_\gamma^1), a_1^0\right) \tag{8-42}$$

and F_1^0 a function

$$F_1^0 = f\left(a_2^1, \text{sign}(\dot{a}_2^1), \dot\alpha_\varepsilon^1\right) \tag{8-43}$$

Surface y_1

$$C_1^1 = \dot\alpha_\varepsilon^1 - \frac{\beta_1^1}{F_2^1} \cdot \left|\dot\alpha_\gamma^1\right| - \frac{\beta_2^1}{F_2^1} \cdot \left|\dot\alpha_\gamma^1\right| = 0 \tag{8-44}$$

$$C_2^1 = \dot{a}_1^1 - F_1^1 \cdot \left|\dot\alpha_\gamma^1\right| = 0 \tag{8-45}$$

$$C_3^1 = \dot{a}_2^1 - F_1^1 \cdot \dot\alpha_\gamma^1 = 0 \tag{8-46}$$

with the dilation/contraction factors:

$$\beta_1^1 = f(\sigma') \tag{8-47}$$

$$\beta_2^1 = f\left(a_1^1, a_2^1, \text{sign}(\dot\alpha_\gamma^1)\right) \tag{8-48}$$

and functions

$$F_1^1 = f\left(\eta, a_2^1, \text{sign}(\dot{a}_2^1)\right) \tag{8-49}$$

$$F_2^1 = f\left(\sigma', a_2^1, \text{sign}(\dot{a}_2^1)\right) \tag{8-50}$$

where η denotes the normalized stress state $\eta = \frac{\tau}{M\sigma'}$. F_j^i are additional functions that control the dependency between the rates of the internal variables $\dot{a}_j^i$ and $\dot{\alpha}_j^i$ or the shear-volumetric coupling.

A detailed explanation of the nature and the influence of each of the functions will be given later in this chapter.

8.3.5 Yield surface

The yield surface is derived following the same steps as in 8.2.3.

From the dissipation (8-36) and the constraints (8-39)–(8-46), the augmented dissipation function is formed:

$$d' = d + \sum_{j=1}^{2} \Lambda_j^0 C_j^0 + \sum_{j=1}^{3} \Lambda_j^1 C_j^1 \geq 0 \tag{8-51}$$

From definition it follows that generalized dissipative stresses are ($i = [0; 1]$):

$$\chi_\varepsilon^i = \frac{\partial d'}{\partial \dot{\alpha}_\varepsilon^i} \tag{8-52}$$

$$\chi_\gamma^i = \frac{\partial d'}{\partial \dot{\alpha}_\gamma^i} \tag{8-53}$$

and

$$\chi_a^i = \frac{\partial d'}{\partial \dot{a}^i} \tag{8-54}$$

The generalized stresses are given as

$$\bar{\chi}_\varepsilon^i = -\frac{\partial g}{\partial \alpha_\varepsilon^i} \tag{8-55}$$

$$\bar{\chi}_\gamma^i = -\frac{\partial g}{\partial \alpha_\gamma^i} \tag{8-56}$$

and

$$\bar{\chi}_a^i = -\frac{\partial g}{\partial a_n^i} = 0 \; ; \; n = [1; 2] \tag{8-57}$$

The generalized stress related to the internal variables a_j^i is always 0, since these variables do not appear in the energy function, which leads to the incremental multipliers Λ_2^i and Λ_3^i being zero ($\Lambda_2^0 = \Lambda_2^1 = \Lambda_3^1 = 0$).

For the internal variable related to the plastic strain of surface y_0, differentiation of the dissipation function produces

$$\chi_\varepsilon^0 = \frac{\partial d'}{\partial \dot{\alpha}_\varepsilon^0} = \Lambda_1^0 \tag{8-58}$$

$$\begin{aligned}\chi_\gamma^0 = \frac{\partial d'}{\partial \dot{\alpha}_\gamma^0} &= \beta_1^0 \cdot \sigma' \cdot \operatorname{sign}(\dot{\alpha}_\gamma^0) + \beta_{2,2}^0 \cdot \sigma' - \Lambda_1^0 \cdot \beta_1^0 \cdot \operatorname{sign}(\dot{\alpha}_\gamma^0) - \Lambda_1^0 \cdot \beta_2^0 \\ &= \beta_1^0 \cdot \sigma' \cdot \operatorname{sign}(\dot{\alpha}_\gamma^0) + \beta_{2,2}^0 \cdot \sigma' - \Lambda_1^0 \cdot \beta_1^0 \cdot \operatorname{sign}(\dot{\alpha}_\gamma^0) - \Lambda_1^0 \cdot \beta_{2,1}^0 - \Lambda_1^0 \cdot \beta_{2,2}^0 \end{aligned} \tag{8-59}$$

Please note that $\beta_{2,2}^0$ is a function of $\operatorname{sign}(\dot{\alpha}_\gamma^0)$, but this does not change the derivative with respect to $\dot{\alpha}_\gamma^0$, since

$$\frac{\partial f\!\left(\operatorname{sign}(\dot{\alpha}_\gamma^0)\right)}{\partial \dot{\alpha}_\gamma^0} = \frac{\partial f(u)}{\partial u} \cdot \frac{\partial u}{\partial \dot{\alpha}_\gamma^0} \text{ with } u = \operatorname{sign}(\dot{\alpha}_\gamma^0) \tag{8-60}$$

$$\frac{\partial u}{\partial \dot{\alpha}_\gamma^0} = 0 \text{ therefore } \frac{\partial f\!\left(\operatorname{sign}(\dot{\alpha}_\gamma^0)\right)}{\partial \dot{\alpha}_\gamma^1} = 0 \; \forall \; \dot{\alpha}_\gamma^0 \neq 0 \tag{8-61}$$

The generalized stresses are

$$\bar{\chi}_\varepsilon^0 = -\frac{\partial g}{\partial \alpha_\varepsilon^0} = \sigma' \tag{8-62}$$

$$\bar{\chi}_\gamma^0 = -\frac{\partial g}{\partial \alpha_\gamma^0} = \tau - h_0 \cdot \alpha_\gamma^0 \tag{8-63}$$

Using Ziegler's orthogonality, the yield surface y_0 can be derived:

$$y_0 = 0 = \tau - h_0 \cdot \alpha_\gamma^0 + \sigma' \cdot \beta_{2,1}^0 \tag{8-64}$$

From the appearance of (8-64), it can be seen that surface y_0 is always active.

The formulation for the surface y_1 is derived in the same way:

$$\chi_\varepsilon^1 = \frac{\partial d'}{\partial \dot{\alpha}_\varepsilon^1} = \Lambda_1^1 \tag{8-65}$$

$$\begin{aligned}\chi_\gamma^1 = \frac{\partial d'}{\partial \dot{\alpha}_\gamma^1} &= \left[\left(\frac{M}{2}\right) \cdot L_1(C_1, a_1^1) + \frac{\beta_1^1}{F_2^1}\right] \cdot \sigma' \cdot \operatorname{sign}(\dot{\alpha}_\gamma^1) + \left[\left(\frac{M}{2}\right) \cdot L_1(C_1, a_2^1) + \frac{\beta_2^1}{F_2^1} \cdot \operatorname{sign}(\dot{\alpha}_\gamma^1)\right] \cdot \sigma' \\ &\quad - \Lambda_1^1 \left[\frac{\beta_1^1}{F_2^1} + \frac{\beta_2^1}{F_2^1}\right] \cdot \operatorname{sign}(\dot{\alpha}_\gamma^1) - \Lambda_2^1 \cdot F_1^1 \cdot \operatorname{sign}(\dot{\alpha}_\gamma^1) - \Lambda_3^1 \cdot F_1^1 \end{aligned} \tag{8-66}$$

The generalized stresses are given as

$$\bar{\chi}_\varepsilon^1 = -\frac{\partial g}{\partial \alpha_\varepsilon^1} = \sigma' \tag{8-67}$$

$$\bar{\chi}_\gamma^1 = -\frac{\partial g}{\partial \alpha_\gamma^1} = \tau \tag{8-68}$$

whilst the generalized stresses $\bar{\chi}_a^1$ are always 0 (compare (8-57)).

Therefore

$$\chi_{a_1^1}^1 = \frac{\partial d'}{\partial \dot{a}_1^1} = \Lambda_2^1 = 0 \tag{8-69}$$

$$\chi_{a_2^1}^1 = \frac{\partial d'}{\partial \dot{a}_2^1} = \Lambda_3^1 = 0 \tag{8-70}$$

Using Ziegler's orthogonality, the yield surface can be derived to be

$$y_1 = 0 = \tau - \left(\frac{M}{2}\right) \cdot L_1(C_1, a_1^1) \cdot \sigma' \cdot \text{sign}(\dot{\alpha}_\gamma^1) - \left(\frac{M}{2}\right) \cdot L_1(C_1, a_2^1) \cdot \sigma' \tag{8-71}$$

8.3.6 Description of the governing functions

Whilst for the fundamental derivations of the previous sections the exact nature of the functions describing the development of the model parameters was not of importance, this section describes the behaviour of the different parameters and functions in monotonic and cyclic loading in detail.

Please note that since the behaviour of y_0 is influenced by the development of y_1, but not vice versa, the description will be done against the order of the indices and start with y_1.

In general, it can be noted that as long as y_1 is active, the behaviour is mainly governed by this surface, and the influence of y_0 is small.

<u>Analysis of the functions governing the behaviour of y_1</u>

From the definition of the yield surface (8-71), it follows that y_1 undergoes both isotropic hardening (second term in (8-71)) and kinematic hardening (third term in (8-71)). Therefore (8-71) can also be written:

$$y_1 = 0 = \tau - \left(\frac{M}{2}\right) \cdot L_1(C_1, \mathrm{a}_1^1) \cdot \sigma' \cdot \text{sign}(\dot{\alpha}_\gamma^1) - \left(\frac{M}{2}\right) \cdot L_1(C_1, \mathrm{a}_2^1) \cdot \sigma' =$$
$$= \tau - (\mu_{iso} + \mu_{kin}) \cdot \sigma' = \tau - \mu \cdot \sigma \tag{8-72}$$

with the isotropic part of the yield surface being

$$\mu_{iso} = \left(\frac{M}{2}\right) \cdot L_1(C_1, \mathrm{a}_1^1) \cdot \text{sign}(\dot{\alpha}_\gamma^1) \tag{8-73}$$

and the kinematic part

$$\mu_{kin} = \left(\frac{M}{2}\right) \cdot L_1(C_1, \mathrm{a}_2^1) \tag{8-74}$$

The hardening functions depend on the internal parameters a_1^1 and a_2^1. Both variables are related via their rates ($\dot{\mathrm{a}}_j^i$) to the shear strain rate $\dot{\alpha}_\gamma^1$ with the same function F_1^1 (see constraints (8-45) and (8-46)). The only difference is that $\dot{\mathrm{a}}_1^1$ is related to the absolute value of the strain increments $|\dot{\alpha}_\gamma^1|$, whereas $\dot{\mathrm{a}}_2^1$ depends on $\dot{\alpha}_\gamma^1$ directly.

Without analysing the nature of F_1^1 in more detail, this formulation has the following implications for the development of y_1:

(i)   Isotropic expansion of the yield surface cannot be reversed, since $\mu_{iso} = f(a_1^1)$ and $\dot{a}_1^1 = f(|\dot{\alpha}_\gamma^1|)$.

(ii) The kinematic part of the yield surface describes a rotation of the yield surface that can be reversed if the material is loaded sufficiently in the opposite direction.

(iii) Since the ultimate opening of the yield surface ($\mu_{iso,ult}$) and the ultimate rotation ($\mu_{kin,ult}$) are both equal to half of the inclination of the failure envelope of the material (M), this strength cannot be exceeded.

$$\mu_{ult} = \left(\pm\mu_{iso,ult} \pm \mu_{kin,ult} = \pm\frac{M}{2} \pm \frac{M}{2} = \pm M \right) \tag{8-75}$$

(iv) In the case of positive (respectively negative) loading to the ultimate state, the lower (respectively upper) branch of the yield surface always lies (independent of the stress history) on the abscissa ($\tau = 0$) of the stress space (see Figure 8-10a):

$$\mu'_{ult} = \left(\pm\mu_{iso,ult} \mp \mu_{aniso,ult} = \pm\frac{M}{2} \mp \frac{M}{2} = 0 \right) \tag{8-76}$$

(v)   Owing to the nature of the step functions, the hardening rate ($\frac{d}{dt}\mu$) drops towards zero, i.e. the material becomes infinitely soft, as the stress state approaches the ultimate state; therefore, the introduction of a distinct failure surface is not necessary:

$$\lim_{\mu \to M} \dot{\mu} = 0 \tag{8-77}$$

(vi) During monotonic loading, the rate of isotropic and kinematic hardening is the same ($\dot{\mu}_{iso} = \dot{\mu}_{kin}$), and therefore only the branch of the yield surface in direction of loading moves with the stress state, whilst the opposite branch remains along the abscissa ($\tau = 0$) of the stress space (see Figure 8-10b).

(vii) During cyclic loading, the isotropic hardening portion will initially accumulate, whereas the kinematic portion diminishes in load reversals (see Figure 8-10c, $\mu_{iso} > \mu_{kin}$). After some cycles, the isotropic part approaches its ultimate state i.e. y_1 has become a cone with opening $2\mu_{iso} \to M$ and the hardening behaviour becomes purely governed by the kinematic hardening part (see Figure 8-10d).
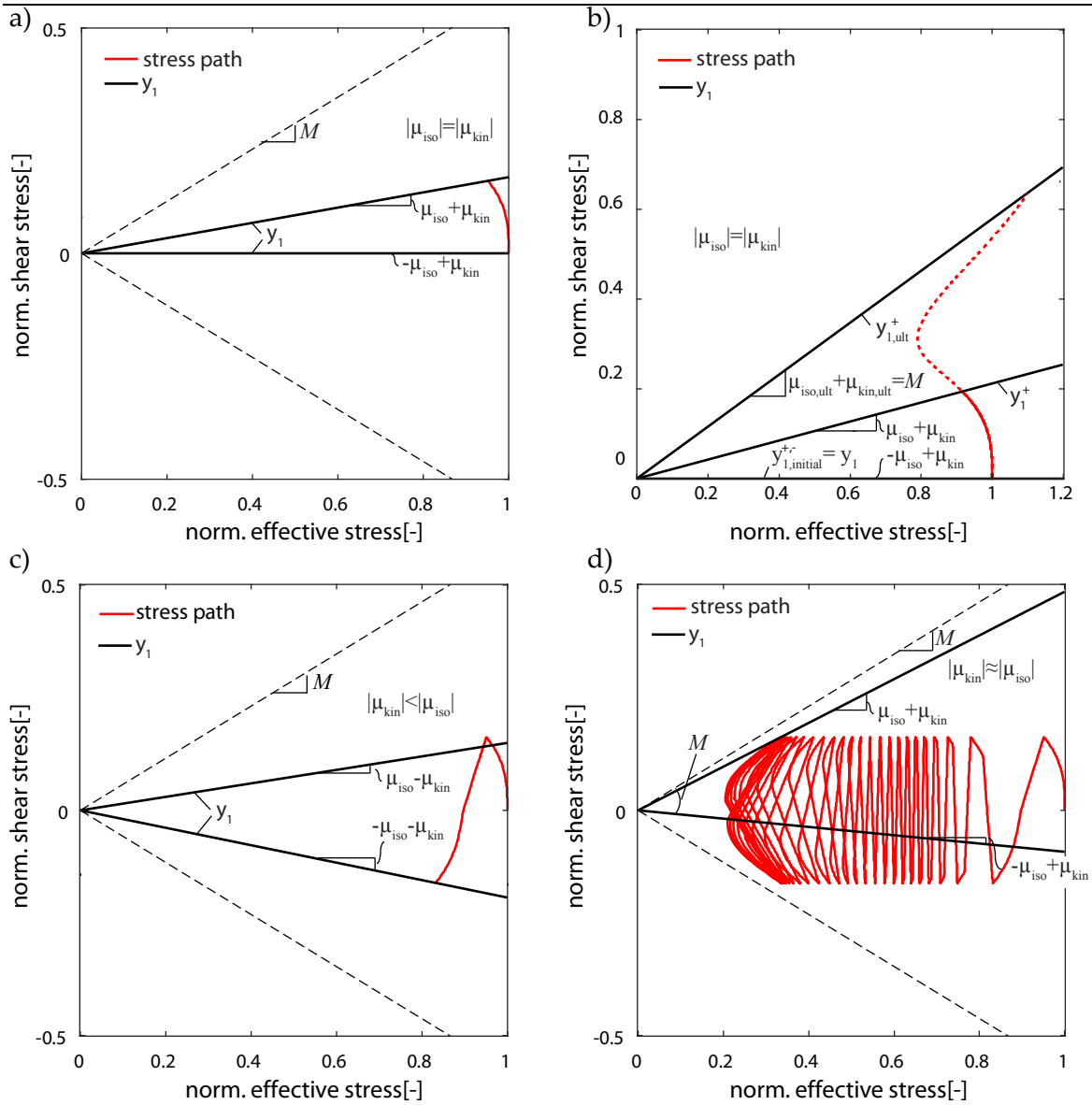
Figure 8-10: Normalized stress path $(\frac{\sigma'}{\sigma'_0} - \frac{\tau}{\sigma'_0})$ and position of yield surface y_1: a) loading stage of the first cycle ≙ monotonic loading ; b) monotonic stress path; c) first cycle – reloading; d) cycle n – loading;

The exact nature of F_1^1 controls the development of a_1^1 and a_2^1 in (8-72) and therefore largely influences the hardening of y_1. From analysis of the stress–strain behaviour in cyclic and monotonic tests, the following requirements for the nature of F_1^1 have been found:

(i) From cyclic stress-controlled tests, it can be seen that the material shows different behaviour in initial "small" strain (solid line in Figure 8-11a) and in "large" strain cycles, i.e. cycles at large excess pore pressures (dashed line in Figure 8-11a).

(ii) In undrained monotonic loading, a sequence that can be described as softening→constant stiffness→failure (see Figure 8-11b) can be observed.

To account for these requirements, the function F_1^1 has been composed of two parts that dominate the behaviour in different loading situations:

$$F_1^1\left(\eta, a_2^1, \text{sign}(\dot{a}_2^1)\right) = \frac{L_2\left(C_2, a_2^1 \cdot \text{sign}(\dot{a}_2^1)\right)}{1 - L_3\left((1 - \eta_0) \cdot \eta\right)} = \frac{F_{1,1}^1}{F_{1,2}^1} \tag{8-78}$$

$\boldsymbol{F_{1,1}^1}$ in (8-78) causes the material to have the following properties:

(i)   It hardens as long as the direction of the rate, $\dot{a}_2^1$, coincides with the direction of the accumulated internal variable a_2^1 $\left(\text{sign}(\dot{a}_2^1) = \text{sign}(a_2^1)\right)$.

(ii)   If the direction of the rate is opposite to the accumulated a_2^1 $\left(\text{sign}(\dot{a}_2^1) \neq \text{sign}(a_2^1)\right)$, the material instantly shows significantly softer behaviour. As shown in Figure 8-11c, the factor controlling the rate of hardening $F_{1,1}^1$ is then given by the value of the "mirror" point, i.e. the value drops instantly from $F_{1,1}^1\left(\left|a_2^1\right|\right)$ to $F_{1,1}^1\left(-\left|a_2^1\right|\right)$.

(iii)   In large strain cycles, $F_{1,1}^1$ will cause the material to harden during loading but have almost no stiffness initially (points 1′ to 2′ or 3′ to 4′ in Figure 8-11). The unloading stage (points 2′ to 3′ in Figure 8-11) is governed by surface y_0. This allows reproducing the shape of large cycles (points 1′ to 4′ in Figure 8-11).

(iv)   Initially, in small strain cycles, (points 1 to 4 in Figure 8-11a), $F_{1,1}^1$ has little influence since the changes in $F_{1,1}^1$ are only small (see points 1 to 4 in Figure 8-11c).

(v)   In monotonic loading (points 1^m to 3^m in Figure 8-11), the function would only cause hardening, which is not consistent with observations and will be corrected with the second part $\frac{1}{F_{1,2}^1}$.

Please note that instead of using the dependency on a_2^1 and $\dot{a}_2^1$ in $F_{1,1}^1$ it would also be possible to relate it directly to α_γ^1 and $\dot{\alpha}_\gamma^1$ since

$$\text{sign}\left(\alpha_\gamma^1\right) = \text{sign}(a_2^1) \text{ and } \text{sign}\left(\dot{\alpha}_\gamma^1\right) = \text{sign}(\dot{a}_2^1) \tag{8-79}$$

However, choosing a dependency on a_2^1 allows one to derive the incremental response in closed form. If the model is formulated in general stresses, it might be useful to come back to a formulation depending on $\alpha_\gamma^1, \dot{\alpha}_\gamma^1$.

Overall, since $F_{1,1}^1$ produces a dependency on strain and strain rate direction, anisotropic behaviour is introduced into the model.

$\frac{1}{F_{1,2}^1}$, the second function in (8-78), causes a loss of stiffness with increasing normalized stress

state $\eta = \frac{|\tau|}{M \cdot \sigma\prime}$. This function dominates during monotonic (points 1ᵐ to 3ᵐ in Figure 8-11) and

in small cycles (points 1 to 4 in Figure 8-11). Its influence can be summarized as follows:

(i)   From the shape of the function in Figure 8-11d, it can be seen that $\frac{1}{F_{1,2}^1}$ drops from

infinity at $\eta = 0$ to 1 meaning that initially the hardening rate is infinite, which allows

the loss of stiffness at small strains to be reproduced.

(ii)   In simulations with a static shear stress ($\tau_0 > 0 \rightarrow \eta_0 > 0$), it has been observed that

the initial stiffness loss seems to be overestimated. Therefore, a term $(1 - \eta_0)$ has been

added that compensates partially for the loss of stiffness e.g. during a stage of

drained shearing (to apply τ_0) before undrained cyclic loading.
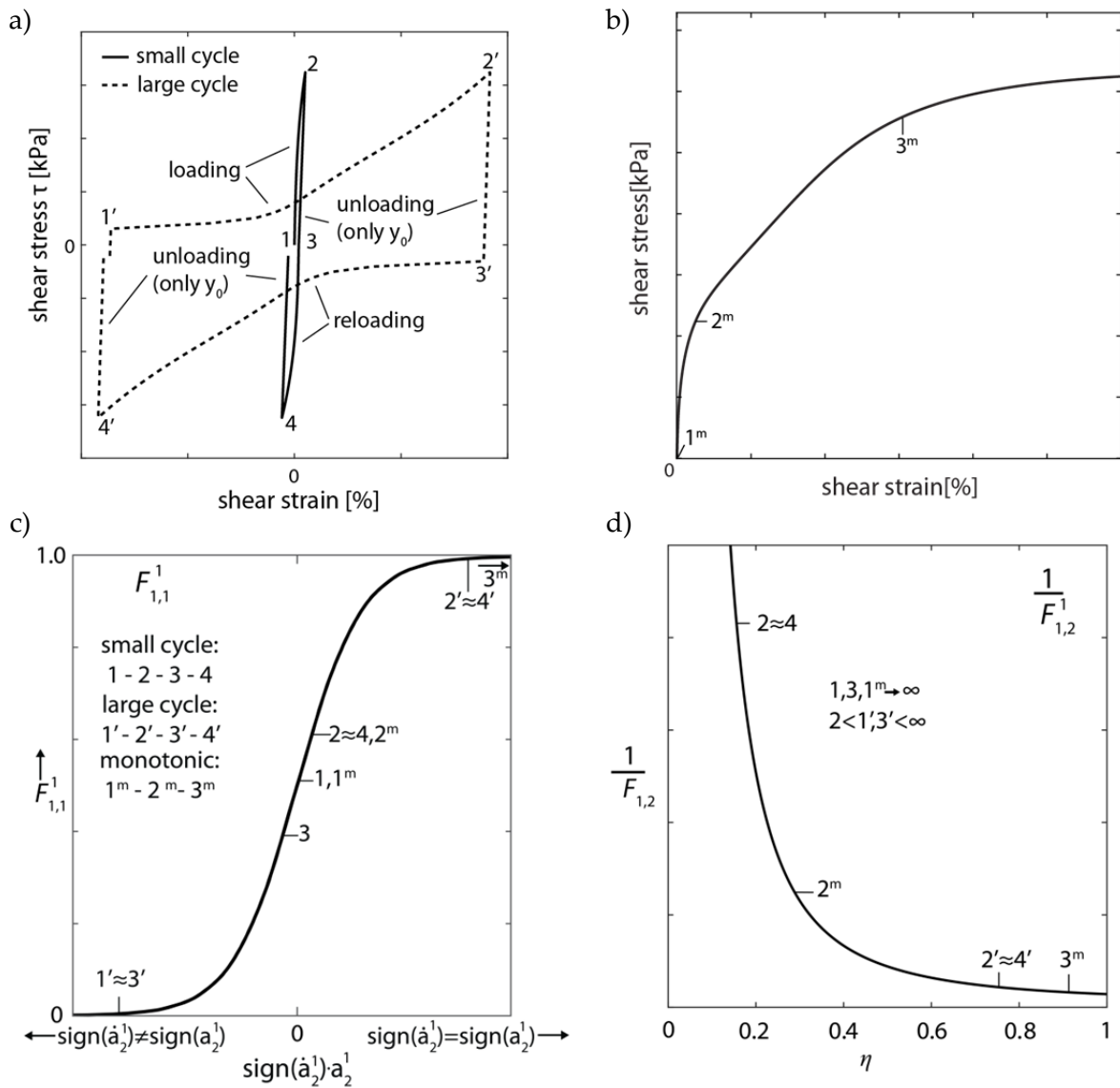
Figure 8-11: Simulations of the stress–strain development in cyclic and monotonic loading and development of the function $F_{1,1}^1$ and $F_{1,2}^1$ (points on the stress–strain plots match to points on the functional development of $F_{1,1}^1$ and $F_{1,2}^1$): a) small and large stress–strain cycles; b) stress–strain plot during monotonic loading; c) development of function $F_{1,1}^1$; d) development of function $F_{1,2}^1$

The volumetric behaviour while loading on y_1 is governed by the two dilation/contraction factors (β_1^1, β_2^1) in combination with the function F_2^1 (see (8-44)). The two dilation coefficients can be viewed as isotropic and anisotropic, since β_1^1 is solely dependent on the effective stress and β_2^1 is dependent on strain and strain rate and the corresponding directions.

$\boldsymbol{\beta_1^1}$ is always positive and multiplied with the absolute strain rate $|\dot{\alpha}_\gamma^1|$; thus it is isotropic and purely contracting. It is chosen to drop linearly with normalized effective stress $\left(\frac{\sigma}{\sigma_0}\right)$, i.e. contraction potential drops as the effective stress drops, with the Macaulay bracket $\langle\ldots\rangle$ ensuring that it can only be larger than or equal to zero:

$$\beta_1^1 = \langle\beta_{1,min}^1 + C_5 \cdot \frac{\sigma'}{\sigma_0'}\rangle \tag{8-80}$$

$\boldsymbol{\beta_2^1}$ is equal to the frictional hardening coefficients of the yield surface formulation y_1 with opposite signs, which ensures thermo-mechanic consistency (see Appendix III.1):

$$\beta_2^1 = \beta_{2,1}^1 + \beta_{2,2}^1 = -\left(\frac{M}{2}\right) \cdot L_1(C_1, a_1^1) - \left(\frac{M}{2}\right) \cdot L_1(C_1, a_2^1) \cdot \text{sign}(\dot{\alpha}_\gamma^1) \tag{8-81}$$

$$\beta_{2,1}^1 = -\mu_{iso} = -\left(\frac{M}{2}\right) \cdot L_1(C_1, a_1^1) \tag{8-82}$$

$$\beta_{2,2}^1 = -\mu_{kin} = -\left(\frac{M}{2}\right) \cdot L_1(C_1, a_2^1) \cdot \text{sign}(\dot{\alpha}_\gamma^1) \tag{8-83}$$

From (8-81) with (8-75), (8-76) and (8-44), it becomes clear that in this formulation:

$$\beta_2^1 \in]-M; 0[\tag{8-84}$$

Thus, the following properties of β_2^1 can be summarized:

(i)   In this formulation, β_2^1 is multiplied with the absolute strain rate $|\dot{\alpha}_\gamma^1|$ and remains always dilative, but the value of β_2^1 depends on the direction of loading.

(ii) As the material is sheared, β_2^1 grows negatively (dilation potential grows) since the dilation coefficient is equal to the negative value of the frictional hardening parameter of the yield surface y_1 $(-|\mu|)$ or the stress state $\left(-\left|\frac{\tau}{\sigma'}\right|\right)$ respectively:

$$\beta_2^1 = -|\mu| = -\left|\frac{\tau}{\sigma'}\right| \tag{8-85}$$

Since the influence of the dilative/contractive behaviour of the other yield surface y_0 is small, the behaviour will change from contractive to dilative whenever $|\beta_2^1|$ exceeds the value of β_1^1.

Consequently, if both β_1^1 and β_2^1, are interpreted as points in the stress space $\left(\sigma' - \frac{\tau}{\sigma'}\right)$, multiplying (8-80) with σ' results approximately in the function of the phase-transformation line, which in this model is not introduced explicitly:

$$\tau_{pt} = \beta_{1,min}^1 \cdot \sigma' + C_5 \cdot \frac{\sigma'^2}{\sigma_0'} \tag{8-86}$$

Figure 8-12 shows the position of the phase transformation line for a symmetric cyclic test and a monotonic test. Additionally, the position of the yield surface y_1 for two phase transformation points (t = 1, 2) is shown. Note that the contraction dilation behaviour in unloading and reloading inside y_1 is governed by y_0 and will be shown later.
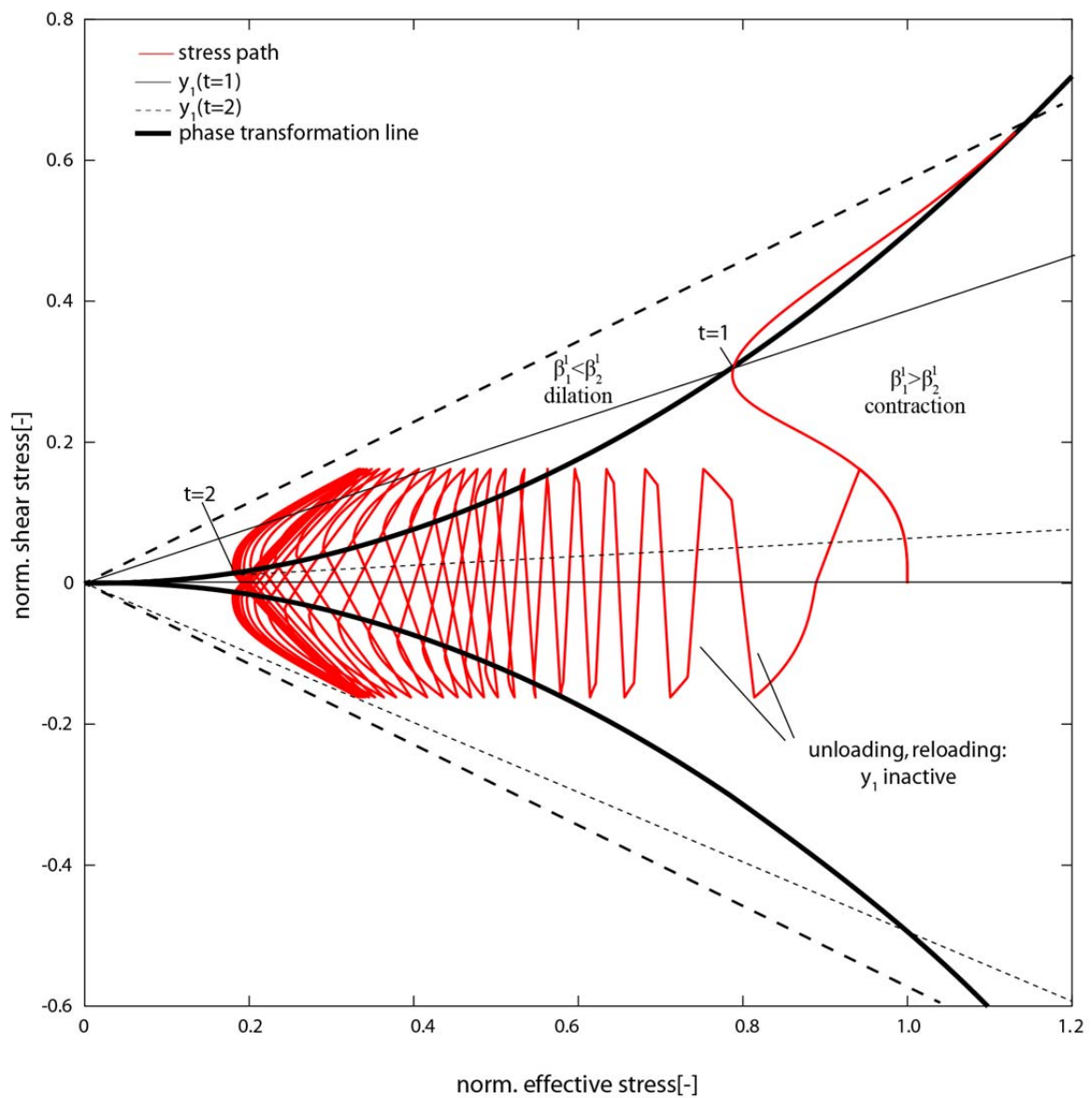
Figure 8-12: Normalized stress path $(\frac{\sigma'}{\sigma_0'} - \frac{\tau}{\sigma_0'})$ **for a cyclic and a monotonic test, and position of the phase transformation line.**

The function F_2^1 is given as:

$$F_2^1 = \frac{1}{L_2\left(C_2, \mathrm{a}_2^1 \cdot \mathrm{sign}(\dot{\mathrm{a}}_2^1)\right)} \cdot \left(\frac{\langle \sigma_0' + \sigma_{ref}' - \sigma'\rangle}{\sigma'} + 1\right) = \frac{1}{F_{1,1}^1} \cdot \left(\frac{\langle \sigma_0' + \sigma_{ref}' - \sigma'\rangle}{\sigma'} + 1\right) \tag{8-87}$$

$\boldsymbol{F_2^1}$ influences the shear-volumetric coupling to achieve the following effects:

(i)   As mentioned before, in large cycles the material almost entirely loses its stiffness during reloading (points 1' and 3', Figure 8-11c). But at the same time, no spike in pore pressure changes can be observed. This indicates that during this soft behaviour almost no volumetric coupling exists $\left(\dot{\alpha}_\varepsilon^1 = f(\beta_1^1, \beta_2^1, F_2^1) \cdot |\dot{\alpha}_\gamma^1|\right.$ with $\left. f(\beta_1^1, \beta_2^1, F_2^1) \to 0\right)$. This is achieved by using the reciprocal of $F_{1,1}^1$ from (8-78), causing F_2^1 to be large whenever $F_{1,1}^1$ is small, i.e. during the soft reloading stage in large cycles. This leads to a reduction of volumetric coupling, since

$$F_{1,1}^1 \to 0 \Leftrightarrow F_2^1 \to \infty \Leftrightarrow \left(\frac{\beta_1^1}{F_2^1}; \frac{\beta_2^1}{F_2^1}\right) \to 0 \tag{8-88}$$

(ii)   Cyclic tests indicate a dependency of dilation and contraction coefficients on the initial effective stress σ_0' which is reflected via the second term in (8-87), $\frac{\langle\sigma_0'+\sigma_{ref}'-\sigma'\rangle}{\sigma'} + 1$. The numerator reflects the influence of deviations of the initial effective stress σ_0' from the stress that has been used for the model calibration σ_{ref}'. Dependence on the reciprocal of the current effective normal stress captures the reduction of volumetric coupling if stress drops relative to the initial stress.

(iii) Additionally, to ensure thermo-mechanical consistency, it must be guaranteed that $F_2^1 \geq 1$. This condition is met since

$$\max(F_{1,1}^1) \to 1 \Leftrightarrow \min\left(\frac{1}{F_{1,1}^1}\right) \to 1 \tag{8-89}$$

and

$$\left(\frac{\langle\sigma_0' + \sigma_{ref}' - \sigma'\rangle}{\sigma'} + 1\right) \geq 1 \tag{8-90}$$

<u>Analysis of the functions governing y_0</u>

The second yield surface y_0 governs the material behaviour if the stress state is inside the cone formed by y_1.

The yield surface y_0 is composed again of two parts:

$$y_0 = 0 = \tau - \mu_1^0 + \sigma' \cdot \mu_2^0 = \tau - h_0 \cdot \alpha_\gamma^0 + \sigma' \cdot \beta_{2,1}^0 \tag{8-91}$$

$\mu_1^0 = h_0 \cdot \alpha_\gamma^0$ in (8-91) is a kinematic hardening term with constant hardening modulus h_0. The only additional feature here is that in the course of calibrating the model it has been recognized that having a fraction of h_0 dependent on the ratio of reference and initial stress $\left(\frac{\sigma_{ref}}{\sigma_0}\right)$ is advantageous:

$$h_0 = h_{0,1} + \frac{\sigma'_{ref}}{\sigma'_0} \cdot h_{0,2} \tag{8-92}$$

where the reference stress, σ_{ref}, is the stress at which calibration of the model is done.

$\mu_2^0 = \beta_{2,1}^0$ in (8-91) causes the yield surface to rotate in addition to the kinematic hardening depending on the development of $\beta_{2,1}^0$ which is necessary to ensure thermomechanical consistency. Figure 8-13 shows a monotonic loading stress path and the development of y_0. The intercept of the y_0 surfaces on the y-axis is given by the kinematic hardening term $h_0 \cdot \alpha_\gamma^0$, the inclination of the surface by $-\beta_{2,1}^0$.
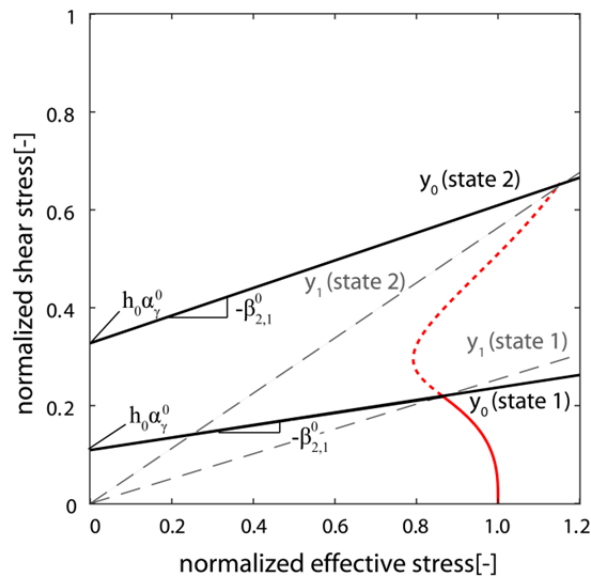
Figure 8-13: Stress path for monotonic test with development of yield surface y_0 (and y_1 as dashed line for comparison)

The volumetric behaviour is controlled by two dilation/contraction parameters:

$$\beta_1^0 = |\mu_{kin}| \cdot \left(1 - L_2(C_2, |\alpha_2^1|)\right) + \beta_{1,3}^0 = \beta_{1,1}^0 \cdot \beta_{1,2}^0 + \beta_{1,3}^0$$

(8-93)

with $\beta_{1,3}^0 > 0$

$$\beta_2^0 = \beta_{2,1}^0 + \beta_{2,2}^0 = -\mu_{kin} - \mu_{kin} \cdot \left(C_4^0 \cdot L_1(C_3, |a_1^0|) \cdot \langle -\dot{\alpha}_\gamma^0 \cdot \alpha_\gamma^1 \rangle^0\right) =$$

$$= \mu_{kin} \cdot \left(\left(C_4^0 \cdot L_1(C_3, a_2^0)\right) \cdot \frac{\text{sign}(\dot{\alpha}_\gamma^0 \cdot \alpha_\gamma^1) - 1}{2} - 1 \right)$$

(8-94)

$\boldsymbol{\beta_1^0}$ has the following properties:

(i) It always remains positive, multiplied with $|\dot{\alpha}_\gamma^0|$, and is independent of the direction of rates; thus it is isotropic and purely causes contraction.

(ii) The first part $(\beta_{1,1}^0)$ corresponds to the absolute value of the kinematic part of y_1, $|\mu_{kin}|$. The formulation is chosen to cause the contraction factor to decrease and increase with kinematic hardening of yield surface y_1.

(iii) From (8-93), it can be seen that the second part of equation (8-93), $\beta_{1,2}^0$, is similar to the numerator from (8-78). It causes the contraction coefficient to decrease if the material is sheared largely in one direction only, e.g. in tests with static shear stress (i.e. asymmetric tests), when plastic shear strains α_γ^1 are accumulated in one direction only.

(iv) The last part of (8-93), $\beta_{1,3}^0 = const > 0$, allows a residual contraction potential that always remains.

$\boldsymbol{\beta_2^0}$ is constructed from two parts $(\beta_{2,1}^0$ and $\beta_{2,2}^0)$. Both parts are linked to the kinematic hardening part of the yield function y_1 (μ_{kin}).

β_2^0 has the following properties:

(i) β_2^0 is multiplied with $\dot{\alpha}_\gamma^0$ and its sign depends on the state of μ_{kin}, and thus it can be contractive or dilative. It induces anisotropy since it depends on the direction of the strain rate. The contraction and dilation potential decreases and increases with the kinematic hardening state of y_1.

(ii) This formulation allows dilative and contractive behaviour even if the stress state is inside y_1. Thermo-mechanical consistency requires $\beta_{2,1}^0$ to also appear in the formulation of the yield surface y_0 (8-91).

(iii) The second part of the formulation (8-94), $\beta_{2,2}^0$, allows having different values for $\dot{\beta}_2^0$ during contraction or dilation: whereas in dilation the coefficient is thermo-

mechanically limited to an ultimate value of $\left|\beta_2^0\right| = \left|\beta_{2,1}^0\right|$, during contraction it can take higher values. The term inside the Macaulay brackets ensures that if and only if the rate of shear strains $\dot{\alpha}_\gamma^0$ is opposite to the accumulated plastic shear strains α_γ^1, i.e. in contraction, the absolute value of the factor is increased by $\left|\beta_{2,2}^0\right|$ (see Figure 8-14b):

$$\dot{\alpha}_\gamma^0 \neq \alpha_\gamma^1 \rightarrow \langle -\dot{\alpha}_\gamma^0 \cdot \alpha_\gamma^1 \rangle^0 = 1 \rightarrow \beta_2^0 = -\mu_{kin} - \mu_{kin} \cdot \left(C_4^0 \cdot L_1(C_3, a_1^0) \right) \qquad (8\text{-}95)$$

$$\dot{\alpha}_\gamma^0 = \alpha_\gamma^1 \rightarrow \langle -\dot{\alpha}_\gamma^0 \cdot \alpha_\gamma^1 \rangle^0 = 0 \rightarrow \beta_2^0 = -\mu_{kin} \qquad (8\text{-}96)$$

(iv)   The increase in contraction potential $\beta_{2,2}^0$ is controlled via the step function $L_1(C_3, a_1^0)$ in (8-94) that depends on the internal variable a_1^0. This variable is linked to the accumulation of negative volumetric strains of y_1 (i.e. a_1^0 grows with dilative volumetric strains, $\dot{\alpha}_\varepsilon^1 < 0$). The growth of a_1^0 is specified via the constraint C_3^0:

$$C_3^0 = 0 = \dot{a}_1^0 - F_1^0 =$$
$$= \dot{a}_1^0 - \left(1 - L_2 \left(C_3, a_2^1 \cdot \text{sign}(\dot{a}_2^1) \right) \right) \cdot \frac{(|\dot{\alpha}_\varepsilon^1| - \dot{\alpha}_\varepsilon^1)}{2} = \dot{a}_1^0 - \left(1 - F_{1,1}^1 \right) \cdot \langle -\dot{\alpha}_\varepsilon^1 \rangle^0 \qquad (8\text{-}97)$$

C_3^0 ensures that a_1^0 only grows with accumulating dilation $\dot{\alpha}_\varepsilon^1 < 0$. The physical interpretation of this formulation is that dilative behaviour of y_1 produces new contraction potential of y_0.

(v)   The rate of accumulation of additional contraction potential (8-97) depends on the direction of shearing and the accumulated shear strain α_γ^1 via the function $F_{1,1}^1$ and internal variable a_2^1 (see (8-97)). This means that if shearing in only one direction occurs, e.g. in tests with static shear stress (i.e. asymmetric tests), when plastic shear strains α_γ^1 are accumulated in one direction only, the rate at which additional contraction potential is built up is smaller than it would be when a reversal of strains α_γ^1 occurs.
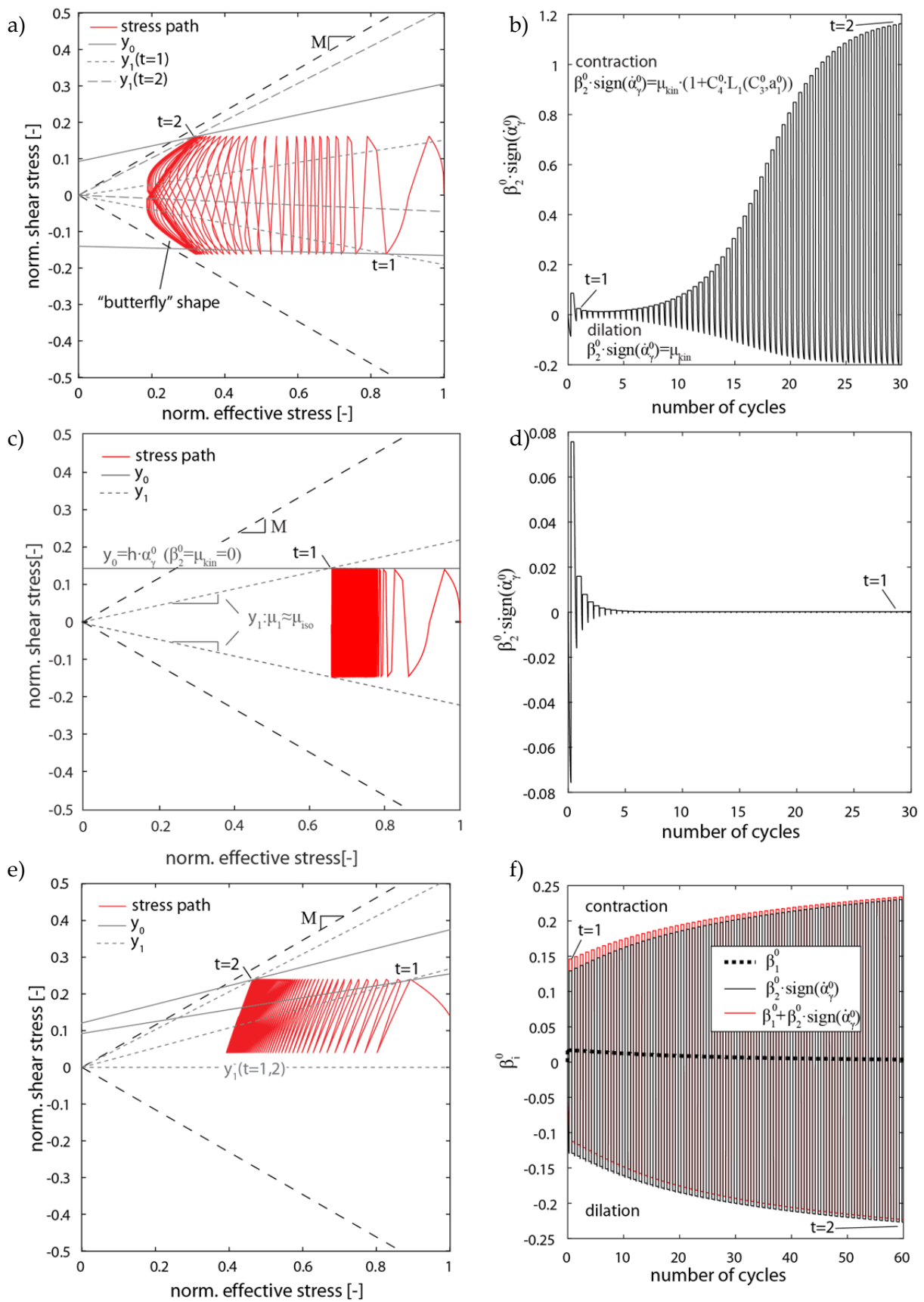
Figure 8-14: a) Normalized stress path for symmetric cyclic loading; **b)** development of β_2^0 in symmetric cyclic loading; **c)** Normalized stress path in symmetric cyclic loading with small amplitude; **d)** development of β_2^0 in symmetric cyclic loading with small amplitude; **e)** Normalized stress path in asymmetric cyclic loading (= loading with static shear stress); **f)** development of β_1^0 and β_2^0 in asymmetric cyclic loading

Figure 8-14 shows the effects of the properties of β_1^0 and β_2^0 for different stress paths. β_1^0 has little influence on symmetric tests and is not shown in Figure 8-14a, b, c and d for these tests. But it allows better reproduction of asymmetric tests (see Figure 8-14e and f).

In symmetric tests, since β_2^0 is coupled to μ_{kin} (compare property (i) in the description of β_2^0) and since the kinematic part of y_1 decreases in early cycles ($\mu_{kin} \rightarrow 0$), also β_2^0 decreases. In later cycles when the kinematic part increases ($\mu_{kin} > 0$) it increases again. Additionally, dilative behaviour of y_1 ($\dot{\alpha}_\varepsilon^1 < 0$) causes the contraction potential of β_2^0 to increase to a larger value than the dilation potential (compare property (ii) and (iii) of β_2^0; see point $t = 2$ in Figure 8-14a and b). This property allows us to reproduce the high rates of excess pore pressure development during unloading in cycles at low effective stresses which, in combination with dilation of y_1, causes the so-called "butterfly shape" (see Figure 8-14a).

In symmetric tests with small amplitudes (see Figure 8-14c and d), the drop in $|\mu_{kin}|$ and thus also in β_2^0 (and β_1^0) causes the rate of excess pore pressure development to drop almost to zero. This prevents the stress state from moving further to the left, and y_1 is not activated again, so μ_{kin} and β_2^0 cannot grow any more. This produces what is called "shakedown".

In asymmetric tests, i.e. tests with static shear stress ($\tau_0 \neq 0$), property (i) in the description of β_2^0 allows us to have contraction during unloading and dilation during reloading (see Figure 8-14e). In Figure 8-14f $\beta_2^0 \cdot \text{sign}(\dot{\alpha}_\gamma^0)$ is shown, where positive values correspond to contractive unloading $\left(\text{sign}(\dot{\alpha}_\gamma^0) \neq \text{sign}(\mu_{kin}) \right)$ and negative values to dilative reloading $\left(\text{sign}(\dot{\alpha}_\gamma^0) = \text{sign}(\mu_{kin}) \right)$. Additionally, β_1^0 causes the contraction/dilation behaviour in asymmetric tests to be slightly biased in the beginning towards contraction (properties (i) and (ii) in the description of β_1^0; see Figure 8-14f). Without this bias, the stress path would be identical in loading and unloading, and no excess pore pressure could develop after the initial loading.

Also, tests indicate that this bias towards contraction is reduced as the number of cycles grows, i.e. the development of remaining excess pore water pressure slows down. This is achieved via property (iii) in the description of β_1^0, which decreases the contraction potential, and property (iv) in the description of β_2^0, which causes the rate at which the contraction potential grows to drop towards zero.

8.3.7 Incremental response

The incremental response can be derived similarly to 8.2.6 for different kind of loadings.

Monotonic (initial) loading

First, monotonic loading will be analysed; this loading also describes the behaviour until the first load reversal in cyclic loading is reached. From the formulation of y_1, it can be shown that in monotonic loading

$$\dot{a}_1^1 = \dot{a}_2^1 \tag{8-98}$$

$$a_1^1 = a_2^1 \tag{8-99}$$

Thus, considering that $\text{sign}(\dot{\alpha}_\gamma^1) = \text{sign}(\dot{a}_2^1)$, y_1 becomes

$$y_1 = 0 = \pm\tau \mp M \cdot L_1(C_1, a_1^1) \cdot \sigma = \pm\tau \mp M \cdot L_1(C_1, a_2^1) \cdot \sigma \tag{8-100}$$

therefore

$$\frac{\tau}{M \cdot \sigma} = \eta = L_1(C_1, a_2^1) = \tanh(C_1 \cdot a_1^1) = \tanh(C_1 \cdot a_2^1) \tag{8-101}$$

and

$$a_1^1 = a_2^1 = \frac{\text{atanh}(\eta)}{C_1} \tag{8-102}$$

For surface y_0, it can be shown that during monotonic loading

$$\beta_{2,1}^0 = \mu_{\text{kin}} = \frac{\tau}{2 \cdot \sigma'} \tag{8-103}$$

Also, during analysis of the model, the special case of $C_2 = 2 \cdot C_1$ has been shown to be capable of reproducing the available data (Donahue, 2007) reasonably well. For simplification, the parameter $\beta_{1,3}^0$ can be neglected during monotonic loading. With these conditions, the incremental response during monotonic loading is given as:

$$
\begin{bmatrix} \dot{\varepsilon} \\ \dot{\gamma} \end{bmatrix} = \left[\begin{array}{c} \dfrac{\kappa}{(1+e_0) \cdot \sigma} - \dfrac{\left(-M \cdot \eta^2 + \eta \cdot \left(\beta_{1,min}^1 + m \cdot \frac{\sigma}{\sigma_0}\right)\right) \cdot (1 - \text{sech}(\eta))}{C_1 \cdot (\sigma_0 + \sigma_{ref}) \cdot (1 - \eta^2)} \\ -\dfrac{(1+\eta^2) \cdot (1 - \text{sech}(\eta)) \cdot 2 \cdot \eta}{C_1 \cdot \sigma \cdot (1 - \eta^2) \cdot (1+\eta)^2} \end{array} \right.
$$

$$
\left. \begin{array}{c} \dfrac{\left(-M \cdot \eta + \left(\beta_{1,min}^1 + m \cdot \frac{\sigma}{\sigma_0}\right)\right) \cdot (1 - \text{sech}(\eta))}{M \cdot C_1 \cdot (\sigma_0 + \sigma_{ref}) \cdot (1 - \eta^2)} - \dfrac{M \cdot \eta}{8 \cdot h_0} \cdot \left(\dfrac{(1+\eta)^2}{1+\eta^2}\right) \\ \dfrac{2 \cdot (1+\eta^2) \cdot (1 - \text{sech}(\eta))}{M \cdot C_1 \cdot \sigma \cdot (1+\eta)^2 \cdot (1-\eta^2)} + \dfrac{1}{2 \cdot h_0} \end{array} \right] \begin{bmatrix} \dot{\sigma}' \\ \dot{\tau} \end{bmatrix}
\tag{8-104}
$$

Unloading

During unloading, only surface y_0 is active. The contraction parameters are given in (8-93) and (8-94). Noting that $\text{sign}(\dot{\alpha}_{\gamma 0}) = \text{sign}(\dot{\tau})$, the incremental response can be derived.

If surface y_1 has not yet dilated:

$$
\begin{bmatrix} \dot{\varepsilon} \\ \dot{\gamma} \end{bmatrix} = \left[\begin{array}{c} -\dfrac{M^2}{8 \cdot h_0} \cdot \tanh^2(C_1 \cdot a_2^1) \cdot (\text{sign}(\dot{\tau}) \cdot \text{sign}(a_2^1) - 2 - \text{sign}(\dot{\tau}) \cdot \tanh(2 \cdot C_1 \cdot a_2^1)) \\[2mm] -\dfrac{M}{2 \cdot h_0} \cdot \tanh(C_1 \cdot a_2^1) \\[4mm] \dfrac{M}{4 \cdot h_0} \cdot \tanh(C_1 \cdot a_2^1) \cdot (\text{sign}(\dot{\tau}) \cdot \text{sign}(a_2^1) - 2 - \text{sign}(\dot{\tau}) \cdot \tanh(2 \cdot C_1 \cdot a_2^1)) \\[2mm] \dfrac{1}{h_0} \end{array} \right] \begin{bmatrix} \dot{\sigma}' \\ \dot{\tau} \end{bmatrix}
$$

(8-105)

In the case that

(i)   surface y_1 has caused negative plastic volumetric strains (dilation, $\dot{\alpha}_\varepsilon^1 < 0$) and

(ii) $\langle -\dot{\alpha}_\gamma^0 \cdot \alpha_\gamma^1 \rangle^0 = 1$

the incremental response in unloading is changed to

$$
\begin{bmatrix} \dot{\varepsilon} \\ \dot{\gamma} \end{bmatrix} = \left[\begin{array}{c} -\dfrac{M^2}{8 \cdot h_0} \cdot \tanh^2(C_1 \cdot a_2^1) \cdot (\text{sign}(\dot{\tau}) \cdot \text{sign}(a_2^1) - 2 - \text{sign}(\dot{\tau}) \cdot \tanh(2 \cdot C_1 \cdot a_2^1) + 2 \cdot C_4 \cdot \tanh(C_3 \cdot a_1^0)) \\[2mm] -\dfrac{M}{2 \cdot h_0} \cdot \tanh(C_1 \cdot a_2^1) \\[4mm] \dfrac{M}{4 \cdot h_0} \cdot \tanh(C_1 \cdot a_2^1) \cdot (\text{sign}(\dot{\tau}) \cdot \text{sign}(a_2^1) - 2 - \text{sign}(\dot{\tau}) \cdot \tanh(2 \cdot C_1 \cdot a_2^1) + 2 \cdot C_4 \cdot \tanh(C_3 \cdot a_1^0)) \\[2mm] \dfrac{1}{h_0} \end{array} \right] \begin{bmatrix} \dot{\sigma}' \\ \dot{\tau} \end{bmatrix}
$$

(8-106)

where a_1^0 given by integration of constraint C_3^0, (8-97).

<u>Reloading</u>

In reloading (y_1 and y_0 active), the simplifications (8-98) , (8-99) and (8-103) are no longer valid. The response therefore cannot be formulated in a compact form like (8-104) and is given here in the most general form:

$$\begin{bmatrix} \dot{\varepsilon} \\ \dot{\gamma} \end{bmatrix} = \begin{bmatrix} K_{1,1} + K_{1,2} & K_{2,1} + K_{2,2} \\ K_{3,1} + K_{3,2} & K_{4,1} + K_{4,2} \end{bmatrix} \begin{bmatrix} \dot{\sigma} \\ \dot{\tau} \end{bmatrix} \tag{8-107}$$

with

$$K_{1,1} = \frac{\kappa}{(1+e_0)\cdot\sigma} + \left(\frac{\beta_1^1}{F_2^1}\cdot\text{sign}(\dot{\alpha}_\gamma^1) + \frac{\beta_2^1}{F_2^1} \right)\cdot K_{3,1} =$$

$$= \frac{\kappa}{(1+e_0)\cdot\sigma} + \frac{\left(\langle\beta_{1,min}^1 + m\cdot\frac{\sigma}{\sigma_0}\rangle^0 \cdot \text{sign}(\dot{\alpha}_\gamma^1) - \left(\frac{M}{2}\right)\cdot\left(\tanh(C_1\cdot a_1^1)\cdot\text{sign}(\dot{\alpha}_\gamma^1) + \tanh(C_1\cdot a_2^1) \right) \right)}{\dfrac{2}{1+\tanh(C_2\cdot a_2^1\cdot\text{sign}(\dot{a}_2^1))}\cdot\left(\dfrac{\langle\sigma_0 + \sigma_{ref} - \sigma\rangle}{\sigma} + 1 \right)}\cdot K_{3,1} \tag{8-108}$$

$$K_{1,2} = (\beta_1^0 + \beta_2^0)\cdot K_{3,2} =$$

$$= \left(\frac{M}{4}\tanh(C_1\cdot a_2^1)\cdot\left(\text{sign}(\dot{\tau})\cdot\text{sign}(a_2^1) - 2 \right.\right.$$

$$\left.\left. - \text{sign}(\dot{\tau})\tanh(2\cdot C_1\cdot a_2^1) + 2\cdot C_4\cdot\tanh(C_3\cdot a_1^0)\cdot\langle-\dot{\alpha}_\gamma^0\cdot\alpha_\gamma^1\rangle^0 \right) \right)\cdot K_{3,2} \tag{8-109}$$

$$K_{2,1} = \left(\frac{\beta_1^1}{F_2^1} + \frac{\beta_2^1}{F_2^1} \right)\cdot K_{4,1} =$$

$$= \frac{\left(\langle\beta_{1,min}^1 + m\cdot\frac{\sigma}{\sigma_0}\rangle^0 \cdot \text{sign}(\alpha_\gamma^1) - \left(\frac{M}{2}\right)\cdot L_1(C_1, a_1^1)\cdot\text{sign}(\dot{\alpha}_\gamma^1) - \left(\frac{M}{2}\right)\cdot L_1(C_1, a_2^1) \right)}{\dfrac{2}{1+\tanh(C_2\cdot a_2^1\cdot\text{sign}(\dot{a}_2^1))}\cdot\left(\dfrac{\langle\sigma_0 + \sigma_{ref} - \sigma\rangle}{\sigma} + 1 \right)}\cdot K_{4,1} \tag{8-110}$$

$$K_{2,2} = (\beta_1^0 + \beta_2^0)\cdot K_{4,2} =$$

$$= \left(-\frac{M}{4}\cdot\tanh(C_1\cdot a_2^1)\cdot\left(\text{sign}(\dot{\tau})\cdot\text{sign}(a_2^1) - 2 \right.\right.$$

$$\left.\left. - \text{sign}(\dot{\tau})\tanh(2\cdot C_1\cdot a_2^1) + 2\cdot C_4\cdot\tanh(C_3\cdot a_1^0)\cdot\langle-\dot{\alpha}_\gamma^0\cdot\alpha_\gamma^1\rangle^0 \right) \right)\cdot K_{4,2} \tag{8-111}$$

$$K_{3,1} = -\frac{M}{2}\cdot\left(\frac{\tanh(C_1\cdot a_1^1)\cdot\text{sign}(\dot{\alpha}_\gamma^1) + \tanh(C_1\cdot a_2^1)}{1 + \frac{M}{2}\cdot\sigma\cdot C_1\cdot\dfrac{1+\tanh\left(2\cdot C_1\cdot a_2^1\cdot\text{sign}(\dot{\alpha}_\gamma^1)\right)}{2\cdot(1-\text{sech}(\eta))}\cdot(\text{sech}^2(C_1\cdot a_1^1) + \text{sech}^2(C_1\cdot a_2^1))} \right) \tag{8-112}$$

$$K_{3,2} = -\frac{M}{2\cdot h_0}\cdot\tanh(C_1\cdot a_2^1) - \frac{M\cdot C_1\cdot\sigma}{2\cdot h_0}\cdot\text{sech}^2(C_1\cdot a_2^1)\cdot\frac{1+\tanh\left(2\cdot C_1\cdot a_2^1\cdot\text{sign}(\dot{\alpha}_\gamma^1)\right)}{2\cdot(1-\text{sech}(\eta))}\cdot K_{3,1} \tag{8-113}$$

$$K_{4,1} = \left(\frac{1}{1 + \frac{M}{2}\cdot\sigma\cdot C_1\cdot\dfrac{1+\tanh\left(C_2\cdot a_2^1\cdot\text{sign}(\dot{\alpha}_\gamma^1)\right)}{2\cdot(1-\text{sech}(\eta))}\cdot(\text{sech}^2(C_1\cdot a_1^1) + \text{sech}^2(C_1\cdot a_2^1))} \right) \tag{8-114}$$

$$K_{4,2} = \frac{1}{h_0} - \frac{M\cdot C_1\cdot\sigma}{2\cdot h_0}\cdot\text{sech}^2(C_1\cdot a_2^1)\cdot\frac{1+\tanh\left(C_2\cdot a_2^1\cdot\text{sign}(\dot{\alpha}_\gamma^1)\right)}{2\cdot(1-\text{sech}(\eta))}\cdot K_{4,1} \tag{8-115}$$

where a_1^0, a_1^1, a_2^1 must be derived from integration of constraints C_3^0, C_2^1 and C_3^1.

8.3.8 Derivation of model parameters

The model's parameters can be derived from monotonic and cyclic simple shear tests, as shown in the following section.

The pressure-dependent bulk modulus (κ) can be derived from oedometer tests:

$$\kappa = \frac{C_s}{\ln(10)} \tag{8-116}$$

The strength of the material in plane strain conditions (M) can be found from monotonic or cyclic simple shear tests as the ultimate observed stress ratio $\frac{\tau}{\sigma'}$.

The linear hardening modulus (h_0) can be estimated from an unloading path after monotonic loading, e.g. the first unloading stage in a cyclic test, since the stress–strain relation is governed solely by the hardening modulus or from cyclic tests with small amplitudes where the kinematic linear hardening of y_0 dominates as well (Figure 8-15):

$$\frac{\Delta\tau}{\Delta\gamma} = h_0 \tag{8-117}$$
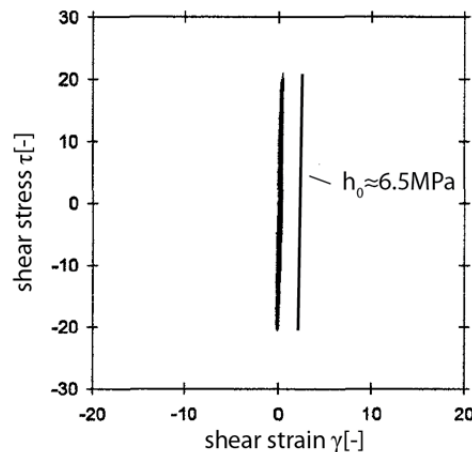
Figure 8-15: Deriving the hardening modulus h_0 from small cycles. Test A5 reproduced from Donahue (2007)

The free parameters C_1 and, in the more general case $(C_2 \neq 2 \cdot C_1)$, also the parameter C_2 can be found from an undrained monotonic stress–strain path, displayed in terms of $\gamma - \eta$.

The incremental response (8-104) can be reformulated to

$$\dot{\gamma} - \frac{\dot{\tau}}{2 \cdot h_0} = \frac{2 \cdot (1 + \eta^2) \cdot (1 - \operatorname{sech}(\eta))}{C_1 \cdot (1 - \eta^2) \cdot (1 + \eta^2)} \cdot \left(-\frac{\dot{\sigma} \cdot \tau}{\sigma^2} + \frac{\dot{\tau} \cdot \sigma}{\sigma^2} \right) = \frac{(1 + \eta^2) \cdot (1 - \operatorname{sech}(\eta))}{C_1 \cdot (1 - \eta^2) \cdot (1 + \eta^2)} \cdot \dot{\eta} \quad (8\text{-}118)$$

$$\gamma - \frac{\tau}{2 \cdot h_0} = \alpha_\gamma^1 = \int_0^{\eta^*} \frac{2 \cdot (1 + \eta^2) \cdot (1 - \operatorname{sech}(\eta))}{C_1 \cdot (1 - \eta^2) \cdot (1 + \eta^2)} \cdot d\eta \quad (8\text{-}119)$$

The integral (8-119) has to be solved numerically and allows the parameter C_1 to be found by fitting the test data in $\alpha_\gamma^1 - \eta$ space, provided h_0 and M have been found previously (since the influence of y_0 is negligible, it is also possible to use $\gamma - \eta$ space):
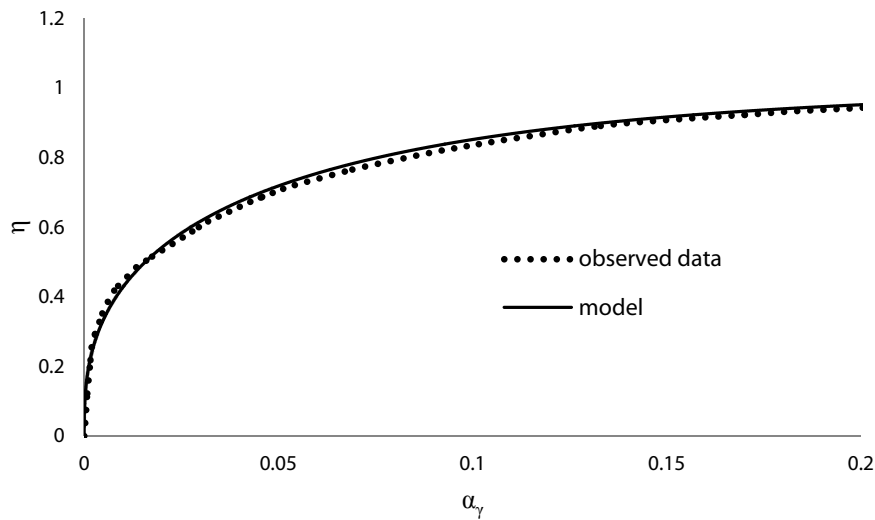
Figure 8-16: Fit of function (8-119) to data on η and γ from a monotonic DSS test. Data reproduced for test A3 from Donahue (2007)

The parameters (C_5 and $\beta_{1,min}^1$) of the linear function controlling the isotropic contraction behaviour of y_1 (8-80) can be found by analysing the turning points (change from contractive to dilative behaviour) of cyclic and monotonic tests.

Figure 8-17a,b and c show the fitting procedure for the function (8-80) using three points taken from a cyclic and a monotonic test. Herein, only the most characteristic points from the tests are used. These are the points at which minimum effective stress is reached (P_1 in butterfly shape), the point where behaviour changes from contractive to dilative in monotonic loading (P_2) and the point where failure is reached (P_3, when behaviour would become contractive again). A linear fit to the data in Figure 8-17c allows one to find the parameters $\beta_{1,min}^1$ and C_5 of function (8-80).
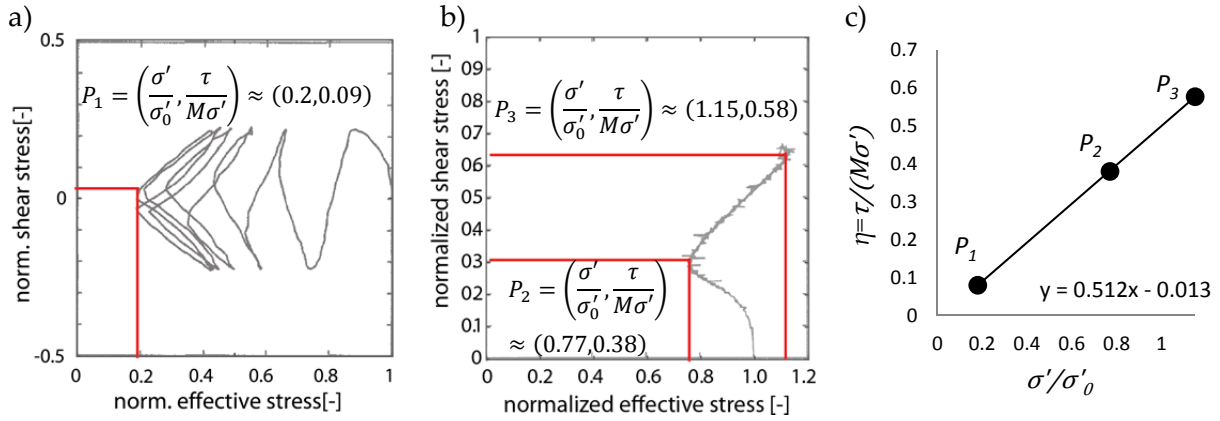
Figure 8-17: Fitting procedure of function (8-80). Tests A11 and A3 reproduced from Donahue (2007). a) Identification of the "butterfly" point in a cyclic test; b) identification of the turning points in a monotonic test; c) plot of all three points in a $\frac{\tau}{\sigma} - \frac{\sigma}{\sigma_0}$ plot and linear fit

The free parameter C_4 can be approximated using the unloading stress path during cycles at low effective stresses (butterfly behaviour) as shown in Figure 8-18, after having derived the previously mentioned parameters.
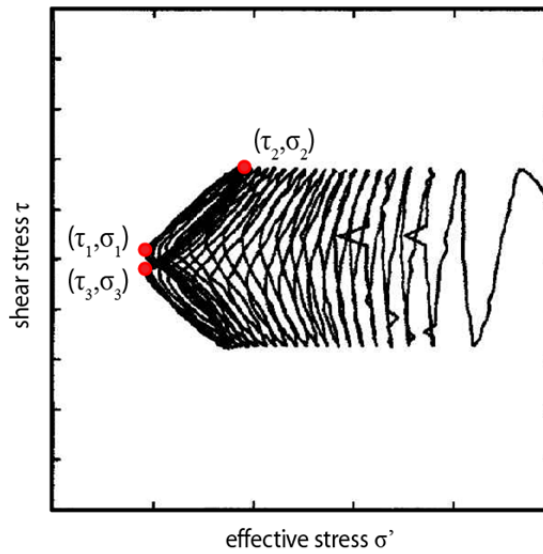
Figure 8-18: Points of the "butterfly" behaviour that allow parameter C_4 to be found. Test A7 reproduced from Donahue (2007)

Once the behaviour has stabilized and the stress path takes approximately the same course in each cycle, the loading unloading sequence $(\sigma_1', \tau_1) \rightarrow (\sigma_2', \tau_2) \rightarrow (\sigma_3', \tau_3)$ can be approximated with linear functions to be used for the estimation of C_4:

$$C_4 \approx \frac{-\frac{\kappa}{1+e_0} \cdot \ln\left(\frac{\sigma_3'}{\sigma_2'}\right) \cdot h_0}{|\eta_2 - 0.5| \cdot M \cdot \left((\tau_3 - \tau_2) - (\sigma_3' - \sigma_2')\right)} \tag{8-120}$$

The derivation of (8-120) can be found in Appendix III.2.

The **free parameter** C_3 can be found by simulations of undrained tests and calibrating C_3 such that the model allows one to reproduce the development of excess pore pressure with increasing number of cycles.

The **parameter** $\beta_{1,3}^0$ can be found from simulations of undrained tests with small amplitude (shakedown) and controls the residual increase of excess pore pressures.

The parameters derived for the data from Donahue (2007) are given in Table 8-2:

Parameter		Value	Unit
From oedometer test			
C_s	swelling index for pressure-dependent bulk modulus	0.025	[-]
e_0	void ratio at onset of loading	0.66–0.74	[-]
From first unloading or small cycles			
h_0	y_0 hardening parameter	6500	[kPa]
From monotonic loading			
M	strength of material	0.577	[-]
C_1	y_1 hardening parameter	1.8	[-]
C_2	y_1 hardening parameter	3.6	[-]
From cyclic test			
C_3	parameter to control the rate of contraction potential increase	150	[-]
C_4	parameter to control the maximum additional contraction potential	5.0	[-]
$\beta_{1,3}^0$	parameter to control the residual contraction potential at small cycles	0.0004	[-]
From tests at varying effective stress			
h_{ref}	stress-dependent fraction of h_0	4500	[kPa]
From turning points			
C_5	rate of isotropic contraction potential decrease	0.512	[-]
$\beta_{1,min}^1$	minimum isotropic contraction potential	-0.0128	[-]

Table 8-2: Overview of model parameters for soils "A" from Donahue (2007)

8.3.9   Model performance in comparison with experimental data

With the parameters derived in the previous section, different kinds of tests can be simulated and compared to the data from Donahue (2007). In order to ease the comparison, the data has been taken from the figures provided by Donahue (2007) and is shown as grey lines in the background of plots generated using the model.

Monotonic tests:

a)

b)
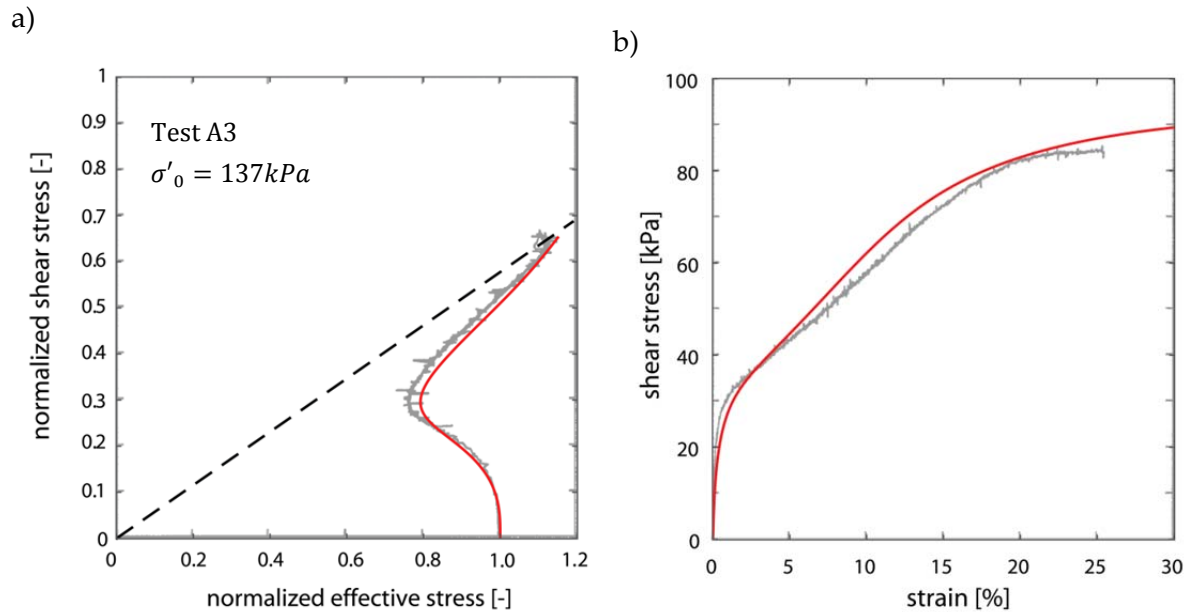
Figure 8-19: Comparison of a simulated monotonic strain-controlled DSS-test (red line) and experimental data reproduced from Donahue (2007): a) stress path; b) stress–strain behaviour

As can be seen from Figure 8-19, the model is capable of capturing the observed phenomena during a monotonic test remarkably well. Both the stress path and the stress–strain behaviour can be reproduced, including all stages of evolution.

Symmetrical cyclic tests with different amplitude:
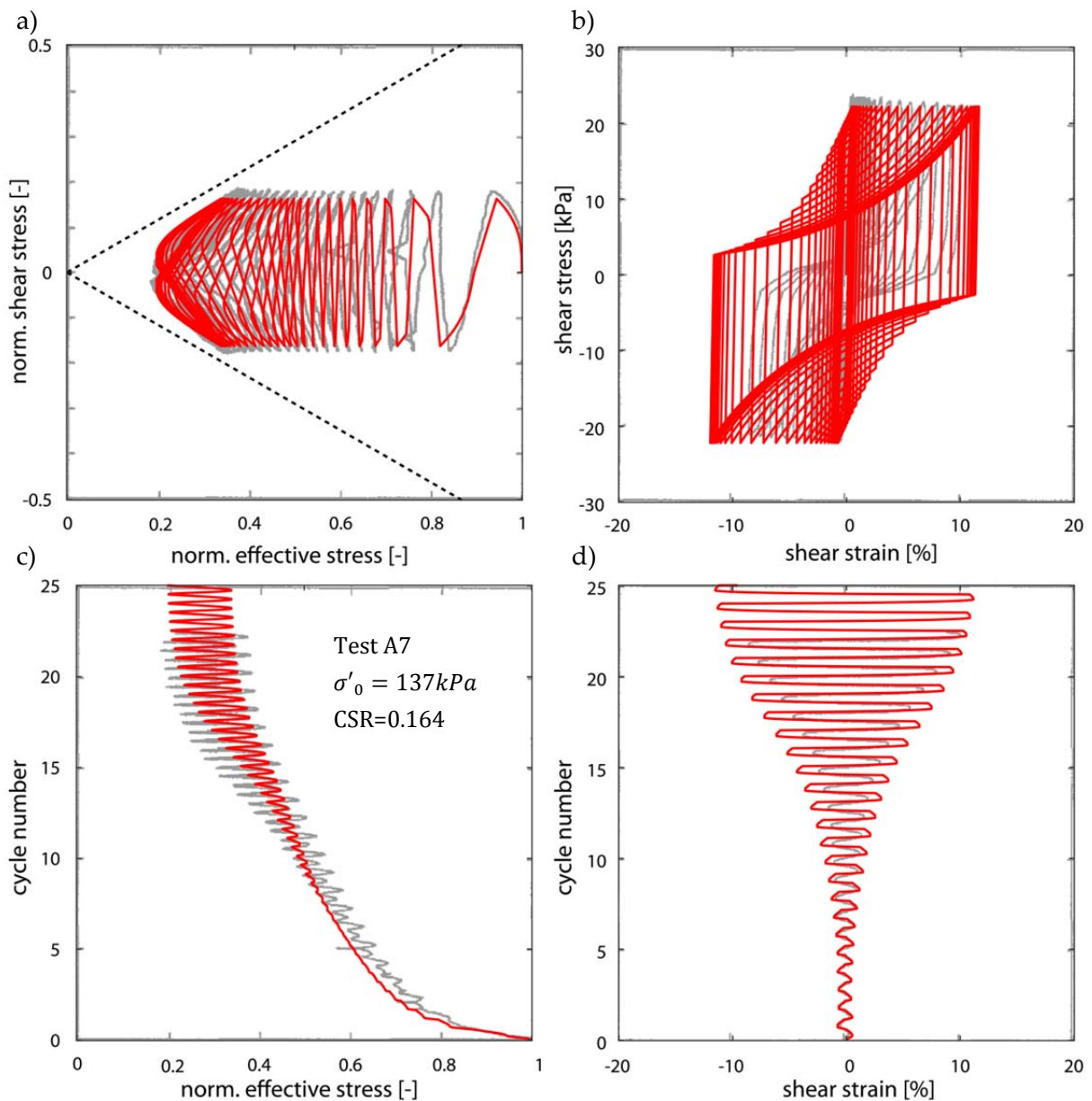
Figure 8-20: Comparison of a simulated stress-controlled cyclic test for CSR = 0.162 (red line) and experimental data for Test A7 reproduced from Donahue (2007): a) stress path; b) stress–strain behaviour; c) effective stress to number of cycles; d) evolution of strain per cycle

Figure 8-20 shows the cyclic test that has mainly been used for the calibration of the model. In Figure 8-20a) the stress path is shown; as can be seen, the model can capture the development of stress quite well, including the fast build-up of excess pore pressure in initial cycles and the butterfly shape in late cycles.

The development of the effective stress with cycles can be reproduced well (see Figure 8-20c). In terms of strains, one can see the change from small strain to large strain cycles. The model allows reproducing the shape of the observed large strain cycles almost exactly; thus, dissipation is only slightly overestimated (see Figure 8-20b). In terms of strain development,

one can again see that the overall increase of strains (softening) with number of cycles is reproduced well (Figure 8-20d). Only the rapidity with which the shape of the stress–strain cycles changes from small strain to the large strain cycles cannot be captured entirely.
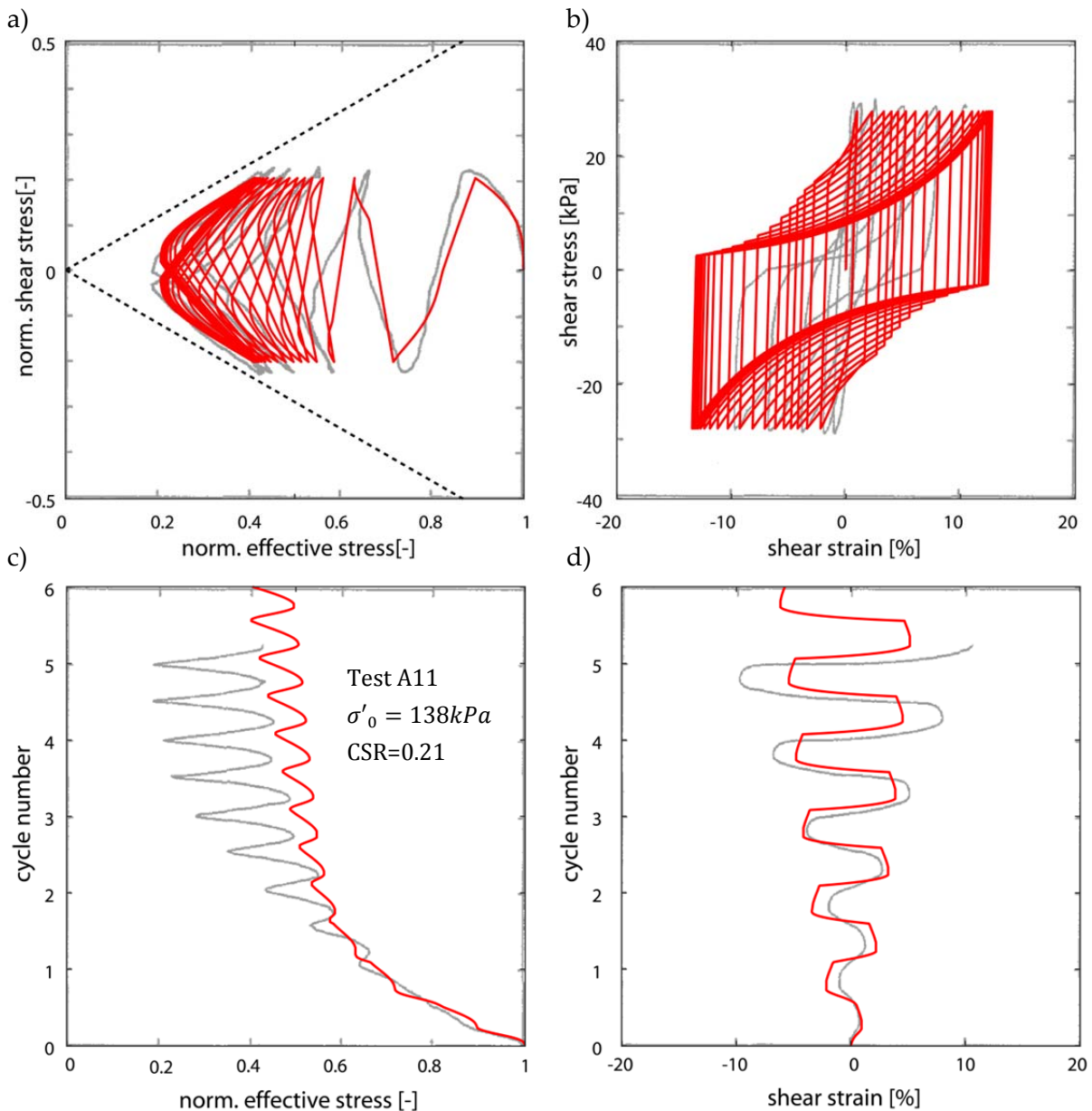
Figure 8-21: Comparison of a simulated stress-controlled cyclic test for CSR = 0.210 (red line) and experimental data (grey line) for Test A11 reproduced from Donahue (2007)): a) stress path; b) stress strain behaviour; c) effective stress to number of cycles; d) evolution of strain per cycle

If cycles at higher amplitude (higher CSR) are simulated, one can see that the model can still capture the overall development of excess pore pressures quite well (Figure 8-21a and c). However, after the first two cycles, the development of excess pore pressures during unloading is underestimated (Figure 8-21c). For that reason, the development of strains is also underestimated after the third cycle (Figure 8-21d). Both excess pore pressures and strains do, however, eventually reach the same size as in the test observed (see Figure 8-21a and b).

Symmetrical cyclic tests with small amplitude (shakedown):
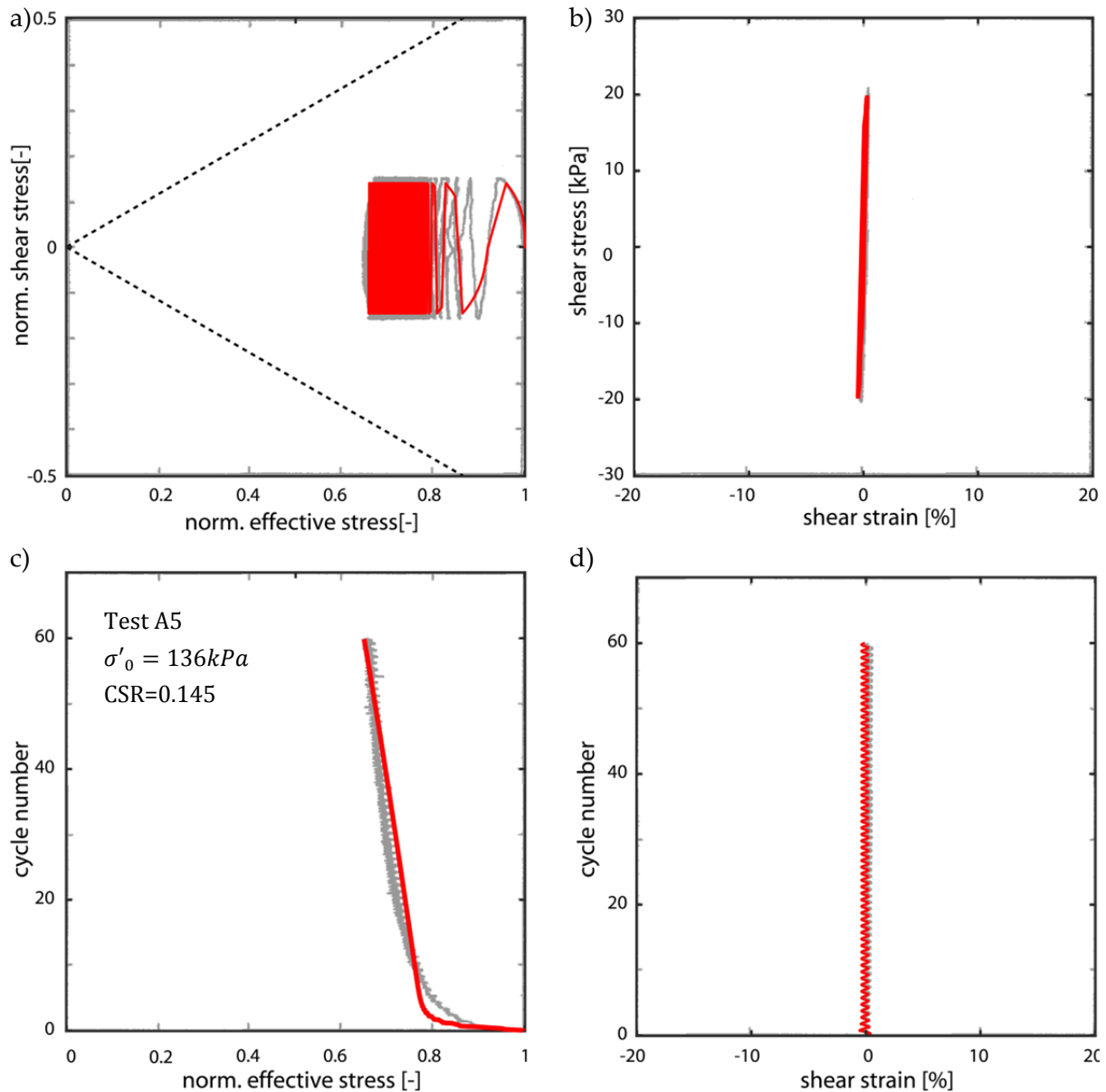
Figure 8-22: Comparison of a simulated stress-controlled cyclic test for CSR = 0.145 (red line) and experimental data (grey line) for Test A5 reproduced from Donahue (2007)): a) stress path; b) stress–strain behaviour; c) effective stress to number of cycles; d) evolution of strain per cycle

If tests with sufficiently small amplitude are simulated, the model will predict a shakedown, i.e. even at a large number of cycles, no further significant increase of pore pressures is observed. As can be seen from Figure 8-22, this behaviour can generally be captured, though the model has not been calibrated specifically for this test. The residual increase in excess pore pressure is only driven by parameter $\beta_{1,3}^{0}$.

Cyclic tests with constant shear stress (asymmetric):
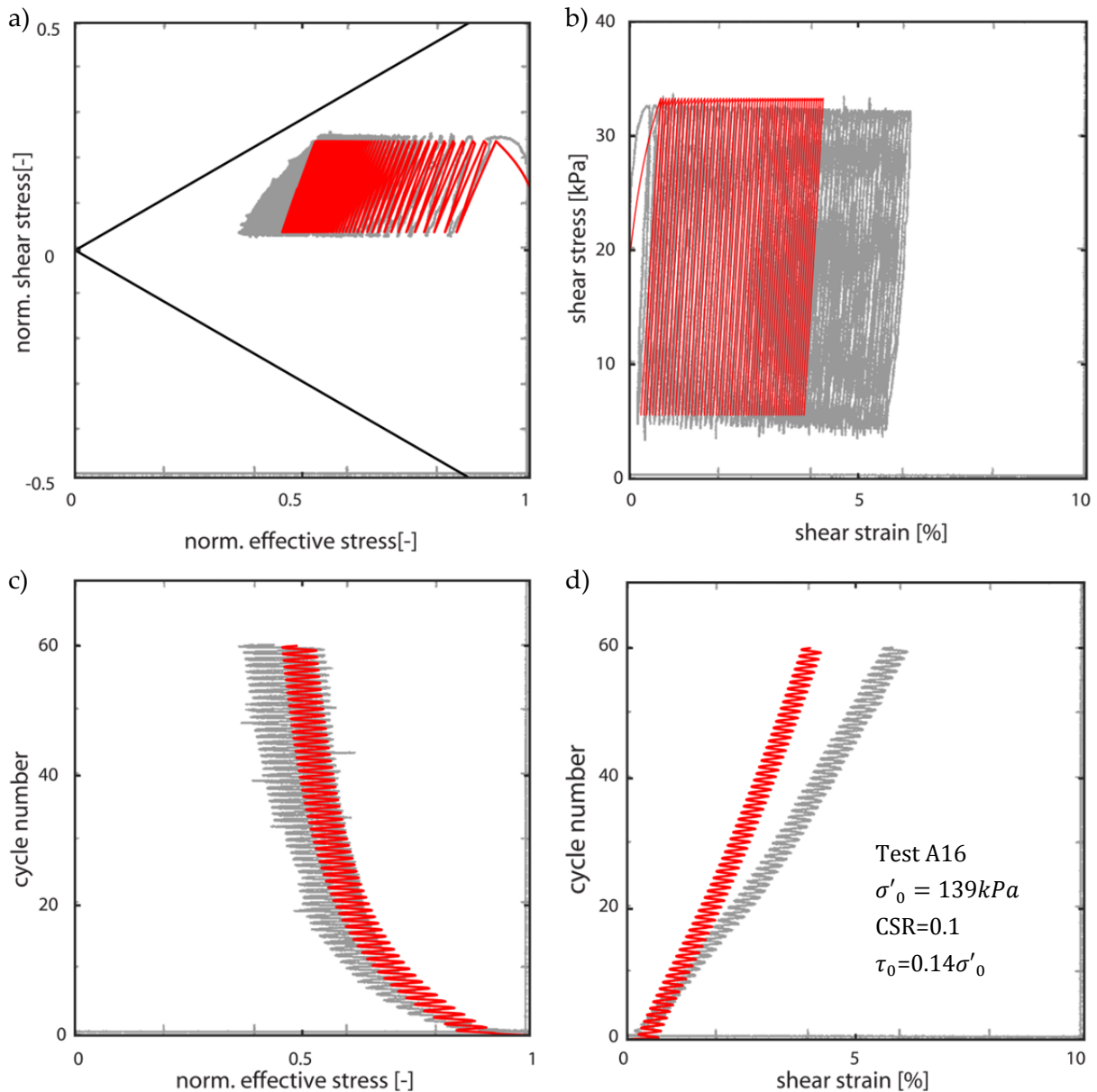
Figure 8-23: Comparison of a simulated stress-controlled cyclic test for CSR = 0.1 (red line) and experimental data for Test A16 with static shear stress ratio $\alpha = \frac{\tau_0}{\sigma'_0} = 0.14$ reproduced from Donahue (2007)): a) stress path; b) stress–strain behaviour; c) effective stress to number of cycles; d) evolution of strain per cycle

Since the original motivation for the formulation of the model was the use in landslides, i.e. in slopes, the model performance in the presence of a static shear stress (i.e. asymmetric tests) is important. Unfortunately, not much data in literature is available for such tests. In the data set used herein, only one test has been performed with asymmetric loading. Since the model cannot yet account for pre-consolidation, it is not simulated, and the exact consolidation path is not taken into account.

The only parameter that takes static shear stress explicitly into account is η_0 in F_1^1 (8-78). Still, it can capture the observed behaviour reasonably well (see Figure 8-23). The fluctuations of

excess pore pressures are slightly underestimated (see Figure 8-23c) which is probably due to the use of only two distinct surfaces and thus the limited ability to model varying stiffness. The formulation intrinsically captures the effect of ratcheting, i.e. the continuous accumulation of strains in direction of the static shear stress (see Figure 8-23d).

<u>Symmetrical cyclic tests at varying effective stress:</u>

The effect of varying effective normal stress can be seen in Figure 8-24 and Figure 8-25. Overall, the model can capture the development of stresses and strains quite well. Only the strains in the test A12 (Figure 8-24b and d) are overestimated.
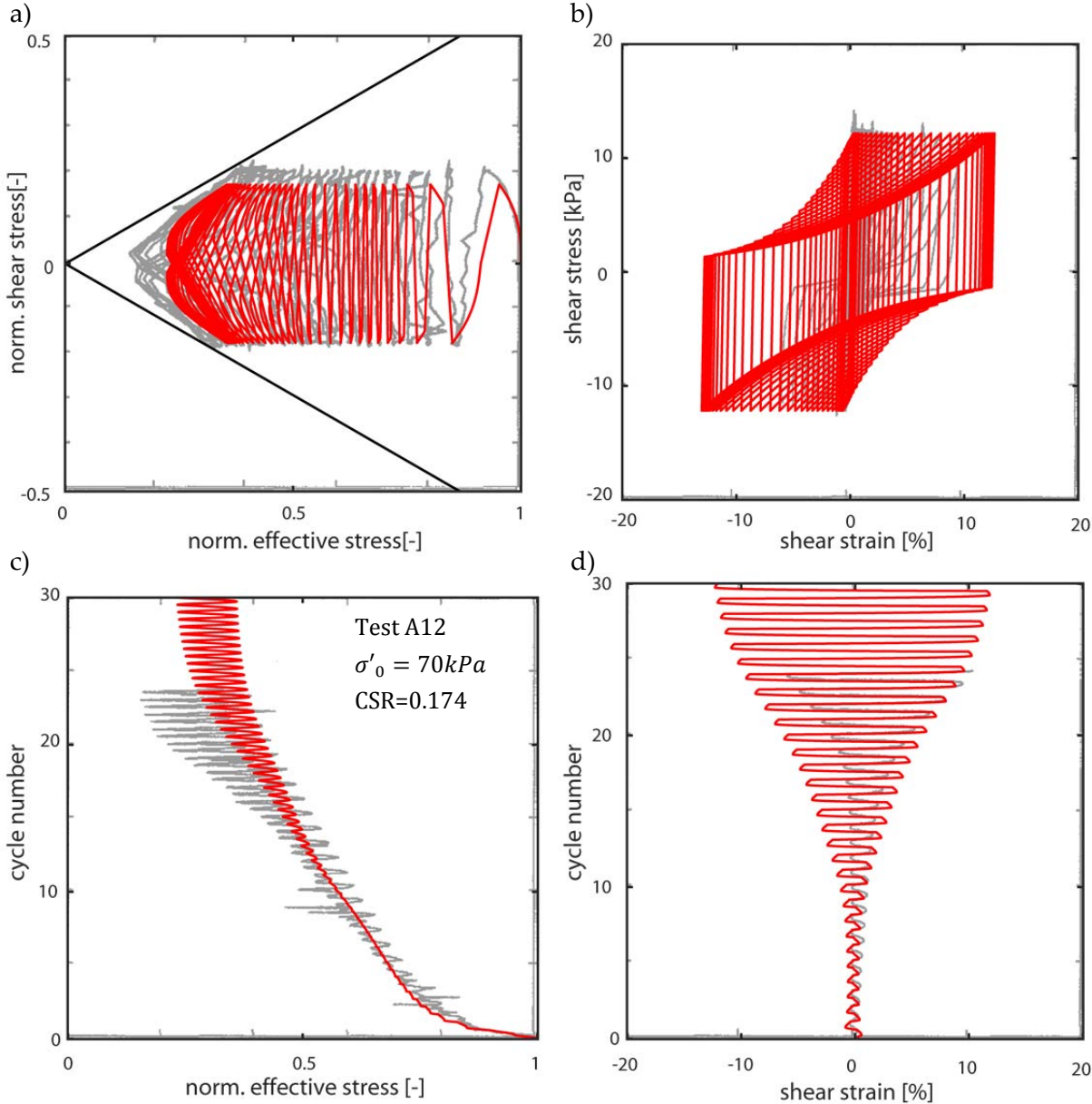
Figure 8-24: Comparison of a simulated stress-controlled cyclic test for CSR = 0.174 and normal effective stress of 70 kPa (red line) with experimental data for Test A12 reproduced from Donahue (2007): a) stress path; b) stress–strain behaviour; c) effective stress to number of cycles; d) evolution of strain per cycle
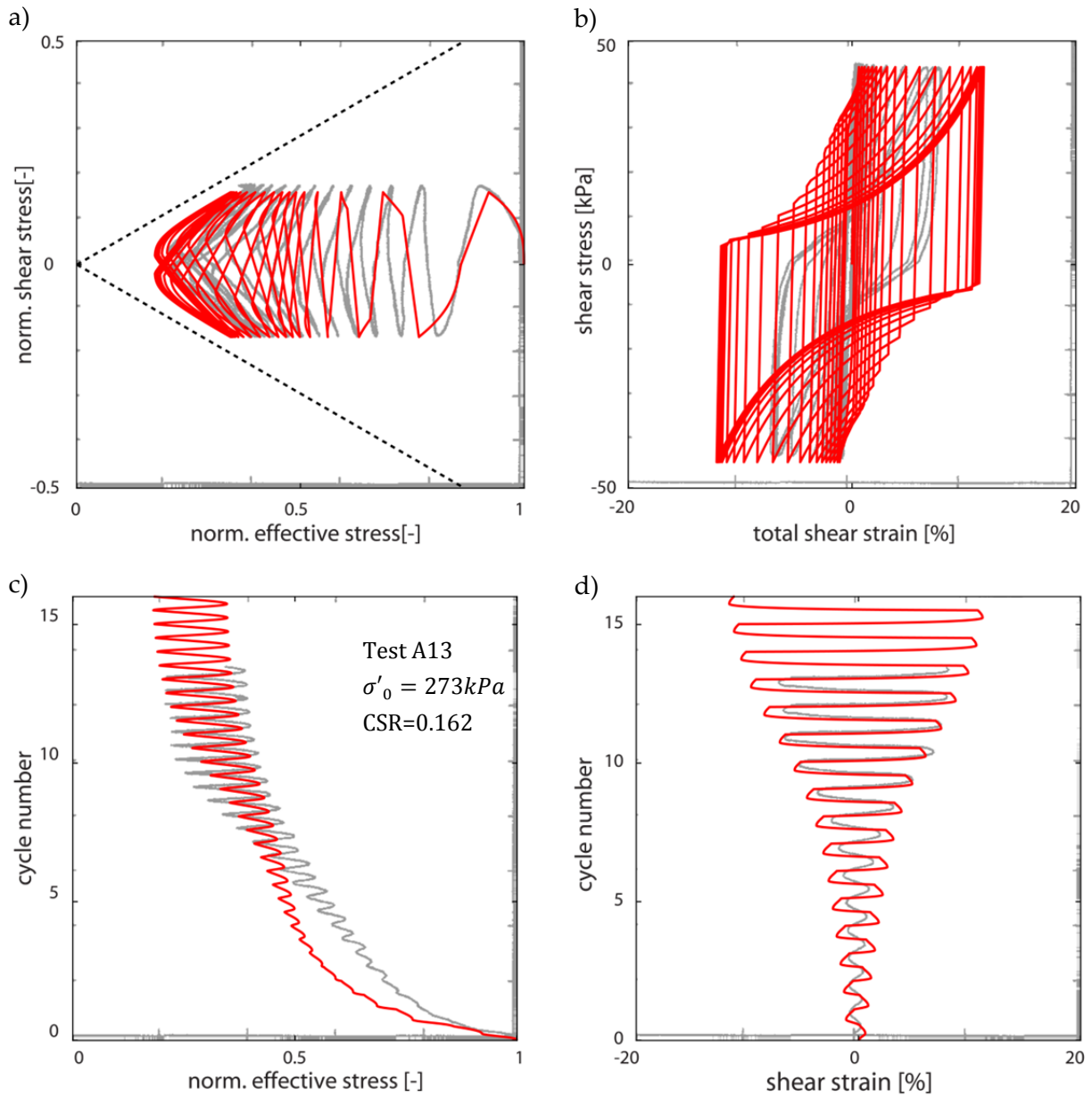
Figure 8-25: Comparison of a simulated stress-controlled cyclic tests for CSR=0.162 and normal effective stress of 273 kPa (red line) with experimental data from Test A13 reproduced from Donahue (2007): a) stress path; b) stress–strain behaviour; c) effective stress to number of cycles; d) evolution of strain per cycle

8.3.10 Performance in irregular loading

In order to investigate irregular rather than just regular cyclic loading and to demonstrate application in a simple boundary value problem, an exemplary problem has been modelled: a homogeneous layer of silty soil on horizontal ground. The model (Figure 8-26) divides the soil layer into multiple sublayers of thickness (d) with corresponding masses (m) and initial stress state. Beneath the soil layers, bedrock, where the acceleration (a) is imposed, is modelled with a quiet base according to Mejia and Dawson (2006); thus downward propagating waves will be absorbed.

Since implicit time steps are used, during the simulation of an earthquake, the shear stress (τ_n^t) in the soil sublayers must be found iteratively. Therefore the step functions (compare 8.3.1) have to be inverted, and consequently their solution is limited to be within the bounds]-1;1[or]0;1[respectively. In order to solve the system of equations, Broyden's (Broyden, 1965) method has been used. Since this method is unconstrained, the target function has been changed so that it does not minimize directly

$$\left\| \tau_{n,guess}^t - \tau_n^t \right\| \leq \Delta \tag{8-121}$$

but rather minimizes

$$\left\| \left(A \cdot M \cdot \tanh(B \cdot x_{n,guess}) \cdot \sigma_{n,guess}'^{\,t} - \tau_n^t \right) \cdot \left(1 + |x_{n,guess}| \right) \right\| \leq \Delta \tag{8-122}$$

where the superscript t denotes the time step and the subscript n the soil layer; $\tau_{n,guess}^t$ and $\sigma_{n,guess}^t$ are the assumed current shear and normal stress in each layer and τ_n^t is the calculated shear stress; $x_{n,guess}$ is a free search variable and M, as before, the inclination of the strength envelope; the parameters A and B are chosen to ensure numerical stability, with A being slightly smaller than 1 (A = 0.99 has been used in the simulations shown herein) to ensure that the inversion of the hyperbolic tangents is numerically feasible. B controls the steepness of the target function. The second part of (8-122), $1 + |x_{n,guess}|$, ensures that the relative change of the target function within a time increment cannot drop to zero if large values of $x_{n,guess}$ are assumed.
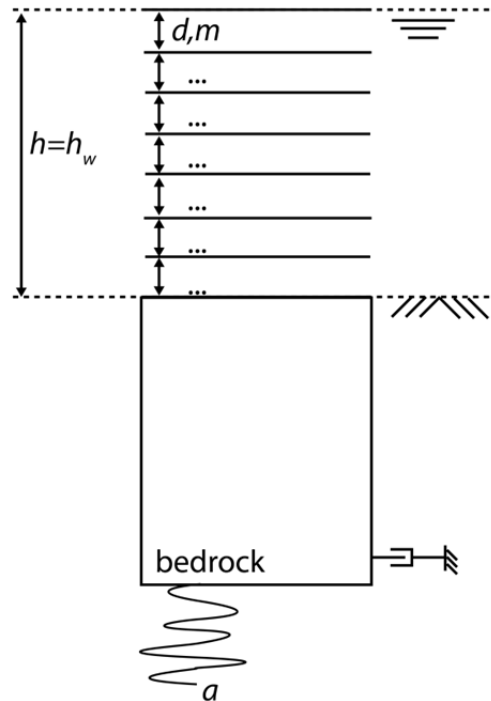
Figure 8-26: Model of the test scenario for irregular loading

The results for the soil column simulation are given in Figure 8-27. Figure 8-27a) shows the motion in terms of particle acceleration on top of the bedrock which has been assumed to be Molasse with $v_s = 1400\,\text{m/s}$ and $\gamma = 26\,\text{kN/m}^3$. The transient nature of the problem, i.e. redistribution of pore pressures during the earthquake among the layers, has been neglected, as flow is assumed to be significantly slower than the time scale of the earthquake. The response time history in terms of displacements on the surface is given in Figure 8-27b), where the solid line indicates a simulation with generation of pore pressure and the dashed line a simulation if no generation of pore pressures would be possible (drained conditions). As expected, the loss of stiffness due to dropping effective stress causes slightly higher displacements in this scenario, whereas the response in terms of accelerations drops (see Figure 8-27e). The stress path including pore pressure generation in the first layer above the bedrock is shown in Figure 8-27c). Final pore pressure distribution over the depth is shown in Figure 8-27d).
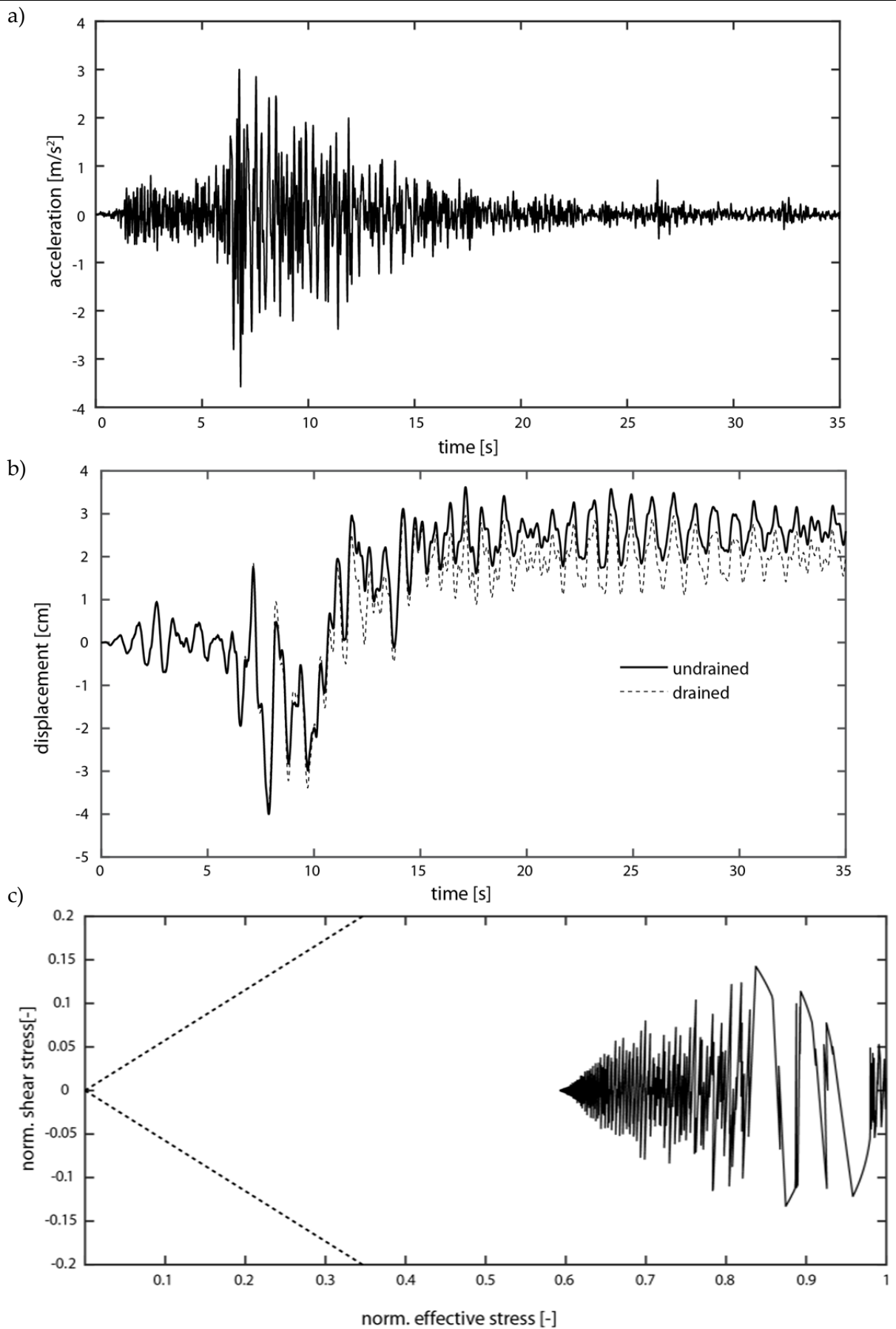
Figure 8-27: a) Input motion on top of the bedrock; b) displacement response on the surface; c) stress path in the deepest layer; d) final distribution of excess pore pressures; e) response spectra (5% damping)
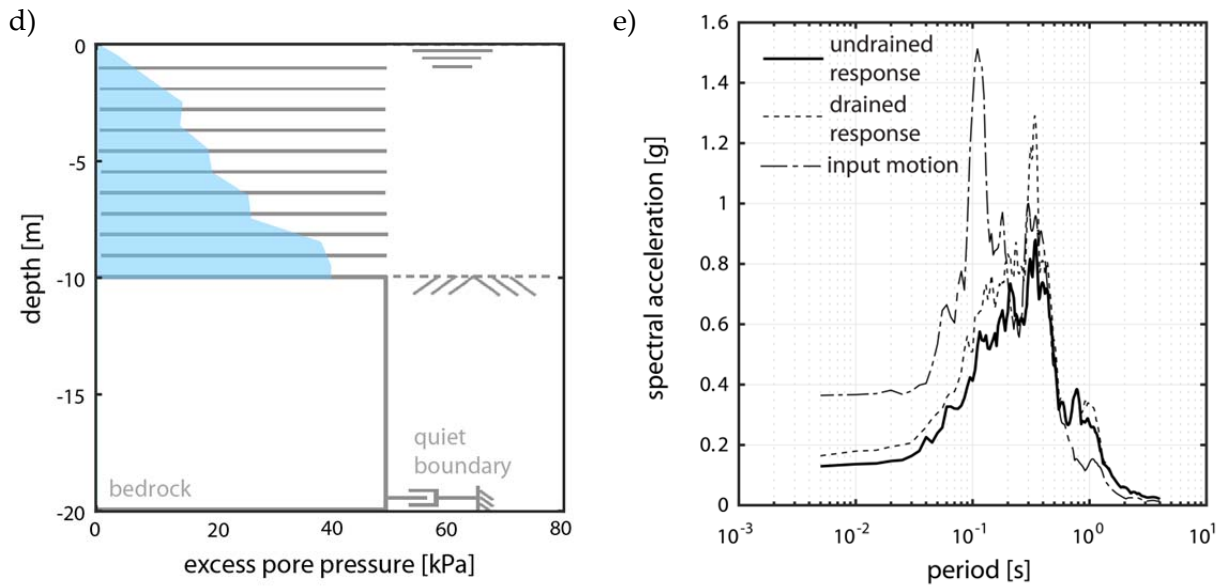
Figure 8-27 continued: a) Input motion on top of the bedrock; b) displacement response on the surface; c) stress path in the deepest layer; d) final distribution of excess pore pressures; e) response spectra (5% damping)

The final distribution of excess pore pressures allows, for example, calculation of the settlements due to the excess pore pressures.

8.3.11 Comparison to other models

Comparing the model to some existing approaches, one can see that the biggest resemblance can, of course, be found with Houlsby (1992) and Houlsby & Mortara (2004) who also introduce anisotropy in form of additional constraints on the dissipation. In contrast to Houlsby & Mortara (2004), only two surfaces are used, but by using a kinematic hardening in form of a yield surface rotation, the same effect as if using infinite surfaces can be achieved. At the same time, having only two surfaces allows one to introduce anisotropy not only to the deviatoric-volumetric coupling but also to the hardening function. This allows the shape of the stress train cycles to be better reproduced, which can be more difficult with multiple surfaces.

In its basic form, the hardening formulation resembles that proposed by Prevost (Prevost, 1985) and used e.g. by Elgamal (2003). Therefore, the shape of the stress–strain cycles resembles that shown e.g. in Elgamal (2003). However, by deriving the model strictly according to the hyperplasticity framework, thermomechanical consistency is ensured and clear limits to the applicability can be given. Also, Elgamal (2003) uses an infinite number of surfaces, whereas the use of only two surfaces in the current model allows observed phenomena to be more easily related to features of the model.

Compared to bounding surface models, similarities can be found since bounding surface models also use only two functions, similar to the two yield surface formulations in the model proposed herein. These functions are a permanently active yield function, comparable to the constantly active yield surface y_0, and the bounding surface formulation. Differences are again the fact that all functions used for the proposed model are derived such that they are thermomechanically consistent. Also, all the functions in the model proposed here depend only on the stress and strain state, whereas bounding surface models always also require calculation of the point on the bounding surface in the direction of the stress path, which can complicate their application to boundary value problems.

9 Application of the model for creeping landslides (Brattas case)

The previously derived constitutive models for the weak layers and the slip surface are now integrated in a model of the boundary value problem according to the concept described in chapter 6. Geometry and parameters are chosen to resemble the case of the Brattas landslide introduced in chapter 3.

9.1 Computational model

The conceptual model shown in chapter 6 is translated into a computational model that is schematically drawn in Figure 9-1.
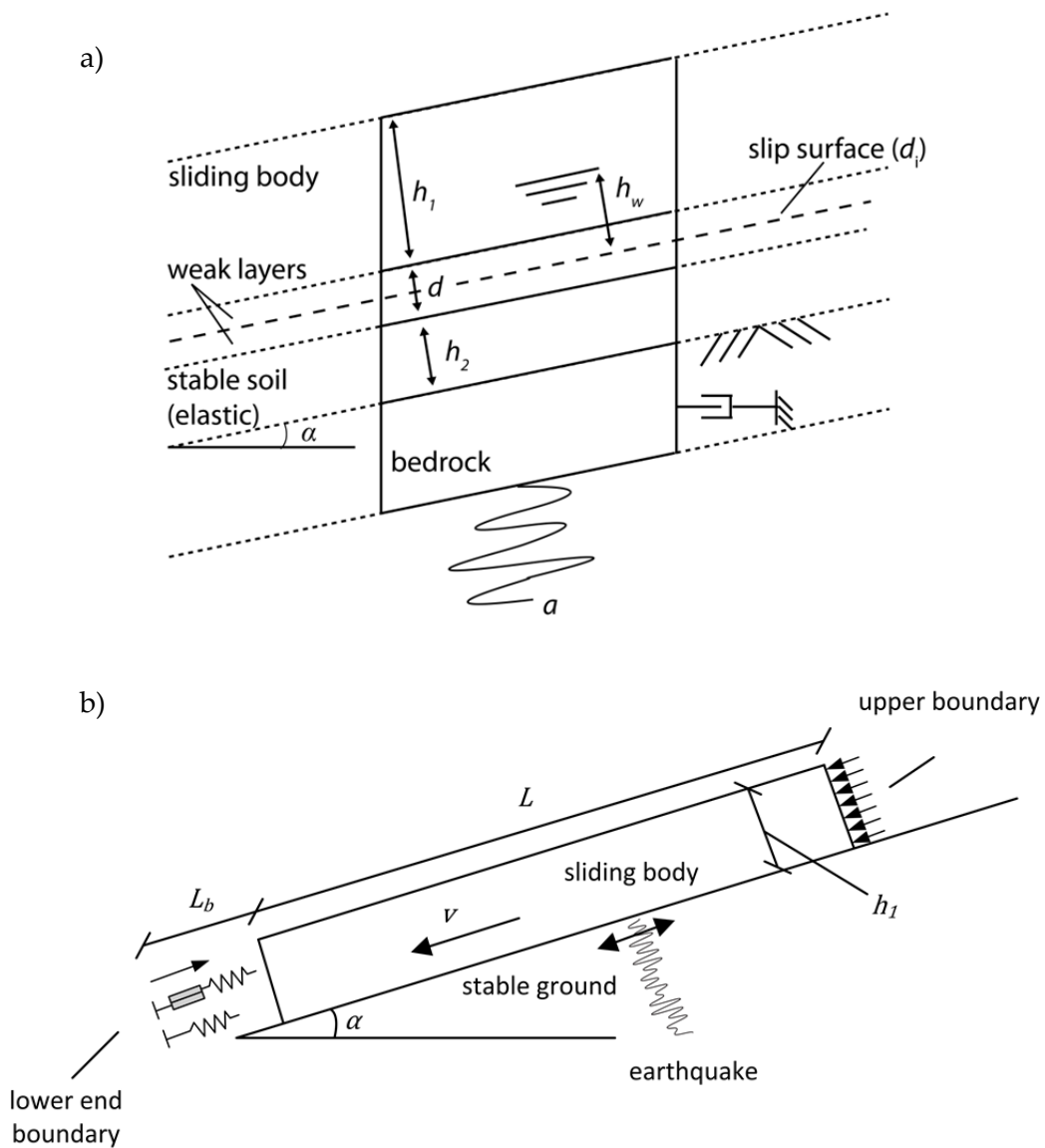
Figure 9-1: Computational model for the seismic analysis of creeping landslides: a) detailed section with weak zone and slip surface; b) section along the landslide with possible boundary conditions

As can be seen in Figure 9-1a, the landslide body is modelled as a rigid block (sliding body) that sits on top of a weak layer. Inside the weak layer the actual slip surface is situated. In this study, the slip surface is assumed to be in the middle of the weak layer and has a thickness d_i, which is taken from the simulations under non-seismic conditions (chapter 5). The thickness of the weak layer is assumed to be $d \approx 20cm$, which has been identified in borings.

Underneath the weak layer, there is assumed to be another layer of soil (elastic, $h_2 = 10m$, SIA 261 (2014) soil class B with $v_s = 650m/s$) and subsequently bedrock (elastic, SIA 261 (2014) soil class A with $v_s = 1400m/s$) with a quiet boundary ensuring the absorption of downwards-propagating shear waves. In longitudinal direction infinite slope conditions are assumed in these layers.

The following boundary conditions can be applied to the sliding body in the longitudinal direction to evaluate their influence:

(i)   no further boundary conditions (≙ infinite slope conditions)

(ii)   constant pressure on top (≙ active failure) and an elastic foot zone (≙ no failure in compression zone)

(iii)   constant pressure on top (≙ active failure) and an elastic-plastic boundary condition in the foot zone (≙ failure in compression zone)

The elastic-plastic boundary at the foot of the landslide is simplified as a single elastic spring (shear deformations neglected) in the longitudinal direction connected to a perfect plastic element (see also Figure 9-1). The properties of the elastic part and the strength of the plastic element are taken from the model of the compression zone (Region III in chapter 5). A more complex visco-elastic-plastic model as in section 5.8.6 seems unnecessary, as the viscous parts from the model of the compression zone, with parameters suitable for very slow deformations, do not contribute to the deformations in fast loading. For the length of the boundary region, the length of the landslide where the material started deforming visco-plastically has been taken.

Acceleration is applied slope-parallel in terms of shear stress (see Mejia and Dawson (2006)) due to the use of a quiet boundary. Slope-normal shaking, as well as longitudinal propagation of the waves along the landslide, is neglected.

The input motions are recorded on rock and stiff soil sites and taken from a set of acceleration-time histories representative for Switzerland (Laue, 2014). Initially, the pore

pressure on the slip surface, i.e. the height of the phreatic surface above the slip surface, is adjusted to cause the landslide to creep with the average velocity of the landslide (0.4 m/yr).

Excess pore pressures that are generated in the weak layers are assumed also to act immediately inside the slip surface. This assumption is appropriate assuming that the slip surface is actually a set of multiple thin surfaces with total thickness d_i that alternate with weak layers; if the slip surface is formed as one surface of thickness d_i it can, depending on the permeability, take time for the pore pressures to propagate into the slip surface. For this first assessment, the more conservative first assumption has been chosen.

For the calculation, the model is discretized underneath the sliding body into slope-parallel slices; in the longitudinal direction the model is not discretized. A finite difference scheme with implicit time steps has been used to solve the problem. Time step size is given by the time steps of the input motion. Discretization is chosen such that the solution does not change if finer steps are chosen and performance is still good enough to run multiple input motions in reasonable time.

The parameters for the interface model have already been shown in chapter 7 and are derived from ringshear tests on material from St. Moritz.

The derivation for parameters for the material in the weak layer is more difficult since no DSS-tests are available, only the triaxial test results shown in chapter 3. Although the model can also be formulated in triaxial stress space, it has not yet been possible to formulate the model in generalized stresses and to transform it to the boundary conditions of the DSS test or the landslide. However, the monotonic triaxial tests on the material from the Brattas landslide show very similar behaviour to the ones by Donahue (2007), as can be seen in Figure 9-2.
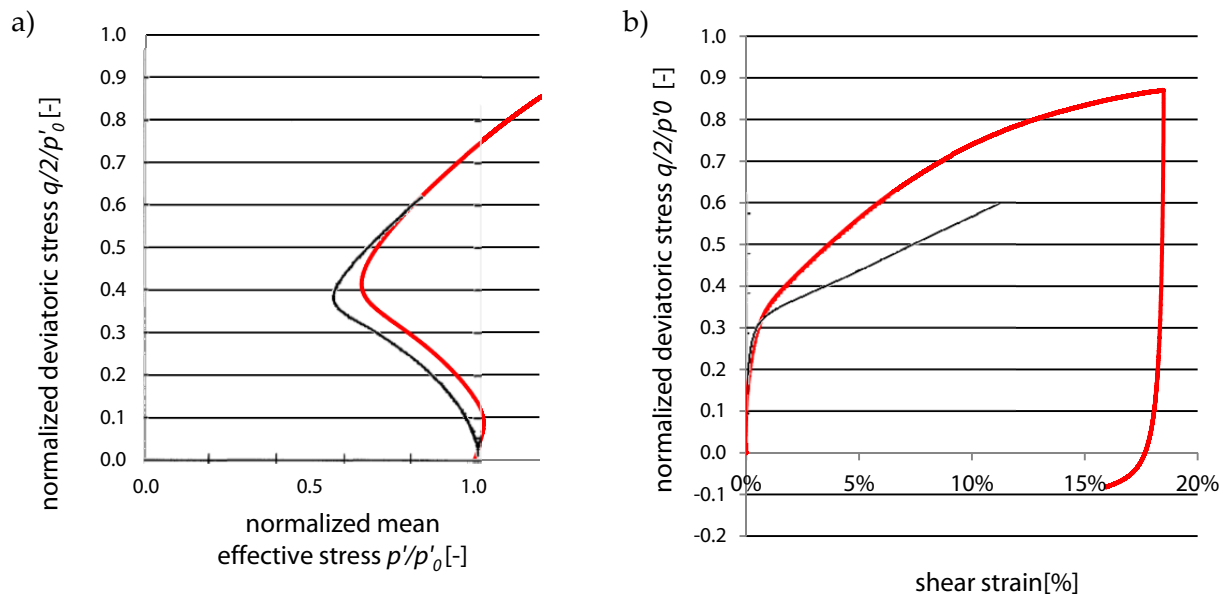
Figure 9-2: Comparison of triaxial tests from Donahue (2007) (black lines) and material from St. Moritz (red lines): a) stress path; b) stress–strain behaviour

Differences between the tests occur in the first moments where the pore pressure development during the test on material from the Brattas is lower than observed in the tests by Donahue (2007), and at larger strains where the material from St. Moritz exhibits more hardening.

The reason for the first difference is potentially the different rates used during the tests. The test from Donahue (2007) uses constant stress rates (1kPa/min) which lead to varying strain rates during the test and thus varying influence of strain-rate dependency. The tests on the material from St. Moritz were performed at an approximately constant strain rate (0.00014 min^{-1}) which leads higher stress rates in the beginning of the test. Therefore, rate effects in the tests from Donahue (2007) are potentially initially smaller than in the tests on material from St. Moritz, which could explain the differences between the tests. The difference in hardening behaviour at larger strains could potentially result from the different mean effective stresses at which the tests have been performed ($p'_{0,\text{Donahue (2007)}} = 100\text{kPa}$; $p'_{0,\text{Brattas}} = 276\text{kPa}$).

Other than this difference, the tests are very similar and also result in the same strength ($\varphi' = 37°$). Therefore, this first analysis of seismic impact on the landslide uses the same parameters as for the material tests in Donahue (2007) (see Table 8-2). Only the parameters that can be derived from oedometer tests have been updated.

All model parameters additional to the ones of the constitutive models are summarized in Table 9-1:

Parameter	Symbol	Value
Geometry		
Thickness of the sliding body [m]	h_{sb}	20
Thickness of the weak zone including slip surface [m]	d_{wz}	0.22
Thickness of the slip surface [m]	d_{ss}	0.02
Thickness of the stable zone underneath the weak zone [m]	h_{sz}	10
Inclination of the landslide [°]	α	20
Length of the landslide above the boundary region [m]	L	670
Length of boundary region [m]	L_b	70
Depth of the phreatic surface [m]	h_w	14.06
Elastic properties of the soil underneath the weak zone		
Shear wave velocity [m/s]	v_s	650
Material properties of the slip surface given in Table 7-1		
Material properties of the weak layers are given in Table 8-2 with exception of		
Consolidation index [-]	C_c	0.087
Swelling index [-]	C_s	0.023

Table 9-1: Additional parameters of the seismic landslide model

9.2 Analysis of the calculation model

As seen in section 9.1, simplifications with respect to geometry, boundary conditions and material properties outside the weak layer have been assumed. Therefore, the model's sensitivity towards variations of several of the model components has been investigated. To make simulations with different conditions comparable, the model has always been calibrated to move with average velocity of 0.4 m/yr before onset of the seismic loading. These investigations show that the model is insensitive towards:

(i)   variations of the length and the type of the boundary region;

(ii)   variations of the thickness of the layer underneath the weak zone and the bedrock

More significant is the influence of the characteristics of an input motion on the development of excess pore pressures. However, choosing representative time-series is difficult. Therefore, understanding the characteristics that have significant influence on the displacements and the development of excess pore pressures can help to better choose appropriate records.

Although no comprehensive study has been performed, the nature of the model for the weak layers makes it clear that the development of excess pore pressures is particularly boosted if an earthquake contains cycles sufficiently large to cause a stress reversal in the weak layer.

Figure 9-3 compares the record of the Friuli earthquake (from the PEER Strong Motion Database, http://peer.berkeley.edu/), an example for a strong earthquake in the alpine region, with the record from Laue (2014) of the highest Arias intensity (Arias, 1970). As can be seen, the records have similar properties (see Table 9-2), with the Arias intensity (usually a good indicator of seismic slope displacements) of earthquake #177 being even higher than the one from the Friuli earthquake. Still, the Friuli record produces slightly higher excess pore pressures due to the fact that it causes one stress reversal. Also, looking at the frequency content, one can see that the Friuli record has more content than #177 in the long period range (T = 0.5–1sec), which causes the long-lasting stress cycles necessary to produce a stress reversal despite the high static shear stress.

	Friuli (Tolmezzo station)	Record #177
Magnitude	6.5	6.6
Arias intensity [m/s]	0.78	1.61
Peak acceleration [m/s²]	3.69	3.67
Distance [km]	15.82	40.23

Table 9-2: Characteristics of the input motion
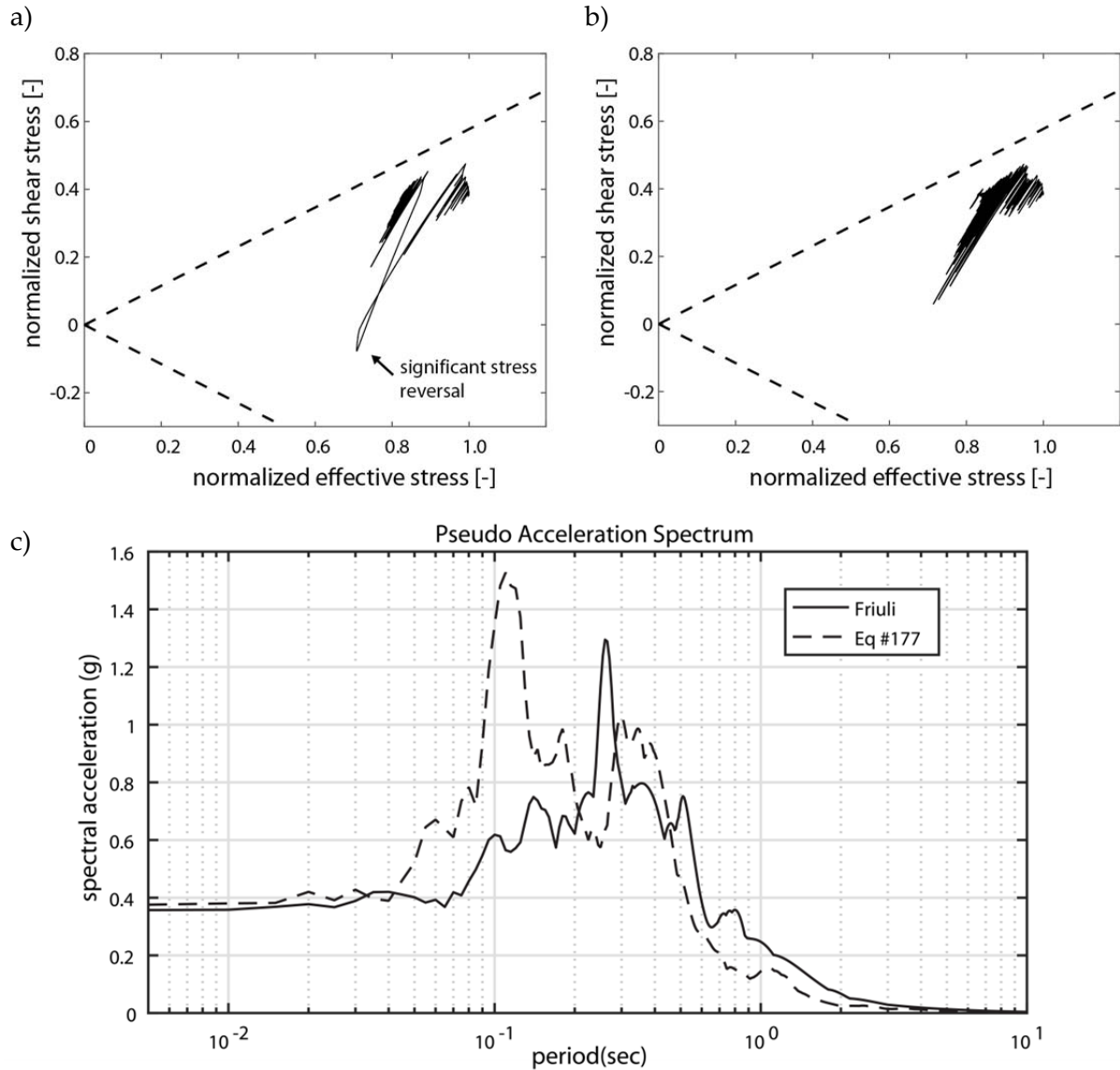
Figure 9-3: Influence of different time/acceleration histories: a) excess pore pressure from Friuli record; b) excess pore pressure from record #177 from Laue (2014); c) spectra from both records

Another analysed factor is the type of rate dependency formulation. As said before, using a linear rate dependency formulation leads an overestimation of mobilized shear resistance at high shearing rates. To demonstrate the consequence of such behaviour, a simulation of the slope with a Herschel–Bulkley interface formulation and a simulation with linear rate dependency interface have been compared.

As can be seen in Figure 9-4, the linear rate dependency formulation leads to almost no displacements during the earthquake; at the same time, it causes greater excess pore pressures. The reason for this observation lies in the nature of the Herschel–Bulkley function which flattens at high rates and cannot mobilize significantly more strength, effectively causing the slip surface to start acting as an isolator.

Therefore, to get reliable results, it is important to use a rate dependency that can capture the entire velocity range from creeping stage to the high rates during the seismic event .
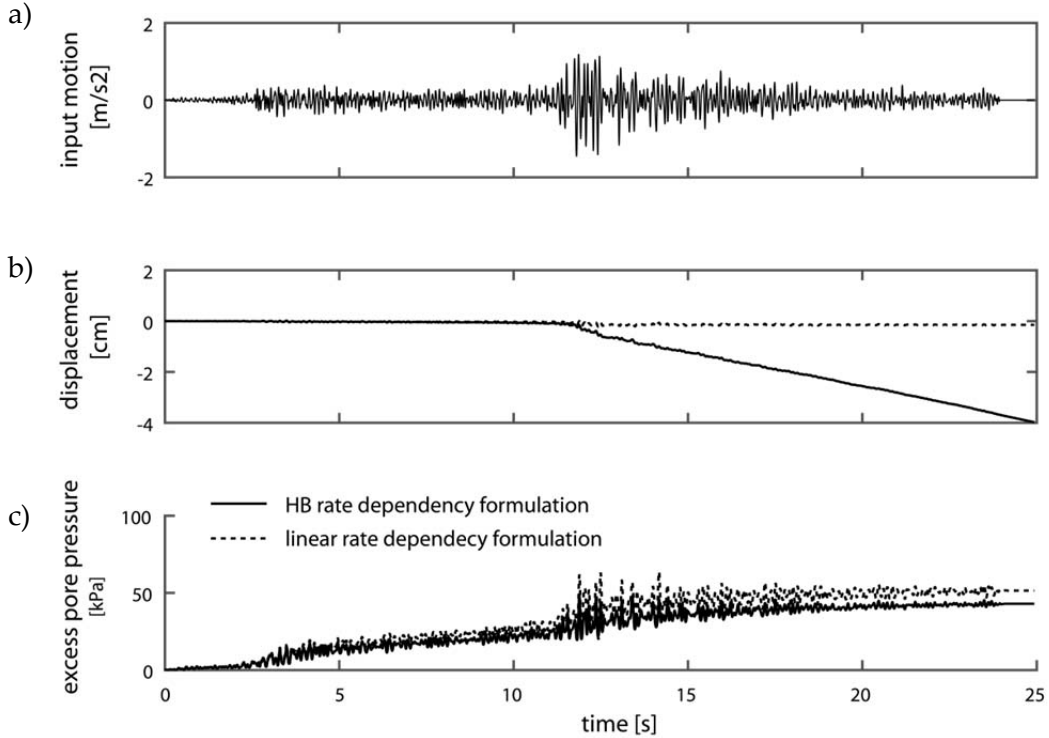
Figure 9-4: Comparison of different rate dependency formulations: a) input motion; b) displacement; c) excess pore pressure

9.3 Simulations of the co-seismic behaviour of the landslide

For a more comprehensive investigation of the landslide reaction to seismic loading, subsets from the representative set of earthquakes (Laue, 2014) are used. First, observations from rock sites are used as input in the bedrock layer; second, to increase the number of simulations, observations from stiff soil sites (500m/s < v_{s30} < 800m/s) are also used as input to the soil layer underneath the weak zone.

Aftershocks have been removed from the records and the remaining acceleration time series has been reduced to a bracketed duration during which the input motion exceeds 0.1m/s². This has been done to analyse only the deformations during the strong motion stage and not deformations that are due to creep of the landslide after the event.

The characteristics of the two sets are given in Table 9-3.

	Records from rock sites (v_{s30} > 800m/s)	Records from stiff soil sites (500m/s < v_{s30} < 800m/s)
No. of records	83	251
Magnitude range	4.3–6.6	4.3–6.6
Distance range	14.8–97.3	6.6–98.0
Total no. of input motions (motions can be applied in two directions)	166	502

Table 9-3: Characteristics of the input motion sets

The results from the simulations in terms of displacement and excess pore pressure are shown in Figure 9-5. The graph contains results from simulations with input motions for both soil types.

As can be expected, both correlate acceptably with the Arias intensity of the earthquakes, independent of where the input motions are applied.

The correlation of excess pore pressure and Arias Intensity flattens above an intensity of approx. 0.1m/s which is, on the one hand, due to the "better seismic isolation" provided by the slip surface at higher rates which, as said in 9.2, is due to the nature of the Herschel–Bulkley function. On the other hand, as the stress state in the weak layers approaches the failure envelope, it reaches a point where it starts alternating between dilative and contractive behaviour with little increase in the remaining excess pore pressure.

Looking at the displacements, the correlation is more linear. For small motions, the displacement due to the earthquake can be of similar magnitude to the displacement caused by increased creep of the landslide.

a)

b)
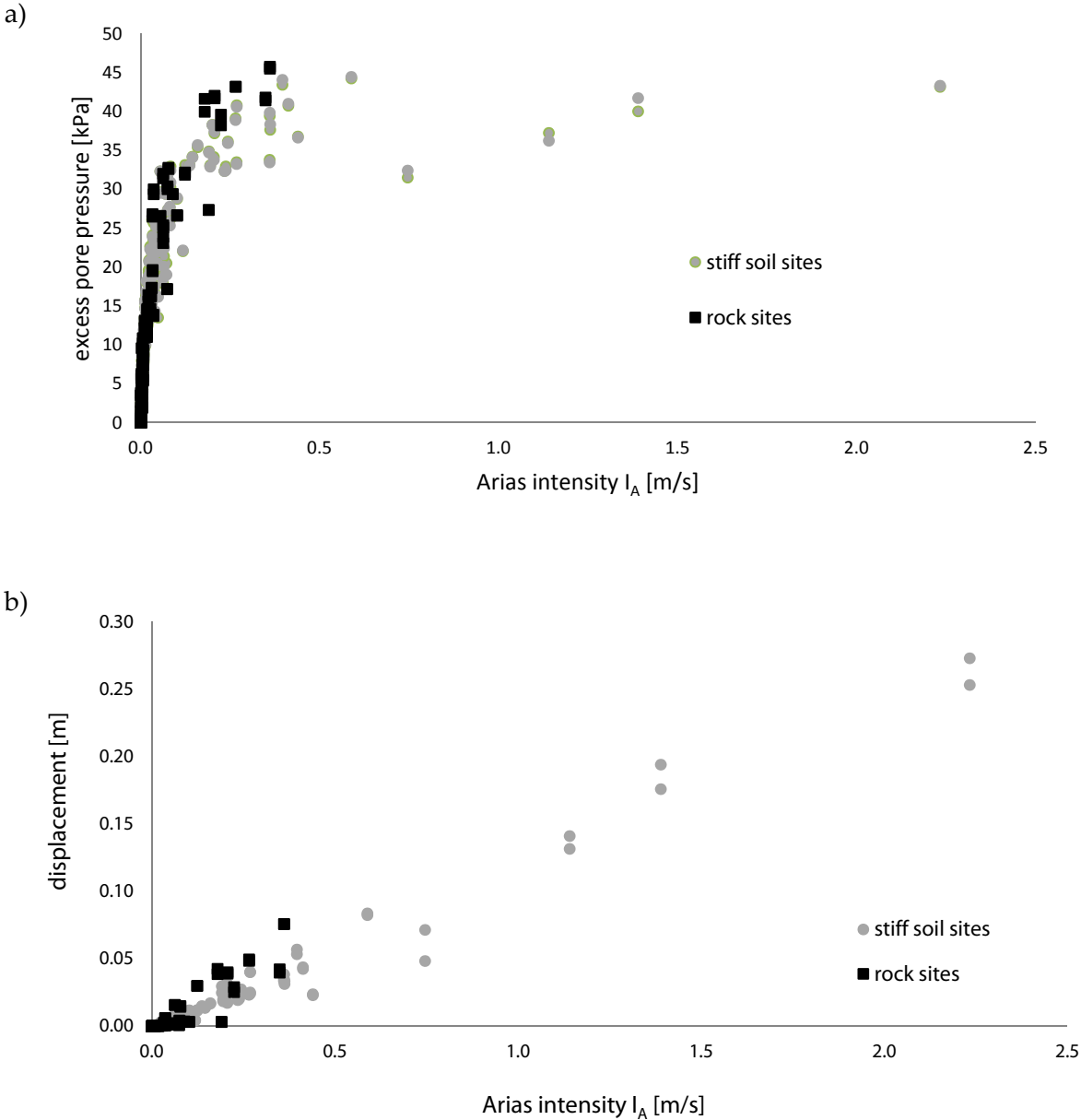
Figure 9-5: Results of the co-seismic simulations in terms of a) Arias intensity to excess pore pressure and b) Arias Intensity to displacements

9.4 Post-seismic evolution of the landslide

Owing to the development of excess pore pressures and therefore reduced shear resistance along the slip surface, the landslide will move after the seismic event with a higher velocity until these pressures have dissipated.

In order to investigate this development, the reduction of excess pore pressures can be treated as a reconsolidation problem and the pore pressures can be integrated into the model shown in chapter 5.

The model assumes that excess pore pressure has developed uniformly in the entire weak layer of the landslide. Thus, only drainage in the direction orthogonal to the landslide is considered, and the problem simplifies to a 1D situation. Therefore, it is simply analysed using 1D consolidation (compare e.g. Yasuhara et al. (1991) or Hashash (2009)) and parameters of the landslide shown in chapter 3:

$$\frac{\partial u_e}{\partial t} = c_v \frac{\partial^2 u_e}{\partial z^2} = \frac{k_s}{m_v \gamma_w} \frac{\partial^2 u_e}{\partial z^2} \tag{9-1}$$

where c_v is the consolidation coefficient, k_s is the permeability of the soil, m_v the constrained modulus and γ_w is the unit weight of water. ∂t and ∂z are time and space increments respectively.

For the analysis of pore pressure dissipation, it is assumed that the rock underneath the landslide is impermeable and the top of the fully saturated zone represents the zero pressure boundary. Figure 9-6 shows as an example the development of pore pressures during 24 hours after the earthquake for an excess pore pressure of 50 kPa.

Please note that in the co-seismic simulations it has been assumed that excess pore pressures immediately also act inside the slip surface. However, if the slip surface has a large enough extension or is less permeable than the soil in the weak zone, pore pressures will propagate into the actual slip surface only after the earthquake, potentially causing deformations mainly after the event.

The development of pore pressures within the slip surface can subsequently be used as an input to the model of the landslide developed in chapter 5 to estimate potential post-seismic displacements. For simplicity, this first investigation assumes that the seismic event has not changed the strain distribution inside the sliding body and all displacement during the seismic event only causes perfectly plastic deformation inside the compression zone. Thus,

the excess pore pressure development can be applied to the landslide model (for the creep stage) at the point in time when the earthquake is assumed to take place.
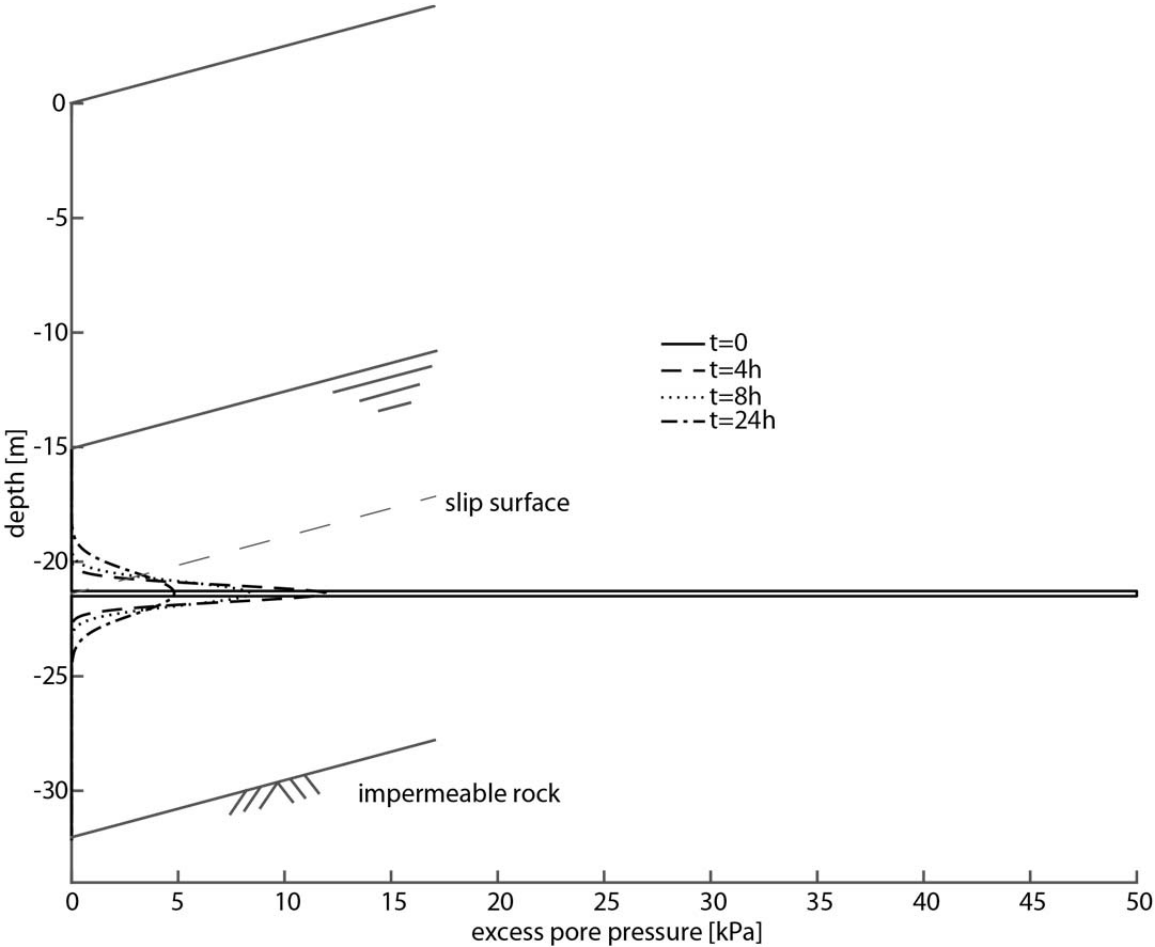
Figure 9-6: Development of excess pore pressures after a seismic event

Figure 9-7 shows the deformations of the landslide after an earthquake for several magnitudes of excess pore pressure. Since the dissipation of excess pore pressures in the scenario investigated herein takes place quite rapidly in the first hours after the event, simulations need to be run with small time steps, which can cause numerical difficulties. To reduce these problems, the time step is continuously increased as the rate of pore pressure dissipation drops.

The dashed lines in Figure 9-7 also show the effect of a higher permeability of the soil surrounding the weak layer. Owing to the faster dissipation of excess pore pressure, the pressure inside the landslide drops faster, and thus less viscous deformations develop.
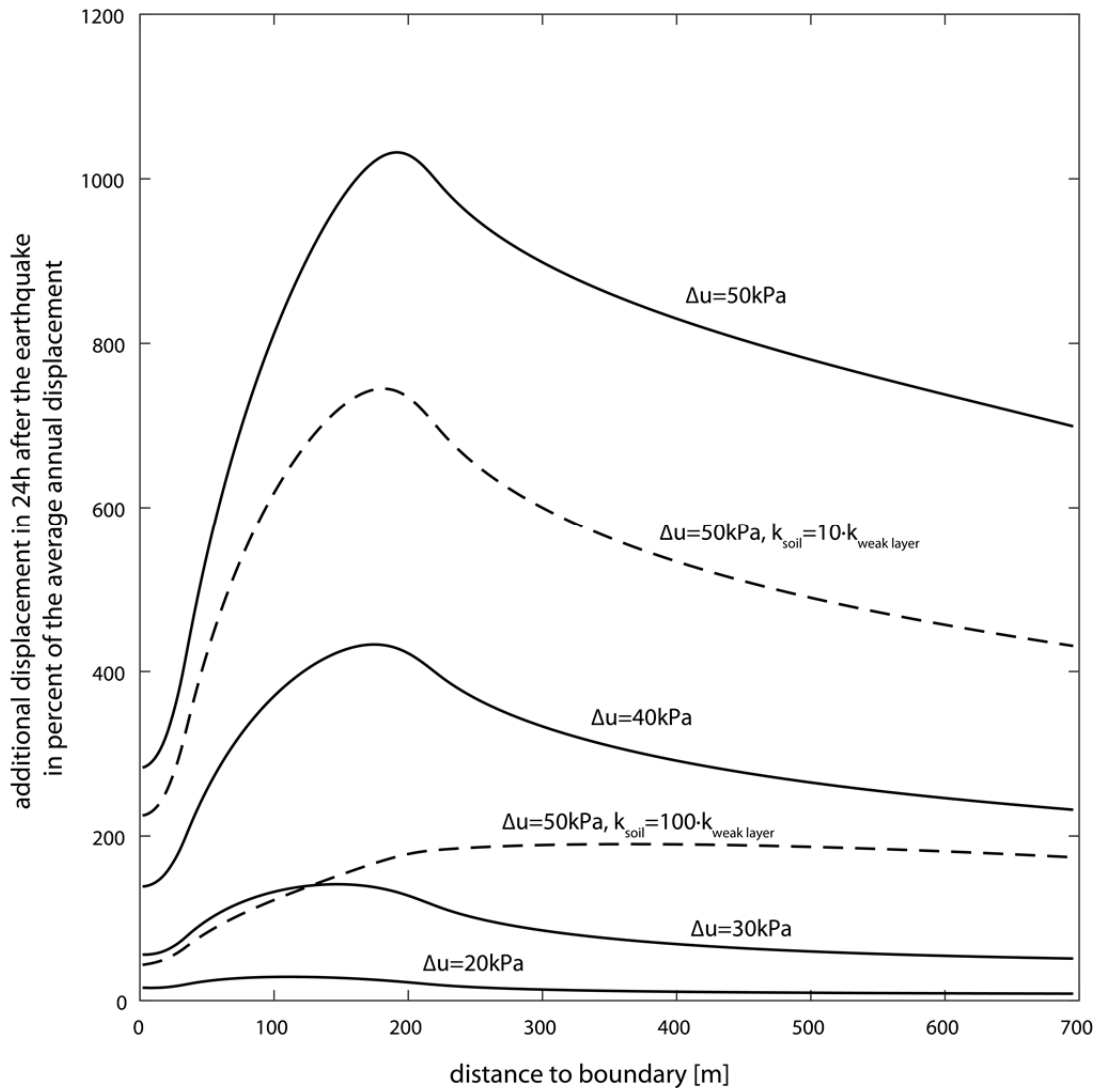
Figure 9-7: Development displacements due to excess pore pressures (Δu) after the earthquake

The results of the post-seismic landslide simulation must be viewed with care as there are large sources of uncertainty regarding the state of the landslide after the event. The question of how much more resistance can be mobilized within the compression zone at the landslide's foot is of particular importance. If the landslide can mobilize more strength in the foot zone, either owing to rate effects inside the landslide body or owing to geometrical effects (geometrical hardening), this could reduce the displacements not only during but also after the event.

Also, since the co-seismic model does not yet allow for elastic deformations along the landslide, potential elastic "pre-stressing" of the landslide, which again would cause post-seismic displacements to reduce, cannot be assessed. On the other hand, the rate at which excess pore pressures dissipate may be different if excess pore pressures developed not only

in the weak layer but also in other parts of the sliding body. Owing to the strong heterogeneity of the material in the Brattas case, this question is not easy to answer.

9.5   Summary and conclusion

As shown in part III, a conceptual model for creeping landslides with predefined slip surface under seismic loading has been developed. In its structure, the model can be viewed as an extension to the Newmark sliding block method. The model focuses on the zones where the displacement of the landslide is concentrated (slip surface) and the surrounding soil layer (weak layer), following the observation that in landslides with one predominant slip plane this plane often develops in a layer of weaker soil.

The model treats the two parts, the slip surface and the weak layer, separately in terms of constitutive models, but couples them through equilibrium of stresses, continuity of strains and pore pressures. For the two parts, constitutive models have been formulated.

For the model of the slip surface, the following points can be noted:

(i)   Owing to the residual state of the material, development of excess pore pressures in the actual slip surface has been neglected.

(ii)   The effect of rate-dependent shear strength has to be reproduced. The difficulty herein is that tests in which rate dependency can be estimated can often only be performed in a velocity range much smaller than that reached in an earthquake. For the same reason, inverse analysis from observations during the creep stage to estimate the rate dependency is difficult.

 For the model of the weak soil layers, the following points can be noted:

(i)   For the material surrounding the slip surface in the Brattas landslide, triaxial tests indicate a potential for the development of excess pore pressures. At the same time, permeability of the material in the landslide is low enough to assume that during an earthquake pore pressures cannot dissipate immediately.

(ii)   Data of triaxial tests cannot be used directly in the formulation of the boundary value problem. Therefore data from DSS-tests, which are believed to better reproduce the boundary conditions of the boundary value problem, from literature (Donahue, 2007) have been used to derive a model for soil types like those found in the Brattas landslide. By following the test data closely and ensuring thermo-mechanical consistency, the intention is to derive a model that is capable of reproducing approximately all the observed phenomena.

(iii)   The derivation of the model is demonstrated as a two-step process (simple and enhanced model). Though the complexity of the observed material behaviour makes a certain level of complexity in the final constitutive model unavoidable, the aim has been to keep this complexity to an acceptable level. Also, the derivation of the model has been done such that functions that control the development of the model parameters can be replaced. Similar to chapter 4, this procedure has been chosen to allow for some flexibility if the model needs to be updated, e.g. for the effects (neglected so far) of over-consolidation or rate dependency.

(iv)   The model can reproduce all important phenomena observed in undrained monotonic and cyclic DSS-tests for normally consolidated soil. In particular, asymmetric tests can be reproduced, which is important for the intended application in slopes.

(v)   All but two parameters can be derived from the analysis of undrained monotonic or cyclic DSS-tests. Simulation of the test, i.e. fitting of the model, is required only for two parameters.

(vi)   The model can be modified to be used in triaxial and potentially also general stress space. This requires data for different boundary conditions (triaxial, DSS, hollow cylinder tests) to ensure that the formulation still covers all important phenomena.

The conceptual model and the two constitutive models can be integrated into a numerical tool relatively easy. The tool has been calibrated for the situation of the Brattas landslide. Variations of several model assumptions have briefly been tested, and the model has shown to be relatively robust. In particular, variations of the boundary conditions in longitudinal direction do not influence the response significantly, which simplifies the analysis of large constrained landslides.

The results show that both excess pore pressures and co-seismic displacement correlate to Arias intensity. Therefore, the choice of representative input motions could be based on this parameter. A short analysis of post seismic behaviour has been demonstrated by applying the calculated excess pore pressures to the model of the landslide from chapter 5. The fact that, depending on the earthquake, the post-seismic displacements due to accelerated creep can be larger than the co-seismic ones, emphasizes the necessity to account for excess pore pressure development.

In general, the methodology allows the user to analyse permanent landslides during earthquake loading and to account for the development of excess pore pressure without using empirical assumptions. Also, the model does not need to virtually increase the strength

of the material to have a static safety factor larger than one, which is a prerequisite for the application of conventional Newmark analysis for creeping slopes.

The methodology proposed herein is still relatively easy to use, and starting from this formulation the model can and should be extended further to analyse e.g. the effect of excess pore pressure development in larger zones of the landslide body, or longitudinal wave propagation.

ACKNOWLEDGEMENTS

Appendix III.1: Necessary conditions to ensure thermomechanical consistency

In order to ensure that the dissipation function remains in any case positive it has been ensured that each term of the dissipation on its own remains positive rather than just the sum of terms. This is more rigorous than necessary but eases derivations. The following derivations are valid for positive free parameters $C_i > 0$ and $\sigma' > 0$:

$$d = \beta_1^0 \cdot \sigma' \cdot |\dot{\alpha}_\gamma^0| + \beta_{2,2}^0 \cdot \sigma' \cdot \dot{\alpha}_\gamma^0 +$$

$$\left[\left(\frac{M}{2}\right) \cdot L_1(C_1, a_1^1) + \frac{\beta_1^1}{K_2}\right] \cdot \sigma' \cdot |\dot{\alpha}_\gamma^1| + \left[\left(\frac{M}{2}\right) \cdot L_1(C_1, a_2^1) \cdot sign(\dot{\alpha}_\gamma^1) + \frac{\beta_2^1}{K_2}\right] \cdot \sigma' \cdot |\dot{\alpha}_\gamma^1| \geq 0 \qquad \text{(III.1-1)}$$

Since the β_1^0 is always larger than zero, consequently also

$$\beta_1^0 \cdot \sigma' \cdot |\dot{\alpha}_\gamma^0| \geq 0 \qquad \text{(III.1-2)}$$

The second term of III.1-1 can be expanded to

$$\beta_{2,2}^0 \cdot \sigma' \cdot \dot{\alpha}_\gamma^0 = -\mu_{kin} \cdot \left(C_4^0 \cdot L_1(C_3, |a_1^0|) \cdot \langle -\dot{\alpha}_\gamma^0 \cdot \alpha_\gamma^1 \rangle^0\right) \cdot \sigma' \cdot \dot{\alpha}_\gamma^0 =$$

$$= -\left(\frac{M}{2}\right) \cdot L_1(C_1, a_2^1) \cdot \left(C_4^0 \cdot L_1(C_3, |a_1^0|) \cdot \langle -\dot{\alpha}_\gamma^0 \cdot \alpha_\gamma^1 \rangle^0\right) \cdot \sigma' \cdot \dot{\alpha}_\gamma^0 \qquad \text{(III.1-3)}$$

Since $C_4^0 > 0$ and $L_1(C_3^0, a_2^0) > 0$, (8-119) becomes a function of a_2^0, $\dot{\alpha}_\gamma^0$ and α_γ^1. Noting that with (8-79), $sign(a_2^1) = sign(\mu_{kin}) = sign(\alpha_\gamma^1)$ and that $\langle -\dot{\alpha}_\gamma^0 \cdot \alpha_\gamma^1 \rangle^0 = 0$ for $sign(\dot{\alpha}_\gamma^0) = sign(\alpha_\gamma^1)$ the sign of $\beta_{2,2}^0$ can be analysed in the following table:

	$\dot{\alpha}_\gamma^0 > 0$	$\dot{\alpha}_\gamma^0 < 0$
$sign(a_2^1) = sign(\alpha_\gamma^1) > 0$	0	+
$sign(a_2^1) = sign(\alpha_\gamma^1) < 0$	+	0

Thus, it can be shown that the second term of (III.1-1) cannot become negative.

The third and fourth terms of (III.1-1) can then be rearranged to form

$$d^1 = \left(\frac{M}{2}\right) \cdot L_1(C_1, a_1^1) \cdot \sigma' \cdot |\dot{\alpha}_\gamma^1| + \left(\frac{M}{2}\right) \cdot L_1(C_1, a_2^1) \cdot \sigma' \cdot \dot{\alpha}_\gamma^1 + \frac{\beta_1^1}{F_2^1} \cdot \sigma' \cdot |\dot{\alpha}_\gamma^1| + \frac{\beta_2^1}{F_2^1} \cdot \sigma' \cdot |\dot{\alpha}_\gamma^1| \geq 0 \qquad \text{(III.1-4)}$$

Since $\beta_1^1 > 0$ and $F_2^1 > 1$, the third term can be left out of the dissipation function, and by substituting (8-81) it becomes:

$$d^1 = \left(\frac{M}{2}\right) \cdot L_1(C_1, a_1^1) \cdot \sigma' \cdot |\dot{\alpha}_\gamma^1| + \left(\frac{M}{2}\right) \cdot L_1(C_1, a_2^1) \cdot \sigma' \cdot \dot{\alpha}_\gamma^1$$
$$+ \frac{-\left(\frac{M}{2}\right) \cdot L_1(C_1, a_1^1) - \left(\frac{M}{2}\right) \cdot L_1(C_1, a_2^1) \cdot \text{sign}(\dot{\alpha}_\gamma^1)}{F_2^1} \cdot \sigma' \cdot |\dot{\alpha}_\gamma^1| \geq 0 \tag{III.1-5}$$

$$d^1 = \left(\frac{M}{2}\right) \cdot L_1(C_1, a_1^1) \cdot \sigma' \cdot |\dot{\alpha}_\gamma^1| + \left(\frac{M}{2}\right) \cdot L_1(C_1, a_2^1) \cdot \sigma' \cdot \dot{\alpha}_\gamma^1$$
$$- \frac{\left(\frac{M}{2}\right) \cdot L_1(C_1, a_1^1)}{F_2^1} \sigma' \cdot |\dot{\alpha}_\gamma^1| - \frac{\left(\frac{M}{2}\right) \cdot L_1(C_1, a_2^1)}{F_2^1} \cdot \sigma' \cdot \dot{\alpha}_\gamma^1 \geq 0 \tag{III.1-6}$$

which produces, with further rearrangement

$$d^1 = \left(\left(\frac{M}{2}\right) \cdot L_1(C_1, a_1^1) \cdot \sigma' \cdot |\dot{\alpha}_\gamma^1| + \left(\frac{M}{2}\right) \cdot L_1(C_1, a_2^1) \cdot \sigma' \cdot \dot{\alpha}_\gamma^1\right) \cdot \left(1 - \frac{1}{F_2^1}\right) \geq 0 \tag{III.1-7}$$

Since $F_2^1 \geq 1$ it is obvious that the second part of (III.1-7) remains positive at all times.

For the first part, it is clear that for $\text{sign}(\dot{\alpha}_\gamma^1) = \text{sign}\left(L_1(C_1, a_2^1)\right) \equiv \text{sign}(a_2^1)$:

$$\left(\left(\frac{M}{2}\right) \cdot L_1(C_1, a_1^1) \cdot \sigma' \cdot |\dot{\alpha}_\gamma^1| + \left(\frac{M}{2}\right) \cdot L_1(C_1, a_2^1) \cdot \sigma' \cdot \dot{\alpha}_\gamma^1\right) \geq 0 \tag{III.1-8}$$

whilst in the case of $\text{sign}(\dot{\alpha}_\gamma^1) \neq \text{sign}\left(L_1(C_1, a_2^1)\right) \equiv \text{sign}(a_2^1)$ the necessary condition to ensure that the part and thus the entire dissipation is positive is $L_1(C_1, a_1^1) \geq L_1(C_1, a_2^1)$. Since $a_1^1 > 0$ (see (8-45)) and $L_1(C_1, a_1^1) > 0$, the condition becomes $a_1^1 \geq |a_2^1|$.

From (8-45) and (8-46) it can be seen that $\dot{a}_1^1$ and $\dot{a}_2^1$ are both functions of $\dot{\alpha}_\gamma^1$:

$$\dot{a}_1^1 = F_1^1 \cdot |\dot{\alpha}_\gamma^1| \tag{III.1-9}$$

$$\dot{a}_2^1 = F_1^1 \cdot \dot{\alpha}_\gamma^1 \tag{III.1-10}$$

therefore it holds that

$$\dot{a}_1^1 \geq |\dot{a}_2^1| \ \forall \ \dot{\alpha}_\gamma^1 \tag{III.1-11}$$

and thus the dissipation function remains always positive for $a_1^1(t = 0) \geq |a_2^1(t = 0)|$.

Appendix III.2: Derivation of the estimate for parameter C4

Noting that, during unloading, only y_0 is active, the deviatoric strain increment during unloading in the "butterfly" cycles (see Figure 8-18) is given by

$$\Delta\gamma_{2-3} = \Delta\alpha_{\gamma,2-3}^0 = \frac{(\tau_3 - \tau_2) - \frac{M}{2} \cdot \tanh(C_1 \cdot a_2^1) \cdot (\sigma_3' - \sigma_2')}{h_0} \qquad \text{(III.2-1)}$$

From (8-37) it follows that in undrained tests the volumetric strain at the two stress states is given by

$$\varepsilon(\sigma) = -\frac{\kappa}{1 + e_0} \cdot \ln\left(\frac{\sigma'}{\sigma_0'}\right) \qquad \text{(III.2-2)}$$

and thus the volumetric strain increment is

$$-\Delta\varepsilon_{2-3} = \Delta\alpha_{\varepsilon,2-3}^0 = \varepsilon(\sigma_3') - \varepsilon(\sigma_2') = -\frac{\kappa}{1 + e_0} \cdot \ln\left(\frac{\sigma_3'}{\sigma_2'}\right) \qquad \text{(III.2-3)}$$

If a stress state $\eta > 0.5$ is reached in cyclic loading, the isotropic hardening part of y_1 can be assumed to have finished:

$$\mu_{iso} = \frac{M}{2}; \; \dot{\mu}_{iso} = 0 \qquad \text{(III.2-4)}$$

thus

$$\mu_{kin} = (\eta - 0.5) \cdot M \qquad \text{(III.2-5)}$$

Since the contraction factors of y_0 depend only on the state of y_1, they stay constant during unloading and can be approximated to

$$\beta_1^0 = |\mu_{kin}| \cdot \left(1 - L_2(C_2, |a_2^1|)\right) = |\eta_2 - 0.5| \cdot M \cdot \left(1 - L_2(C_2, |a_2^1|)\right) \approx 0 \qquad \text{(III.2-6)}$$

$$\beta_2^0 = \mu_{kin} \cdot (-C_4^0 - 1) = |\eta_2 - 0.5| \cdot M \cdot (-C_4^0 - 1) \qquad \text{(III.2-7)}$$

The volumetric strain during unloading is given assuming a linear function:

$$-\Delta\varepsilon(\sigma) = \Delta\alpha_\varepsilon^0 = \beta_2^0 \cdot \Delta\alpha_\gamma^0 \qquad \text{(III.2-8)}$$

$$-\frac{\kappa}{1 + e_0} \cdot \ln\left(\frac{\sigma_3'}{\sigma_2'}\right) = |\eta_2 - 0.5| \cdot M \cdot (-C_4^0 - 1) \cdot \frac{(\tau_3 - \tau_2) - |\eta_2 - 0.5| \cdot M \cdot (\sigma_3' - \sigma_2')}{h_0} \qquad \text{(III.2-9)}$$

and

$$C_4^0 \approx \frac{-\frac{\kappa}{1 + e_0} \cdot \ln\left(\frac{\sigma_3'}{\sigma_2'}\right) \cdot h_0}{|\eta_2 - 0.5| \cdot M \cdot \left((\tau_3 - \tau_2) - (\sigma_3' - \sigma_2')\right)} \qquad \text{(III.2-10)}$$

REFERENCES

Arias, A., 1970. A measure of earthquake intensity, in: Seismic Design for Nuclear Power Plants. pp. 438–483.

Broyden, C.G., 1965. A Class of Methods for Solving Nonlinear Simultaneous Equations. Math. Comput. 19, 557–593.

Donahue, J.L., 2007. The liquefaction susceptibility, resistance, and response of silty and clayey soils. PhD thesis, University of California Berkeley.

Donahue, J.L., Bray, J.D., Riemer, M.F., 2008. The liquefaction susceptibility, resistance, and response of silty and clayey soils - Report No. UCB/GT 2008-01. Berkeley.

Elgamal, A., Yang, Z., Parra, E., Ragheb, A., 2003. Modeling of cyclic mobility in saturated cohesionless soils. Int. J. Plast. 19, 883–905. https://doi.org/10.1016/S0749-6419(02)00010-4

Houlsby, G.T., 1992. Interpretation of dilation as a kinematic constraint. Modern approaches to Plasticity 119–138.

Houlsby, G.T., Mortara, G., 2004. A continuous hyperplasticity model for sands under cyclic loading, in: Cyclic Behaviour of Soils and Liquefaction Phenomena. Taylor & Francis, pp. 21–26. https://doi.org/10.1201/9781439833452.ch3

Houlsby, G.T., Puzrin, A.M., 2000. A thermomechanical framework for constitutive models for rate-independent dissipative materials. Int. J. Plast. 16, 1017–1047. https://doi.org/10.1016/S0749-6419(99)00073-X

Houlsby, G.T., Puzrin, A.M., 2002. Rate-dependent plasticity models derived from potential functions. J. Rheol. 46, 113. https://doi.org/10.1122/1.1427911

Laue, J., 2014. Allgemeine Konzepte des seismischen Entwurfs und der Bemessung in der Geotechnik mit Anwendung auf Hänge. Mitteilungen der Geotech. Schweiz 168, 37–52.

Mejia, L.H., Dawson, E.M., 2006. Earthquake deconvolution for FLAC. Proc. 4th Int. FLAC Symp. Numer. Model. Geomech. 1–9.

Newmark, N.M., 1965. Effects of Earthquakes on Dams and Embankments. Geotechnique 15, 109–129.

Pradel, D., Smith, P.M., Stewart, J.P., Raad, G., 2005. Case history of landslide movement during the Northridge earthquake. J. Geotech. Geoenviron. Eng. 131, 1360–1369. https://doi.org/10.1061/(ASCE)1090-0241(2005)131:11(1360)

Prevost, J.H., 1985. A simple plasticity theory for frictional cohesionless soils. Int. J. Soil Dyn. Earthq. Eng. 4, 9–17. https://doi.org/10.1016/0261-7277(85)90030-0

Puzrin, A.M., 2001. A thermomechanical framework for rate-independent dissipative materials with internal functions. Int. J. Plast. 17, 1147–1165. https://doi.org/10.1016/S0749-6419(00)00083-8

Puzrin, A.M., Houlsby, G.T.T., 2001. Fundamentals of kinematic hardening hyperplasticity. Int. J. Solids Struct. 38, 3771–3794. https://doi.org/10.1016/S0020-7683(00)00238-9

Puzrin, A.M., Schmid, A., 2011. Progressive failure of a constrained creeping landslide. Proc. R. Soc. A - Math. Phys. Eng. Sci. 467, 2444–2461. https://doi.org/DOI 10.1098/rspa.2011.0063

Schlüchter, C., 1988. Instabilities in the area of St. Moritz, Switzerland - Geology, chronology, geotechnology, in: Bonnard, C. (Ed.), 5th International Symposium on Landslides. Balkema, Lausanne, pp. 1375–1380.

SIA, 2014. SIA 261 - Einwirkungen auf Tragwerke. Schweizerischer Ingenieur- und Architekten-Verein, Zurich.

Yasuhara, K., Konami, T., Hyodo, M., Hirao, K., 1991. Scholars' Mine Earthquake-Induced Settlement in Soft Grounds Earthquake-Induced Settlement in Soft Grounds, in: Second International Conference on Recent Advances in Geotechnical Earthquake Engineering & Soil Dynamics.

Zergoun, M., Vaid, Y.P.P., 1994. Effective stress response of clay to undrained cyclic loading. Can. Geotech. J. 31, 714–727. https://doi.org/10.1139/t94-083

Ziegler, H., 1983. An introduction to thermomechanics. North-Holland Pub. Co.

NOTATION – PART III

α slope inclination

α_E internal variable corresponding to volumetric plastic strain at failure

α_ε internal variable corresponding to volumetric plastic strain

α_ε^i internal variable corresponding to volumetric plastic strain of yield surface i

a_j^i internal variable number j of yield surface i

α_Γ internal variable corresponding to plastic shear strain at failure

α_γ internal variable corresponding to plastic shear strain

α_γ^i internal variable corresponding to plastic shear strain yield surface i

B compaction (dilation) coefficient in failure

β compaction (dilation) coefficient

β_j^i compaction (dilation) coefficient number j of yield surface i

β_{HB} Herschel-Bulkley rate dependency function parameter

C_j^i constraint j of yield surface i

C_c consolidation index

C_s swelling index

C_n free parameter number n

c cohesional yield parameter

c_v consolidation coefficient

Δu excess pore pressure

d dissipation function

d' augmented dissipation

d_{wz} thickness of weak zone around slip surface

d_{ss} thickness of slip surface

e_0 initial void ratio

ε volumetric strain

F_j^i Functional number j of yield surface i

G	shear modulus
g	Gibbs free energy
γ	shear strain
$\dot{\gamma}_0$	Herschel-Bulkley rate dependency function parameter
h	hardening modulus
h_0	hardening modulus of surface 0
h_{sb}	thickness of the sliding body
h_w	depth of the phreatic surface
h_{sz}	thickness of the stable zone underneath the weak zone
η	normalized stress state
I_A	Arias intensity
k_s	permeability
κ	logarithmic bulk modulus
L	length of the landslide
L_b	length of boundary region
$L_i(A, x)$	Auxiliary (step) functions
Λ	Lagrange multiplier
M	frictional failure strength
m_v	constrained modulus
μ	frictional yield parameter
μ_{iso}	isotropic hardening frictional yield parameter
μ_{kin}	kinematic hardening frictional yield parameter
η_{HB}	Herschel-Bulkley rate dependency function parameter
σ'	effective normal stress
σ'_0	initial effective normal stress
τ	shear stress
v_s	shear wave velocity

v_{s30} shear wave velocity in top 30m of soil

$\chi^i_{\varepsilon,\gamma}$ dissipative generalized stress

$\bar{\chi}^i_{\varepsilon,\gamma}$ generalized stress

Part IV: Hazard and risk assessment for creeping landslides

Abstract

Chapter 10 proposes some ideas to perform a risk analysis for creeping landslides. In the first section, simple models to estimate exposures in terms of weather data and seismic impact are shown. The second half of the chapter then uses the models derived in the previous chapters in combination with the exposure functions in order to estimate the hazard posed by the landslide in the form of expected displacement. Vulnerability and consequences for the simple case of structures isolated from the landslide are provided. Lastly, a potential approach for structures that have a more complex interaction with the landslide is outlined briefly.

10 Application of phenomenological landslide models for the risk analysis of creeping landslides

10.1 Introduction

The previously derived models for the analysis of creeping landslide movements can be used to predict future development of these landslides. That means that the hazard in terms of potential future displacements of the landslide can be calculated.

The first part of this chapter (Section 10.2) shows potential probabilistic models for exposures in terms of future weather patterns and seismic loading. These models can be used as input for the landslide models in order to produce predictions for future displacement distributions.

Such distributions may then be used to assess risk to structures in the landslide. Some possibilities for assessing vulnerability and consequences for structures in creeping landslides are demonstrated, and exemplary proposals for risk assessment in creeping slopes are given.

All steps of the risk analysis process are demonstrated using the example of the Brattas landslide in St. Moritz but could be applied to landslides of similar properties at other locations.

10.2 Exposures

As shown in the previous chapters, the two main external influences apart from human factors that affect movement of the landslide are precipitation and earthquakes.

For precipitation, analysis of data from St. Moritz shows that mainly long-term precipitation patterns govern the behaviour of the landslide. That means that, at least according to the evaluated data, the landslide in St. Moritz seems not to be significantly sensitive towards extreme short-time precipitation events. Therefore, predictive modelling of precipitation influence needs to capture the long-term fluctuation, which means that it needs to preserve the long-term statistical properties of the weather patterns.

Unfortunately, many existing weather prediction models can only poorly account for inter-annual variability and do not allow the generation of monthly series of precipitation and temperature as is required for the long-term modelling of slow creeping landslides.

In order to estimate the effects of long-term variations, a simple weather generator for monthly weather data has been developed that allows the effect of varying long-term weather series on creeping landslides to be studied. However, any other effective precipitation data could be used as input to the model.

10.2.1 Weather model

In order to investigate long-term weather influence on creeping landslides, it is necessary to generate long-term series of monthly precipitation and temperature that can later be converted into series of effective precipitation, as shown in chapter 5. For that purpose, 151 years of weather data from the stations Samedan and Segl Maria (Source: Meteo Swiss) has been combined and analysed in order to find a statistically acceptable model for St. Moritz.

Precipitation:

First, 151 years of monthly precipitation data has been analysed by calculating Spearman's rank correlation coefficient (compare Piantadosi et al., 2009). For a 5% confidence level, it can be shown that monthly precipitation can be treated as independent random variables, as a correlation exists only for the months February, March and May, June (see Table 10-1)

Month	P value	Month	P value
Jan	0.699	Jul	0.319
Feb	0.032	Aug	0.366
Mar	0.132	Sep	0.360
Apr	0.577	Oct	0.727
May	0.008	Nov	0.834
Jun	0.247	Dec	0.178

Table 10-1: Spearman's correlation between precipitation of successive months (grey highlighted cells indicate correlation between successive months)

In order to model the amount of monthly precipitation, various different distributions have been evaluated in literature (e.g. Wilks and Wilby, 1999). The two-parameter Gamma distribution is a common choice to model daily and monthly precipitation and also is in good agreement with the data of the observed months:

$$P_{tot,i} = \Gamma(a_i, b_i) \tag{10-1}$$

The parameters for each month are given in Table 10-2. More complex probability distributions and different distributions for each month could be applied to better represent e.g. large rain amounts, but according to Wilks and Wilby (1999) this has little influence on the result.

Month	a	b	Month	a	b
Jan	1.0028	37.6442	Jul	6.6435	15.5029
Feb	1.2056	26.7204	Aug	4.5574	23.8849
Mar	1.6372	27.7936	Sep	2.0878	41.7857
Apr	2.1545	26.0407	Oct	1.406	58.8958
May	3.7441	20.687	Nov	1.4437	48.2766
Jun	4.9375	18.483	Dec	1.7852	25.8754

Table 10-2: Parameters for the Gamma distributions used to model monthly precipitation amount in St Moritz

Figure 10-1 shows the comparison between generated and observed monthly totals of precipitation for two months, indicating an acceptable agreement between model and observations.
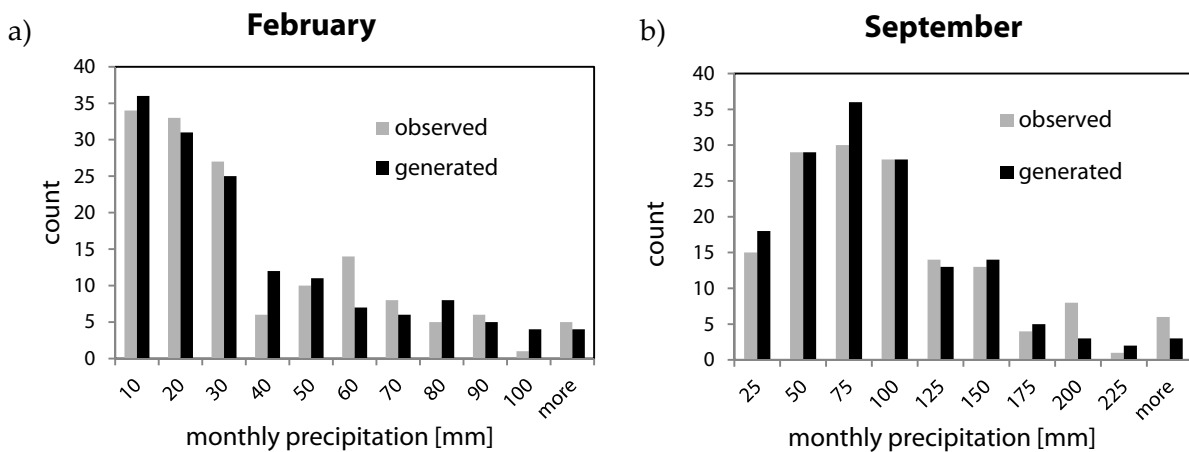
Figure 10-1: Comparison between observed and generated monthly precipitation for a) February and b) September

Trends in precipitation development are not considered for this investigation as the monthly data does not indicate either a strong decrease or strong increase in precipitation amount. Also, the Swiss climate scenario report states that uncertainty with respect to the trends of seasonal precipitation means is large, and until 2035 either an increase or a decrease is possible (CH2011, 2011).

<u>Temperature:</u>

In contrast to precipitation, monthly mean temperatures are usually correlated both with the mean temperature of the previous month (see Table 10-3) and the amount of precipitation during the month.

Month	P value	Month	P value
Jan	0.170	Jul	0.001
Feb	0.012	Aug	0.000
Mar	0.001	Sep	0.018
Apr	0.002	Oct	0.005
May	0.002	Nov	0.171
Jun	0.017	Dec	0.065

Table 10-3: Spearman's correlation between temperature of successive months (grey highlighted cells indicate correlation between successive months)

An autoregressive process (AR-model) can be used to model weather variables other than precipitation, in this case monthly mean temperature (compare Wilks & Wilby, 1999). In order to reflect the dependency of monthly mean temperature on the amount of precipitation, this model is extended by an explanatory variable, which is monthly precipitation, similar to Kilsby et al. (2007), resulting in a so called ARX-model which is derived for each month of the year (index $i = 1$ to 12):

$$\bar{T}_i = C_{1,i} \cdot \bar{T}_{i-1} + C_{2,i} \cdot \bar{P}_i + \varepsilon_i \tag{10-2}$$

where ε_i is a white noise term and $C_{j,i}$ are regression constants that are calibrated for each month separately in order to reflect seasonal dependence of temperature. $\bar{T}_i$ and $\bar{P}_i$ are the standardized monthly average temperature and monthly total precipitation:

$$\bar{T}_i = \frac{T_i - \mu_{T,i}(t)}{\sigma_{T,i}} \text{ and } \bar{P}_i = \frac{P_i - \mu_{P,i}}{\sigma_{P,i}} \tag{10-3}$$

with $\mu_{T,i}(t) = K_{1,i} \cdot t + K_{2,i}$

In (10-3) $\mu_{P,i}$ is the mean of the monthly precipitation, $\sigma_{P,i}$ and $\sigma_{T,i}$ are standard deviation of precipitation (P_i) and temperature (T_i). As can be seen from (10-3), the mean of the average temperature ($\mu_{T,i}(t)$) changes linearly with time (parameters $K_{1,i}$ and $K_{2,i}$), reflecting the climate change induced trend towards higher temperatures. In order to achieve a stationary time series, the observed trend is first removed from the temperature data, and subsequently the time series is standardized by dividing it by its standard deviation. The trend is treated here as a deterministic, therefore subtracting it from the data should preserve the properties of the AR-process (Yue and Pilon, 2003).

The regression constants $C_{1,i}$ and $C_{2,i}$ are found by minimizing the following equation:

$$\left(\bar{T}_{i,obs} - C_{1,i} \cdot \bar{T}_{i-1,obs} + C_{2,i} \cdot \bar{P}_{i,obs} \right)^2 = R^2 \tag{10-4}$$

where the subscript *obs* indicates the use of the observed temperature and precipitation data.

This simple formulation allows the generation of a series of monthly temperatures based upon previously generated monthly total precipitation.

Combined precipitation and temperature model:

The performance of the combined precipitation/temperature generation model was assessed by simulating the 151 years of observations. Figure 10-2 shows the comparison between observed quantiles and quantiles for 1000 generated series of 151 years of precipitation and temperature. Both mean values and variances can be captured acceptably well.
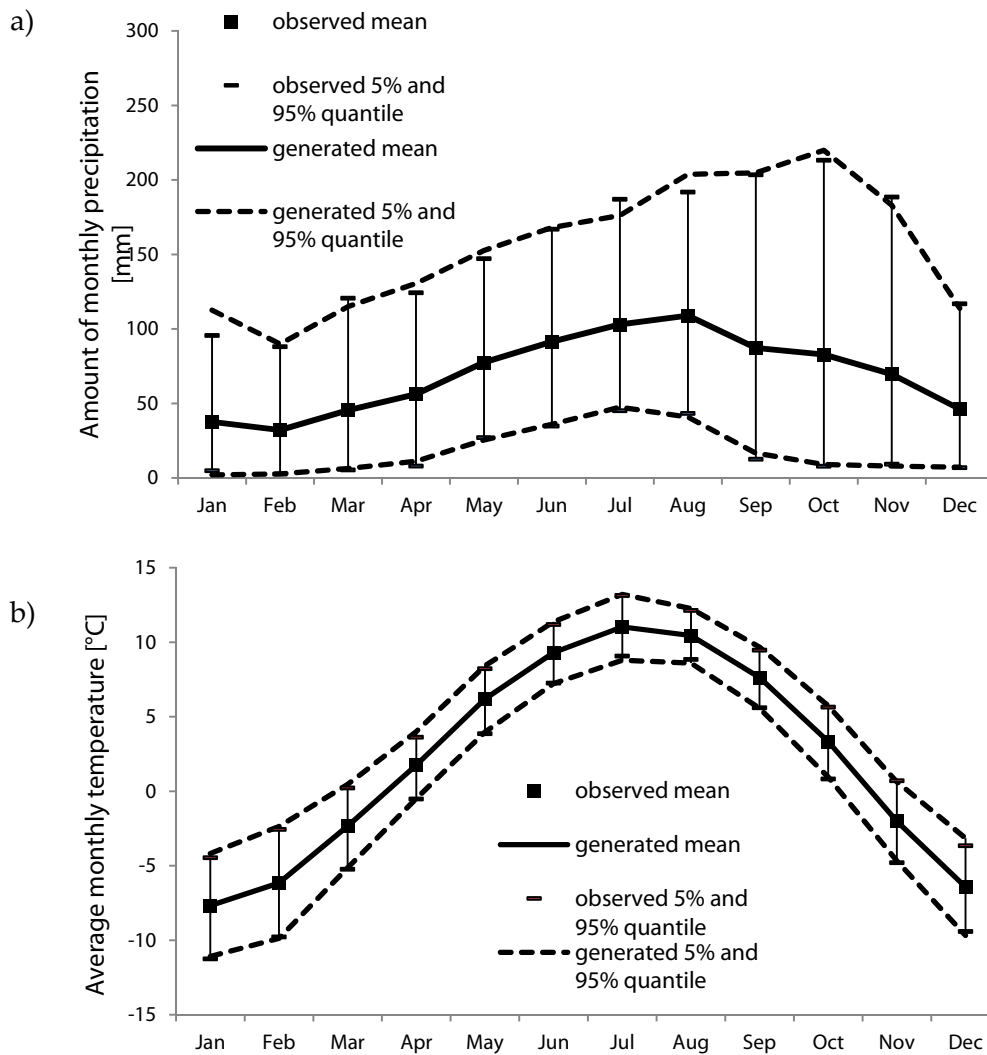
Figure 10-2: Comparison of observed and generated weather variables for *n* **= 1000 simulations: a) monthly precipitation; b) monthly average temperature**

Additionally, the model allows the correlation between precipitation amount and average temperature to be preserved (Figure 10-3).
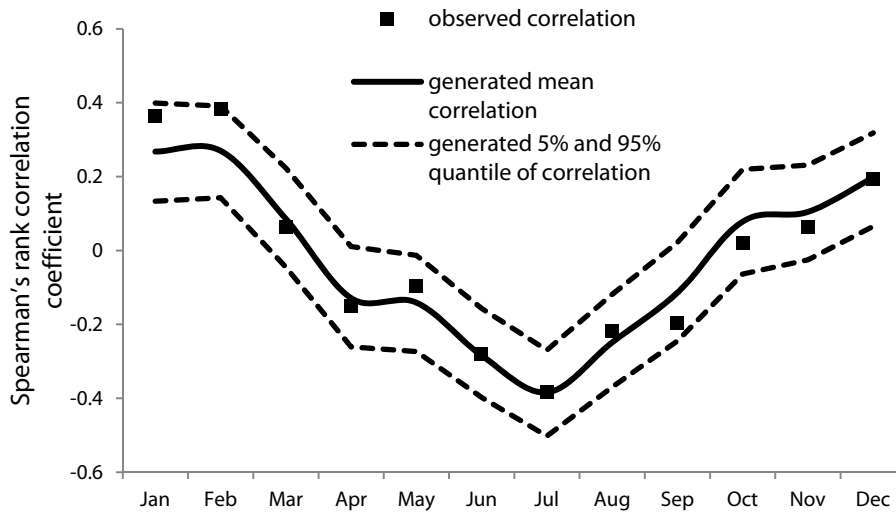
Figure 10-3: Comparison between observed and generated Spearman's rank correlation between precipitation amount and average monthly temperature coefficient for n = 1000 simulations

Also, the annual statistic can be preserved, which indicates that the generated precipitation series are applicable for long-term simulations as well. The distribution of annual precipitation amount (Figure 10-4) as well as the first two moments and the temperature trend of the annual weather data (Table 10-4) can be captured.
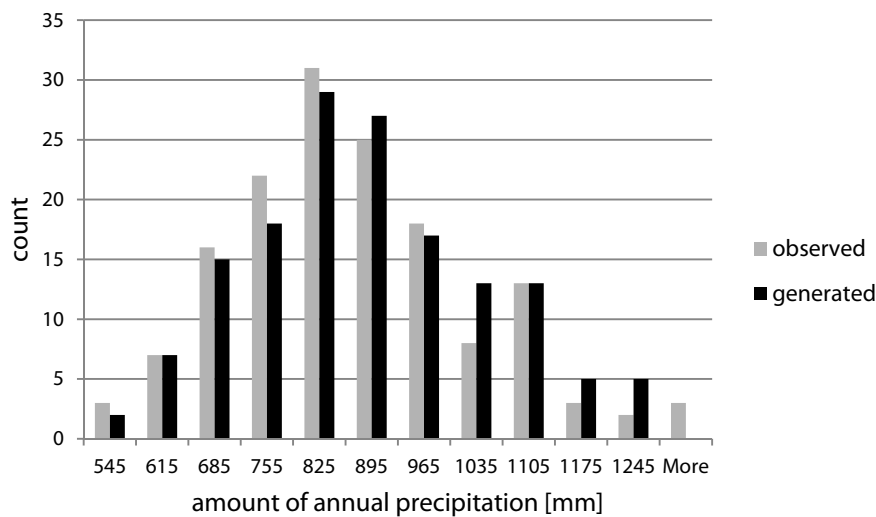
Figure 10-4: Comparison of observed and generated annual precipitation for 151 years

	Precipitation		Temperature		
	Mean	Std deviation	Mean	Std deviation	Trend
Observed	838 mm	165.3 mm	2.08 °C	0.671 °C	+0.01 °C/yr
Generated	838 mm	159.7 mm	2.09 °C	0.679 °C	+0.01 °C/yr

Table 10-4: Comparison between observed and generated annual statistics for $n = 1000$ simulations

Extreme monthly precipitation and snowmelt:

Extreme monthly precipitation or snowmelt was generated from distributions of precipitation or snowmelt. Since, for the Brattas landslide, low-frequency fluctuations imposed by snowmelt and monthly precipitation seem to govern the deformations of the landslide and the relation between daily precipitation and pore pressure fluctuations is not yet established, the investigation is limited to monthly extremes.

As an example, an analysis of snowmelts according to the simple snowmelt model from chapter 5 – precipitation stored in month with average temperature below freezing point and released in the first month with temperature above freezing point – was used to calibrate an extreme value distribution of snow water equivalents (SWE) to simulate strong snowmelt. Figure 10-5 shows the probability plot and cumulative distribution of the observed SWEs and a fit of a Gumbel distribution.
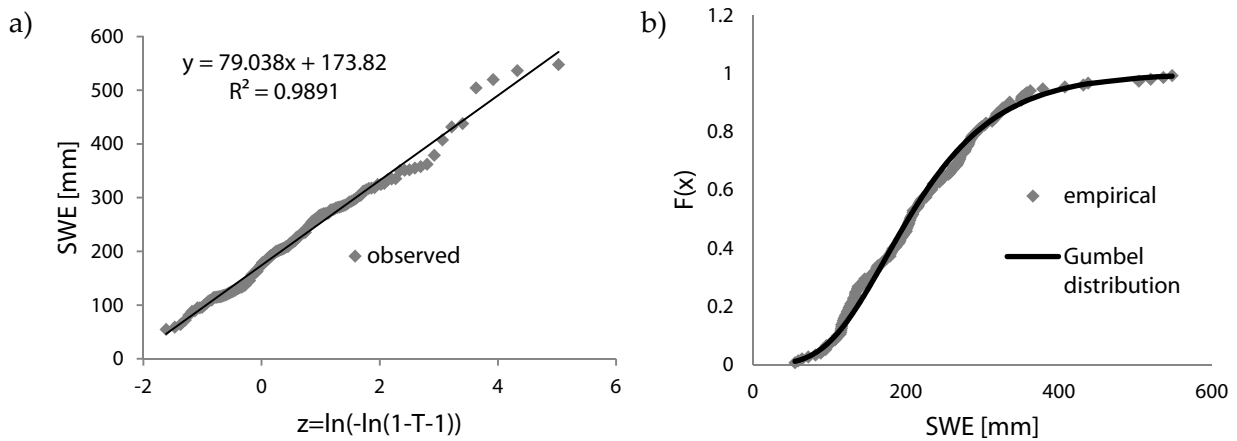
Figure 10-5: a) Gumbel probability plot and b) distribution for SWE during snowmelt

10.2.2 Seismic exposure

For the calculation of earthquake hazard, the input motions of the set from Laue (2014) have been used (see chapter 9). However, this does not yet allow one to choose motions that are representative within a certain time frame for a specific area of Switzerland.

Since, as shown in chapter 9, co-seismic displacements and excess pore pressure correlate with Arias Intensity, the easiest option to choose a seismic exposure would be to base it on Arias Intensity.

Unfortunately, the Swiss seismic hazard model (Wiemer et al., 2016) does not yet allow the probability to be derived for events of a certain Arias Intensity. A potential solution to this problem could be to derive the exposure based upon correlations of Arias Intensity and other seismic parameters of known probability. For example, Abrahamson et al. (2016) demonstrate how to estimate Arias Intensity from $v_{s\,30}$ (shear wave velocity in the upper 30 m of soil), magnitude, peak ground acceleration (PGA) and spectral acceleration at T=1s ($SA_{T=1}$) for the NGA-West 2 Ground Motion Model (Ancheta et al., 2014). If this correlation could be adopted for Swiss conditions, and disaggregated seismic hazard data is provided, exposure based on Arias Intensity could be calculated.

For the sake of demonstration, a simplified approach proposed by Abrahamson et al. (2016) has been used. In order to find Arias Intensity, PGA and $SA_{T=1}$ are taken from the design spectra of the Swiss codes (SIA 261, 2014) which have a return period of 475 years; the magnitude has been chosen so as to have the same return period (from www.seismo.ethz.ch). Since the co-seismic model has been run for input motions of rock and stiff soil sites, predicted Arias Intensity is also calculated for both types of site, but the difference is small (see Table 10-5).

	Rock input motions	Stiff soil site (Type B from SIA 261)
v_{s30} **[m/s]**	1400	650
Magnitude	6 (R < 50km)	6 (R < 50km)
PGA [g]	0.1	0.1
$SA_{T=1}$ **[g]**	0.1	0.15
Arias Intensity [m/s]	0.08	0.11

Table 10-5: Parameters and predicted Arias Intensity for design earthquakes at different soil sites

10.3 Hazard modelling

Using the exposure models described in 10.2 in combination with the landslide models derived in chapters 5 and 9, hazard given in the form of expected displacements for the Brattas landslide can be calculated. In the following section, expected displacement will be produced using either synthetic long-term monthly weather patterns or data for extreme monthly precipitation and snowmelt amounts.

10.3.1 Long-term simulations with weather exposure

The synthetic weather data generated according to the models described in section 10.2.1 can be converted to effective precipitation input (accounting for winter and snowmelt) according to the procedure shown in chapter 5. The generated input is then applied to the calibrated model of the landslide.

This allows the long-term behaviour of the landslide to be modelled and allows one to assess the influence on the variability of the predicted displacements due to precipitation patterns. Additionally, the influence of climate change can be studied e.g. by applying synthetic precipitation and temperature from different time periods.

Figure 10-6a shows the expected displacement distribution in the vicinity of the leaning tower in St. Moritz 10 years from a starting point in 2016, using weather data also generated for the period 2016 to 2026.

Figure 10-6b shows the same prediction, only using weather data generated for the period 1950–1960. As can be seen, the predicted displacement distribution for the weather data 2016–2026 has slightly lower mean value (see Figure 10-6c) than the one simulated with data from 1950–1960.

This observation results from the fact that owing to generally higher temperatures but constant precipitation amount, the effective precipitation decreases. Since effective precipitation is the main driver of the landslide, a drop in effective precipitation leads to a drop in pore pressures on the slip surface and therefore a smaller velocity of the landslide.
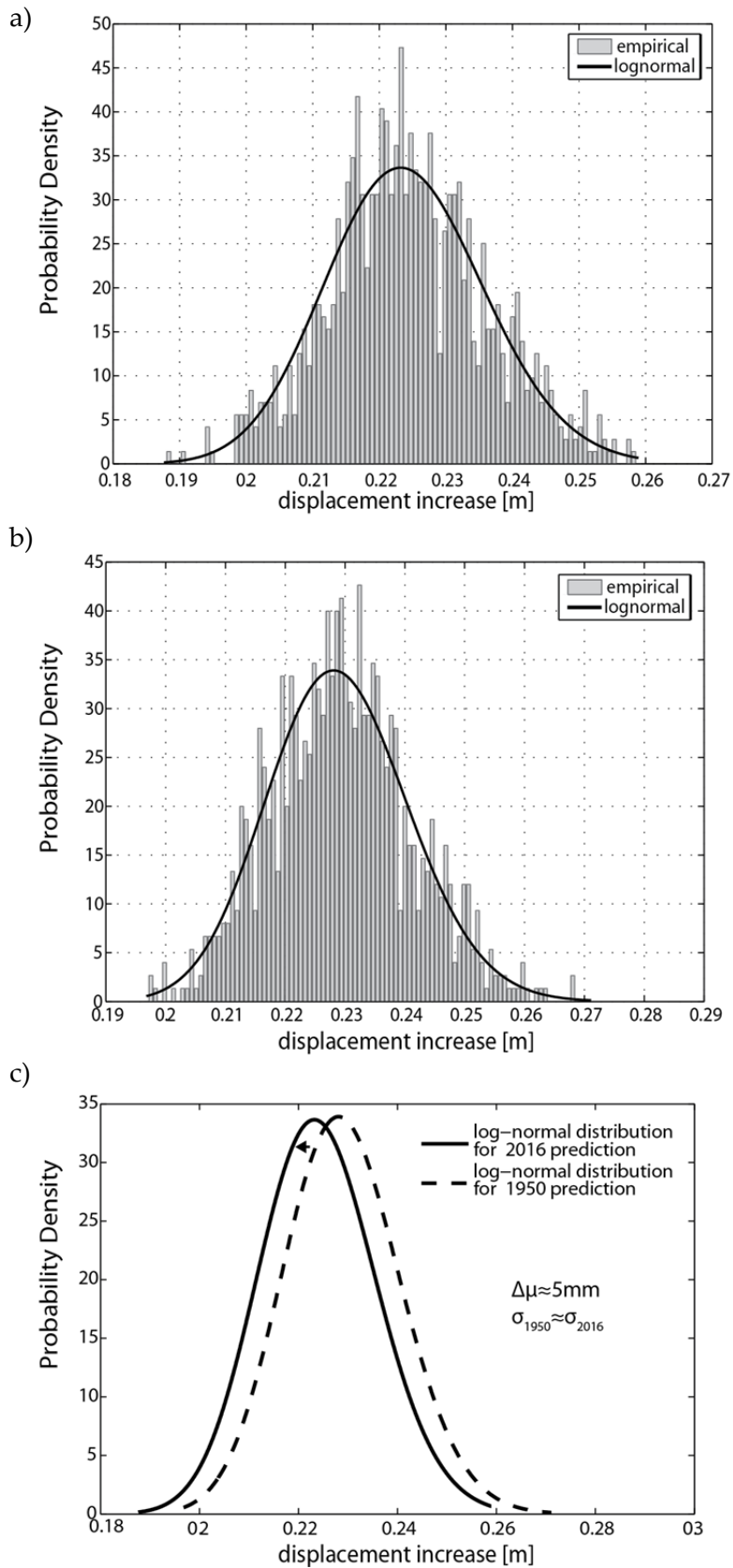
Figure 10-6: Expected distribution of displacement increase near the leaning tower for 10 years: a) precipitation data generated 2016–2026; b) precipitation data generated 1950–1960; c) comparison of probability distributions

To compare the results generated using the probabilistic weather model, change factors for temperature and precipitation provided by the Swiss meteorological service (Meteo Swiss) have been used. These seasonal change factors can be applied to monthly temperature and precipitation data for the period 1980–2009 and result in data that is representative for the period 2021–2050 (CH2011, 2011). For the missing years between 2016 and 2021, data from the past 5 years has simply been repeated. To compare the results, the data from 1980–2009 is also applied without change factors, forming a base scenario (without further climate change).

Change factors for several climate change scenarios are given and, depending on the scenario used, predictions show a small increase or decrease in predicted landslide displacements (Figure 10-7). This confirms the results of simulations with synthetic precipitation data.
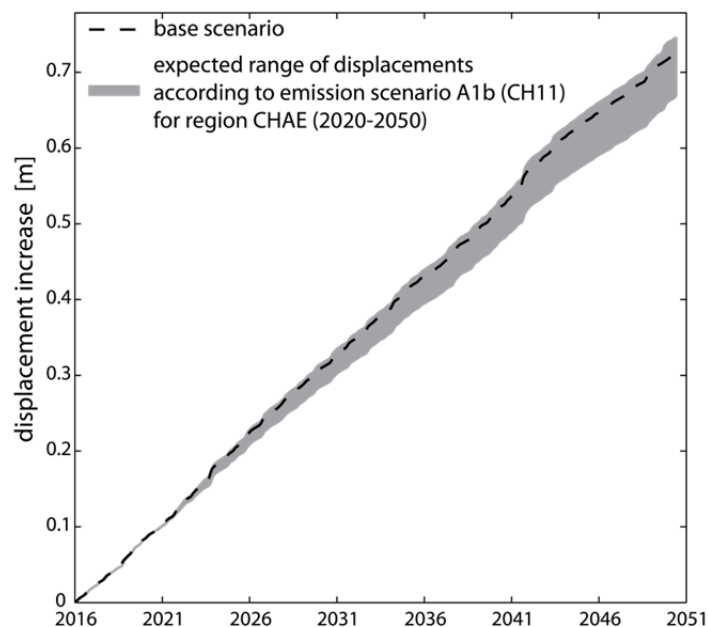
Figure 10-7: Predicted range of displacements for temperature and precipitation modified according to Swiss climate change scenarios (CH2011, 2011) in the vicinity of the leaning tower

These results could be interpreted as if changing climate may not have an adverse effect on the creep behaviour of the slope. However, this impression might be wrong. First of all, the influence of more frequent extreme precipitation events is still unclear. Periods of concentrated rain would potentially be less affected by evapotranspiration, and thus the effect of higher temperature would diminish. Besides a change in precipitation patterns, other phenomena might also cause more displacement to accumulate. For example, higher temperatures might cause the snow above the landslide to melt faster in spring, causing the snowmelt-induced peak of pore pressures to be even larger. But these phenomena are difficult to quantify as of now, and more observations as well as a better hydrological understanding of the landslide and its surroundings will be required.

10.3.2 Extreme snowmelts and autumn precipitation

With the distributions for monthly precipitation amount and extreme snowmelt, rainy months and severe snow melt events can be investigated. In 2009, the eighth largest snowmelt according to the simplified snowmelt model has been observed. Figure 10-8a shows, for 2009, the modelled reaction to snowmelt amounts of various return periods (including the observed amount with return period of 19 years).

Similarly, the effect of rainy autumn months (the second reason for larger fluctuations of the pore pressures) has been investigated (Figure 10-8b).

For both cases, the model predicts different reactions to the extreme exposure depending on the foregoing stress history of the landslide and the long-term fluctuations of the phreatic surface. In Figure 10-8b, it can be seen that the same amounts of October precipitation create a different reaction in 2007 and 2009. This emphasizes the need for observations along the entire length of the landslide in order to capture and validate long-term behaviour and interaction between different parts of the landslide.

a)

b)
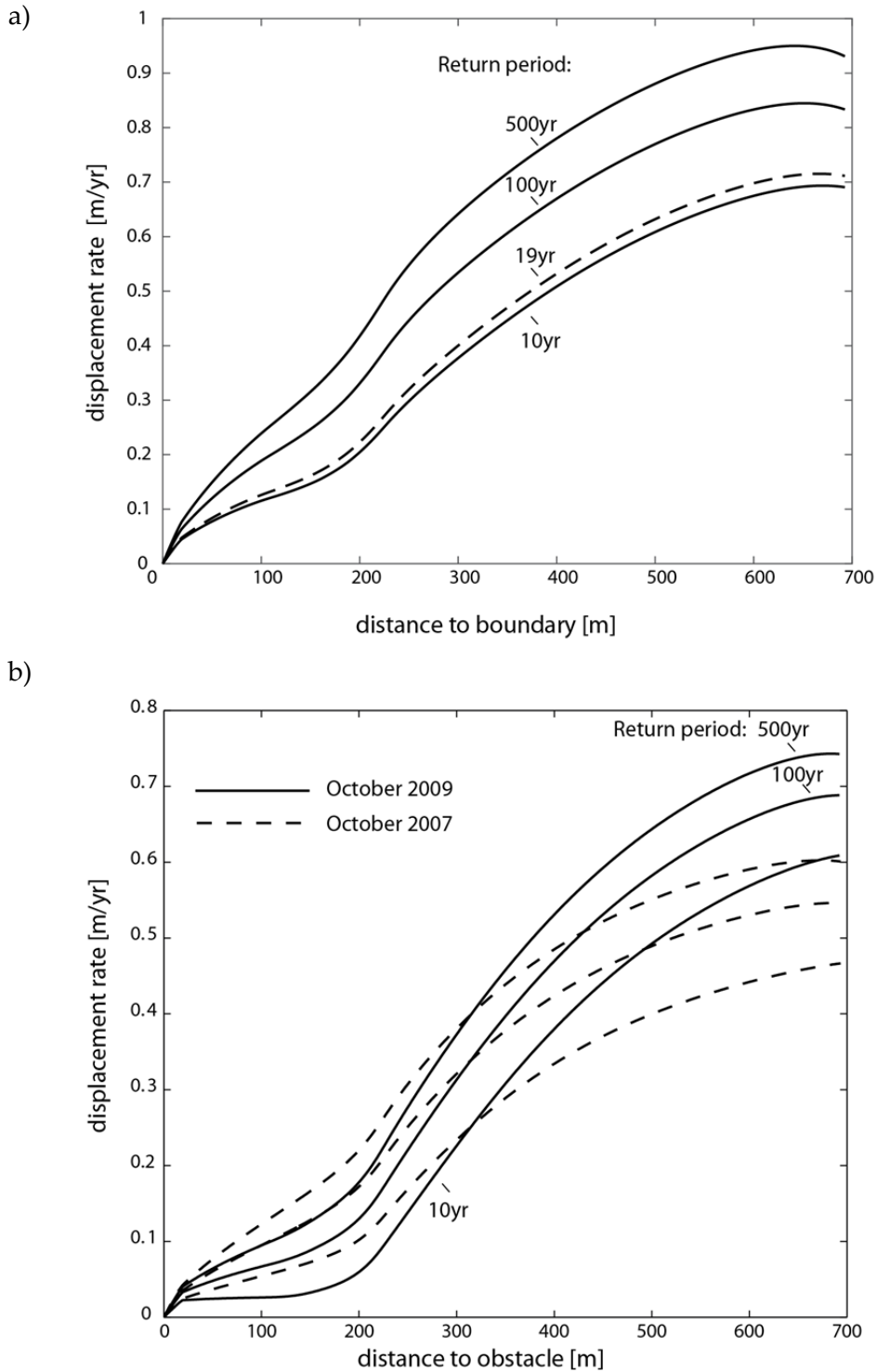
Figure 10-8: a) Modelled reaction to snowmelts of various return periods in 2009; b) modelled reaction to amounts of rain of varying return periods in the years 2009 and 2007

10.3.3 Earthquake loading

In order to assess the hazard given by the displacement due to an earthquake, the relation established in chapter 9 can be used. As an example, a linear function has been fitted to the co-seismic displacement ($\delta_{co-seismic}$) – Arias Intensity (I_A) data (Figure 10-9):

$$\delta_{co-seismic} = A \cdot I_A \tag{10-5}$$

with $A = 0.1179\ [s]$

A logarithmic relation relates excess pore pressure (Δu) to Arias Intensity (I_A) data from chapter 9 (Figure 10-10):

$$\Delta u = B \cdot \ln(I_A) + C \tag{10-6}$$

with $B = 6.50\ [kPa]$ and $C = 42.59\ [kPa]$

The functions allow the estimation of expected co-seismic displacement and excess pore pressure for a given exposure in terms of Arias Intensity.
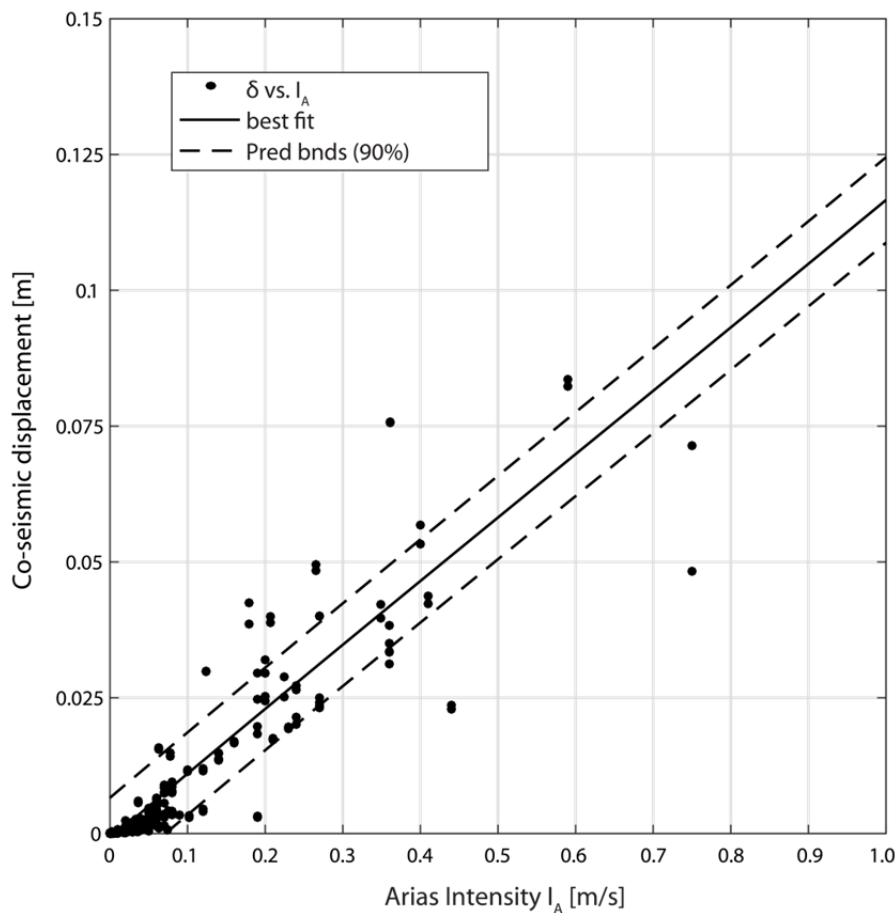
Figure 10-9: Co-seismic displacement vs. Arias intensity (*I_A*)
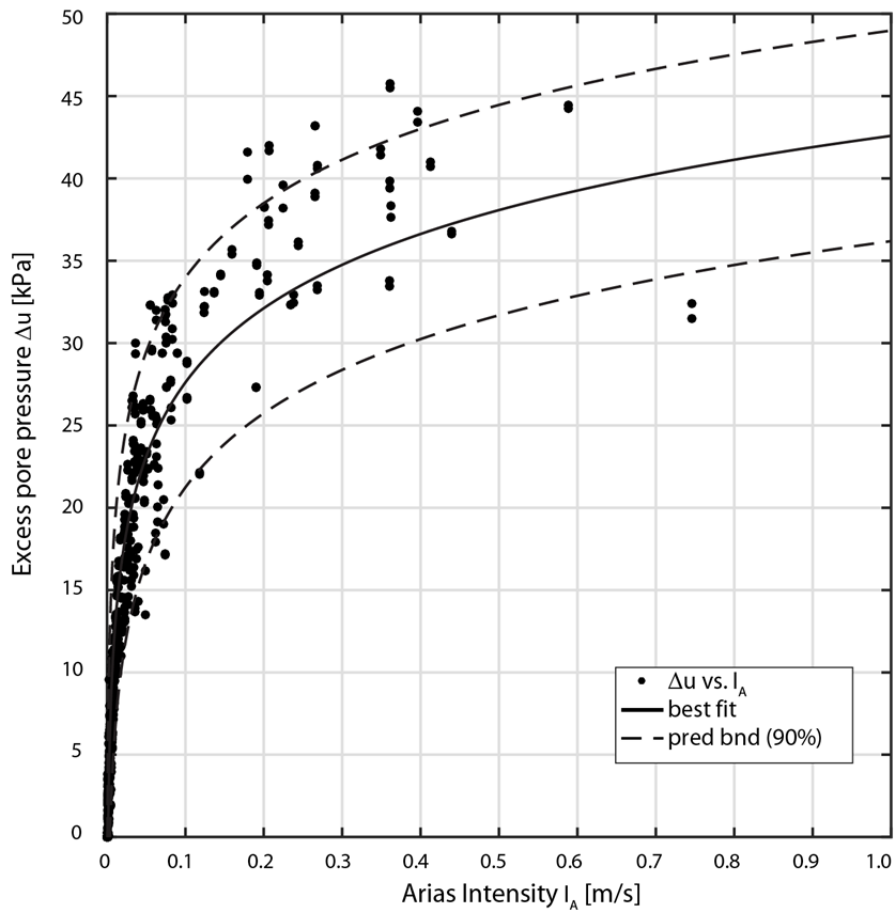
Figure 10-10: Excess pore pressure (Δu) vs. Arias Intensity (I_A)

For the exposure scenario of 10.3.3 with Arias Intensity of around 0.1m/s, a co-seismic displacement of approx. 2cm and excess pore pressure of about 34kPa can be found. According to section 10.4, post-seismic displacements of 100–200% of the annual average have to be expected in 24 hours after the earthquake.

10.4 Analysis of vulnerability and risk for structures in creeping slopes

In order to assess the risk associated with creeping landslides, the consequences and vulnerability of elements at risk have to be determined. In general, the risk to humans can be neglected as long as the landslide is only creeping. However, structures within the creeping soil mass are continuously damaged. Thus it is necessary to relate movements of the landslide (hazard) to damages caused to structures. This is not an easy task, as reliable models do not yet exist, and information about the damage state and characteristics of existing structures in creeping slopes is often difficult to obtain.

In principle, three construction strategies to cope with creeping landslides can be distinguished:

(i)   Isolating of the structure from the landslide

(ii)   Allowing the deformation of the structure by the landslide

(iii)   Resisting the deformations of the landslide

10.4.1 Vulnerability in the case of isolation from the landslide or acceptance of movements

For structures isolated from the landslide, the vulnerability function can, for example, be defined in terms of accumulated displacements:

$$V = P\big(D|\delta_{ls}(t)\big) \tag{10-7}$$

where $P(D|\delta_{ls})$ is the probability of a certain damage (D) given that the structure has experienced the displacements δ_{ls} of the landslide.

In cases where the structure moves with the landslide (accepting movement), often the damage process is governed not by the total displacement of the landslide but by the differential displacements ($\Delta\delta_{ls}$) that are imposed by the landslide on a structure. Thus (10-7) becomes

$$V = P\big(D|\Delta\delta_{ls}(t)\big) \tag{10-8}$$

Since both total and differential displacements in a creeping landslide are functions of time, the damage is related to the development of displacements in time. For an isolated structure, the vulnerability function can often be written in a very simple form:

$$V = \begin{cases} 0 \; for \; \delta(t)_{ls} < \delta_{limit} \\ 1 \; for \; \delta(t)_{ls} \geq \delta_{limit} \end{cases} \tag{10-9}$$

which indicates that the structure does not get damaged until a limiting displacement (δ_{limit}) is reached. Once this limit is reached, the structure loses its functionality and either the entire structure or the isolating measures need to be renewed. There are a number of examples for

such structures: the "Ganter Bridge" at the Simplon Pass is founded on hollow cylinder caissons that can move with the landslide. The actual piers of the bridge are connected such that they can be corrected once they have reached a certain deflection (Puzrin et al., 2012).

10.4.2 Risk assessment example: The leaning tower of St. Moritz

In order to assess the risk for specific structures, the hazard in terms of displacements derived in 10.3, the structure-specific vulnerability function and consequences have to be combined. In the following paragraphs, this process is demonstrated for the case of the leaning tower in St. Moritz.

For the leaning tower in St. Moritz, since 1983, a strategy which can be viewed as a combination of isolation and acceptance has been used. The historical structure has been founded on two later-installed concrete plates, and thus the actual tower is isolated from the landslide. The two foundation plates are allowed to move with the landslide; consequently, for the entire structure, the displacements due to the landslide are accepted. At the same time the tower has been pre-stressed to allow a relatively large amount of tilt. Since the foundation plates not only move with the landslide but also rotate, the connection between the foundation and the historic tower has been designed such that it allows the correction of some of the tower inclination induced by the landslide movement. Thus, similar to isolated structures, whenever a certain limiting inclination θ_{limit} which correlates with the landslide displacement is reached, the tower has to be stabilized, i.e. the inclination has to be reduced. The limiting inclination has been determined by the community of St. Moritz and by experts, in the form of maximum acceptable overhang (d_{limit}) at level of the bell chamber ($h_{bc} = 21.3$m):

$$d_{limit} = \theta_{limit} \cdot h_{bc} \tag{10-10}$$

The associated costs for the stabilization are given by the costs for design and execution of the stabilization works. The vulnerability for the leaning tower can be written as:

$$V_{leaning\ tower} = \begin{cases} 0\ for\ \theta_{tower} < \theta_{limit}\ with\ \dot{\theta}_{tower} \sim \dot{\delta}_{ls} \\ 1 for\ \theta_{tower} \geq \theta_{limit}\ with\ \dot{\theta}_{tower} \sim \dot{\delta}_{ls} \end{cases} \tag{10-11}$$

θ_{tower} is the inclination and $\dot{\theta}_{tower}$ the increase in inclination of the tower that correlates linearly with the increase in displacement of the landslide in the area $\dot{\delta}_{ls}$. The correlation is given in terms of tower inclination as:

$$\theta_{tower,t} = \theta_{tower,t-1} + \int_{t-1}^{t} \dot{\delta}_{ls} \cdot K_{ls-\theta}\ dt \tag{10-12}$$

with $K_{ls-\theta}$ being the correlation coefficient that relates landslide movement to tower inclination.

This relation can also be written in terms of tower deflection:

$$d_{tower,t} = d_{tower,t-1} + \int_{t-1}^{t} \delta_{ls} \cdot K_{ls-\theta} \cdot h_{bc} \, dt = d_{tower,t-1} + \int_{t-1}^{t} \delta_{ls} \cdot K_{ls-d} \, dt \qquad (10\text{-}13)$$

Consequently, the risk associated with the tower can be written in terms of landslide displacement:

$$R_{leaning\ tower} = P(\theta_{tower} \geq \theta_{limit}|E) \cdot V(\theta_{tower} \geq \theta_{limit}) \cdot C_{stabilization} \qquad (10\text{-}14)$$

This can be rewritten with (10-11) and (10-12):

$$R_{leaning\ tower} = P(\delta_{ls} \geq \delta_{limit}|E) \cdot C_{stabilization} \qquad (10\text{-}15)$$

where E is the exposure, e.g. the future precipitation distribution and $C_{stabilization}$ is the cost for the stabilization of the tower.

Stabilization works at the tower and its surrounding walls can alter the correlation between displacements and inclination. During the first stabilization, the works were limited to the connections between tower and foundation, and therefore the relation between landslide movements and tower inclination or deflection remained almost the same.

For the second stabilization, some earthworks have also been performed and more importantly, around the same time, the surrounding walls have been renewed, both of which seem to have influenced the tower rotation more than the previous stabilization. Therefore, some observations may be necessary after a stabilization to re-establish the correlation for future predictions. After 3 years of observations, a new correlation coefficient has been determined which can be used for first predictions but may be adapted again once more information becomes available. Figure 10-11a shows the observed and predicted tower deflection and the correlation coefficients. In Figure 10-11b, the expected distribution of tower inclination for the year 2031 is shown. The results can be represented with a log-normal distribution from which the probability of exceeding the limit of 2m deflection can be calculated to 4%.

For an earthquake, the lack of information with respect to uncertainties of the seismic exposure does not allow a comprehensive risk analysis. But for the event with 475-year return period (section 10.2.2), a total displacement (co-seismic and post-seismic) of approximately 6cm of the landslide in the vicinity of the tower can be estimated which would cause 1cm additional deflection due purely to landslide displacement.
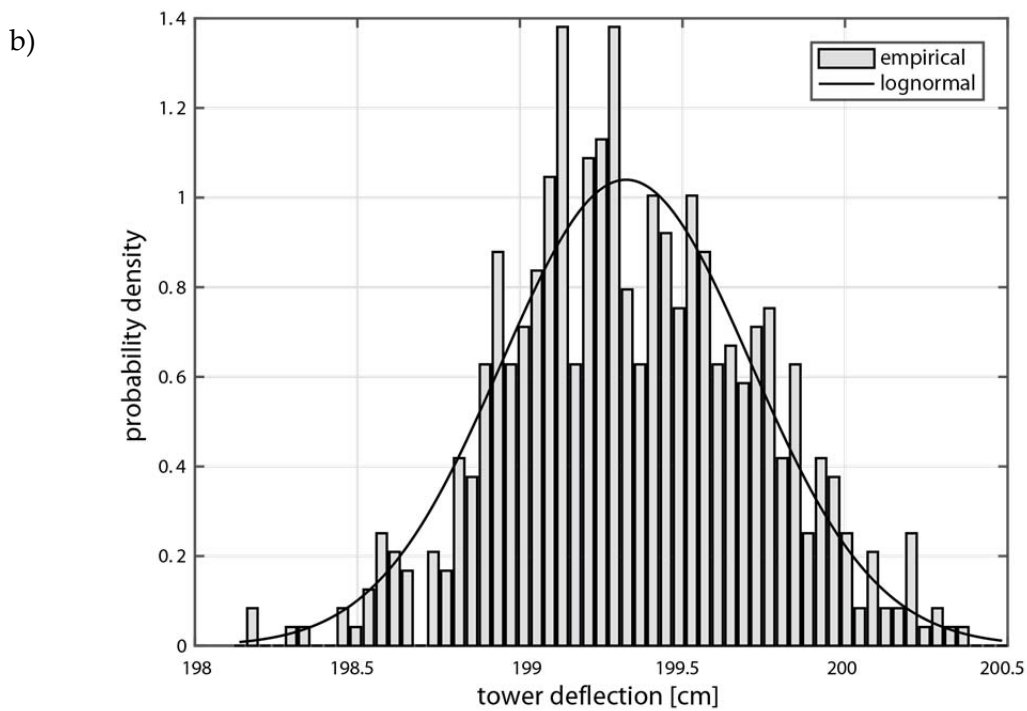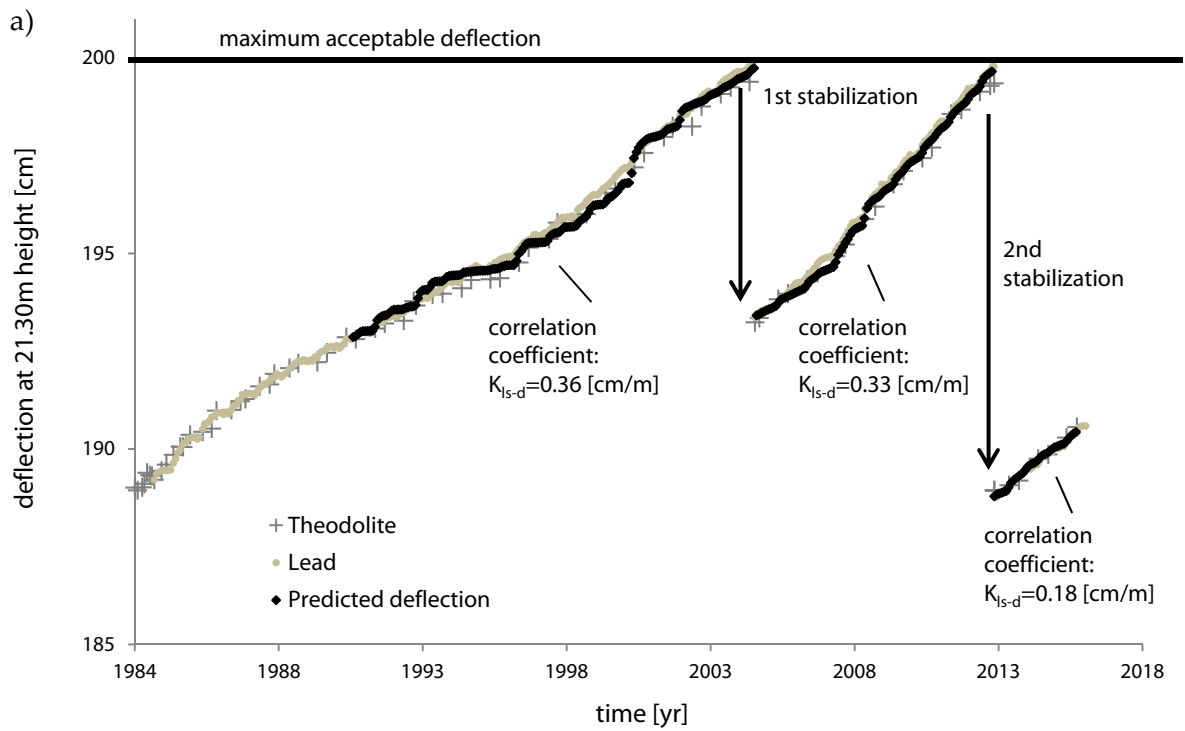
Figure 10-11: a) Observed and predicted deflection of the bell chamber of the leaning tower for the years 1984–2016; b) predicted distribution of tower inclination for *n* = 1000 simulations with the exposure model shown in 10.2.1 in 15 years

10.4.3 Outlook: Risk assessment for structures embedded in the landslide

For structures that are built to resist the movements of the landslide, vulnerability and risk cannot simply be assessed purely via displacements, but the interaction between structure and landslide needs to be taken into account.

In landslides that are compressing (i.e. a velocity increases from the bottom to the top), like the Brattas landslide, pressure on structures that resist the landslide movements increases. The pressure on the structure will grow until either visco-elastic load redistribution allows the velocity field to homogenize around the structure or one of four collapse scenarios occurs:

(i)   failure of the soil not involving the structure (global failure of the landslide)

(ii)   collapse of the structure

(iii)   failure of the soil and the soil–structure interface around the structure, e.g. the structure starts "slipping"

(iv)   combined failure of soil and structure

During the time until one of the scenarios occurs, pressure on the building increases and damage grows. Estimating the vulnerability of structures as function of damage vs. displacements is difficult and, as mentioned in chapter 2, so far only empirical relations exist (e.g. Palmisano et al. (2016), Uzielli et al. (2015)).

Another way to approach vulnerability and subsequently risk assessment for existing structures could be to estimate the ultimate loads that can be provided by the creeping landslide (before soil fails) and to compare them to the structural resistance.

For structures built into creeping slopes but founded in stable ground, e.g. retaining walls, Friedli et al (2017) were able to derive a complete solution for the pressure that can be provided by the landslide. For structures that are not founded deep enough to reach stable ground and can be treated simply as rigid blocks inside a compressing landslide body, Hug et al. (2017) used upper bound limit analysis and finite element simulations to calculate the pressure that can ultimately act on them.

Their calculations allow the calculation of the theoretical ultimate load acting on structures in creeping landslides. This load can then be compared to the ultimate resistance of a structure. Provided the uncertainties with respect to structural and soil parameters can be quantified, the probability of collapse can be calculated. The vulnerability function remains in this case binary with $V = 1$ in the case of collapse (full realization of damage) and 0 in the case of no collapse.
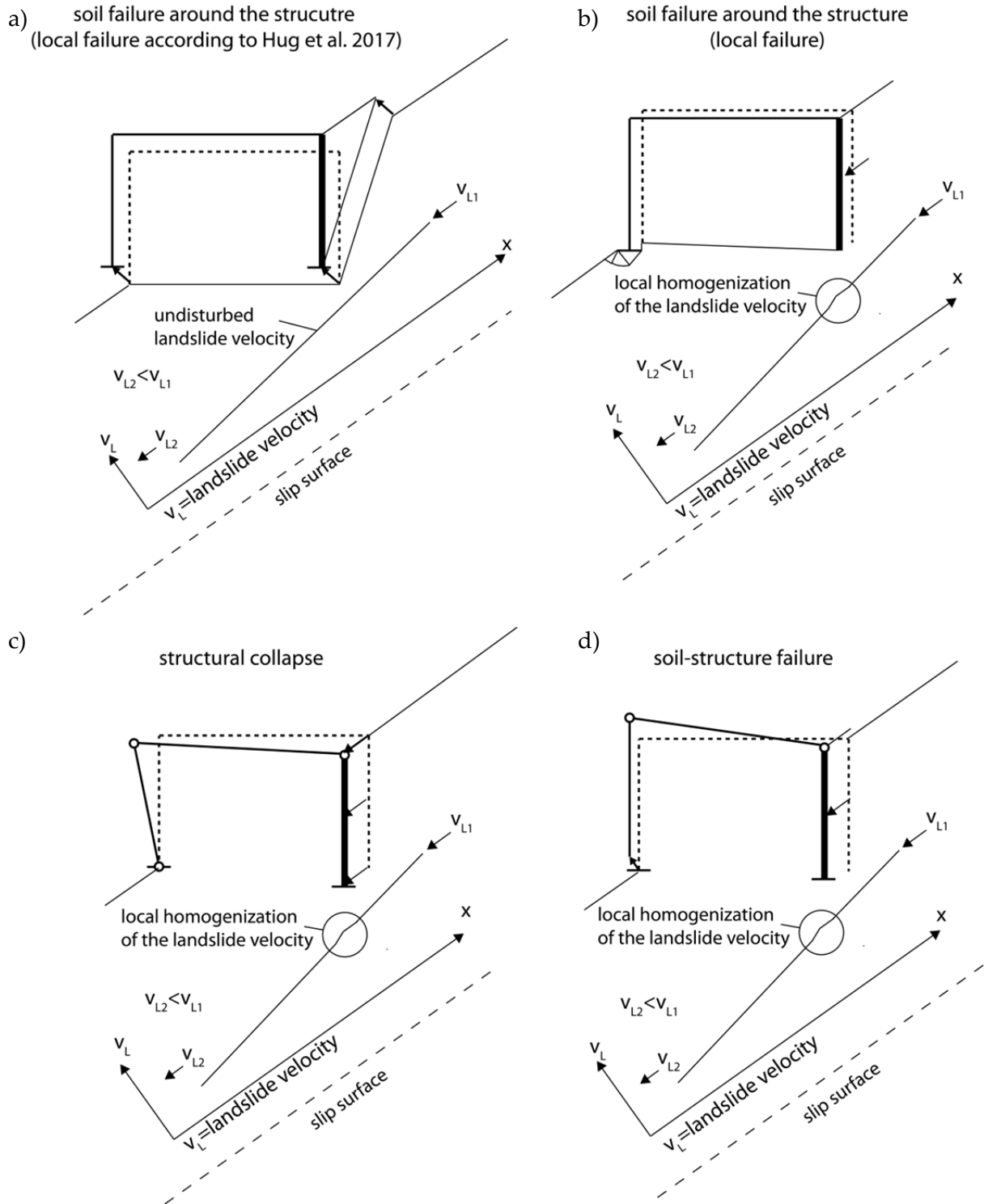
Figure 10-12: Example for collapse mechanisms of frame structures in creeping landslide: a) local mechanism according to Hug et al. 2017; b) local failure mechanism without failure behind the upslope wall; c) structural collapse; d) combined soil–structure failure

However, Hug et al. (2017) simplified the structure in the landslide as a rigid block; therefore, their approach requires further work in order to use it for the assessment of more complex structures. For example, the seemingly simple case of a moment resisting frame

allows an illustration of how the methodology could be developed further and of the questions that can arise.

In Figure 10-12a), the mechanism according to Hug et al. (2017) applied to a frame structure is given. As can be seen, this mechanism allows the velocity distribution (v_L) of the landslide to remain unchanged. However, it is uncertain whether failure always needs to involve the entire vicinity of the structure or whether a small velocity gradient can be accommodated without failure (e.g. through visco-elastic load redistribution).

In contrast to Figure 10-12a), Figure 10-12 b) to d) assume that the velocity gradient at the upslope wall of the house is not large enough to cause failure of soil, which is the case if the velocity field can locally homogenize owing to visco-elastic load redistribution. Therefore a failure of structure or soil is necessary only over the length of the entire frame to accommodate the difference in velocity, potentially leading to smaller forces acting on the frame than the original mechanism. Additional numerical and analytical work is required to determine which mechanism becomes governing and how loads are distributed in the structure.

Lastly, it has to be noted that for a full risk assessment the time-dependent development of pressure needs to be investigated. This means that in cases where calculations indicate that the resistance of the structure will ultimately be exceeded, the time necessary for this pressure to develop is still unknown. Hug et al. (2017) performed a first attempt of quantification by relating pressure to strain in the landslide, but further research in this field is necessary.

Overall, assessing structures in terms of their limit state (analytical or numerical) instead of trying to assess risk by correlating damages to displacements seems to be a promising extension to existing approaches. As said, more limit states, also including 3D situations, could be analysed, and guidelines for the assessment of structures could be derived.

10.5 Conclusions

The simulations of the landslide models performed here, in combination with exposures in terms of weather and seismic loading, allow several first conclusions to be drawn:

Exposures and Hazard:

(i)   Uncertainty is introduced into the model of the landslide only with respect to the exposures. Complexity of the model did not yet permit to investigate in depth parameter or model uncertainty.

(ii)   Weather prediction models as they exist today are often intended for the generation of shorter time periods and in relatively small time steps (days or hours). However, for application in simulations of very slow landslides, long-term data would be necessary that reproduces long-term fluctuations of precipitation and temperature correctly. Also, to simplify calculations, generation of data with larger time steps would be favourable. Of course, the correct time step should be determined case-specifically, as smaller landslides are likely to react more strongly to short time precipitation changes.

(iii)   For the Brattas landslide and probably other alpine landslides, snowmelt is the strongest driver in terms of pore pressure changes throughout the year. Records indicate that short-time (hourly and daily) heavy rains do not cause larger displacements. Only long-lasting wet periods could cause pore pressure changes similar to snowmelts.

(iv)   If the landslide is solely driven by the rainwater balance, reduction of effective precipitation due to increasing temperatures (climate change) reduces the velocity of the landslide slightly.

(v)   In order to choose suitable seismic exposures, it should be provided in terms of Arias intensity which seems to correlate best with co-seismic displacement and excess pore pressure. Alternatively, region-specific input motions for given return periods would be necessary.

(vi)   Provided that exposures in terms of precipitation or earthquakes are available, an estimate of the hazard posed by the landslide in form of expected displacements can be generated.

Vulnerability and Risk:

(i)   For structures isolated from the landslide, risk can be derived easily if hazard in terms of displacement is given.

(ii)   For other structures, definition of vulnerability remains challenging, as the complex interaction between structure and landslide needs to be taken into account. The approach by (Hug et al., 2017) seems promising to be able to assess the limit state of a

structure, provided enough knowledge about the structure is available. The approach could be extended in order to treat the structure not just as a rigid block inside the landslide, but also e.g. to allow for combined failure mechanisms of soil and structure.

ACKNOWLEDGEMENTS

REFERENCES

Abrahamson, C., Michael Shi, H.-J., Yang, B., 2016. Ground-Motion Prediction Equations for Arias Intensity Consistent with the NGA-West2 Ground-Motion Models (Report). Berkeley.

Ancheta, T.D., Eeri, M, Darragh, R.B., Stewart, J.P., Seyhan, E., Silva, W.J., Chiou, B.S.-J., Wooddell, K.E., Graves, R.W., Kottke, A.R., Boore, D.M., Kishida, T., Donahue, J.L., Eeri, M., 2014. NGA-West2 Database. Earthq. Spectra 30, 989–1005. https://doi.org/10.1193/070913EQS197M

CH2011, 2011. Swiss Climate Change Scenarios CH2011 (Report). Zurich.

Friedli, B., Hauswirth, D., Puzrin, A.M., 2017. Lateral earth pressures in constrained landslides. Géotechnique 1–16. https://doi.org/10.1680/jgeot.16.P.158

Hug, S., Friedli, B., Oberender, P., Puzrin, A.M., 2017. Ultimate loads on buildings in landslides. Géotechnique 1–34. https://doi.org/10.1680/jgeot.17.p.134

Kilsby, C.G., Jones, P.D., Burton, A., Ford, A.C., Fowler, H.J., Harpham, C., James, P., Smith, A., Wilby, R.L., 2007. A daily weather generator for use in climate change studies. Environ. Model. Softw. 22, 1705–1719. https://doi.org/10.1016/j.envsoft.2007.02.005

Laue, J., 2014. Allgemeine Konzepte des seismischen Entwurfs und der Bemessung in der Geotechnik mit Anwendung auf Hänge. Mitteilungen der Geotech. Schweiz 168, 37–52.

Palmisano, F., Vitone, C., Cotecchia, F., 2016. Methodology for Landslide Damage Assessment. Procedia Eng. 161, 511–515. https://doi.org/10.1016/j.proeng.2016.08.679

Piantadosi, J., Boland, J., Howlett, P., 2009. Generating synthetic rainfall on various timescales-daily, monthly and yearly. Environ. Model. Assess. 14, 431–438. https://doi.org/10.1007/s10666-008-9157-3

Puzrin, A.M., Schmid, A., Schwager, M. V, Eberhardt, E., Froese, C., Keith Turner, A., Leroueil, S., 2012. Case studies of constrained creeping landslides in Switzerland, in: 11th International Symposium on Landslides and Engineered Slopes ISL. Taylor & Francis Group, Banff, Canada, pp. 1795–1800.

SIA, 2014. SIA 261 - Einwirkungen auf Tragwerke. Schweizerischer Ingenieur- und Architekten-Verein, Zurich.

Uzielli, M., Catani, F., Tofani, V., Casagli, N., 2015. Risk analysis for the Ancona landslide— II: estimation of risk to buildings. Landslides 12, 83–100. https://doi.org/10.1007/s10346-014-0477-x

Wiemer, S., Danciu, L., Edwards, B., Marti, M., Fäh, D., Hiemer, S., Wössner, J., Cauzzi, C., Kästli, P., Kremer, K., 2016. Seismic Hazard Model 2015 for Switzerland (SUIhaz2015). Zurich. https://doi.org/10.12686/a2

Wilks, D.S., Wilby, R.L., 1999. The weather generation game: a review of stochastic weather models. Prog. Phys. Geogr. 23, 329–357. https://doi.org/Doi 10.1177/030913339902300302

Yue, S., Pilon, P., 2003. Interaction between deterministic trend and autoregressive process. Water Resour. Res. 39. https://doi.org/10.1029/2001WR001210

NOTATION – PART IV

C   cost of repair

D   damage

d deflection of the leaning tower

Δu excess pore pressure

$\Delta \delta$ relative displacement

δ displacement

E exposure

$\Gamma(a_i, b_i)$ two parameter Gamma distribution

h_{bc} height of the bell chamber of the leaning tower

θ inclination of leaning tower in St. Moritz

I_A Arias Intensity

$\mu_{P,i}$ mean monthly precipitation of month i

$\mu_{T,i}$ mean monthly average temperature of month i

P_i amount of precipitation in month i

$\bar{P}_i$ standardized amount of precipitation in month i

$P(\ldots | \ldots)$ conditional probability

PGA   peak ground acceleration

$\bar{T}_i$ standardized temperature of month i

T_i monthly average temperature of month i

$SA_{T=1}$ spectral amplification at T=1s

$\sigma_{P,i}$ standard deviation of precipitation of month i

$\sigma_{T,i}$ standard deviation of temperature of month i

V vulnerability

v_L velocity of the landslide

v_{s30} shear wave velocity in top 30m of soil

11 Conclusions and outlook

11.1 Summary and main results

Modelling and predicting the behaviour of creeping (constrained) landslides remains a challenging task, in particular when it comes to exceptional loading situations.

Because of the lack of knowledge with respect to geometry, material parameters and interactions, reproducing the behaviour of such landslides is difficult. During this thesis, several conceptual models have been formulated in order to capture the behaviour of creeping landslides in different loading situations.

The demonstrated approaches reproduce the observed and expected behaviour of creeping landslides in different loading situations reasonably well. They allow simple hazard and risk assessment to be performed for creeping landslides and can form the basis for further development of modelling and risk analysis tools.

For the different problems that have been assessed, the following conclusions can be drawn.

Part II: Development of a method to analyse the steady and transient state of creeping landslides

An approach for the derivation of models for creeping landslides under the influence of precipitation and snowmelt has been shown. The landslide is treated herein as a visco-elastic-plastic slab moving on a so-called slip surface, which is the boundary between stable and unstable soil. Existing visco-elastic-plastic material models for the sliding body and the slip surface have been combined and further extended to create a modelling framework that allows a constitutive model to be built for the landslide from simple visco-elastic and visco-plastic elements in order to reproduce its movements.

Laboratory experiments do not allow testing of material from the landslide at a scale that is even close to the scale of the problem, which would be necessary to analyse the very heterogeneous material found in many alpine landslides. Therefore, in this work it is proposed that the calibration of the landslide model should, whenever possible, be done by using observations of the landslide itself ("observation-guided constitutive modelling"). The data gained from observations can be complemented with data from laboratory experiments for the parts where observation of the material behaviour is not possible (e.g. the slip surface).

Calibration of the model should take into account fluctuations of the load in terms of pore pressure fluctuation in the landslide, since, during the early development of the approach, it became clear that a model that can reproduce the load fluctuation may be significantly different from a model that reproduces only the steady state.

To simulate the fluctuations of pore pressure, data from piezometers can be used. If such data is not available or if the goal is to expose the landslide model to data of precipitation patterns, a relation between pore pressure fluctuations and precipitation is necessary. In this work, a simple hydrological relation between effective precipitation and fluctuation of the phreatic surface was sufficient to allow reproduction of the behaviour of the landslide used as a case study, the Brattas landslide in St. Moritz.

Whilst calibrating the model, it has also been found that it is important to use as complete an observational data set as possible. For the case of the Brattas landslide, it was only possible to calibrate the constitutive model and in particular the hydrological model correctly by complementing the data from observations at the landslide foot with data from the upper parts of the landslide.

The approach has made it possible to find a suitable model for the Brattas landslide, whose behaviour is relatively complex, particularly at its lower end where it is stopped by a rock outcrop and heavily overbuilt. The complexity of observed phenomena requires the approach to be pushed quite far but also shows that, despite the simplicity of the model parts, even complex behaviour with variations over time and space can be reproduced.

Part III: Analysis of seismic impact on creeping slopes

Whilst the approach for finding a model in part II is heavily based on field observations of the landslide, this is not possible if earthquake loading of the landslide is investigated. In general, this problem has had only very little attention so far, and no established approach has been found during the course of this thesis.

In order to gain a first insight into this problem, the problem formulation is simplified to a sliding body on top of the slip surface, as already established in part II. Since cyclic tests on material from the layer around the slip surface show a potential for the development of excess pore pressure, the model has been extended by introducing a weak soil layer around the slip surface in which excess pore pressures can develop. Since the material of the sliding body is very stiff, heavily compressed and heterogeneous, focus has been set on modelling the behaviour in the weak layer and the slip surface.

For the slip surface, the rate-dependent increase of shear strength has been modelled based on laboratory results.

For the weak layer, the development of excess pore pressure has been the focus. Here a model based on test data from literature has been derived. Since it was unclear in advance which phenomena were most important, the model aims to reproduce all observations as well as possible. This makes a certain complexity of the formulation unavoidable; but by

using only two yield surfaces and relating phenomena and formulations it has been tried to outline the influence of each of the functions of the model.

The constitutive models have subsequently been integrated into a modification of Newmark's sliding block model. This model has been run for the conditions of the Brattas landslide. It can be shown that the boundary conditions at the foot of the landslide do not have great influence, which is to be expected for long landslides. The model makes it possible to calculate co-seismic deformations and excess pore pressure development. Additionally, the model from part two and the estimated excess pore pressure calculated via the seismic model can be combined to estimate post-seismic deformations. The simulations indicate that these deformations can be significant.

In general, the model allows for a relatively easy extension of the well-known Newmark sliding block model. This allows a first estimate to be obtained for the deformations and excess pore pressures developing in a landslide during and after an earthquake.

Part IV: Hazard and risk assessment for creeping landslides

In the final part, the applicability of the previously derived methods for hazard and risk analysis of creeping landslides has been investigated.

In terms of exposures, it should be mentioned that the existing Swiss methods for weather generation or determining representative earthquakes seem not yet to be suitable to be used for the application shown herein.

Since simulations of the landslide model indicate that long-term precipitation patterns have more influence on the development of the landslide than short-term extremes, for weather generation a model that can produce long-term series with correct variations is important. Similar to what has been found in other research, the effect of climate change causes a slight deceleration of the landslide, provided that weather is the only influence taken into account.

With respect to earthquakes, it can be shown that both excess pore pressures and deformations correlate reasonably well with Arias Intensity. Therefore, this would be a suitable parameter to be used in a probabilistic analysis of the problem.

The models derived in the previous parts allow for multiple simulations in reasonable time; thus, they can be used in order to estimate hazard in terms of displacement of the landslide. Displacement can subsequently be used to calculate the probability that a structure will reach its limit state, provided that this limit state can be expressed in terms of absolute or relative displacements. For structures for which the ultimate limit state cannot be expressed in terms of deformations, assessing the vulnerability and consequences is still difficult. One approach that has briefly been outlined is to investigate the limit states of soil and structures

in terms of loads and compare them, provided that the structure can be simplified sufficiently.

11.2 Future research

Two approaches for the investigation of landslides under the influence of precipitation and earthquake loading have been proposed. The derived models reproduce the behaviour phenomenologically and provide a basis for the assessment of creeping landslides, given different loading scenarios. Additional research into the topic of creeping landslides would make it possible to enhance the developed approaches and rule out uncertainties with respect to assumptions and simplifications made in this work.

11.2.1 Future research: Modelling of creeping landslides (non-seismic)

To further develop the approach of observation-guided constitutive modelling and the use of simplified phenomenological models to predict landslide motions, but also for any other attempt to model creeping landslides reliably, collection of more data from different sites is crucial.

Therefore, it would be favourable if data about this specific hazard could be collected and stored more systematically. Based on this work, the following minimum requirements for future data collection can be formulated:

(i)   Displacements should not be measured solely at one point in the landslide but along axes that cover the length and width of the landslide. This allows assessment of whether the landslide deforms uniformly.

(ii)   Measurements should be performed until sufficient data is collected to understand the landslide's behaviour. This means that the reaction to annual and monthly precipitation changes can be identified and also the reaction to extreme precipitation has been observed.

(iii)   For first time observations, the temporal resolution of the observations must be high enough to be able to analyse the effect of short heavy rain events. This means that initially a relatively small observation interval should be chosen (e.g. monthly) which can be increased if an immediate reaction can be ruled out.

Of course, it is acknowledged that such systematic data collection is a challenge. Perhaps more rigorous requirements with respect to landslide observations for permits for future construction into creeping slopes would be a way to collect more data.

This data would allow further mechanical understanding to be gained of the processes acting in creeping landslides beyond phenomenological representation. At this stage, it is believed

that derivation of models based e.g. on FEM that aim for a more realistic representation of the problem is hindered by a lack of information.

An option could be to use "hybrid" models that combine phenomenological models for parts of the landslide that are either simple to capture or where there is little data, and more complex models for parts where there is more data and more accurate predictions are required.

11.2.2 Future research: Seismic influence on permanent landslides

Building upon the insights gained during this work, a new research project that focuses solely on the analysis of seismic impact on creeping slopes or potentially also dormant landslides has already been launched on behalf of the Swiss Federal Office of Energy, SFOE. This project aims to further develop the analysis tool to include additional features such as full hydro-mechanical coupling and propagation of compression waves.

Within this project, one focus will be the better understanding of rate dependency along the slip surface. As said before, the velocity of a creeping landslide may change several orders of magnitude when accelerated during an earthquake. The relation that governs the rate dependent behaviour of shear strength along the slip surface (over the entire range of velocities) greatly influences the deformations that develop during and after the earthquake. As shown in this work, rate dependency is usually measured in ring-shear devices. But the changes in mobilized shear resistance when the shear rate changes are difficult to measure, since they can be of the order of or even smaller than the measurement error produced by the test device. Therefore, a novel design for a ring-shear device has been developed which aims on the one hand to minimize friction between the rings forming the sample chamber and on the other hand to make it possible to measure the residual friction caused by the device. This device should hopefully allow more reliable rate dependency formulations to be produced.

Another field of research will be the formation of the slip surface in order to better understand how the surface could form in nature and to better determine its thickness.

The constitutive formulation for the material in the weak zone around the slip surface should be developed further to be applicable for stress paths other than the plain strain DSS paths used for the calibration shown herein. To produce results that can be used to calibrate and benchmark the model for landslides in Switzerland, it is planned to run plain strain tests in a hollow cylinder device.

Lastly, within the scope of this project, it is intended to further research simplifying assumptions that have been made within the scope of the work shown herein. One of these

points is the effect of boundary conditions at the foot of the landslide. Though in this research the effect has shown to be small, it may be more significant for smaller landslides and may require better understanding, especially if effects such as geometric hardening have to be investigated.

Additionally, efforts should be made to reduce uncertainties with respect to the assumption that excess pore pressure develops mainly in one layer (weak layer) and with respect to the post-seismic dissipation of pore pressures. For more homogeneous slopes, the model can easily be changed to account for these conditions. For landslides made of glacial till or other heterogeneous materials, these will remain difficult questions. More insight could be gained by instrumenting a landslide with deformation measurements and pore pressure sensors at different depths. Such a setup would generally help to benchmark the estimates made by seismic landslide analysis models.

11.2.3 Future research: Hazard and risk analysis for creeping landslides

In order to further develop the hazard assessment, more dialogue with institutions responsible for the development of exposure modelling (in Switzerland: Meteo Swiss and the Swiss Seismological Service) would be favourable, so that knowledge from hazard models is back-propagated to ensure that exposure models cover the requirements necessary for the assessment of creeping landslide hazard. In practice, this means that weather models should allow data to be generated at a relatively coarse timescale and long-term variations (including climate change) to be reflected; seismic exposure, on the other hand, needs to be provided in terms of representative time-acceleration series or another suitable earthquake intensity parameter (e.g. Arias Intensity).

As shown, if vulnerability can be expressed in terms of displacement either as a continuous function or as a discrete function (e.g. for isolated structures), hazard assessment is possible with the shown methods. Depending on the structure, absolute or relative displacement may be the relevant hazard, and risk assessment frameworks should not mix them by default.

For structures that are built into the creeping slope and resist its movements, the interaction between the structure and the soil has to be taken into account. Finding damage functions that account for this interaction remains difficult. The approach proposed by Hug et al. (2017) allows the limit load to be found in terms of how much load can be provided by the landslide before the soil fails. This load could be used in risk analysis in cases for which the limit load of the structure can be found and uncertainties related to the parameters involved in the estimation can be quantified. More mechanisms e.g. in three dimensions should be analysed to further develop such an approach.

Curriculum Vitae – Philipp Wolfgang Walter Oberender

Personal Details

Date of Birth:	27.04.1986
Nationality:	German
Family status:	married

Work

since 09|2011	**Research Assistant, Institute for Geotechnical Engineering, ETH Zurich**	Zurich, Switzerland
06|2011-09|2014	**Polyport GmbH, Co-Founder**	Zurich Switzerland
01|2009--06|2009	**Obermeyer Planen und Beraten (OPB), Internship**	Munich, Germany
08|2005--09|2005	**Nemetschek AG München, Internship**	Munich, Germany

Education

09|2009 - 10|2011	**Eidgenössische Technische Hochschule Zürich** MSc in Civil Engineering, 5.66/6	Zurich, Switzerland
09|2005 - 05|2008	**Eidgenössische Technische Hochschule Zürich** BSc in Civil Engineering, 5.27/6	Zurich, Switzerland
08|2002 - 05|2005	**Michaeli Gymnasium** Abitur, 1.6/1	Munich, Germany

Language skills

German	mother tongue
English	fluent
French	basic knowledge
Latin	Latinum

Publications

11|2017	**S. Hug, B. Friedli, P. W. Oberender & A. M. Puzrin**, Ultimate loads on buildings in landslides, Géotechnique, in print	London, UK
03|2016	**P. W. Oberender & A. M. Puzrin.** Observation-guided constitutive modelling for creeping landslides, Géotechnique 2016, 66:3, PP. 232-247	London, UK
09|2012	**M. V. Schwager, P. W. Oberender & A. M. Puzrin**, Effects of time dependency on earth pressure measurements taken by inclinodeformometer, Proc. 4th Int. Conf. on Geotechnical and Geophysical Site Characterization, Porto de Galinhas, Brazil, 2012, PP. 571-577	Porto de Galinhas, Brasilien